Microinstabilities and Turbulent Transport in the Reversed Field Pinch

by

Daniel Richard Carmody

A dissertation submitted in partial fulfillment of
the requirements for the degree of

Doctor of Philosophy
(Physics)

at the

University of Wisconsin – Madison

2014

Defended on 10 December 2014

Dissertation approved by the following members of the Final Oral Committee:

Paul W. Terry · Professor of Physics

John Sarff · Professor of Physics

Chris Hegna · Professor of Engineering Physics

Stanislav Boldyrev · Professor of Physics

Cary Forest · Professor of Physics

M. J. Pueschel · Research Associate of Physics

Abstract

The work presented in this thesis is concerned with addressing the nature of drift wave microturbulence in the reversed field pinch (RFP). Microturbulence is an important phenomenon and contributor to heat and particle transport in tokamaks, where it has been studied for several decades, but its role in the RFP is a rather new topic of study. As such, the nature of RFP drift waves and their relationship to their tokamak counterparts is still developing, and many of the results in this work are focused on addressing this challenge.

Fundamental advances in microturbulence research have been made in recent decades through two parallel developments: the theoretical framework encompassed in the gyrokinetic model, and the computational power offered by massively-parallel, high-performance computing systems. Gyrokinetics is a formulation of kinetic theory in such a way that the fast timescale gyromotion of particles around magnetic field lines is averaged out. The implementation and use of RFP equilibrium models in gyrokinetic codes constitutes the bulk of this thesis.

A simplified analytic equilibrium, the toroidal Bessel function model (TBFM), is used in the gyrokinetic code Gyro to explore the fundamental scaling properties of drift waves in the RFP geometry. Two drift wave instabilities, the ion temperature gradient (ITG) mode and the microtearing mode (MTM) are found to occur, and the relationship of their critical threshold in driving gradients and plasma β is explored. The critical values in these parameters are found to be above those of similar tokamak cases by roughly a factor of the flux surface aspect ratio. The MTM is found to be stabilized by increasing the RFP pinch parameter Θ, making it unlikely for it to unstable in the high-Θ improved confinement pulsed poloidal current drive (PPCD) discharges.

Efforts are also made to address microinstabilities in specific experimental discharges of the Madison Symmetric Torus (MST). A semi-analytic equilibrium, the adjusted circular model (ACM), is developed and implemented in the gyrokinetic code Gene to investigate representative PPCD discharges. The flexibility of the ACM enables it to be used for the high-Θ PPCD discharges where the TBFM breaks down. The dominant linear instabilites

for the discharges modeled here – ITG and the trapped electron mode (TEM) – are studied, as are their scaling properties in the PPCD regime. It is found that these instabilities are present outside of the reversal surface, where the driving gradients are strongest. Nonlinear simulations of the TEM turbulence are performed, the first such done for the RFP, and zonal flows are found to play an important role in the nonlinear saturation mechanism. These zonal flows lead to a large Dimits-like shift and suppressed transport. There is also evidence that residual global tearing mode fluctuations are a necessary part of modeling transport in the RFP, even in improved confinement PPCD discharges, and by modeling these residual fluctuations through the use of an externally imposed perpendicular magnetic field perturbation it is possible to bring simulated fluxes into agreement with experiment.

Finally, the nature of the collisionless MTM, an instability seen to arise in some parameter regimes of the RFP, is investigated analytically using a fluid expansion in the drift-kinetic framework. Particular attention is paid to the role of magnetic drifts, and some evidence for their role in the collisionless instability is presented. Comparisons are made to gyrokinetic simulations and to earlier theory on the magnetic-curvature drift instability.

Acknowledgements

The work presented in this thesis would not have been possible without critical support and contributions from various people throughout my academic career, not to mention all the people that have supported me outside of my academic life.

This started first of all with my parents, who have always encouraged me to follow my interests and have given me advice and support along the way as I went where these interests took me. In taking me to various science museums and making available countless learning resources they nurtured an interest in science and the natural world that inevitably led to a pursuit of a scientific career. I can't appreciate enough everything they have done on my behalf.

A critical juncture in my scientific career came in the choice to attend the regional magnate school, the Thomas Jefferson High School for Science and Technology. In this environment I found excellent and enthusiastic teachers and fellow students who had the same appreciation for the sciences that I did. In particular I would like to express my gratitude to my various science teachers: Mr. McFaden, Dr. Acio, Dr. Dell, and Mr. Latham. They were able to explain the natural world with excitement and wonder, and for that I am grateful. I also found strong friendships and intellectually stimulating conversations with members of the cross country team, many of whom went on to pursue their own careers in science.

I attended Carnegie Mellon University intent on studying physics, and while there I found excellent guidance from Professors Vogel and Holman, and it was in a course taught by Prof. Russ that I developed my interest in pursuing research in nuclear fusion and plasma physics. I am also indebted to the crew of physics students at CMU, with whom I spent hours upon hours working on problem sets and discussing ideas in physics. Their comradery made sure it was time well spent.

For the work presented in this thesis, I am of course endebted to my advisor, Prof. Paul Terry, who provided the freedom to pursue interesting research topics and much needed guidance along the way. Plasma students at UW-Madison are fortunate to be able to work

with and be taught by many excellent professors, and I have benefited from classes taught by Professors Terry, Boldyrev, Sovinec, and Hegna. Prof. Hegna was also the source of several useful conversation concerning some of the work presented in this thesis. Many thanks are also due to Varun Tangri, who introduced me to the basics of gyrokinetics and the GYRO code, and to M. J. Pueschel, whose expertise with GENE enabled far more progress in this work than would have otherwise been possible. Other members of Prof. Terry's group, past and present, have also pushed me along in my graduate career, especially independent study sessions organized by Kirit Makwana which helped to fill in some of the gaps in my knowledge of plasma physics.

And finally I would like to thank my friends and fellow graduate students in Madison, especially other members of the incoming class of 2009, who created such a wonderful environment in which to spend a few years and who have made Madison such a hard place to leave.

This thesis is dedicated to Kevin and Cora, my wonderful parents, whose guidance and support have been with me since before I can remember and without whom I wouldn't have been able to come as far as I have.

Contents

Abstract i

Acknowledgements iii

Contents **vi**

List of Figures **ix**

List of Tables **xx**

1 Introduction **1**

1.1 The Energy Picture 1

1.2 Nuclear Fusion Processes 5

1.3 Fusion Power 6

1.4 Drift Wave Instabilities and Turbulence 9

1.5 Present Work 11

2 Gyrokinetics **13**

2.1 The Gyrokinetic Model 14

2.2 Gyrokinetic Codes 25

2.3 Chapter Summary 31

3 The Reversed Field Pinch **32**

3.1 General Features of the Reversed Field Pinch 33

3.2 Madison Symmetric Torus 35

3.3 RFP Equilibrium Modeling 39
3.4 Chapter Summary 51

4 Fundamental microinstability studies in an RFP equilibrium 53
4.1 Equilibrium Modeling 54
4.2 Beta Scan 55
4.3 ITG β Suppression 60
4.4 Microtearing Modes 63
4.5 Chapter Summary 72

5 Microturbulence studies of improved confinement discharges 76
5.1 Modeling 77
5.2 Linear Results 82
5.3 Nonlinear Results 95
5.4 Chapter Summary 103

6 The collisionless microtearing mode 110
6.1 Microtearing Mechanisms 111
6.2 Microtearing and Magnetic Drifts 114
6.3 Derivation 117
6.4 Parallel Current Structure 121
6.5 $\Phi = 0$ Result 124
6.6 $\Phi \neq 0$ Result 127
6.7 Chapter Summary 131

7 Conclusions 135
7.1 Summary of Results 136
7.2 Future Work 139

Appendix A Derivation of expressions for the collisionless microtearing mode 141

A.1 Parallel current 141

Bibliography **149**

List of Figures

1.1 Proportion of U.S. energy consumption from different sources. Over 80% of U.S. consumption comes from fossil fuels. Source: U.S. Energy Information Administration. 2

1.2 World energy consumption, data and predictions. Consumption is expected to increase by about 50% over current levels by 2040. Source: U.S. Energy Information Administration. 3

1.3 Moore's law in the fusion triple product, a measure of the efficiency of laboratory fusion experiments. The progress of fusion energy research has outpaced similar measures of progress in other fields. Source: Ikeda (2010) 7

1.4 Physical mechanism of a drift wave. A small perturbation in density in the presence of a background gradient leads to electric fields and a resultant $E \times B$ drift that causes a wave to propagate in the transverse (y) direction. Under certain conditions, the original perturbation may be reinforced and amplified, leading to instability. Source: *Introduction to Plasma Physics and Controlled Fusion*, F. Chen 10

2.1 Schematic of the gyro-center transform. The fast gyromotion of a particle around a magnetic field line is averaged over, eliminating a phase-space variable and essentially reducing the physics to that of a moving charged ring. 15

3.1 Schematic diagram of an RFP. Key features of the magnetic field geometry can be seen: concentric circular flux surfaces, a toroidal field that reverses out towards the edge of the device, and toroidal and poloidal fields that are roughly equivalent in strength throughout much of the plasma volume. Courtesy J. S. Sarff. 34

3.2 A q-profile for a 'standard' RFP discharge showing the radial extent of magnetic island structures. These overlapping islands are associated with the stochastic field seen in the Poincaré plot in Fig. 3.3. Source: Sarff et al. (2003) 35

3.3 Poincarè puncture plot for a standard (non-PPCD) MST discharge. Overlapping magnetic islands result in a stochastic magnetic field structure. 37

3.4 Poincaré puncture plot for a sample PPCD discharge. By flattening the current profile, global tearing modes are largely stabilized and magnetic flux surfaces are better-behaved as compared to the standard discharge. 38

3.5 Toroidal field (blue) and poloidal field (green) for the Bessel function model, with $\Theta = 1.35$. This model contains the essential feature of the RFP, which is the reversal of the toroidal field and a $q = 0$ surface. 42

3.6 The TBFM (green dashes) and experimental magnetic field (blue dots) at $\Theta = 1.5$. Shown are both the toroidal and poloidal components of the magnetic field. The TBFM still somewhat follows the equilibrium field, but it is starting to break down. 45

3.7 The magnitude of the magnetic field for the experimental field (blue dots), the TBFM (green dashes), and the ACM (red line) for a $\Theta = 2.96$ equilibrium. The ACM does a good job of describing the equilibrium, in contrast to the TBFM. 45

3.8 The experimental magnetic field (blue dots) along with the circular equilibrium (red dashes). By not allowing for a minor radius dependence of the toroidal field the circular model encounters a singularity at the $q = 0$ (reversal) surface. Roughly twenty radial points are used to create these curves, which leads to a peak in the magnetic field for the circular equilibrium rather than a true singularity. 48

3.9 The toroidal magnetic field for the experimental field (blue dots), the TBFM (green dashes), and the ACM (red line) for a $\Theta = 2.96$ equilibrium. The toroidal field of the TBFM reverses direction twice, a feature seen in neither the experimental field nor the ACM fit. 50

3.10 The poloidal magnetic field for the experimental field (blue dots), the TBFM (green dashes), and the ACM (red line) for a $\Theta = 2.96$ equilibrium. The TBFM poloidal field erroneously contains a reversal, while the fit provided by the ACM successfully matches the experimental field. 50

3.11 Comparison of growth rates and frequencies between GYRO (green) and GENE (red) for a $\Theta = 1.35$ equilibrium plotted against normalized wavenumber $k_\theta \rho_s$, with $r/a = 0.5$, $q = 0.186$, $\hat{s} = -0.716$. The TBFM provides the equilibrium model for the GYRO results and the ACM for the GENE results. There is good agreement in this parameter regime. Other parameters, and more information on the GYRO results, can be found in Tangri et al. (2011). Other results for these sets of parameters can be found in Ch. 4. 52

4.1 Growth rate and mode frequency plotted as a function of β for $k_\theta \rho_s = 0.372$. ITG is stabilized with increasing β, and MTM requires a critical β for instability. A transition of the dominant mode from ITG to MTM occurs at $\beta \approx 5\%$. Also shown is the growth rate for a case where $a/L_{Te} = 3.0$, where MTM is stabilized, to show more complete suppression of the ITG. In GYRO's sign convention, positive (negative) frequencies denote the electron (ion) direction. 57

4.2 Growth rate and frequency as a function of wavenumber $k_\theta \rho_s$ for two different values of β. ITG is seen to be dominant at $\beta = 1\%$, microtearing at $\beta = 9\%$. In this convention, a negative (positive) real frequency indicates a mode in the ion (electron) diamagnetic direction. Collisions are turned off for these simulations. 58

4.3 Growth rate and mode frequency plotted as a function of $k_\theta \rho_s$ for $\beta = 0.04$. At this value of β ITG and MTM exist at similar scales. 59

4.4 Beta stabilization of ITG for the parameters $r/a = 0.4, q = 0.244, a/L_{Te} = 0, a/L_n = 0.08$. A parabolic fit has been used to project out to a critical beta for stabilization of $\sim 9\%$. The critical β estimated by Eq. (4.9) is $\sim 19\%$, roughly a factor of two larger than that seen in the simulations. 62

4.5 Eigenmode structure for the MTM in electrostatic potential Φ and magnetic potential $A_\parallel$ with both real (green dashed curve) and imaginary (red solid curve) components. The fields are plotted against the magnetic-field following ballooning angle θ_*. This mode displays tearing parity, which is recognized as even parity in $A_\parallel$ and odd parity in Φ. 64

4.6 Eigenmode structure for the ITG mode in electrostatic potential Φ (upper plot) and magnetic potential $A_\parallel$ (lower plot) with both real (pink curve) and imaginary (orange curve) components. The fields are plotted against the magnetic-field following ballooning angle θ_*. This mode displays ballooning parity, which is recognized as odd parity in $A_\parallel$ and even parity in Φ. As an electrostatic mode plotted for $\beta = 0.001$ the magnetic vector potential fluctuation is quite small. . 65

4.7 Growth rate plotted against temperature gradient for $k_\theta \rho_s = 0.372$ in the case of MTM (red squares) and ITG (green circles). Both instabilities have a threshold around $a/L_T \approx 3.5 - 4.0$, for their respective driving gradients, although these thresholds may differ for an alternate set of parameters. 66

4.8 Growth rate plotted against the temperature ratio T_i/T_e for $k_\theta \rho_s = 1.488$. Shown are MT (a) and ITG (b). The qualitative dependence is consistent with expectations of modes with either ion or electron gradient drives. 67

4.9 MTM growth rate and frequency plotted against ν for $k_\theta \rho_s = 1.488$. There appear to be two distinct regmes: a region of constant growth rate and constant real frequency at low ν and a separate region at ν with a peak in growth rate and a real frequency that scales linearly with ν. 70

4.10 MTM wavenumber spectrum at $\nu = 1$ (a) and collisionality scan (b) for different values of r/a. The corresponding values of q_0 and shear are — $r/a = 0.4$: $q_0 = 0.209$, $\hat{s} = -0.382$ (red solid curve); $r/a = 0.5$: $q_0 = 0.186$, $\hat{s} = -0.716$ (green dashed curve); $r/a = 0.6$: $q_0 = 0.155$, $\hat{s} = -1.344$ (blue dotted curve). There is stabilization of MTM with increasing radius r/a, especially prevalent at low ν. Increased radius coincides with increased shear, which may play a role in stabilization. 71

4.11 MT wavenumber spectrum at $\nu = 1$ for different values of Θ, the RFP pinch parameter. The corresponding values of q_0 and shear are — $\Theta = 1.1$: $q_0 = 0.255$, $\hat{s} = -0.4$ (blue curve); $\Theta = 1.2$: $q_0 = 0.224$, $\hat{s} = -0.507$ (green curve); $\Theta = 1.35$: $q_0 = 0.186$, $\hat{s} = -0.716$ (red curve); $\Theta = 1.5$: $q_0 = 0.153$, $\hat{s} = -1.011$ (cyan curve); $\Theta = 1.7$: $q_0 = 0.115$, $\hat{s} = -1.637$ (purple curve). There is stabilization of MTM with increasing Θ. Increased Θ corresponds to increased shear, which may play a role in stabilization. This also suggests that higher-Θ PPCD discharges may be stable to MTM. 72

4.12 The role of magnetic drift in the MTM instability. The parameter α is a factor regulating the strength of the magnetic drift (including both curvature and ∇B drifts) in the code. Shown are $\nu = 0.001$ (a) and $\nu = 1.0$ (b), as well as $k_\theta \rho_s = 1.488$ (red solid curve) and $k_\theta \rho_s = 0.186$ (green dotted curve). This behavior is similar to that seen in Finn and Drake (1986). The points at low α represent a separate mode that has not been studied in detail. 73

5.1 Radial profiles for the safety factor and the temperature for the 200 kA case. The red vertical lines indicate the radial locations at which simulations were performed. The blue shaded region indicates high shear ($|\hat{s}| \gtrsim 10$) and has been excluded from modeling. 79

5.2 Radial profiles for the safety factor and the density for the 500 kA case. The red vertical lines indicate the radial locations at which simulations were performed. The blue shaded region indicates high shear ($|\hat{s}| \gtrsim 10$) and has been excluded from modeling. 80

5.3 Peak growth rates versus minor radius for the 200 kA (a) and 500 kA (b) cases. The blue shaded region indicates high shear ($|\hat{s}| > 10$) and has been excluded from modeling. $\gamma_{\max}$ is the maximum growth rate attained from a k_y scan. . . 83

5.4 Growth rates (a) and frequencies (b) as functions of wavenumber at different radial locations for the 200 kA case. For $r/a \leq 0.84$ the modes are in the ion direction and interpreted to be ITG. The outermost radius displays a smooth transition from electron to ion direction with wavenumber and is identified as an ITG/TEM hybrid. 85

5.5 Growth rates (a) and frequencies (b) plotted against ion temperature gradient for the 200 kA case for multiple radial locations. The modes at $r/a \leq 0.84$ display a strong dependence on this gradient and are identified as ITG. The black squares denote growth rates and frequencies at the experimental gradients. 86

5.6 Growth rates plotted against electron temperature gradient for the 200 kA case for multiple radial locations. Except for the outermost mode, which has hybrid characteristics, there is not a strong dependence on this gradient. 87

5.7 Growth rates (a) and frequencies (b) plotted against density gradient for the 200 kA case. The complicated dependence of the instability at $r/a = 0.89$ and a real frequency that transitions smoothly from ion direction to electron direction are characteristics for a hybrid mode. The black squares denote growth rates and frequencies at the experimental gradients. 88

5.8 The value of $\eta \equiv (d\ln T/dr)/(d\ln n_0/dr)$ versus minor radius. $T_i \propto T_e$ in these runs, so $\eta = \eta_e = \eta_i$. The shaded region indicates the critical range $\eta_i = 1.2-1.4$, above which instabilities tend to be ITG and below TEM, in relatively good agreement with the observations from the present simulation data. Near the threshold, the dominant instabilities may become hybrid modes with characteristics of both ITG and TEM. 89

5.9 Growth rates (a) and frequencies (b) as functions of wavenumber at different radial locations for the 500 kA case. These modes are driven by the density gradient and are identified as TEM; only at the outer radii and higher k_y can signatures of ubiquitous modes be seen. 90

5.10 Growth rates (a) and frequencies (b) plotted against density gradient for the 500 kA case. The dominant modes for the nominal parameters show a strong dependence on density gradient and are identified as density-gradient-driven TEM. The black squares denote growth rates and frequencies at the experimental gradients. 91

5.11 Growth rates plotted against β for the 200 kA case. All modes show little variation with β, a characteristic that is related to a high β threshold for electromagnetic instabilities. The frequencies are similarly unaffected by variations of β. 92

5.12 Growth rates plotted against electron temperature gradient for the 500 kA case. There is no critical gradient. 93

5.13 Growth rates plotted against ion temperature gradient for the 500 kA case. There is some stabilization of the TEM growth rate with increasing ion temperature gradient, with a likely ITG mode eventually arising for $r/a = 0.76$. 94

5.14 A time trace of the nonlinear fluxes for a density gradient of $R_0/L_n = 58.8$. The dominant channels are electron heat flux Q_e^{es} (blue) and particle flux Γ^{es} (green). There is a large overshoot in the beginning due to strong linear growth rates, but this is countered by strong nonlinear saturation mechanisms. 96

5.15 The flux spectra for (a) $r/a = 0.86$ and $R_0/L_n = 52.3$ and (b) $r/a = 0.91$ and $R_0/L_n = 71.9$. Shown are the electrostatic particle flux Γ^{es} (blue dashed line) and the electrostatic electron heat flux Q_e^{es} (green solid line). At $r/a = 0.86$, the spectra peak at $k_y\rho_s = 0.3$, while at $r/a = 0.91$ the peak shifts to $k_y\rho_s = 0.2$. In comparison, the linear growth rates peak at $k_y\rho_s = 0.6$ for both cases. . . . 98

5.16 Electron heat and particle fluxes are plotted as a function of density gradient for the 500 kA case at $r/a = 0.86$. The linear growth rates for these parameters are also shown for comparison. Straight line fits have been applied to the fluxes, and a cubic fit has been applied to the TEM portion of the linear growth rate curve. The onset for the nonlinear fluxes occurs at $R_0/L_n \approx 37$, roughly a factor of 3 greater than the linear threshold of $R_0/L_n \approx 13$. The vertical dashed line indicates the nominal experimental value of R_0/L_n. 103

5.17 Contours of electrostatic potential Φ and electron density n for the 500 kA case at (a) $r/a = 0.86$ and $R_0/L_n = 52.3$ and (b) $r/a = 0.91$ and $R_0/L_n = 71.9$. Strong vertical features ($k_y = 0$) in Φ are indicative of zonal flow activity, while the density contours show some (but relatively weaker) zonal structures as well. 104

5.18 (a) Particle flux versus density gradient for three different values of magnetic shear, $\hat{s} = (r/q)(dq/dr)$. (b) Zonal flow shearing rate divided by linear growth rate versus density gradients for different values of magnetic shear. For $\hat{s} = 2.5$ the zonal flow shearing rate drops below $10\gamma_{\text{lin}}$ (indicated by the black dashed line in the lower plot) and the flux substantially increases. Other parameters are as given for the 500 kA case at $r/a = 0.86$. 105

5.19 A profile of the magnetic diffusivity as calculated by the MAL code. The calculation is only intended to be valid from $r/a = 0.5 - 0.7$, but it serves as an upper limit and a useful order of magnitude of this quantity at the radius simulated in this work. Since the nonlinear fluxes are sensitive to the strength of the imposed field, it is important to determine the experimental magnetic diffusivity as accurately as possible. For the original figure and more on the MAL code and the calculation of D_m, see B. Hudson, Ph.D. Thesis (2006). 106

5.20 Poincaré puncture plots without (a) and with (b) a small added resonant perturbation to $A_\parallel$. Though the flux surfaces are still largely intact, the imposition of a small resonant radial magnetic field leads to the reduction of zonal flows and a large increase in transport. More details on the field line integration routine may be found in Pueschel et al. (2013). 107

5.21 Electron heat (blue) and particle flux (green) before and after the inclusion of an imposed perturbation on $A_\parallel$. The imposed magnetic diffusivity weakens zonal structures and results in a large increase in the transport levels. Shown are the fluxes after instituting the artificial perturbation (solid lines) as compared with those same quantities before (dashed lines). 108

5.22 Contours of Φ and n for the $r/a = 0.86$ case where a resonant $A_\parallel$ perturbation has been implemented to introduce a small radial perturbation to the magnetic field. The effect is to greatly diminish the zonal structures evident in Fig. 14 (a). 109

6.1 Schematic of the thermal force, responsible for the collisional MTM instability mechanism. Electrons streaming along the magnetic field line encounter frictional forces associated with collisions. A radially perturbed magnetic field in the presence of a background temperature gradient leads to an imbalance between the collisional friction and the creation of a parallel current. This parallel current can then reinforce the original magnetic perturbation, leading to instability. 112

6.2 Results from the GENE code showing MT growth rate versus f_c, a parameter that scales the strength of the magnetic drift in the Vlasov equation. A parity selection procedure has been implemented acting on Φ and $A_\parallel$ so that only tearing parity modes are allowed. The strength of the instability scales with η_e. Adiabatic ions are used and other parameters are $R_0/L_n = 1.74$, $k_y\rho_s = 1.4$, and $\beta = 0.09$. 116

6.3 Growth rate plotted against curvature drift frequency, with both quantities normalized to the diamagnetic frequency, for the magnetic-curvature drift mode of Finn and Drake. A peak occurs around $\omega_c/\omega_{*p} \simeq 1$. Multiple values of $f \equiv \omega_{*t}/\omega_{*p}$ are shown, so that higher values of f, with constant density gradient, can be associated with a stronger temperature gradient. Note that the parameter f_c in Fig. 6.2 corresponds with ω_c/ω_{*p} here, rather than f. Source: Finn and Drake (1986). 117

6.4 Real (blue curve) and imaginary (orange curve) portions of $J_\parallel(x)$ for $\hat{\omega}_D = 0$, $\eta = 10$, $\tau = 1$. The assumption $\hat{\omega} = 1 + \eta$ has been used. The real part is even in x while the imaginary part is odd. 122

6.5 $|J_\parallel(x)|$ for $\hat{\omega}_D = 0$, $\eta = 10$, $\hat{\omega} = 1 + \eta$, $\tau = 1$. 122

6.6 $|J_\parallel(x)|$ for $\hat{\omega}_D = 0$ (blue curve) and $\hat{\omega}_D = 1$ (orange curve). Other parameters are $\eta = 10$, $\hat{\omega} = 1 + \eta$, and $\tau = 1$. 123

6.7 $|J_\parallel(x)|$ for $\hat{\omega}_D = 0$ (blue curve) and $\hat{\omega}_D = 1$ (orange curve). Other parameters are $\eta = 1$, $\hat{\omega} = 1 + \eta$, and $\tau = 1$. 123

6.8 Real frequency (top plot) and growth rate (bottom plot) as functions of η for $\hat{\omega}_D = 0$. All roots of the dispersion relation are shown. Quantities are normalized to ω_n^*. Root 4 has features of the drift-tearing mode, with $\omega \approx 1 + 4\eta/3$ and in the direction of ω_n^* (electron direction). All roots are stable. 131

6.9 Real frequency (top plot) and growth rate (bottom plot) as functions of $\hat{\omega}_D$ for $\eta = 10$. Quantities are normalized to ω_n^*. For positive $\hat{\omega}_D$ a coupling occurs between modes, yielding an instability in the electron direction driven by the magnetic drift. 132

6.10 Real frequency (top plot) and growth rate (bottom plot) as functions of η for $\hat{\omega}_D = 1$. Quantities are normalized to ω_n^*. The parameter η is destabilizing, although there is no critical threshold. 133

6.11 Growth rate versus $R = -\Delta' \hat{\omega} c^2/(d\omega_{pe}^2) \propto \beta^{-1}$ for the $\hat{\omega}_D$-driven mode with $\eta = 10$ and $\hat{\omega}_D = 1$. The growth rate goes to zero near $R \approx 500$, implying that there is a critical β threshold for this instability. 134

List of Tables

3.1 Machine specifications and normal operating parameters for the Madison Symmetric Torus (see Chapman et al. (2009)). These ranges include both standard and improved confinement discharges. 36

5.1 Physical parameters for the two MST discharges studied in this work, as obtained from the MSTFit equilibrium reconstruction code. It has been assumed that $T_i = 0.4T_e$, and therefore $R_0/L_T = R_0/L_{T_e} = R_0/L_{T_i}$. For more on MSTFit, see Anderson et al. (2004). 77

Chapter 1

Introduction

> "Energy transitions have been among the most important processes of technical evolution: they are driving our inventiveness, shaping the modern industrial, and postindustrial, civilization, and leaving their deep imprints on the structure and productivity of economies as well as on the organization and welfare of societies."
>
> Vlacav Smil, *Energy at the Crossroads*, 2003

> "I believe that water will one day be employed as fuel, that hydrogen and oxygen which constitute it, used singly or together, will furnish an inexhaustible source of heat and light, of an intensity of which coal is not capable."
>
> Jules Verne, *Mysterious Island*, 1874

1.1 The Energy Picture

Civilization, in the modern context, has long relied on the consumption of energy, and some of the most important issues of the late twentieth and early twenty-first centuries have revolved around the topic of energy supply. From consumer-scale "price at the pump" to international geopolitics, energy has been a key consideration in both household and

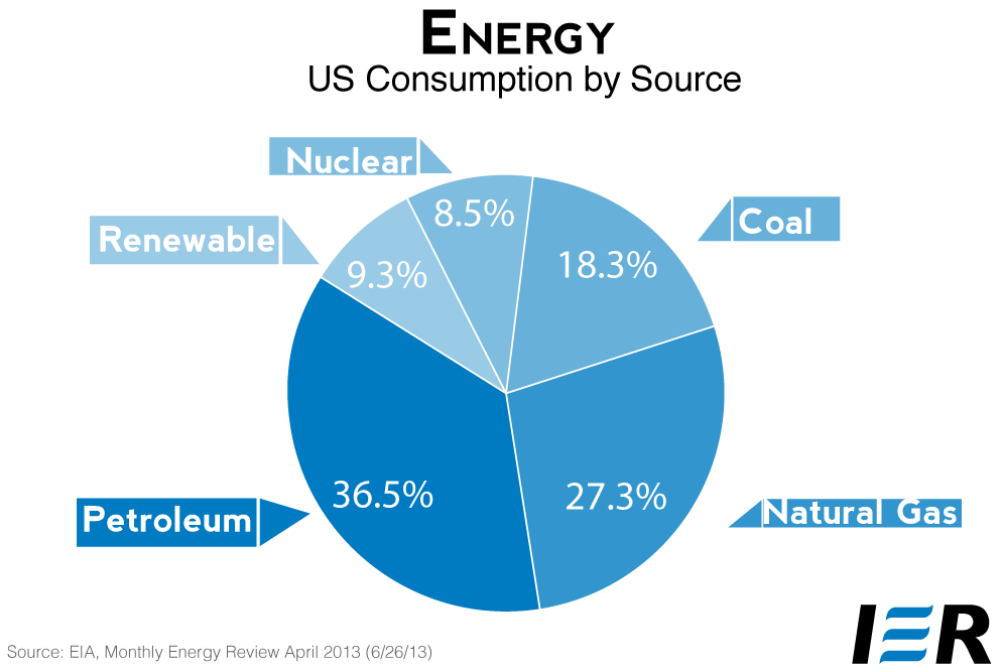

Figure 1.1: Proportion of U.S. energy consumption from different sources. Over 80% of U.S. consumption comes from fossil fuels. Source: U.S. Energy Information Administration.

national planning, and it is likely to continue to be important in the unfolding events of the new millenium. Electricity consumption has come to be a necessary element of daily life for much of the world's population, allowing access to means of communication, efficient household and industrial practices, and educational material, among other uses. However, this consumption carries with it costs beyond the standard measure of cents per kilowatt-hour. These additional costs stem from the complicated means that determine where energy comes from and how it is used, and they can include costs to social or ecological systems.

The energy supply of the United States is currently very heavily dependent on fossil fuels, which constitute roughly 80% of consumption (Fig. 1.1). The remainder is divided roughly equally between nuclear fission and renewables. Each of these energy sources carries its own set of costs and benefits.

The issues associated with energy policy are vast. On a local scale, pollution from fossil fuel plants and gasoline vehicles contribute to air quality degradation and water contamination. On a national level, energy hungry businesses and consumers require a

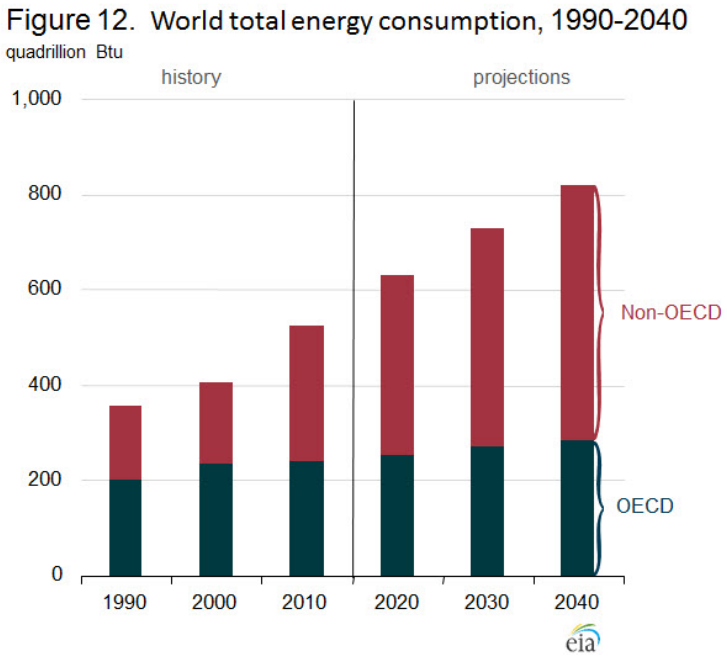

Figure 1.2: World energy consumption, data and predictions. Consumption is expected to increase by about 50% over current levels by 2040. Source: U.S. Energy Information Administration.

cheap and secure energy supply for a strong economy, thereby entangling a nation's domestic interests with the politics of its energy suppliers. Finally, on a global scale, climate change, driven to a large extent by CO_2 emissions from the burning of fossil fuels, threatens to upset the planet's weather systems and ecosystems in ways that are still not well understood.

The U.S. Energy Information Administration has projected the world's energy consumption to increase by 56% by the year 2040, as can be seen in Fig. 1.2. And although there are ample supplies of conventional energy resources to meet these needs for a while (coal reserves alone are estimated at over a hundred years [1]), the issues presented above are likely to be exacerbated by increased consumption. Addressing these challenges is a high priority.

Potential Solutions

There are often two broad categories of solutions offered up to deal with these problems: improvements in technological capability, or changes in personal habit and industrial methods (with some obviously strong connections between the two).

One of the main avenues to address these issues is to find alternative sources of energy, often with the focus being on renewables such as wind, solar, and hydroelectricity. Although an improvement on the existing system in many ways, these renewable energy sources have their own drawbacks and limitations.

These limitations have been discussed in depth elsewhere [2]. Among them are the problems of intermittency and energy storage, energy density and land area, transmission losses, and the need for extensive mining of raw materials. The conclusion to be drawn from a consideration of these limitations is that, although renewable energy sources will play an important and growing role in the world's energy supply in the years ahead, they are unlikely to be a silver bullet, the one approach that solve all energy-related problems. Therefore, it should be expected that a future energy portfolio will be a diversified mix of fossil fuels, renewables, and nuclear power. This last option can be separated into nuclear fission, the process on which all currently operating nuclear power plants are based, and nuclear fusion.

As an energy source, nuclear fusion provides many benefits over existing energy technologies. A good overview of the advantages of fusion power may be found in Freidberg (2007) [2]. Nuclear fusion, in the context of a potential commercial power plant, relies on fuel that is both abundant and relatively cheap to produce, consisting of reactions between certain isotopes of hydrogen: deuterium, which can be easily extracted from seawater, and tritium, which can be bred from lithium, an element that occurs naturally on earth. If fusion were to provide the entire global energy needs, then at the current rate of consumption it is estimated that supplies of lithium would last for 20,000 years and deuterium for billions of years [2]. The extraction of lithium from seawater could extend the feasible range of fusion even further.

Fusion power generation, like nuclear fission or renewable sources, does not involve the production of CO_2 or other greenhouse gases. Fusion processes also do not involve any long-lived radioactive products, so both waste disposal and proliferation concerns would not be as much of an issue as they are with nuclear fission. Additionally, there is no threat of a meltdown or catastrophic failure as there is with fission plants, making fusion inherently safer. Fusion could provide clean, carbon-free electricity with high capacity factor and no threat of large-scale disasters, and unlike renewable sources it has the capability to be a location-independent baseload source. It is these features that makes energy from nuclear fusion such an exciting and desirable prospect.

1.2 Nuclear Fusion Processes

Nuclear fusion is the process by which atomic nuclei collide, combine, and release energy. As the process fueling the Sun, nuclear fusion is essentially the source of almost all energy on earth (with exceptions being nuclear fission and geothermal energy, which is itself a result of fission). Solar and wind energies are powered by either direct or passive heating of the earth's surface, and all fossil fuels were once living plants and animals that received their energy either directly (in the case of plants) or indirectly (in the case of animals) from the Sun.

The process of fusion that takes place in the Sun was first outlined by Hans Bethe [3], for which he was awarded the 1967 Nobel Prize in Physics. This process involves nuclear reactions with hydrogen or its isotopes – deuterium (D), composed of one proton and one neutron or tritium (T), composed of one proton and two neutrons.

The energetically easiest fusion reaction to achieve in an accessible temperature range is the deuterium-tritium (D-T) reaction [2], and this property makes it the primary approach of fusion energy research. The basic reaction can be written as

$$\mathrm{D} + \mathrm{T} \rightarrow \alpha + \mathrm{n} + 17.6\mathrm{MeV} \tag{1.1}$$

where α represents an α-particle (helium nucleus). In this reaction, 17.6 MeV is generated

due to mass differences and supplies kinetic energy to the reaction products. It is this energy that can be extracted as part of an energy generating process.

In order to achieve the fusion of the elements on the left side of Eq. (1.1), it is necessary to overcome the strong Coulomb repulsion that exists between the two postively charged nuclei. Overcoming this powerful force presents the fundamental challenge of fusion research.

Extremely high temperatures are needed to achieve fusion, on the order of millions of degrees. At these temperatures, elements exist in the plasma state, in which particles are partially or completely ionized and exhibit collective, long-range interaction. One of the major issues for terrestial plasma experiments is confinement, since plasmas are highly energetic and cannot be confined by material walls. This problem is overcome in the Sun with gravitational confinement, but this is not an option at the scale of laboratory experiments. Therefore, an alternative approach to confinement is needed. Although there are several techniques that have been developed to achieve this, the present work focuses on just one: magnetic confinement. In this approach, geometric shaping of strong magnetic fields is used to create a 'magnetic bottle' of sorts that contains the plasma. Thus confined, the plasma may be heated to fusion.

1.3 Fusion Power

There are some important metrics for assessing the success of a fusion reactor. One of these is the Lawson parameter, or Lawson triple product, $nT\tau_E$ [4]. A product of the density n, the temperature T, and the energy confinement time τ_E, this parameter is a measure of the ability of a plasma confinement scheme to maintain a high energy density plasma (as measured by nT) for a long period of time (τ_E). Having a sufficiently high triple product is crucial for a viable fusion reactor, and the progress in fusion research as measured by this parameter is given in Fig. 1.3.

Another important measure for a fusion power plant is the gain factor Q. This is defined as

$$Q = \frac{\text{net thermal power out}}{\text{total heating power in}} \tag{1.2}$$

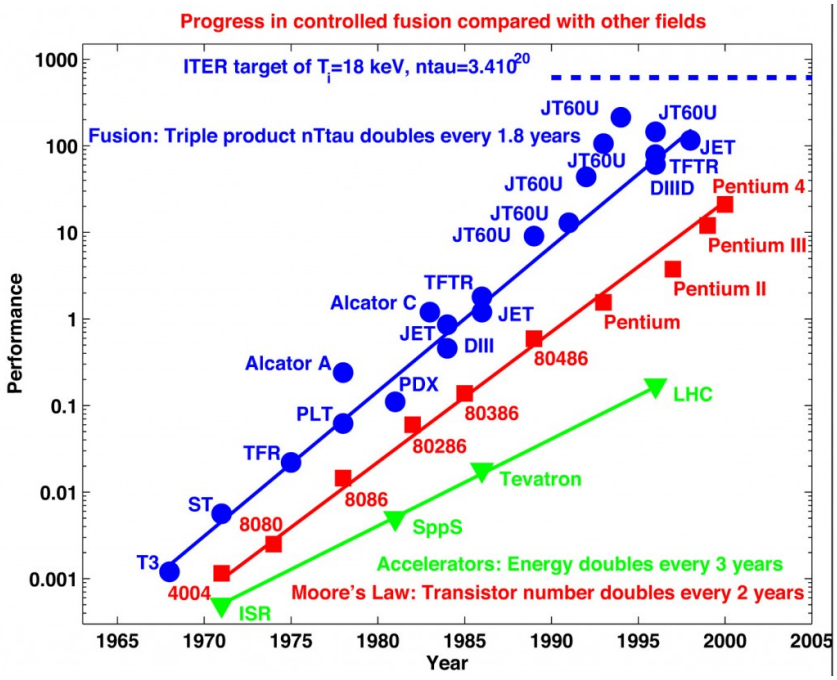

Figure 1.3: Moore's law in the fusion triple product, a measure of the efficiency of laboratory fusion experiments. The progress of fusion energy research has outpaced similar measures of progress in other fields. Source: Ikeda (2010)

and is simply a measure of the efficiency of energy production in the power plant. A value of $Q > 1$ means that the thermal energy generated by fusion reactions is greater than that required to heat the plasma. The limit $Q = \infty$ corresponds to ignition, when no heating is required and the fusion reactions are entirely self-sustaining, given appropriate refueling.

The history of fusion research is one of continuous refinement and advance. The first experiments conducted in the 1950s were limited by large scale instabilities and had energy confinement times on the order of only microseconds. As Fig. 1.3 shows, significant progress has been made in improving the confinement capabilities of fusion devices since then, and in fact the fusion triple product has progressed faster than the Moore's law followed by transistors. Today's machines can reach energy confinement times orders of magnitude larger than those attained in the first plasma confinement experiments, with energy confinement times on the order of a second, and with some machines able to stably operate for periods of hours [5]. The latest in this series of experiments is ITER, the experimental fusion reactor

currently under construction in Cadarache, France [5]. ITER is designed to reach a Q of 10.

Although ITER and much of the world's fusion research is pursuing the tokamak design, there are alternative approaches as well. The work presented in this thesis is primarily concerned with a different type of magnetic confinement device: the reversed field pinch (RFP). Like the tokamak, the RFP is a toroidal confinement device, but it differs in a few key ways, resulting in a different set of benefits and drawbacks relative to the tokamak [2].

The RFP is designed to have a smaller toroidal field than the tokamak, requiring smaller magnetic coils and cheaper construction costs. It is also capable of achieving higher values of normalized plasma pressure (β). Furthermore, due to the high toroidal current and the presence of finite resistivity, it is able to resitively heat to ignition, a process referred to as Ohmic heating. This may alleviate some of the need for expensive external heating sources. Once fusion becomes realizable in a laboratory environment it then becomes an economic problem, rather than a scientific or engineering one, and only as a cost-effective method for energy production can it make serious contributions as an alternative energy. The potentially cost-saving advantages of the RFP configuration are therefore an important consideration.

There are several disadvantages to the RFP approach, however, that pose a slightly different set of challenges than the tokamak and must also be considered. The low toroidal magnetic field means that the RFP is susceptible to magnetohydrodynamic (MHD) instabilities, notably global tearing modes, although there are techniques for controlling these, as will be discussed. Additionally, since the large toroidal current plays a key role in the magnetic equilibrium, an external current drive is needed. However, just as the tokamak design has been able to overcome the many of the challenges of large scale instabilities, it is expected that the RFP can as well. The RFP is therefore an important area of research in magnetic confinement fusion.

Along with the increase in energy confinement time seen in Fig. 1.3 there has been an associated decrease in the spatial scales of the phenomena that tend to limit confinement.

Early on, devices were limited by large scale disruptions, sudden and catastrophic events that were characterized by bulk movement of the plasma to the wall and its immediate loss. With large scale instabilities stabilized and disruption events eliminated, the task of fusion research becomes that of reducing the slower processes of particle and heat transport. This transport may arise due to a number of various effects, all of which cause the diffusion of particles and energy to the edge of the device, where it is lost. The dominant source of transport in many devices is now due to small scale "drift wave" instabilities.

1.4 Drift Wave Instabilities and Turbulence

The dominant source of transport in most fusion devices is now believed to be due to drift wave driven microturbulence, sometimes referred to as 'anomalous' transport since it was first identified only because it exceeded predictions from classical transport (diffusion driven by Coulomb collisions).

Drift waves arise in plasmas due the creation of diamagnetic currents $\mathbf{J}$ that are needed to satisfy radial force balance $\mathbf{J} \times \mathbf{B}/c = \nabla p_e + \nabla p_i$, with $\mathbf{B}$ the background magnetic field and p_e and p_i the electron and ion pressures. The currents are associated with diamagnetic drift velocities $\mathbf{v}_{Dj} = (1/(q_j n_j B))\nabla p_j$, for j a label for a particle species with charge q_j, n_j, and pressure p_j. Drift wave instabilities are driven by gradients in plasma pressure, temperature, and/or density and have frequencies on the order of the diamagnetic drift frequency $\omega_j^* = \mathbf{k} \cdot \mathbf{v}_{Dj}$. The essential physics of drift waves is presented in Fig. 1.4. Gradients perpendicular to the background magnetic field enable the propagation of waves in the diamagnetic direction through the generation of an $E \times B$ drift. Under certain circumstances, phase differences may arise between the various fluctuations that can generate a positive growth rate and lead to instability.

There are a variety of different instabilities that fall under the heading of drift waves, among them the ion temperature gradient (ITG) and electron temperature gradient (ETG) modes, the trapped electron mode (TEM), the kinetic ballooning mode (KBM), and the microtearing mode (MTM). These modes may also be affected by other physical character-

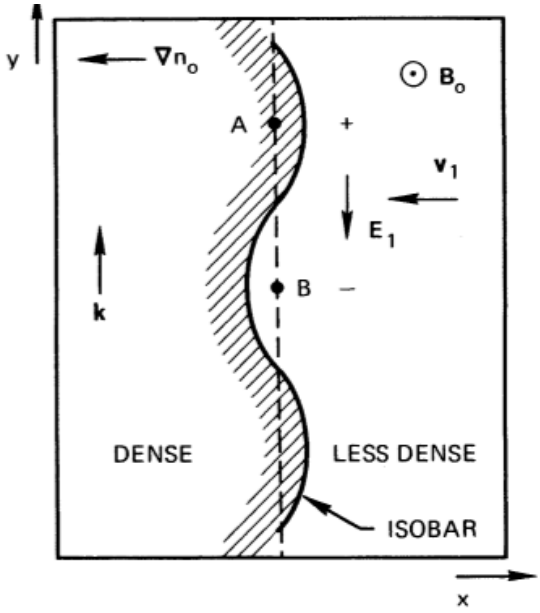

Physical mechanism of a drift wave. FIGURE 6-14

Figure 1.4: Physical mechanism of a drift wave. A small perturbation in density in the presence of a background gradient leads to electric fields and a resultant $E \times B$ drift that causes a wave to propagate in the transverse (y) direction. Under certain conditions, the original perturbation may be reinforced and amplified, leading to instability. Source: *Introduction to Plasma Physics and Controlled Fusion*, F. Chen

istics of the plasma, including plasma pressure, collisionality, and the shape of the magnetic geometry. For more on the physics of drift waves and their role in transport, see the review by Horton [6].

Turbulence and transport have been identified as one of the major challenges facing magnetic confinement fusion research by the National Research Council's Plasma 2010 Committee report on plasma science [7]. This report identified three scientific goals concerning microinstabilities, turbulence, and transport:

- develop more accurate predictive models of turbulence and transport
- find regimes where turbulence and transport are reduced
- advance the science of low-collisionality plasma turbulence

These goals are to be met through progress in theoretical capabilities, especially the analysis of nonlinear physics, and through the the improvement of diagnostic capablities and comparisons between theoretical predictions and experimental measurements. This thesis is concerned with a portion of the theoretical aspects of these challenges.

1.5 Present Work

The goal of the present work is to begin assessing the role that microinstabilities play in the turbulence and transport characteristics of the reversed field pinch. As will be discussed in more detail in the following chapters, RFP research has largely been the realm of larger scale instabilities, with microinstabilities an after-thought or not considered at all. This has changed, however, as novel techniques have enabled the RFP to enter regimes of operation in which these large scale modes are suppressed and microinstabilities may be playing important roles in determining transport levels. Among these techniques is pulsed poloidal current drive (PPCD), which modifies the current profile and stabilizes global tearing modes.

The main thrust of this work has been to incorporate the RFP magnetic field geometry into the gyrokinetic framework – both analytic theory and numerical codes – and to determine the nature of the dominant instabilities and their role in heat and particle transport. The complexity of the problem is such that the equations must be solved numerically with the aid of sophisticated codes and powerful parallel computing systems. Where possible, some simplifications can be introduced and analytic results attained. These results form a foundation for continued collaboration between theoretical predictions and experimental observations.

Thesis Outline

The remainder of the thesis is as follows:

Chapter 2 introduces gyrokinetics, the mathematical framework on which this thesis is based, and a brief derivation of the framework is provided. Due to the multidimensional,

integro-differential nature of the resultant equations and the complexity of the geometries in which they are implemented, numerical solvers are used. Two codes used in this thesis – GYRO [8, 9] and GENE [10, 11] – are introduced and their relationship to each other and to the underlying gyrokinetic framework is discussed.

Chapter 3 deals with the geometry of the reversed field pinch, the device that is the focus of the present work. Various analytic models are presented, including their benefits and drawbacks and their implementation into the gyrokinetic codes. Two models in particular play large roles in this thesis: the toroidal bessel function model (TBFM) and the adjusted circular model (ACM).

Chapter 4 contains results from using the TBFM and a representative RFP equilibrium in the GYRO code. Basic linear results are presented, including critical gradient thresholds and scaling properties, as well as analytic calculations of the critical β limit for ITG suppression. These results present some initial explorations of the physics of microinstabilities in the RFP and provide fundamental insights into their scalings.

Chapter 5 contains results from using the ACM to model specific high confinement discharges of the Madison Symmetric Torus. The results in this chapter and were attained using the GENE code. Linear results from two different MST discharges are presented, as well as nonlinear results associated with one of these parameter sets. Comparisons are made with experimental observations.

Chapter 6 presents a discussion of the collisionless microtearing mode, with particular attention on the role of magnetic drifts in the instability drive. A fluid expansion of the drift-kinetic equation is performed, yielding a dispersion relation with some features of the microtearing mode.

Finally, Chapter 7 provides a summary and discussion of this work. The general features of RFP microinstabilities are summarized and potential implications for the Madison Symmetric Torus are given. Avenues for future research are discussed.

Chapter 2

Gyrokinetics

"Hamiltonian mechanics cannot be understood without differential forms."
- V.I. Arnol'd, *Mathematical Methods of Classical Mechanics* (1989)

"In mathematics, you don't understand things, you just get used to them."
- John von Neumann

A plasma can be described generally as a collection of charged particles that exhibit collective motion. Unlike a neutral gas, in which particles only interact with one another via binary collisions, the ions and electrons in a plasma can generate electric and magnetic fields that act back on the plasma itself and affect its behavior. A comprehensive method by which to investigate microinstabilities in toroidal plasma devices is the gyrokinetic framework, in which fast particle gyromotion has been removed from the kinetic equations through a gyrophase averaging procedure [12]. This procedure reduces the problem description from the original 6D phase space to a more computationally tractable 5D.

The presentation of the gyrokinetic derivation that follows is based on a number of references, among them the discussion of the Lie perturbation method by Littlejohn and Cary [13], the review of nonlinear gyrokinetics by Brizard and Hahm [12], and several graduate theses, including Goerler, Pueschel, Merz and Lapillonne [14, 15, 16, 17].

Even with the simplifications of gyrokinetics, the resultant equations in an arbitrary

geometry are far too difficult to solve analytically, and so sophisticated gyrokinetic solvers have been developed for this purpose. Two such codes are used in this thesis: GYRO [18] and GENE [10, 11]. The gyrokinetic code that provides results presented in Ch. 4 is GYRO; and the results of Ch. 5 and Ch. 6 were attained with GENE. Both codes can be run linearly (providing complex frequencies and linear eigenmode structures) and nonlinearly (providing transport fluxes and turbulent fluctuation information). Unless stated otherwise, the discussion in this chapter is based on the gyrokinetic equation as formulated for and implemented in GENE.

2.1 The Gyrokinetic Model

From the evolution of equilibrium quantities, which takes place at system size, down to particle scale phenomena, there is a wide range of scales that fall within the realm of plasma physics. Properly addressing these scales is one of the most challenging aspects of modeling plasmas. One phenomenon that is the focus of this thesis is plasma turbulence and transport, which often involves interactions between physics taking place at opposite ends of the scale. The correlation lengths and time scales of turbulent processes generally lie between the larger and relatively slower phenomena of magnetohydrodynamics and the fast, small-scale motion of individual particles. This is a large part of what makes plasma turbulence such an interesting and complicated problem.

At low temperatures plasmas are highly collisional, and these collisions are quite effective in thermalizing the plasma and enabling the use of two-fluid or magnetohydrodynamic descriptions. In high temperature regimes, collisions are mostly absent and the plasma must be described using a kinetic approach. In this formulation, the plasma is characterized by a particle distribution function, $f(\mathbf{x}, \mathbf{v}, t)$, which gives the probability density of finding a particle at any given location in space $\mathbf{x}$, velocity space $\mathbf{v}$, and time t. The plasma density can be found as the zeroth moment of the distribution function,

$$n = \int d^3v \; f(\mathbf{x}, \mathbf{v}, t) \quad . \tag{2.1}$$

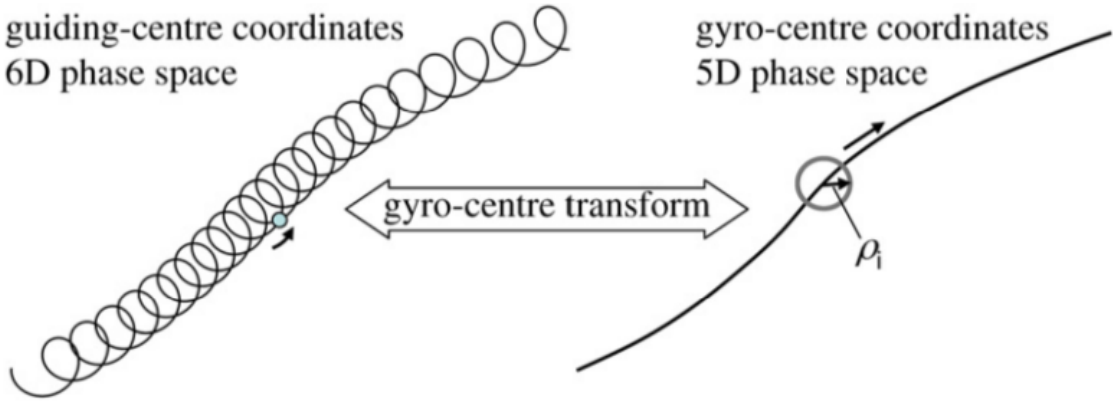

Figure 2.1: Schematic of the gyro-center transform. The fast gyromotion of a particle around a magnetic field line is averaged over, eliminating a phase-space variable and essentially reducing the physics to that of a moving charged ring. Source: Garbet et al. (2010)

The particle distribution function provides a very complete description of a plasma, but it is often too cumbersome to be practical. The formulation can be simplified by making use of the separation of scales that is characteristic of many plasmas. For magnetically confined plasmas, in which strong magnetic fields provide shaping and confinement, charged particles spiral around the magnetic field lines in a behavior referred to as gyromotion (see Fig. 2.1). The rotational time scale is given by the gyrofrequency $\Omega_j = q_j B/m_j c$, and the length scale of this gyromotion is denoted by the gyroradius $\rho_j = v_{Tj}/\Omega_{Tj}$, where $v_{Tj} = (2T_j/m_j)^{1/2}$ is the thermal velocity of species j with mass m_j at temperature T_j. Also often used is the ion sound gyroradius, $\rho_s = c_s/\Omega_i$, where $c_s = (T_e/m_i)^{1/2}$ is the ion sound speed and $j = e, i$ denotes electron or ion properties, respectively.

When the time scale of this gyromotion is considered unimportant to the phenomena of interest, it may be removed from the particle dynamics through an averaging procedure. This procedure essentially reduces the dynamical description from one of particles to one describing a distribution of charged rings. This forms the basis of the gyrokinetic model, one of the primary tools for addressing issues of microturbulence. The gyrokinetic formulation is a useful framework for studying microturbulence due to several key characteristics that this turbulence is assumed to have. These characteristics are known collectively as the gyrokinetic ordering.

First, the radius of the gyromotion (gyroradius) is assumed to be small compared to the variation of the background quantities L, and the dynamic time scale of interest (indicated by the frequency ω) is small compared to the gyrofrequency Ω_j,

$$\frac{\omega}{\Omega_j} \sim \frac{\rho_j}{L} \equiv \rho_* \sim \mathcal{O}(\epsilon_g) \ll 1 \quad . \tag{2.2}$$

An inherent part of this assumption is that there is a strong equilibrium magnetic field B_0 ("strong guide field"), which restricts particle motion to the magnetic field line. In this case, the length scale of the fluctuations along the magnetic field line (parallel direction) is assumed to be much longer than that in the perpendicular direction,

$$\frac{k_\parallel}{k_\perp} \sim \mathcal{O}(\epsilon_g) \quad . \tag{2.3}$$

Additionally, it will be assumed that the amplitudes of the turbulent fluctuations are small compared to the background quantities, an assumption that will allow for a 'δf' splitting in the distribution function. This includes the fluctuations in density δn, magnetic field B_1, and electrostatic potential Φ_1,

$$\frac{\delta n}{n} \sim \frac{B_1}{B_0} \sim \frac{e\Phi_1}{T} \sim \mathcal{O}(\epsilon_g) \quad . \tag{2.4}$$

As a result of this ordering, the gyrokinetic Vlasov-Maxwell system of equations derived in the following sections is valid up to $\mathcal{O}(\epsilon_g)$.

Derivation

With this ordering established, we may proceed with the derivation. Though early derivations consisted simply of a coordinate transformation and gyrophase average [19], modern gyrokinetic theory relies heavily on the techniques supplied by differential geometry and Lie perturbation theory[20, 21, 13, 12]. These advanced mathematical formulations overcome many of the problems with early gyrokinetic derivations, namely retaining the energy and momentum conservation laws of the original Vlasov-Maxwell equations [12]. The derivation to follow provides the basis for the gyrokinetic equation as implemented in the GENE code.

An outline of the derivation presented below is as such:

- the one-form description of particle dynamics is presented (where the one-form is given by γ)
- the one-form is separated into background and perturbed components ($\gamma \rightarrow \gamma_0 + \gamma_1$)
- the one-form is transformed from particle coordinates to guiding center coordinates ($\gamma \rightarrow \Gamma$)
- the one-form is transformed from guiding center coordinates to gyrocenter coordinates using Lie perturbation methods ($\Gamma \rightarrow \bar{\Gamma}$)
- the evolution equation of the gyrokinetic distribution function is derived using the Euler-Lagrange equations

The derivation of the gyrokinetic distribution function starts with the Hamiltonian H for a single non-relativistic particle moving in a magnetic potential $\mathbf{A}(\mathbf{x})$ and electrostatic potential $\Phi(\mathbf{x})$

$$H(\mathbf{x}, \mathbf{v}) = \frac{1}{2} m v^2 + q\Phi(\mathbf{x}) \quad , \tag{2.5}$$

where the particle has mass m, charge q, and particle phase space coordiantes $(\mathbf{x}, \mathbf{v})$. This can also be written in the Lagrangian formulation

$$L(\mathbf{x}, \mathbf{v}) = \mathbf{p}(\mathbf{v}) \cdot \dot{\mathbf{x}} - H(\mathbf{x}, \mathbf{v}) = \left(m\mathbf{v} + \frac{q}{c}\mathbf{A}(\mathbf{x}) \right) \cdot \dot{\mathbf{x}} - \left(\frac{1}{2} m v^2 + q\Phi(\mathbf{x}) \right) \quad , \tag{2.6}$$

with $\mathbf{p}(\mathbf{v}) = m\mathbf{v} + \frac{q}{c}\mathbf{A}(\mathbf{x})$ the canonical momentum and $\dot{\mathbf{x}}$ represents the time derivative of $\mathbf{x}$.

The coordinates $\mathbf{x}$ and $\mathbf{v}$ are not the most useful for describing particle dynamics in a strong guide field. This is largely due to the fast gyromotion of particles in strong magnetic fields, a motion that causes much quicker movement in some directions than others. Through careful consideration of individual particle motion, it is possible to choose a more natural coordinate system, thus simplifying the description. A more useful set of coordinates for describing particle behavior are the guiding center variables $\mathbf{Z} = (\mathbf{X}, v_\parallel, \mu, \varphi, t)$. These are the gyrophase angle

$$\varphi = \arctan\left(-\frac{v_x}{v_y} \right) \quad ,$$

the guiding center $\mathbf{X}$

$$\mathbf{X} = \mathbf{x} - \rho(\mathbf{X}, \mu)\mathbf{a}(\varphi) \quad , \tag{2.7}$$

where $\rho(\mathbf{X}, \mu) = v_\perp(\mathbf{X})/\Omega(\mathbf{X})$ is the gyroradius and $\mathbf{a}(\varphi) = \cos\varphi\hat{\mathbf{e}}_1 + \sin\varphi\hat{\mathbf{e}}_2$. Here a local coordinate system has been introduced in which $\hat{\mathbf{b}}_0$ is the direction of the equilibrium magnetic field and $\hat{\mathbf{e}}_1 \times \hat{\mathbf{e}}_2 = \hat{\mathbf{b}}_0$. Besides this, there are the velocity space coordinates: the parallel velocity

$$v_\parallel = v_z$$

and the magnetic moment

$$\mu = \frac{m_j v_\perp^2}{2B_0} = \frac{m_j(v_x^2 + v_y^2)}{2B_0} \quad .$$

The coordinate transformation is completed using methods from differential geometry, in particular the geometric object known as a one-form. Here, we define the one-form $\gamma(\mathbf{x}, \mathbf{v})$ by its relation to the Lagrangian

$$\int L(\mathbf{x}, \mathbf{v})dt = \int \gamma(\mathbf{x}, \mathbf{v}) \quad . \tag{2.8}$$

Transforming from a one-form γ expressed in terms of coordinates $\mathbf{z} = (\mathbf{x}, \mathbf{v})$ (particle coordinates) to a one-form Γ in terms of coordinates $\mathbf{Z}$ (guiding center coordinates) takes place in the following way:

$$\Gamma_\mu = \gamma_\nu \frac{dz^\nu}{dZ^\mu} \quad , \tag{2.9}$$

where μ and ν denote the phase space components of γ, Γ, $\mathbf{z}$, and $\mathbf{Z}$.

Before proceeding with the coordinate transformation, the one-form (γ) will be separated into perturbed (γ_1) and unperturbed (γ_0) parts, corresponding to the perturbed and unperturbed fields with which it is defined. Since equilibria are generally assumed to be in a condition of quasineutrality, it is assumed that there is no background electric field and $\Phi_0 = 0$:

$$\gamma_0 = \left(m\mathbf{v} + \frac{q}{c}\mathbf{A}_0(\mathbf{x})\right) \cdot d\mathbf{x} - \frac{1}{2}mv^2 dt \tag{2.10}$$

and

$$\gamma_1 = \frac{q}{c}\mathbf{A}_1(\mathbf{x}) \cdot d\mathbf{x} - q\Phi_1(\mathbf{x})dt \quad . \tag{2.11}$$

After applying the coordinate transformation, we arrive at the one-form expressed in guiding center coordinates. Because the gyroradius is much smaller than the spatial variation of the background quantities, it is a good approximation to simply replace the $\boldsymbol{x}$-dependence with $\boldsymbol{X}$. Additionally, the gyroaverage for the unperturbed component can be performed by simply taking an integral over the gyrophase angle ($(1/2\pi)\int d\varphi$). These techniques do not work well for the perturbed one-form, however, since the fluctuating quantities have much shorter spatial variations. In this case, a more sophisticated coordinate transformation method will be needed. The transformed one-forms are (and where the overbar denotes the gyroaveraged quantity)

$$\bar{\Gamma}_0 = \left(mv_\parallel \hat{\boldsymbol{b}}_0(\boldsymbol{X}) + \frac{q}{c}\boldsymbol{A}_0(\boldsymbol{X})\right)\cdot d\boldsymbol{X} + \frac{\mu mc}{q}d\varphi - \left(\frac{1}{2}mv_\parallel^2 + \mu B_0(\boldsymbol{X})\right)dt \tag{2.12}$$

and

$$\begin{aligned}\Gamma_1 = \frac{q}{c}\boldsymbol{A}_1(\boldsymbol{X}+\boldsymbol{r})\cdot d\boldsymbol{X} + \frac{\boldsymbol{A}_1(\boldsymbol{X}+\boldsymbol{r})\cdot a(\varphi)}{v_\perp(\boldsymbol{X})}d\mu + \\ \frac{mv_\perp(\boldsymbol{X})}{B_0(\boldsymbol{X})}\boldsymbol{A}_1(\boldsymbol{X}+\boldsymbol{r})\cdot c(\varphi)d\varphi - q\Phi_1(\boldsymbol{X}+\boldsymbol{r})dt \quad .\end{aligned} \tag{2.13}$$

The transformation of the perturbed one-form from guiding center to gyrocenter coordinates ($\Gamma_1 \rightarrow \bar{\Gamma}_1$) can be achieved through the use of a Lie transform, a near-identity transformation that allows for a continuous variation based on a smallness parameter ϵ, here representing the gyrokinetic ordering presented above. Using the vector g^μ, called the generator, a new set of coordinates $\bar{Z}$ is related to the initial coordinates Z by the equation

$$\frac{\partial \bar{Z}^\mu}{\partial \epsilon}(Z,\epsilon) = g^\mu(\bar{Z}(Z,\epsilon)) \quad , \tag{2.14}$$

where $\bar{Z}^\mu(Z,0) = Z^\mu$ define the initial conditions when $\epsilon = 0$. This can also be written in terms of an operator $T(\epsilon)$

$$\bar{Z}^\mu(Z,\epsilon) = T(\epsilon)Z^\nu \quad , \tag{2.15}$$

where the Lie transform is defined in its operator form:

$$T^* = exp(\epsilon L) \quad T^{*-1} = exp(-\epsilon L) \quad . \tag{2.16}$$

Here ϵ is a small parameter and L is the Lie derivative operator. For operators, the exponential is defined in terms of its Taylor expansion

$$exp(\epsilon L) = 1 + \epsilon L + \epsilon^2 L^2/2 + ... \quad , \tag{2.17}$$

where the "near-identity" nature of the Lie transform becomes apparent. The Lie derivative can be expressed in terms of the generating functions g^μ when operating on a scalar (f) or a one-form (γ)

$$L(f) = g^\alpha \frac{\partial f}{\partial Z^\alpha} \quad (L\gamma)_\alpha = g^\beta \left(\frac{\partial \gamma_\alpha}{\partial Z^\beta} - \frac{\partial \gamma_\beta}{\partial Z^\alpha} \right) \quad . \tag{2.18}$$

We apply the transform to Γ (which is in guiding center coordinates) to get $\bar{\Gamma}$ (which is in gyrocenter coordinates). It is then possible to use gauge freedom to eliminate gyrophase dependency.

The expression to transform the one-form is given by

$$\bar{\Gamma} = T^{*-1}\Gamma + dS \quad . \tag{2.19}$$

Here dS represents the total derivative of a gauge function that we are free to choose. The gyroaveraging occurs when dS is chosen to eliminate φ dependence from the RHS of Eq. (2.19). This is possible since adding a total derivative to the one-form will not change the equations of motion (in other words, the Lagrangian on the left hand side of Eq. (2.8) remains unchanged).

Up to second order in ϵ, the operator T^{*-1} becomes (where $L = L_1 + \epsilon L_2 + \mathcal{O}(\epsilon^2)$)

$$T^{*-1} = exp(-\epsilon L_1) exp(-\epsilon^2 L_2) = 1 - \epsilon L_1 + \epsilon^2 \left(\frac{1}{2} L_1^2 - L_2 \right) + \mathcal{O}(\epsilon^3) \quad . \tag{2.20}$$

Eq. (2.19) can then be written out order by order (expanding $\bar{\Gamma}$, Γ, and S):

$$\bar{\Gamma}_0 = \Gamma_0 + dS_0$$

$$\bar{\Gamma}_1 = \Gamma_1 - L_1\Gamma_0 + dS_1$$

$$\bar{\Gamma}_2 = \Gamma_2 - L_1\Gamma_1 + (\frac{1}{2}L_1^2 - L_2)\Gamma_0 + dS_2 \quad .$$

The zeroth order one-form has already been given above in Eq. (2.12). With suitable choices for the generating functions and the gauge function S_1 (for these expressions, see,

e.g., Ref. [14]), these transformations will lead to an expression for $\bar{\Gamma}_1$. Expressions for the gyroaveraged field quantities can be found in Appendix A of Ref. [16]. We then arrive at the gyrocenter one-form up to first order:

$$\bar{\Gamma} = \bar{\Gamma}_0 + \bar{\Gamma}_1 = \left(m v_\parallel \hat{\mathbf{b}}_0 + \frac{q}{c}\mathbf{A}_0 + \frac{q}{c}\bar{A}_{1\parallel}\hat{\mathbf{b}}_0 \right) \cdot d\mathbf{X} + \frac{\mu m c}{q} d\varphi - \left(\frac{1}{2} m v_\parallel^2 + q\Phi_1 + \mu(B_0 + \bar{B}_{1\parallel}) \right) dt \quad . \tag{2.21}$$

The Gyrokinetic Vlasov Equation

Now that the gyrokinetic one-form has been determined, it is relatively straightforward to generate the gyrokinetic Vlasov equation that describes the evolution of the distribution function in the absence of collisions. The Vlasov equation expressed in terms of gyrocenter coordinates is

$$\frac{dF}{dt} = \frac{\partial F}{\partial t} + \dot{\mathbf{X}} \cdot \nabla F + \dot{\mu}\frac{\partial F}{\partial \mu} + \dot{v}_\parallel \frac{\partial F}{\partial v_\parallel} = 0 \quad . \tag{2.22}$$

The equations of motion for the various gyrocenter coordinates are determined from the the Euler-Lagrange equations

$$\frac{d}{dt}\left(\frac{\partial L}{\partial \dot{Z}^\nu} \right) - \frac{\partial L}{\partial Z^\nu} = 0 \quad . \tag{2.23}$$

The Lagrangian employed in the Euler-Lagrange equations is found from the one-form via the relationship given in Eq. (2.8). With these substitutions we arrive finally at the evolution equation for the gyrokinetic equation

$$\frac{\partial F_j}{\partial t} + \left(v_\parallel \hat{\mathbf{b}}_0 + \frac{B_0}{B_{0\parallel}^*}(\mathbf{v}_{E\times B} + \mathbf{v}_{\nabla B} + \mathbf{v}_c) \right) \cdot \left(\nabla F_j + \frac{1}{m_j v_\parallel} \left(q_j \mathbf{E} - \mu \nabla (B_0 + \bar{B}_{1\parallel}) \right) \frac{\partial F_j}{\partial v_\parallel} \right) = 0 \quad , \tag{2.24}$$

where $B_{0\parallel}^* = \boldsymbol{b}_0 \cdot \left(\nabla \times \left(\boldsymbol{A}_0 + \frac{m_j c}{q_j} v_\parallel \boldsymbol{b}_0 \right) \right)$. The drifts are given by:
the ExB velocity

$$\mathbf{v}_{E\times B} = \frac{c}{B_0}\hat{\mathbf{b}}_0 \times \nabla \chi_j \quad , \tag{2.25}$$

the grad-B drift

$$\mathbf{v}_{\nabla B} = \frac{\mu}{m_j \Omega_j}\hat{\mathbf{b}}_0 \times \nabla B_0 \quad , \tag{2.26}$$

and the curvature drift

$$\mathbf{v}_c = \frac{v_\parallel^2}{\Omega_j}(\nabla \times \hat{\mathbf{b}_0})_\perp = \frac{v_\parallel^2}{\Omega_j B_0}\left(\hat{\mathbf{b}}_0 \times \left(\nabla B_0 + \frac{\beta_{\rm tot}}{2}\frac{\nabla p_0}{p_0}\right)\right) \quad , \tag{2.27}$$

where $\chi_j = \bar{\phi} - \frac{v_\parallel}{c}\bar{A}_{1\parallel} + \frac{\mu}{q_j}\bar{B}_{1\parallel}$ is the gyro-averaged modified potential, $p_0 = n_0 T_0$ is the pressure, and $\beta_{\rm tot} = 8\pi p_0/B_0^2$ is the total normalized plasma pressure.

In the event that plasma pressure is negligible ($\beta = 0$) the grad-B and curvature drifts may be combined as

$$v_{Dj} = \frac{1}{\Omega_j}\left(v_\parallel^2 + v_\perp^2/2\right)\left(\hat{\mathbf{b}}_0 \times \frac{\nabla B_0}{B_0}\right) \quad . \tag{2.28}$$

This is often a useful simplification for analytic purposes, and it one that will be employed for various estimates in this thesis.

Collisions

The physics of collisions has so far been neglected in the above derivation. In a fusion plasma temperatures are expected to be high enough so that the collisionless limit is a reasonable approximation, however in most magnetic confinement experiments collisional effects still play important roles in much of the dynamics. If collisions are included, the RHS of the Vlasov equation (Eq. (2.22)) picks up an additional term that contains the effects of particle correlations (collisions), which will be denoted $C(f)$.

Due to the long-range nature of the forces within the plasma (the Coulomb force), collisions betweens particles can be considered to be the result of many small-angle deflections. This results in a collisional term represented by the Landau-Boltzmann collision operator [16]

$$C(f_j, f_{j'}) = \frac{\partial}{\partial \vec{v}} \cdot \left(\mathbf{D} \cdot \frac{\partial}{\partial \vec{v}} - \vec{R}\right) f_j \quad , \tag{2.29}$$

where $\mathbf{D}$ is the diffusion tensor and $\vec{R}$ is the dynamical friction,

$$\mathbf{D} = \frac{\gamma_{jj'}}{m_j^2}\frac{\partial^2 G_{j'}}{\partial \vec{v}\partial \vec{v}} \qquad \vec{R} = \frac{2\gamma_{jj'}}{m_j m_{j'}}\frac{\partial H_{j'}}{\partial \vec{v}} \quad . \tag{2.30}$$

These are in turn defined in terms of the Rosenbluth potentials G and H

$$G_{j'}(\vec{v}) = \int d^3v' f_{j'} u \qquad H_{j'}(\vec{v}) = \int d^3v' f_{j'} \frac{1}{u} \quad , \tag{2.31}$$

and where $\vec{u} = \vec{v} - \vec{v}'$ and $\gamma_{jj'} = 2\pi q_j^2 q_{j'}^2 \ln \Lambda_c$, with $\ln \Lambda_c$ representing the Coulomb logarithm.

The Landau-Boltzmann prescription is the collision operator implemented in GENE. A simplification of this operator, called pitch-angle scattering, is employed in GYRO.

Pitch-angle scattering

The treatment of collisional processes can be further simplified by assuming infinitely heavy ions and taking $v_{Ti} \to 0$. This eliminates collisional energy transfer between electrons and ions and reduces the effect of collisions to just a diffusion in pitch-angle $\xi = \sigma\sqrt{1 - \lambda B}$, where $\lambda = \frac{v_\perp^2}{v^2 \hat{B}}$, $\hat{B}$ is the normalized magnetic field, and σ denotes sign (direction of $v_\parallel$).

For a species j, the collision operator is taken to be an energy-independent Lorentz operator

$$C(f_j) = \frac{\nu_j(\epsilon_j)}{2} \frac{\partial}{\partial \xi}(1 - \xi^2)\frac{\partial f_j}{\partial \xi} \quad , \tag{2.32}$$

where $\epsilon_j = E_j/T_j = m_j v^2/2T_j$ is the normalized energy. The collisionality coefficient $\nu_j(\epsilon_j)$ is energy dependent and has a different form depending on whether it is describing electron or ion collisions. For the electrons, it has the form

$$\nu_e(\epsilon_e) = \frac{\nu_{ei}}{\epsilon_e^{3/2}} \left[Z_{eff} + H\left(\sqrt{\epsilon_e}\right)\right] \quad , \tag{2.33}$$

while for the ions, it is given by the equation

$$\nu_j(\epsilon_j) = \frac{\nu_{ii}^{(j)}}{\epsilon_j^{3/2}} \sum_{k=1}^{N_{ion}} \frac{Z_k^2 n_k}{n_j} + H(\sqrt{\frac{m_k}{m_j}\epsilon_j}) \quad , \tag{2.34}$$

where j indicates the ion species, N_{ion} is the total number of ion species used in the simulations, and $\nu_{ii} = \nu_{ei}\sqrt{e/m_j}(T_e/T_j)^{3/2}(n_j/n_e)Z_j^2$. Z_j is the nuclear charge of the jth ion species and Z_{eff} is the effective nuclear charge. The function $H(x)$ is

$$H(x) = \frac{e^{-x^2}}{\sqrt{\pi}x} + \left(1 - \frac{1}{2x^2}\right)\mathrm{erf}(x) \quad . \tag{2.35}$$

All simulations performed in the present work contain just one ion species. In GYRO, the level of collisionality is set through the parameter ν_{ei}.

Field Equations

It still remains to derive the gyrokinetic field equations, which describe the evolution of the perturbed electrostatic potential Φ and magnetic vector potential $\mathbf{A}$, with the background fields being described by the equilibrium conditions. These equations are found by combining Maxwell's equations (the Poisson equation for Φ and Ampère's law for $\mathbf{A}$) with the appropriate velocity moments of the gyrokinetic distribution function.

The Poisson equation describes the evolution of the electrostatic potential Φ in terms of the density, which is derived from the zeroth moment of the distribution function (Eq. (2.1))

$$-\nabla^2\Phi_1(x) = 4\pi\sum_j n_{1j}(x)q_j \quad . \tag{2.36}$$

The magnetic vector potential $\mathbf{A}$ is described by Ampère's law

$$\nabla^2\mathbf{A} = -\frac{4\pi}{c}\mathbf{j} + \frac{1}{c}\frac{\partial\mathbf{E}}{\partial t} \quad . \tag{2.37}$$

This is defined in terms of the current, which involves the first velocity moment of the distribution function

$$\mathbf{j} = q_j\int d^3v\mathbf{v}f(\mathbf{x},\mathbf{v},t) \quad , \tag{2.38}$$

which involves the particle phase space distribution function instead of the gyrocenter distribution. The transformation to guiding center variables from gyrocenter space can be achieved through the use of the pull back operator ($T^* = \exp(\epsilon L)$). The resultant equations govern the behavior of the fluctuations in Φ, $B_\parallel$, and $A_\parallel$. These expressions are [15]

$$\sum_j q_j(1-\Gamma_0(b_j))\frac{q_j\Phi}{T_{0j}} = \sum_j q_j\left((\Gamma_0(b_j)-\Gamma_1(b_j))\frac{B_\parallel}{B_0} + \frac{2\pi B_0}{m_j n_{0j}}\int J_0(\lambda_j)f_j dv_\parallel d\mu\right) \quad , \tag{2.39}$$

$$\begin{aligned}(1+\sum_j 4b_j\beta_j(\Gamma_0(b_j)-\Gamma_1(b_j))\frac{B_\parallel}{B_0} = \\ = -\sum_j 2\beta_j\left(\frac{B_0}{n_{0j}T_{0j}}\int\mu\frac{2iI_1(i\lambda_j)}{\lambda_j}f_j d^3v + \frac{q_j\Phi}{T_{0j}}(\Gamma_0(b_j)-\Gamma_1(b_j))\right) \quad ,\end{aligned} \tag{2.40}$$

and

$$\nabla_\perp^2 A_\parallel = -\frac{8\pi^2 B_0}{c}\sum_j \frac{q_j}{m_j}\int v_\parallel J_0(\lambda_j) f_j dv_\parallel d\mu \quad , \tag{2.41}$$

with J_0 the zeroth order Bessel function, I_0 and I_1 modified Bessel functions, and

$$\lambda_i = i\rho_j \nabla_\perp \quad , \quad \Gamma_i = I_i(b_j)e^{-b_j} \quad , \quad b_j = \lambda_j^2 = -\frac{T_j}{m_j\Omega_j^2}\nabla_\perp^2 \quad . \tag{2.42}$$

For a more complete derivation of these expressions, refer to, e.g., Ref. [16]. It is worth noting that in the resultant equations $A_\parallel$ is described independently while Φ and $B_\parallel$ are coupled. However, all simulations presented in the chapters to follow have $B_\parallel = 0$.

2.2 Gyrokinetic Codes

Solving the equations given above in specific experimental geometries is too difficult a task for analytic theory without using severely limiting simplifying assumptions. To avoid the necessity for these assumptions, and the limitations of the conclusions drawn from them, a variety of gyrokinetic codes have been developed to deal with this task. This thesis contains results from two different gyrokinetic codes: GYRO and GENE. Both of these codes provide numerical solutions of the gyrokinetic system of equations presented above but differ in their choice of coordinates and discretization methods. Such differences will be outlined here. For more complete descriptions please refer to Ref. [18, 22, 23] for GYRO and Ref. [11, 10, 24] for GENE.

Both codes contain the ability to do either local or global domains, though all work in this thesis is restricted to the local (flux-tube) approximation. In this approximation, background quantities are fixed and vary linearly over the simulation domain according to the background gradients.

Both GYRO and GENE are Eulerian solvers (also called "continuum" codes). As opposed to Lagrangian solvers (or PIC - "particle-in-cell" codes), which compute characteristic curves in phase space, Eulerian codes use a fixed grid in phase space. Eulerian codes allow for greater flexibility in the choice of numerical algorithms and are not as susceptible to numerical noise as PIC codes.

The gyrokinetic equation is further simplified for numerical computation by employing δF splitting, in which the distribution function is separated into background (F, usually taken to be a local Maxwellian distribution) and perturbed ($f \equiv \delta F$) components. This prescription has already been partially employed in the derivation given above in the assumed ordering between fluctuating fields and background quantities.

Field-following coordinates

Having derived the gyrokinetic system system of equations above, it now remains to solve them in a particular magnetic geometry. At this stage, a further simplification can be made by implementing a field following coordinate system (note that now coordinate system refers to the physical coordinates of the simulation domain, rather than the phase space coordinates of the distribution function.) This choice is motivated by the anisoptropic nature of microinstabilities ($k_\parallel/k_\perp \ll 1$), which means that only the perpendicular directions require the use of high resolutions.

A natural coordinate system to use for describing the magnetic field geometry is the straight field line coordinate system, denoted by the variables (Ψ, χ, ϕ). Here Ψ is a flux surface label, χ is the straight field line poloidal angle (defined through the safety factor $q = \boldsymbol{B} \cdot \nabla\phi / \boldsymbol{B} \cdot \nabla\chi$), and ϕ is the toroidal angle. These coordinates form a system in which magnetic fields are simply described by straight lines.

The transformation into field-aligned coordinates essentially involves a rotation in the $\chi - \phi$ plane, aligning one coordinate axis with the magnetic field direction. The symbols used for the field aligned system will be (x, y, z), where the radial coordinate x is defined as

$$x = \frac{q_0}{r_0 B_0} \Psi - x_0 \quad , \tag{2.43}$$

the coordinate y defines the binormal direction (perpendicular to both the radial direction and the magnetic field line)

$$y = \frac{r_0}{q_0} \left[q' \chi \nabla\Psi + q \nabla\chi - \nabla\phi \right] \quad , \tag{2.44}$$

and z is the direction along the field line, defined as

$$z = \chi \quad . \tag{2.45}$$

In these definitions r_0 is the radius of the magnetic surface at the midplane and $(x = x_0, y = y_0, z = 0)$ defines the center of the flux tube. Here q_0 is the safety factor at r_0.

In the GENE code, many of the geometric terms in the gyrokinetic set of equations are written in terms of the metric g^{ij}. (See Ref. [25]). The components of this are

$$g^{xx} = \nabla x \cdot \nabla x = \left(\frac{q_0}{r_0 B_0}\right)^2 g^{\Psi\Psi} \quad , \tag{2.46}$$

$$g^{xy} = \frac{1}{B_0}\left(q'\chi g^{\Psi\Psi} + q g^{\Psi\chi}\right) \quad , \tag{2.47}$$

$$g^{yy} = \left(\frac{r_0}{q_0}\right)^2 \left[(q')^2\chi^2 g^{\Psi\Psi} + 2qq'\chi g^{\Psi\chi} + q^2 g^{\chi\chi} + g^{\phi\phi}\right] \quad , \tag{2.48}$$

$$g^{xz} = \frac{q_0}{r_0 B_0} g^{\Psi\chi} \quad , \tag{2.49}$$

$$g^{yz} = \frac{r_0}{q_0}\left(q'\chi g^{\Psi\chi} + q g^{\chi\chi}\right) \quad , \tag{2.50}$$

and

$$g^{zz} = g^{\chi\chi} \quad . \tag{2.51}$$

These metric coefficients will pick up a particular form when some specific magnetic equilibrium model is defined.

Normalization

Since numerical solvers work most naturally in the realm of dimensionless numbers, and not physical units, it becomes necessary to normalize the above system of equations and remove all dimensional dependence. Towards this end, several basic reference values are defined for the normalization procedure. These include the elementary electric charge e, a reference temperature T_{ref}, a reference mass m_{ref}, a macroscopic reference length L_{ref}, and a reference magnetic field B_{ref}. Physical quantities may be extracted from the normalized results by substituting in experimentally relevant values for these reference quantities.

Additionally, some derived reference units are employed for normalization. These include a reference sound speed

$$c_{\text{ref}} = \left(\frac{T_{\text{ref}}}{m_{\text{ref}}} \right)^{1/2} \quad , \tag{2.52}$$

and a reference gyroradius

$$\rho_{\text{ref}} = \frac{c_{\text{ref}}}{\Omega_{ci}} \quad . \tag{2.53}$$

In the results of chapters to follow, $T_{\text{ref}} = T_e$, $m_{\text{ref}} = m_i$, $L_{\text{ref}} = R_0$, and B_{ref} is taken as the on-axis magnetic field. Consequently, $c_{\text{ref}} = c_s$, the ion sound speed, and $\rho_{\text{ref}} = \rho_s$, the ion sound gyroradius.

Flux tube approximation

To cut down on more of the numerical expense, a further approximation is made by simplifying the computational domain. This is the "flux tube", or "local", approximation. Rather than simulating the entire toroidal volume, for many cases it suffices to model just a flux tube, a restricted domain that follows a magnetic field line for some integer number of poloidal turns. For axisymmetric devices like the tokamak or reversed field pinch, one poloidal turn is sufficient to capture all geometric variation ($z \in [-\pi, \pi]$).

The flux tube domain is also restricted in the x and y directions, so that the domain has some finite box size given by L_x and L_y. Equilibrium quantities are Taylor expanded around the center of the domain and are thus assumed to vary linearly across the flux tube. This simplification requires the assumption that the radial box size (L_x) is sufficiently small as compared to the machine size. The edges of the domain are handled by employing periodic boundary conditions. This ensures the conservation of particles and energy, but requires that L_x and L_y are larger than any structures that may arise in the ensuing turbulence. It is therefore important to perform convergence checks of these quantities to ensure properly converged results.

The implementation of a quasi-periodic boundary condition in the parallel (z) direction requires a bit more care than the other coordinates, since the existence of finite magnetic shear leads to a simulation domain that is sheared in the y direction. This shear, in turn,

leads to a coupling of k_x modes. The parallel boundary condition can be expressed as (see, for instance, Ref. [14])

$$F(k_x, k_y, z + L_z) = F(k'_x, k_y, z)e^{2\pi i k_y \hat{s} r_0} \quad , \tag{2.54}$$

where $k'_x = k_x + 2\pi\hat{s}k_y$, L_z is the parallel box size, and $\hat{s} = (r_0/q_0)dq/dr$. Although the definition of the magnetic shear $\hat{s}$ used here is the same as that regularly defined for the tokamak, the term here arises from a Taylor expansion of the safety factor q and does not rely on underlying tokamak assumptions. The parallel boundary condition is of particular importance to the modeling of the RFP due to the high values of $\hat{s}$ that exist in the device. High shear requires high radial resolution, one feature of RFP simulations that tends to make them more computationally expensive than their tokamak counterparts. More discussion on the difference between the tokamak and RFP definitions of shear and the implications for simulations is contained in Ch. 5 on page 81.

Since background quantities are not allowed to evolve in the local approximation, the simulations are not entirely self-consistent. This issue can be addressed through the use of global simulations. Global runs may differ from local ones due to a number of effects, including the role of ρ_* and the existence of avalanche transport processes. Although some of these effects may be quite important and unknowable a priori, global simulations require additional computational resources and, in the case of the RFP, careful consideration of the high-shear geometry and the reversal surface. Therefore, all work included in this thesis is performed using the flux-tube approximation.

The GYRO code

The work presented in Ch. 4 is based on simulations completed with the initial-value gyrokinetic code GYRO [18, 9, 23], which differs in several ways from GENE.

Although GYRO has been developed to solve the same basic set of equations as GENE, differences in the implementation arise as a result of the choice of coordinate system (both real space and velocity space) and in the way this system is discretized. These choices in

turn affect the numerical algorithms chosen to solve the system differential equations that constitute the gyrokinetic framework.

The coordinate system used in GYRO is based on the Miller equilibrium model [26] and is expressed in terms of the coordinates (r, θ, ζ), where r is the flux surface label, θ is an angle in the poloidal plane, and the toroidal angle variable is given by $\zeta = \phi - \int_0^\theta d\theta' \hat{q}$, where ϕ is the physical toroidal angle and $\hat{q} = \hat{b} \cdot \nabla\phi / \hat{b} \cdot \nabla\theta$ is the locally defined safety factor.

To deal with numerical challenges that arise at the bounce points θ_b for trapped particles, where $v_\parallel(\theta_b) = 0$, the normalized orbit time τ is used instead of the poloidal angle. This is defined as

$$\tau_0(\lambda, \theta) \equiv \begin{cases} \int_{-\theta_b}^{\theta} \frac{G_\theta(\theta')d\theta'}{\sqrt{1-\lambda\hat{B}(\theta')}}, & \text{if } \lambda \leq \frac{1}{\hat{B}(\pi)} \text{ (trapped)} \\ \int_{-\pi}^{\theta} \frac{G_\theta(\theta')d\theta'}{\sqrt{1-\lambda\hat{B}(\theta')}}, & \text{if } \lambda > \frac{1}{\hat{B}(\pi)} \text{ (passing)} \end{cases}, \tag{2.55}$$

where θ_b is the bounce point and $G_\theta(r, \theta) = \frac{B}{B_{\text{unit}}} \frac{R}{R_0} \frac{1}{r|\nabla r|} \frac{1}{|\nabla\theta|}$.

The velocity space coordinates are chosen to be energy $\varepsilon \equiv m(v_\parallel^2 + v_\perp^2)/2T$, the pitch angle variable $\lambda \equiv v_\perp^2 / \hat{B} v^2$ ($\hat{B}$ is normalized magnetic field), and the sign of the parallel velocity $\sigma \equiv sgn(v_\parallel)$.

The discretization methods for these coordinates are as follows [9]: the toroidal angle is treated spectrally, the radial and orbit-time derivatives are performed using upwind differences, the energy integrals for ε and λ are treated using Gauss-Legendre quadrature, and the time-stepping is done using 2nd-order Runge-Kutta.

Unlike GENE, GYRO remains in physical space for the radial direction, performing derivatives with an upwind difference method rather than spectral multiplication. This has the potential to introduce numerical dissipation, although with sufficient resolution this is not an issue.

Another way that GYRO differs from GENE is in the treatment of collisions. In GYRO, collisions are treated with the pitch-angle scattering operator — a special case of the more general Landau-Boltzmann operator given before.

Conventions

Besides differences in coordinate choices and discretization methods, there are differences of convention between GYRO and GENE. The normalization of the timescale in GYRO differs from that in GENE by a factor of the aspect ratio, so growth rates and real frequencies are expressed in terms of c_s/a, rather than c_s/R_0 (where a is the minor radius and R_0 is the major radius). Additionally, the sign convention of electron/ion direction is reversed, so that in GYRO a negative real frequency indicates a drift wave in the ion diamagnetic direction, while in GENE a negative frequency indicates the electron direction. Although they do not affect the numerical computations, these differences are reflected in the results presented in the respective chapters and should be taken account when doing side-by-side comparisons. Furthermore, wavenumbers are expressed in terms of 'poloidal wavenumber' k_θ, which, despite the notation, represents the binormal direction and therefore has the same meaning as k_y used in GENE. In the tokamak, where the toroidal field dominates, the binormal coordinate is predominantly in the poloidal direction. Conversely, near the reversal surface in the RFP geometry the y-axis points more in the toroidal than poloidal direction.

2.3 Chapter Summary

The gyrokinetic Vlasov-Maxwell system of equations have been presented, with an outline of the Lie perturbation method for the derivation of the evolution equation for the gyrokinetic distribution function. The field equations describing the evolution of the electrostatic and magnetic potentials were also described. Taken together, this set of equations described the gyrokinetic framework, one of the primary methods of analysis for microturbulence in magnetic confinement devices. For the purposes of numerical solving, the normalization and discretization of these equations was discussed. The two gyrokinetic codes used in this these, GYRO and GENE, were presented along with several key differences in their methods and conventions.

Chapter 3

The Reversed Field Pinch

"Essentially, all models are wrong, but some are useful."

- George E. P. Box, *Empirical Model-Building and Response Surfaces* (1987)

Research on magnetic confinement fusion has predominantly concentrated on developing the tokamak concept, and although this design is perhaps the most well advanced, other promising approaches exist as well. One of these, the reversed field pinch (RFP), is the focus of the present work. Like the tokamak, the RFP is an axisymmetric toroidal device that provides a "magnetic bottle" for plasma confinement. Unlike the tokamak, the formation of the RFP's magnetic field is largely a process of self-organization, rather than the result of externally imposed fields. In this process, an initial magnetic structure "relaxes" into a lower energy state subject to certain topological constraints [27].

During standard operation the RFP is dominated by large-scale tearing mode events, known as sawteeth, which produce stochastic magnetic fields and large magnetic-fluctuation-induced transport [28, 29]. These tearing modes drastically reduce energy confinement time and diminish the usefulness of the RFP as a magnetic confinement fusion concept. It is possible to improve upon the standard operating characteristics of the RFP by using pulsed poloidal current drive (PPCD) [30, 31, 32, 33, 34], a current profile control technique that flattens the current profile and removes the drive for the global tearing modes. In this regime, the transport fluxes may start to approach levels more in line with expectations

from microturbulent driven 'anomalous transport' with some cases of PPCD seeing energy confinement time increase by as much as a factor of ten over standard discharges [32].

Although the experimental observations for fluctuations that are independent of global tearing modes is still fragmentary, there is growing evidence for drift wave activity [29, 35, 36, 37, 38, 39]. The tearing modes couple to a broad cascade that delivers magnetic energy to small scales and simultaneously brings kinetic energy closer to equipartition as the wavenumber increases [29, 35], in keeping with MHD. However, at smaller scales, the kinetic energy eventually becomes greater than the magnetic energy. In this regime there are notable changes in the coherence and cross phase between magnetic field and density, likely associated with a different type of fluctuation. The observed radial structure indicates a standing wave pattern consistent with collisional shear Alfvén waves or microtearing modes [36]. Other observations suggest that temperature and density gradients in the edge are close to critical values.

Exploring and characterizing the microinstability spectrum in the RFP is a major focus of the present work. This chapter outlines the development of various RFP equilibrium models and their implementation into gyrokinetic codes.

3.1 General Features of the Reversed Field Pinch

The dominant feature of the RFP magnetic geometry is a toroidal magnetic field that reverses towards the edge of the plasma, a characteristic that differentiates it from the tokamak. This results in a safety factor q that goes through zero and toroidal and poloidal fields that may be the same order of magnitude throughout a large portion of the device. A schematic diagram of the Madison Symmetric Torus (MST), an RFP at the University of Wisconsin that is the focus of this thesis, and a representative equilibrium magnetic field profile is given in Fig. 3.1.

While having a weaker toroidal magnetic field removes the need for external magnetic field coils and contributes to making the RFP a cheaper alternative to the tokamak, this design choice has a negative effect on stability. The tokamak strives to maintain a q-profile

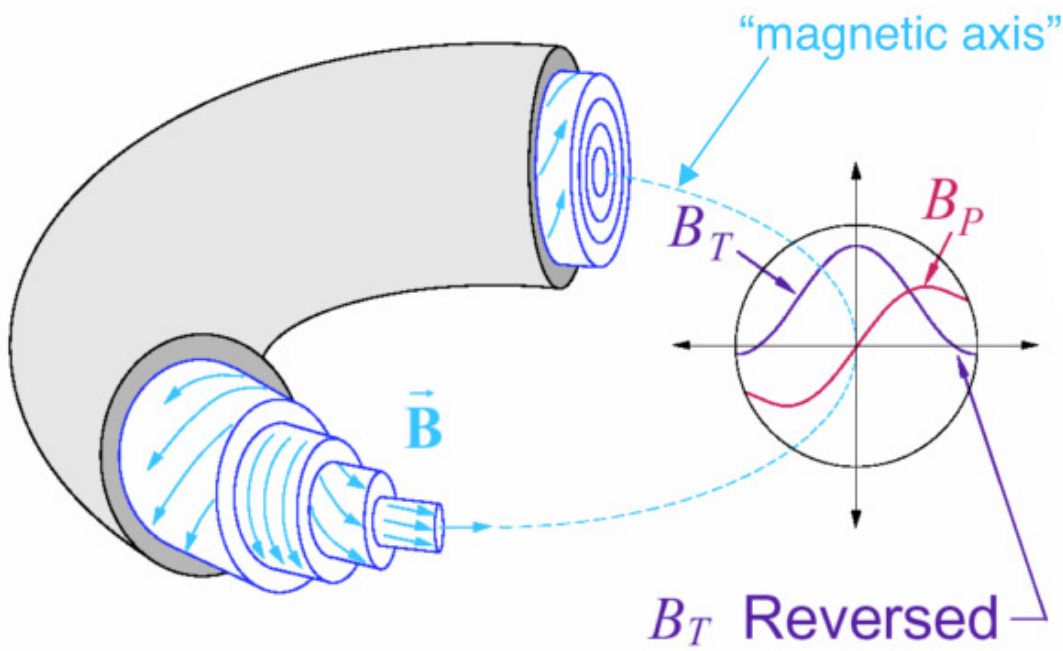

Figure 3.1: Schematic diagram of an RFP. Key features of the magnetic field geometry can be seen: concentric circular flux surfaces, a toroidal field that reverses out towards the edge of the device, and toroidal and poloidal fields that are roughly equivalent in strength throughout much of the plasma volume. Courtesy J. S. Sarff.

always above 1, ensuring that a strong toroidal field is present and able to suppress certain instabilities, such as kink-tearing modes. In the RFP, however, the q-profile generally starts at $q \approx 0.2$ in the core and decreases from there. This means that multiple $m = 1$ and $m = 0$ tearing modes are unstable, creating large magnetic island structures that overlap to create a stochastic magnetic field [40]. An example q-profile is shown in Fig. 3.2, with the radial extent of various island structures indicated. The stochastic magnetic field and large tearing mode activity have a detrimental effect on energy confinement. As will be discussed, this is countered to some extent through the application of current profile control, which leads to conditions more favorable to the observation of drift wave microinstabilities.

The equivalent strengths of the poloidal and toroidal fields in the RFP lead to a higher degree of poloidal curvature and a smaller radius of curvature as compared to the tokamak, a feature that affects the type and characteristics of the microinstabilities present. Various geometric properties – such as q, magnetic shear $\hat{s}$, and the magnetic gradient and curvature

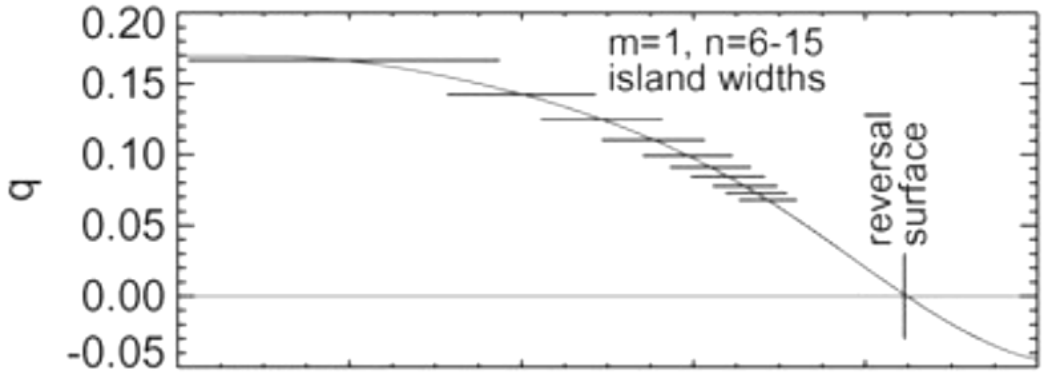

Figure 3.2: A q-profile for a 'standard' RFP discharge showing the radial extent of magnetic island structures. These overlapping islands are associated with the stochastic field seen in the Poincaré plot in Fig. 3.3. Source: Sarff et al. (2003)

drifts – constitute a different regime than those investigated in tokamaks. As such, it can be expected that instabilities will have different scaling and stability properties in the RFP.

3.2 Madison Symmetric Torus

Many of the results presented in this thesis have been formulated specifically for the Madison Symmetric Torus (MST) RFP [41]. Reporting first plasma in 1990, MST is one of the longest running RFP experiments. It is constructed out of a close-fitting symmetric aluminum shell, and has a major radius of $R_0 = 1.54$ m and a minor radius of $a = 0.52$ m. The conductive shell serves several functions, both forming the vacuum vessel and operating as a toroidal field winding. Current coils wrapped around a large iron core through the center of MST inductively drive a large toroidal plasma current and a large poloidal magnetic field within the device. Through a process of nonlinear magnetic self-organization a dynamo is created that results in the reversal of the toroidal field towards the edge of the plasma. Typical parameter ranges for MST are given in Tab. 5.1.

Magnetic equilibria, an important component of the modeling process detailed in this chapter, are arrived at via the MSTFit code [42], a nonlinear Grad-Shafranov solver developed specifically for MST. This approach finds numerical solutions to the Grad-Shafranov equation while at the same time attempting to satisfy radial force balance ($\mathbf{J} \times \mathbf{B} = \nabla P$)

plasma current	0.2 MA – 0.6 MA
major radius	1.54 m
minor radius	0.52 m
density	$\sim 1 \times 10^{-19}\mathrm{m}^{-3}$
electron temperature	up to 2 keV
poloidal beta	up to 26%
confinement time	1 ms – 12 ms

Table 3.1: Machine specifications and normal operating parameters for the Madison Symmetric Torus (see Chapman et al. (2009)). These ranges include both standard and improved confinement discharges.

and applying a best-fit procedure to match available experimental measurements. MSTFit follows an iterative procedure, computing an equilibrium profile and predicted signals for a suite of available diagnostics [43, 42, 44]. The electron temperature profile is measured through Thomson scattering, density measurements come from FIR interferometry, and magnetic fluctuations are measured by Faraday rotation polarimetry. The on-axis magnetic field is determined via motional Stark effect. For the discharges studied in this thesis there are no independent T_i measurements. The χ^2 difference between the predicted and measured quantities is evaluated, and available free parameters are adjusted and a new equilibrium calculated in an attempt to minimize the χ^2 value. Equilibrium calculated by MSTFit provide the experimental anchor against which the accuracy of simpler analytic models are evaluated.

Improved confinement discharges

As has been discussed, confinement in the reversed field pinch (RFP) is dominated by global tearing modes under ordinary circumstances. These large scale modes create stochastic magnetic fields (see Fig. 3.3) that have hugely detrimental effects on transport. Consequently, microscale drift-type fluctuations have received far less attention in the RFP than they have in the tokamak. However, operational modes such as pulsed poloidal current drive [45], which applies an external force to flatten the current gradient, and the quasi-single-helicity state [46], whose quasi-spontaneous formation leads to a suppression of multiple-helicity tearing modes, have gained success in reducing global tearing mode activ-

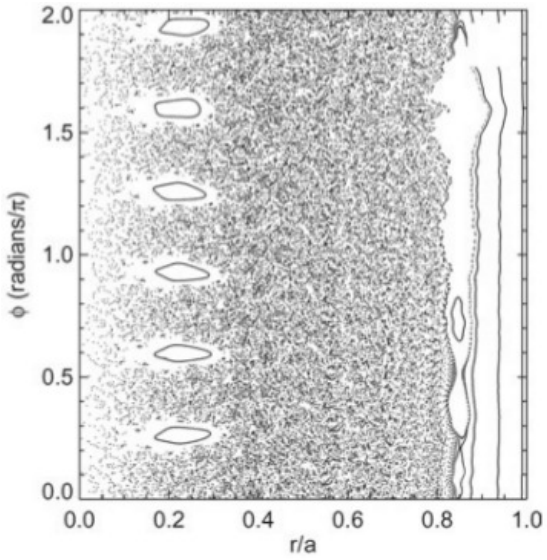

Figure 3.3: Poincarè puncture plot for a standard (non-PPCD) MST discharge. Overlapping magnetic islands result in a stochastic magnetic field structure. Source: Sarff et al. (2003)

ity. In this regime, confinement time can improve significantly, and equilibrium density and temperature gradients can steepen [32, 47]. This produces conditions in which microscale turbulence might emerge as a factor in confinement, just as it does in the tokamak.

The MHD mode activity of standard RFP discharges creates radial magnetic field fluctuations that destroy flux surfaces and lead to stochastization. This is a scenario that in turn leads to high levels of transport through parallel conduction of electrons [48]. This stochasticity is demonstrated in Fig. 3.3 through a magnetic field puncture plot. In the puncture plot, or Poincarè plot, flux surfaces (vertical lines at constant r/a) are populated with a number of sample field lines which are then traced multiple times around the torus. Radial magnetic diffusion results in a wandering of the field lines and a 'noisy' plot.

With PPCD, a poloidal current is inductively driven in the outer region of the device, flattening the current profile. This reduces the global tearing mode activity and generates smaller magnetic island structures and better-behaved magnetic fields. A puncture plot for a PPCD discharge is presented in Fig. 3.4. The radii that will be the focus of much of the present work occur out past the reversal surface ($r/a \approx 0.7$, depending on the discharge) where the flux surfaces are largely intact and there is very little magnetic stochasticity,

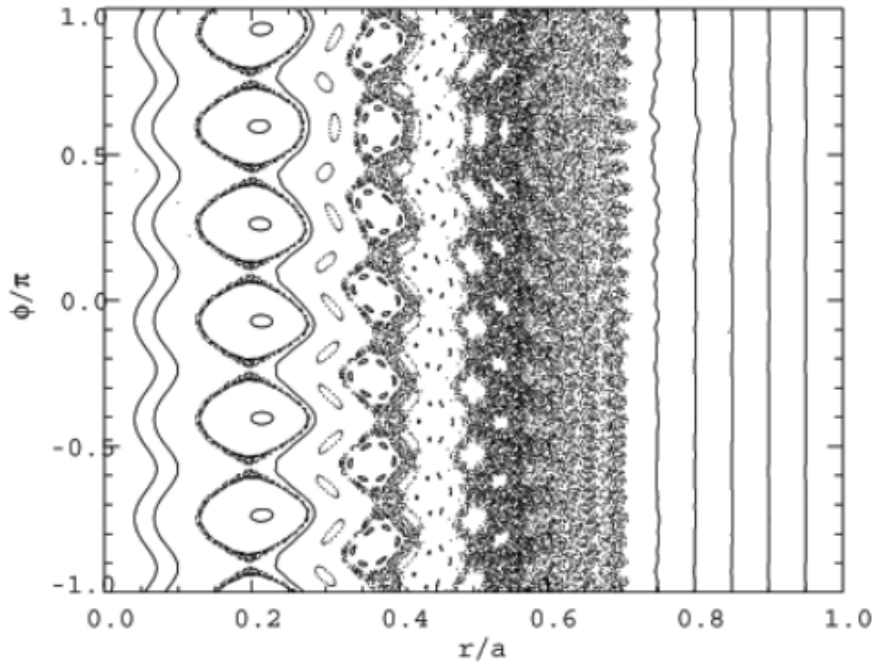

Figure 3.4: Poincaré puncture plot for a sample PPCD discharge. By flattening the current profile, global tearing modes are largely stabilized and magnetic flux surfaces are better-behaved as compared to the standard discharge. Source: B. Hudson, Ph.D. Thesis (2006)

although a small amount remains that will be shown to play an important role in the physics of nonlinear saturation.

A number of drift wave microinstabilities have been identified in the tokamak, and although many of the same modes might be expected to be unstable in the RFP, their exact characteristics and the parameter regimes in which they are unstable are not known a priori. As has been described, the magnetic geometry of the RFP differs in several significant ways from the tokamak, and these differences can be expected to affect the scaling properties of the instabilities in the device, perhaps even presenting a different set of likely modes. Accurate modeling of microinstabilities in the RFP requries the use of an RFP-specific geometry. There are several models that may be used for this, a few of which will be described now.

3.3 RFP Equilibrium Modeling

The implementation of an RFP equilibrium into a gyrokinetic code requires some important geometric considerations, since many codes have been formulated based on toroidal flux, which increases monotonically in a tokamak but can be multivalued in an RFP. Therefore, RFP equilibrium implementations must work around this constraint. Additionally, there are other, sometimes more subtle ways that tokamak assumptions may be built into gyrokinetic codes. Examples of this may emerge in the definitions of the parallel wavenumber $k_{\|}$ and the magnetic shear $\hat{s}$.

Two common tokamak equilibrium models often implemented in gyrokinetic codes are the s-α [49] and Miller [26] models. The first of these, s-α, is an equilibrium consisting of shifted concentric circular flux surfaces and is parameterized by magnetic shear $\hat{s}$ and the plasma ballooning parameter $\alpha = -q^2 R(d\beta/dr)$. The Miller equilibrium model is a more sophisticated and adaptable model that allows for geometric variation in the flux surface shape, including such parameters as triangularity and elongation. This flexibility enables the modeling of non-circular flux surfaces.

The need for an RFP specific equilibrium was demonstrated in Tangri et al. [50], where it was shown that the tokamak s-α equilibrium underestimated ITG growth rates at radial locations with poloidal curvature dominant. While the more sophisticated Miller equilibrium did a better job, it still fell short at large r/a or high values of k_y. This work demonstrated the need for RFP-specific equilibria to be implemented in gyrokinetic codes, and it will be shown in Ch. 5 that, for MST, it is these larger radial locations that are the most important from the perspective of drift wave turbulence.

There are a number of different equilibrium models that can be used to describe the magnetic field geometry of the RFP. Much of the difference between the RFP and the tokamak lies in the behavior of the toroidal magnetic field. As a toroidal device, the RFP's toroidal field contains a $1/R$ dependence, like that of the tokamak, however there is also a strong dependence on the minor radius r that the tokamak does not have. Among other things, this minor radius dependence changes the scale of the magnetic drifts, so that these

drifts in the RFP are larger than their tokamak counterparts by roughly a factor of the aspect ratio.

Taylor relaxation and the Bessel function model

The origin of the difference between the magnetic field geometries of the tokamak and RFP comes from the methods for creating the magnetic fields. In the former, the magnetic field structure is largely determined by external field coils, while in the latter the magnetic field comes about as a result of a process of self-organization. In this process there is a spontaneous reversal of the toroidal magnetic field that occurs due to reapportionment of helicity through the plasma volume. Generally, this is achieved by creating a small toroidal field with external coils and using an induced toroidal current to generate a poloidal field. The pinch effect caused by the toroidal current can trigger self-organization, manifested by a reversal of the toroidal field in the outer portion of the plasma, from which the reversed field pinch gets its name.

The relaxation process that forms the RFP geometry was first described by Taylor (1974) [27]. This is a process of energy minimization subject to certain topological constraints. Making the assumption that plasma internal energy is negligible ($\beta = 0$), this theory essentially relies on the minimization of magnetic energy,

$$W = \frac{1}{2}\int_V (\nabla \times \mathbf{A}) d\tau \quad , \tag{3.1}$$

where the integral is taken over some flux tube volume V, $d\tau$ is a volume element, and $\mathbf{A}$ is the magnetic vector potential. With the additional assumption of a perfectly conducting magnetic fluid, the magnetic field cannot break or reconnect, and the topology must be preserved. One consequence of this is the conservation of helicity over V,

$$K = \int_V \mathbf{A} \cdot \mathbf{B} d\tau \quad , \tag{3.2}$$

where $\mathbf{B} = \nabla \times \mathbf{A}$ is the magnetic field.

With the minimization of energy and the conservation of helicity it can be found that the equilibrium of the final relaxed state will be determined by the condition

$$\nabla \times \mathbf{B} = \mu(r, \theta)\ \mathbf{B} \tag{3.3}$$

for a function $\mu(r, \theta)$, dependent on radius r and poloidal angle θ, that is constant along magnetic field lines. Eq. (3.3) describes what is known as a force-free state, in which the plasma current (proportional to $\nabla \times B$) is in the same direction as the magnetic field.

With some departure from an ideal plasma (resistivity or electron inertia) it becomes possible for magnetic reconnection to occur and for the topology to change. In this case, it is necessary to relax Eq. (3.2). Now, it is only the total helicity

$$K_0 = \int_{V_0} \mathbf{A} \cdot \mathbf{B} d\tau \tag{3.4}$$

that needs to be conserved, where the integral is now over the total plasma volume V_0. This results in a unique solution to Eq. (3.3), where μ now represents a constant across all magnetic field lines.

A simplified solution of Eq. (3.3) (for μ constant) can be found in the cylindrical limit (the limit of infinite aspect ratio). In this limit, the poloidal and toroidal components of Eq. (3.3) become the defining equations of the Bessel functions, J_0 and J_1. The magnetic field components can therefore be expressed as

$$B_\phi = B_0 J_0 \left(2\Theta \frac{r}{a}\right) \tag{3.5}$$

and

$$B_\theta = B_0 J_1 \left(2\Theta \frac{r}{a}\right) \quad , \tag{3.6}$$

where B_0 is the magnetic field strength on-axis and $\Theta = \mu a/2 = \langle B_\theta \rangle^{\text{wall}} / \langle B_\phi \rangle^{\text{vol}}$ (the ratio of wall-averaged poloidal field over volume-averaged toroidal field) is known as the RFP pinch parameter. These functions are plotted in Fig. 3.5 for $\Theta = 1.35$. It can be seen that the Bessel function model (BFM) captures the essential nature of the RFP magnetic fields, that is, a toroidal field that decreases from the core, becoming weaker than the poloidal field and eventually reversing sign.

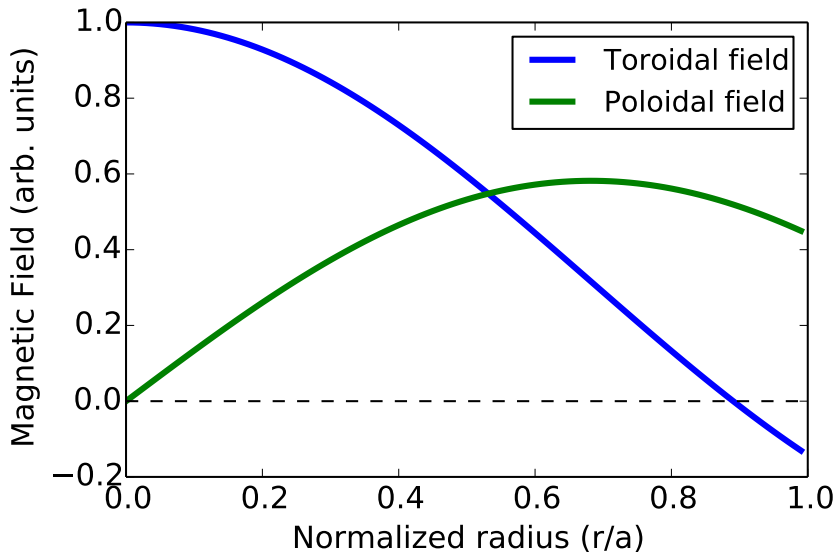

Figure 3.5: Toroidal field (blue) and poloidal field (green) for the Bessel function model, with $\Theta = 1.35$. This model contains the essential feature of the RFP, which is the reversal of the toroidal field and a $q = 0$ surface.

Toroidal Bessel Function Model

Although the BFM captures the basic features of the RFP equilibrium, by being a cylindrical approximation it cannot account for the sometimes important effects that arise as a result of toroidal curvature, especially particle trapping. Furthermore, it may not be straightforward to incorporate the BFM into a gyrokinetic code such as GYRO [18, 9], which assumes an equilibria that is a solution of the Grad-Shafranov equation and requires a toroidal magnetic field of the form $B_\phi \equiv F(\Psi)/R$.

Work has been done to extend the BFM, incorporating toroidal and finite β effects. This model, called the toroidal Bessel function model (TBFM) is discussed in detail in Ref. [50]. An outline of the derivation will be given here.

As with the derivation of many similar equilibria, the starting point is the assumption of an axisymmetric equilibrium consisting of nested flux surfaces labeled by unique values Ψ. For the RFP, it is also a good assumption that the flux surfaces are circular, and that flux surfaces are characterized by the variables $R(\Psi)$ and $Z(\Psi)$. Being an axisymmetric

equilibrium, Ψ obeys the Grad-Shafranov equation [51, 52]

$$\Delta^*\Psi = -\mu_0 R^2 p' - F\frac{dF}{d\Psi} \quad , \tag{3.7}$$

where $p' = dp/d\Psi$ is the gradient of pressure and the magnetic field $\mathbf{B}$ is described as

$$\mathbf{B} = (1/R)\nabla\Psi \times \mathbf{e}_\phi + (F/R)\mathbf{e}_\phi \quad , \tag{3.8}$$

with the toroidal and poloidal components of the magnetic field obeying the relations $RB_\phi = F(\Psi)$ and $B_\theta = |\nabla\Psi|/R$. In the coordinate system used here

$$\Delta^* \equiv R^2\nabla\cdot\left(\frac{\nabla\Psi}{R^2}\right) = R\frac{\partial}{\partial R}\left(\frac{1}{R}\frac{\partial\Psi}{\partial R}\right) + \frac{\partial^2\Psi}{\partial Z^2} \quad . \tag{3.9}$$

It is useful to transform from toroidal coordinates (R, ϕ', Z) to cylindrical coordinates ($\hat{r}$, θ, ϕ), with the definitions $\hat{r} = r/a$, $R = R_0 + a\hat{r}\cos\phi$, $Z = a\hat{r}\sin\phi$, and $\phi' = -\phi$. With this transformation, the left hand side of the Grad-Shafranov equation (Eq. (3.7)) becomes

$$\left[\frac{\partial^2}{\partial\hat{r}^2} + \frac{1}{\hat{r}}\frac{\partial}{\partial\hat{r}} + \frac{1}{\hat{r}^2}\frac{\partial^2}{\partial\theta^2} - \frac{a}{R_0 + a\hat{r}\cos\theta}\left(\cos\theta\frac{\partial}{\partial\hat{r}} - \frac{\sin\theta}{\hat{r}}\frac{\partial}{\partial\theta}\right)\right]\Psi \quad . \tag{3.10}$$

This equation is often solved numerically to generate an equilibrium. A simplified analytic equilibrium can be found by making the approximation

$$\frac{dF(\Psi)}{d\Psi} = \mu \quad , \tag{3.11}$$

where

$$F(\Psi) = \mu(\Psi - \Psi_s) \tag{3.12}$$

and where μ and Ψ_s are assumed to be constants. Eq. (3.11) is motivated from experimental RFP equilibria on MST. If low β is assumed, the p' term can be neglected in Eq. (3.7), from which comes the solution

$$\Psi(\hat{r}) = \frac{aB_0}{2\Theta}\left[J_0(2\hat{r}\Theta) - J_0(2\Theta)\right] \quad . \tag{3.13}$$

From this equation, as well as Eq. (3.8), the form of the magnetic field in the TBFM is derived:

$$B_\phi = \frac{B_0 J_0(2\Theta\hat{r})}{1 + (\hat{r}a/R_0)\cos\theta} \tag{3.14}$$

and

$$B_\theta = \frac{B_0 J_1(2\Theta\hat{r})}{1 + (\hat{r}a/R_0)\cos\theta} \quad . \tag{3.15}$$

This equilibrium is now in a form that can be implemented in the GYRO code. This model is a function of the parameters Θ, $\hat{r}$, and θ. The specifics of this implementation and initial results were presented in Ref. [50]. Further results based on this model constitute the bulk of Ch. 4.

Limits of the TBFM

Although the TBFM is an improvement on the BFM, it still has severe limitations. In particular, the TBFM breaks down for $\Theta \gtrsim 1.8$ and is not capable of accurately describing high-Θ PPCD discharges.

A comparison of the TBFM model with an experimental equilibrium in which $\Theta = 1.5$ is given for the poloidal and toroidal magnetic fields in Fig. 3.6. Although the model still captures the essential features at this Θ value, it has begun to depart from the experimental fields and is no longer an accurate representation of the actual experimental magnetic geometry. At the pinch parameter $\Theta = 2.96$, the TBFM no longer captures the equilibrium accurately, as can be seen in Fig 3.7. For these cases a new approach must be taken.

Adjusted Circular Model

With the limitations posed by the TBFM, and the strong need to accurately model high-confinement PPCD discharges, it is necessary to implement a different equilibrium model. The approach taken here to achieve this is to make use of the highly flexible GENE code [10, 11] and to modify the circular equilibrium used therein. GENE does not rely on underlying tokamak assumptions in the implementation of a chosen geometry and is therefore capable of incorporating a wide range of magnetic field equilibria.

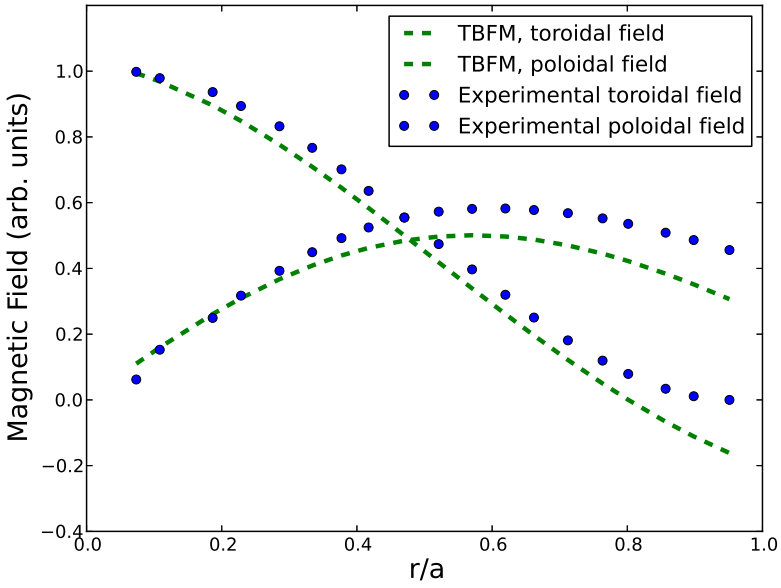

Figure 3.6: The TBFM (green dashes) and experimental magnetic field (blue dots) at $\Theta = 1.5$. Shown are both the toroidal and poloidal components of the magnetic field. The TBFM still somewhat follows the equilibrium field, but it is starting to break down.

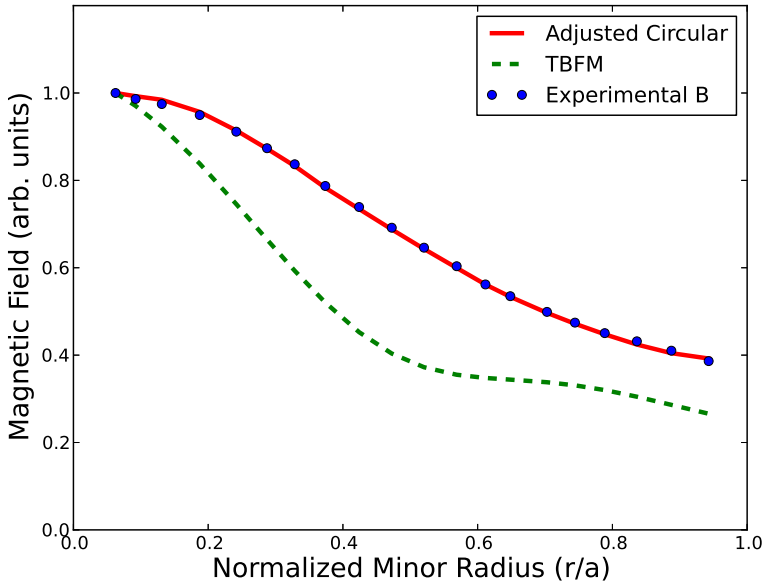

Figure 3.7: The magnitude of the magnetic field for the experimental field (blue dots), the TBFM (green dashes), and the ACM (red line) for a $\Theta = 2.96$ equilibrium. The ACM does a good job of describing the equilibrium, in contrast to the TBFM.

Circular model

The gyrokinetic code GENE contains a circular equilibrium, called the 'circular model', discussed in detail in Ref. [25]. The circular model is an improvement upon the more basic s-α equilibrium model, which due to the definition of the poloidal angle has been shown to contain inconsistencies on the order of the inverse aspect ratio $\epsilon \equiv r/R_0$ [25].

In the circular model, the form for the magnetic field is given as

$$\mathbf{B} = \frac{B_0 R_0}{R}\left(\mathbf{e}_\phi + \frac{r}{R_0 \bar{q}}\mathbf{e}_\theta\right) \quad , \tag{3.16}$$

where the magnitude of the field is given by

$$B = |\mathbf{B}| = \frac{B_0 R_0}{R}\left(1 + \left(\frac{\epsilon}{\bar{q}}\right)^2\right)^{1/2} \quad , \tag{3.17}$$

and where $\bar{q} = q\sqrt{1-\epsilon^2}$. The derivative of the field, another important component used in the GENE code, is

$$\begin{aligned}\frac{dB}{dr} &= B_0\left[-\frac{(1+(\frac{\epsilon}{\bar{q}})^2)^{1/2}}{(1+\epsilon\cos\theta)^2}\frac{\cos\theta}{R_0} + \frac{(1+(\frac{\epsilon}{\bar{q}})^2)^{-1/2}}{1+\epsilon\cos\theta}\frac{\epsilon}{\bar{q}}\left[\frac{1}{R_0\bar{q}} - \frac{\epsilon}{\bar{q}^2}\bar{q}'\right]\right] \\ &= \underbrace{B_0\frac{(1+(\frac{\epsilon}{\bar{q}})^2)^{1/2}}{1+\epsilon\cos\theta}}_{B}\left[-\frac{\cos\theta}{R_0}\frac{1}{1+\epsilon\cos\theta} + \frac{1}{1+(\frac{\epsilon}{\bar{q}})^2}\frac{\epsilon}{R_0\bar{q}^2}\left[1 - \frac{r}{\bar{q}}\bar{q}'\right]\right] \quad .\end{aligned} \tag{3.18}$$

Although the circular model is an improvement upon s-α, by itself it is not capable of describing the RFP magnetic fields. This is due to the strong dependence of the RFP's toroidal field on minor radius r, which is not captured in this model. A naive use of this model with RFP parameters vastly overestimates the B-field in the region of the reversal surface. This is demonstrated in Fig. 3.8. This particular case is for a 200 kA PPCD equilibrium with $\Theta \approx 3$, but the evident error between the model and the experiment would be an inevitable outcome of using the circular model with any RFP equilibrium.

To get a better sense of the deficiencies of the circular model in describing the RFP equilibrium, we may transform the TBFM into a similar form as Eq. (3.17) and note the

differences. The specification for the magnetic field in the TBFM is

$$\begin{aligned}\mathbf{B} &= \frac{B_0 R_0 J_0(2\Theta r/a)}{R}\mathbf{e}_\phi + \frac{B_0 R_0 J_1(2\Theta r/a)}{R}\mathbf{e}_\theta \\ &= \frac{B_0 R_0}{R} J_0(2\Theta r/a)\left(\mathbf{e}_\phi + \frac{J_1(2\Theta r/a)}{J_0(2\Theta r/a)}\mathbf{e}_\theta\right) \\ &= \frac{B_0 R_0}{R} J_0(2\Theta r/a)\left(\mathbf{e}_\phi + \frac{\epsilon}{q}\mathbf{e}_\theta\right) \quad ,\end{aligned}$$

where the cylindrical approximation for q has been employed ($q = rB_\phi/RB_\theta$). The magnitude of the magnetic field in this prescription is

$$B = |\mathbf{B}| = \frac{B_0 R_0}{R}|J_0(2\Theta r/a)|\left(1 + \left(\frac{\epsilon}{q}\right)^2\right)^{1/2} \quad . \tag{3.19}$$

This expression is very similar to the circular equilibrium model (Eq. (3.17)), with the difference lying in the Bessel function multiplier $J_0(2\Theta r/a)$ which captures the minor radius dependence of the toroidal field. This term is a necessary difference from the circular model in that it counteracts the singularity at the reversal surface and keeps B finite as $q \to 0$. This demonstrates that additional modifications to the circular model are required to capture the RFP geometry.

Although additional r dependence could be added and a generic RFP equilibrium incorporated into this model by simply including the BFM in the prescription for the magnetic field, this is not desirable due to the limitations of the BFM itself. Therefore, a more general approach will be taken by replacing $J_0(2\Theta r/a)$ with some function $g(r)$ that depends only on r.

Adjusted Circular Model

We choose to take a $g(r)$ of the form $g(r) = qf(r)$, where q is the safety factor and $f(r)$ is a polynomial determined by a fit to the experimental field. The explicit inclusion fo q in this expression is for the purpose of achieving an exact cancellation with the $1/q$ term in $|\mathbf{B}|$, thereby ensuring a well-behaved expression even at the $q = 0$ surface. The original, unmodified circular model may be reproduced by choosing $f(r/R_0) = |q|^{-1}$.

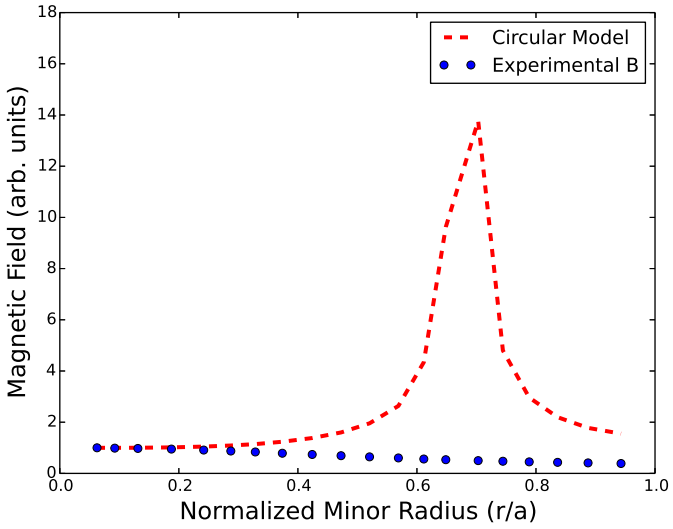

Figure 3.8: The experimental magnetic field (blue dots) along with the circular equilibrium (red dashes). By not allowing for a minor radius dependence of the toroidal field the circular model encounters a singularity at the $q = 0$ (reversal) surface. Roughly twenty radial points are used to create these curves, which leads to a peak in the magnetic field for the circular equilibrium rather than a true singularity.

This function is incorporated into the model as follows. Taking the fitted function $f(\epsilon = r/R_0)$ such that

$$\mathbf{B} = \frac{B_0 R_0}{R} q f(\epsilon = r/R_0) \left(\mathbf{e}_\phi + \frac{r}{R_0 \bar{q}} \mathbf{e}_\theta \right) \quad , \tag{3.20}$$

and where the magnitude of the field is given by

$$B = \frac{B_0 R_0}{R} |q| f(\epsilon) \sqrt{1 + (\epsilon/\bar{q})^2} \quad . \tag{3.21}$$

This expression forms the basis for a 'semi-analytic' equilibrium model, in which the function $f(\epsilon)$ is fit to an experimental equilibrum profile generated by MSTFit. More specifically, the f is fitted to $B_{\exp} \frac{R}{R_0} \frac{1}{|q|} (1 + (\epsilon/\bar{q})^2)^{-1/2}$. In this way an experimental magnetic equilibrium can be incorporated into GENE in an entirely analytic way. The radial derivative of this model is given as

$$\frac{dB}{dr} = |q| f(\epsilon) \frac{d}{dr} \left(\frac{B_0 R_0}{R} \left(1 + (\epsilon/q)^2)^{1/2} \right) \right) + |B| \left(\frac{q'}{q} + \frac{f'}{f} \right) \quad , \tag{3.22}$$

where $f' = df/dr = df/d\epsilon \cdot 1/R_0$ and $q'/q = \hat{s}/r$. In some of the plots that follow, the adjusted circular model is sometimes referred to as 'Fit'.

The difference between the ACM and the original circular model is the inclusion of the factor $|q|f(r/R_0)$, which captures the dependence of the toroidal magnetic field on r and allows for a smoothly varying expression through the reversal surface, where q and the toroidal field go to zero. Although this choice enables the ACM to include the reversal surface, the inclusion of this surface in gyrokinetic codes presents additional difficulties due to the low q and high $\hat{s}$. This problem is elaborated on in Ch. 5.

The differences between the ACM and the TBFM can be seen by plotting the components of the magnetic fields for each model, along with the experimental field. Fig. 3.9 shows the toroidal component of the field, where it can be seen that at this value of Θ the TBFM contains a double reversal, clearly a non-physical effect. The polodial component of the magnetic field is plotted in Fig. 3.10, where it can again be seen that the TBFM is not capable of matching the experimental field in these high-Θ discharges. The ACM fit, conversely, matches the experimental field well. The ACM, like the original circular model, is limited in that it is only capable of modeling circular flux surfaces. However, this is an assumption that is well-satisifedin MST [42].

Benchmarking

Since gyrokinetic simulations are a relatively new topic of study for the RFP, it is important to compare results from separate codes with slightly different handling of geometric quantities. This exercise, referred to as benchmarking, serves as a check on both the implementation of the equilibrium model into the separate codes, as well ensuring the codes are solving the gyrokinetic system of equations in a consistent and repeatable way.

The TBFM as implemented in GYRO and the ACM as implemented in GENE have been benchmarked against each other for the case of a $\Theta = 1.35$ equilibrium with $\beta = 0$, $a/L_T = 5.0$, and $a/L_n = 0.58$, where $1/L_n = -d\ln n/dr$ and $1/L_T = -d\ln T/dr$. The ion and electron temperature gradients are assumed to be equal. The results of this benchmark

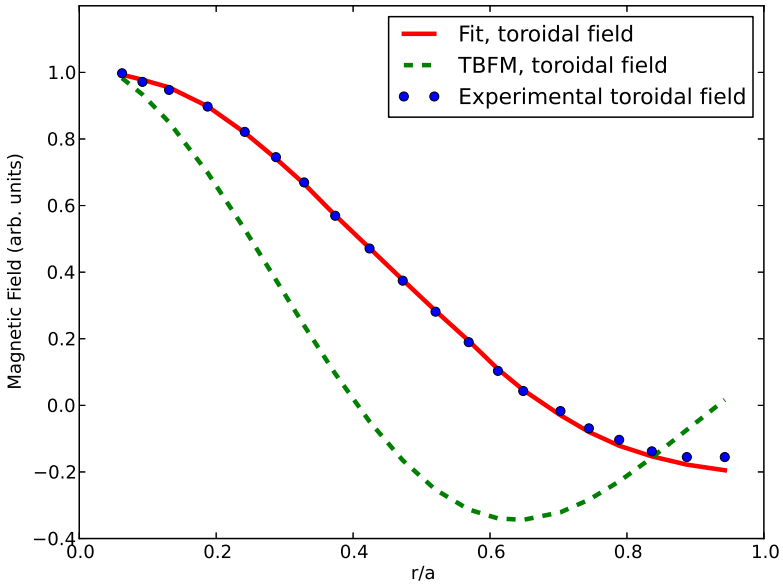

Figure 3.9: The toroidal magnetic field for the experimental field (blue dots), the TBFM (green dashes), and the ACM (red line) for a $\Theta = 2.96$ equilibrium. The toroidal field of the TBFM reverses direction twice, a feature seen in neither the experimental field nor the ACM fit.

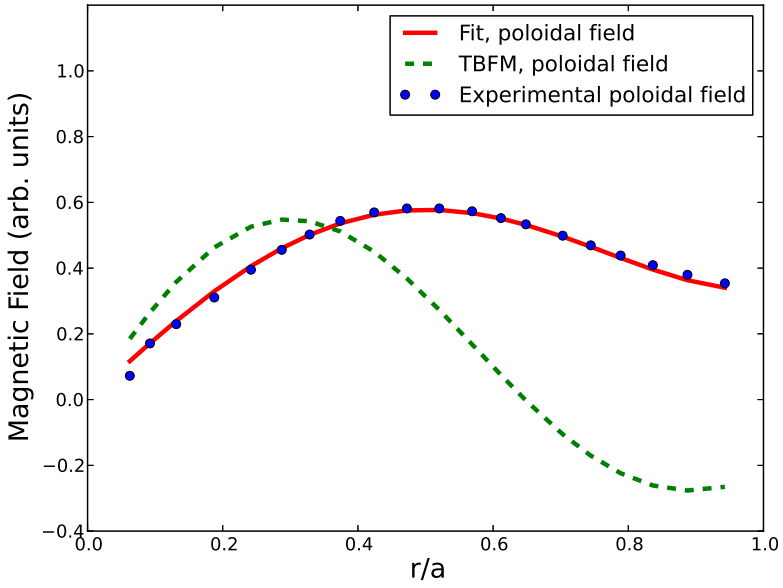

Figure 3.10: The poloidal magnetic field for the experimental field (blue dots), the TBFM (green dashes), and the ACM (red line) for a $\Theta = 2.96$ equilibrium. The TBFM poloidal field erroneously contains a reversal, while the fit provided by the ACM successfully matches the experimental field.

are shown in Fig. 3.11. The original GYRO results have been published in Tangri et al. [50], and more details can be found there.

The polynomial component of the ACM magnetic field has been determined through a fit to the $\Theta = 1.35$ TBFM, rather than to any experimental field measurements. This is effectively an exercise in verification and provides a check on the implementation of the ACM into GENE, rather than an exploration of the detailed differences between the models. As can be seen in Fig. 3.11, there is very good agreement for a low-Θ non-PPCD case where the TBFM is well-suited to describe the magnetic geometry. One advantage of the ACM is its ability to accommodate more general equilibria than the TBFM, such as high-Θ PPCD discharges where the TBFM breaks down. This allows the modeling of PPCD equilibria with parameters drawn directly from MST discharges.

3.4 Chapter Summary

The essential features of the reversed field pinch were presented along with several analytic equilibrium models. The RFP is a device in which microinstability studies are a relatively new topic, and work has been done to incorporate the RFP geometry into gyrokinetic codes for the purpose of addressing this issue. Some of the limitations of Taylor's original Bessel function model are removed with the development of the toroidal Bessel function model, which has been incorporated into the GYRO code. However, due to the limitations of these Bessel function based models in accurately modeling the geometry of higher-Θ discharges a new model was developed based on the GENE code's circular model. The adjusted circular model provides a flexible equilibrium model capable of addressing the geometries of specific experimental discharges. The following chapters contain results from using these models and the aforementioned gyrokinetic codes to study the types and characteristics of microinstabilities in the Madison Symmetric Torus.

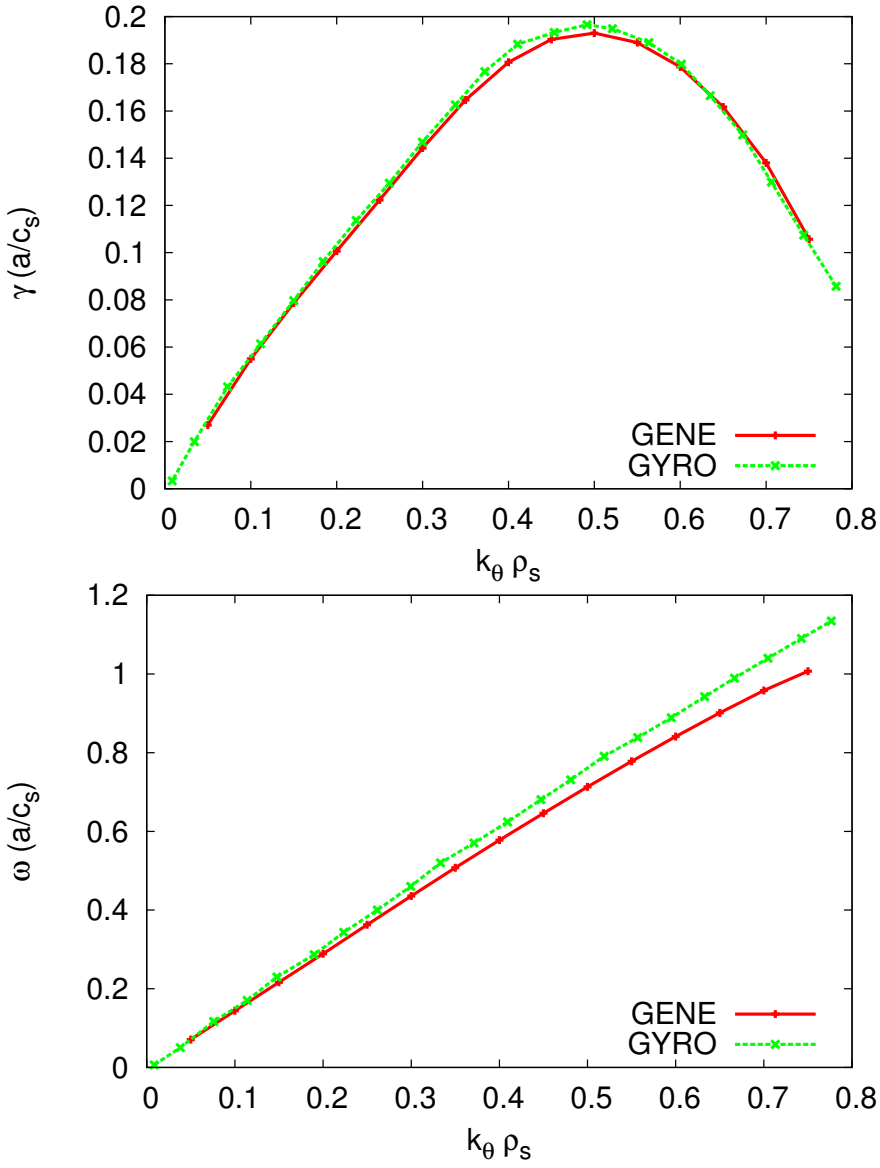

Figure 3.11: Comparison of growth rates and frequencies between GYRO (green) and GENE (red) for a $\Theta = 1.35$ equilibrium plotted against normalized wavenumber $k_\theta \rho_s$, with $r/a = 0.5$, $q = 0.186$, $\hat{s} = -0.716$. The TBFM provides the equilibrium model for the GYRO results and the ACM for the GENE results. There is good agreement in this parameter regime. Other parameters, and more information on the GYRO results, can be found in Tangri et al. (2011). Other results for these sets of parameters can be found in Ch. 4.

Chapter 4

Fundamental microinstability studies in an RFP equilibrium

Microinstabilities have been a topic of study in the tokamak for a number of years, and after some uncertainty about what modes may be most compatible with the high shear and low safety factor conditions of the RFP, numerical solutions of gyrokinetic models in RFP geometry have shown that many instabilities familiar from the tokamak may also arise in the RFP [53, 54, 50]. In the present chapter two such modes are explored in some detail: the ion temperature gradient (ITG) driven mode and the microtearing mode (MTM). As will be discussed, a general feature of the RFP versions of these instabilities are critical thresholds in the driving gradients and in β (here and in the following β refers to electron pressure $\beta = 8\pi n_0 T_{e0}/B^2$, where B_0 is the magnetic field, n_0 is the background density, and T_{e0} the background electron temperature) that are larger than their tokamak counterparts by roughly a factor of the aspect ratio R/a.

The results presented in this chapter use the toroidal bessel function model (TBFM) as implemented in the Gyro code. A description of this implementation, and initial results, were published in Tangri et al. [50]. The following results can be considered to build on those and have been published in Carmody et al. [55]. Although not modeling any specific discharge, by containing some of the general features of the RFP equilibrium — such as

high magnetic shear and strong poloidal curvature — this model is capable of providing an initial characterization of the instabilities that arise in this device.

4.1 Equilibrium Modeling

The work presented here is performed with the GYRO code using the TBFM model described in Ch. 3. As mentioned previously, the TBFM is an analytic equilibrium that captures the essential features of the RFP. Flux surfaces are assumed to be circular, and to lowest order in β the magnetic fields are given as:

$$B_\theta = \frac{B_0 J_1(2\Theta r/a)}{1 + r\cos\theta/R_0}, \quad B_\phi = \frac{B_0 J_0(2\Theta r/a)}{1 + r\cos\theta/R_0} \quad , \tag{4.1}$$

where Θ is the RFP pinch parameter. Although the TBFM is not capable of modeling high-Θ PPCD equilibria, or addressing the unique geometric characteristics of specific MST discharges, the low q and high $\hat{s}$ are representative of conditions unique to the RFP. These results can therefore shine some light on general characteristics of instabilities in this device.

In addition to the background magnetic equilibrium, certain of the gyrokinetic operators are generalized to the RFP geometry. These generalizations stem from characteristics of the RFP equilibrium that differentiate it from the tokamak. Primarily, the poloidal magnetic field in the RFP is much stronger relative to the toroidal field as compared to the tokamak, and in the case where the normalized radius of the simulation domain is $r_0/a \sim 0.5$, they are roughly the same order of magnitude. Under these circumstances, the common tokamak approximation $B \sim B_\phi$ cannot be made, and the more general form $B = B_\phi(1+(\epsilon_t/q_0)^2)^{1/2}$ must be used, where B_ϕ is the toroidal magnetic field and $\epsilon_t = r_0/R_0$ is the inverse aspect ratio of the flux surface. This difference affects operators such as the curvature drift frequency and parallel transit operators, the latter of which in its general form will pick up an additional factor

$$\mathbf{b}\cdot\nabla \sim k_\parallel = \frac{1}{\sqrt{1+(\epsilon_t/q_0)^2}}\frac{1}{q_0 R_0} \quad . \tag{4.2}$$

Besides being incorporated into the code, these geometric modifications must also be taken into account in analytic estimates whenever generalizing a tokamak analysis to an RFP envi-

ronment. The next section provides an example of this in the context of finite-β suppression of ITG. Let it also be noted that, for the GENE work described in Ch. 5, the modifications to $k_\parallel$ and the curvature drift are not required, since GENE is formulated based on more general descriptions of geometry than GYRO is.

Parameters

The MST has a major radius of $R_0 = 1.54\,\mathrm{m}$ and a minor radius of $a = 0.5\,\mathrm{m}$, yielding an inverse aspect ratio of $\epsilon_t \approx 1/3$. Simulations presented here look mainly at the radial location $r_0/a = 0.5$, with, unless otherwise stated, the other parameters being: $q = 0.186$, $\hat{s} = -0.716$, $\Theta = 1.35$, $a/L_n = 0.58$, $a/L_T = 5.0$, $T_i/T_e = 0.4$, $\nu(a/c_s) = 0$. The collision frequency ν, in particular, plays an important role in the dynamics of the MT mode, which will be discussed in Sec. 4.4. The numerical resolution parameters used for these simulations are typical for microtearing simulations, with 8 pitch angles, 8 energy gridpoints, 20 gridpoints in orbital time, and 64 radial gridpoints. In particular, the radial resolution must be high enough to resolve the narrow current channel physics of the microtearing mode. It is important to note that the simulations performed here are linear and for a generic RFP equilibrium. Modeling a more realistic equilibrium or performing nonlinear work has different resolution requirements, and the results of just such an approach can be found in Ch. 5.

4.2 Beta Scan

Since β values of 10% and higher are not unusual in the RFP, it is important to perform an analysis of potential electromagnetic instabilities that may arise. When increasing β, it is reasonable to expect that the ITG mode is eventually stabilized – it is thus helpful to know at what critical $\beta_{\mathrm{crit}}^{\mathrm{ITG}}$ stabilization occurs and how $\beta_{\mathrm{crit}}^{\mathrm{ITG}}$ scales with various geometric and equilibrium parameters. It is also important to determine whether a new instability emerges at higher β, and if so, at what critical β the instability arises and what characteristics apply to it. In the tokamak, the kinetic ballooning mode becomes unstable as β is increased

beyond a certain threshold. In the RFP, it would not be surprising for a microtearing mode (MTM) [56, 57, 58, 59, 60] to become unstable for β values above the low-β ITG regime, as it does in certain parameter regimes in the tokamak [61, 62, 63], provided the electron temperature gradient that drives the MTM is comparable to the ion temperature gradient for ITG instability.

It is natural to consider the MTM as a potential instability for the RFP, if only because it is the small-scale extension of global tearing modes [64], which dominate confinement in ordinary discharges [29]. The MTM is not a current driven mode: current driven tearing modes require that a current gradient that varies on the scale of the minor radius a be larger than the flux discontinuity at the resistive layer, which goes like $-2k_\theta$, ensuring that $\Delta' > 0$, where Δ' is the standard parameter of the MHD tearing mode. With the binormal wavenumber k_θ large, microtearing modes have $\Delta' < 0$. However, they can be driven by electron temperature gradients just like other drift modes, including trapped electron modes and electron temperature gradient driven modes.

A scan over β from 0 to 10% was performed to determine the variety of modes that might be dominant across this range. The results can be seen in Fig. 4.1. It should be noted that for this scan, the pinch parameter is kept constant and does not vary self-consistently with β. At low β, the dominant instability is identified as an electrostatic ITG mode. As β increases this mode is suppressed and eventually overtaken by a MTM at a β of approximately 4.5%. The transition can be seen most clearly in the real frequency plot. Here, the frequency of the ITG mode is in the ion direction (negative sign in this convention) and that of the MTM is in the electron direction (positive sign).

One interesting feature of the low-β versus high-β instabilities is the range of scales at which these modes are unstable. This difference can be seen in Fig. 4.2. At low β, the ITG mode ranges from $k_\theta \rho_s = 0.1$ to $k_\theta \rho_s = 0.9$, achieving a peak near 0.5. Initially, the MTM arises at these same scales, with a peak at roughly the same value, although with a slightly broader range. Fig. 4.3 shows the growth rates and frequencies versus wavenumber for $\beta = 4\%$. It can be seen that the ITG mode remains relatively unchanged and the

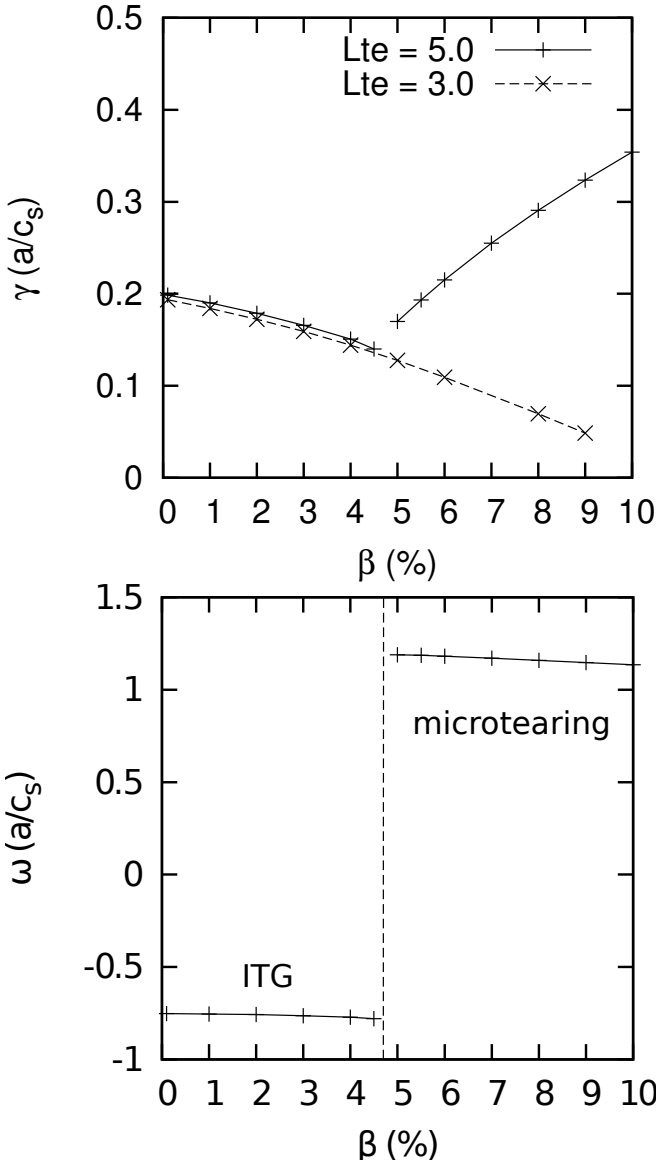

Figure 4.1: Growth rate and mode frequency plotted as a function of β for $k_\theta \rho_s = 0.372$. ITG is stabilized with increasing β, and MTM requires a critical β for instability. A transition of the dominant mode from ITG to MTM occurs at $\beta \approx 5\%$. Also shown is the growth rate for a case where $a/L_{Te} = 3.0$, where MTM is stabilized, to show more complete suppression of the ITG. In GYRO's sign convention, positive (negative) frequencies denote the electron (ion) direction.

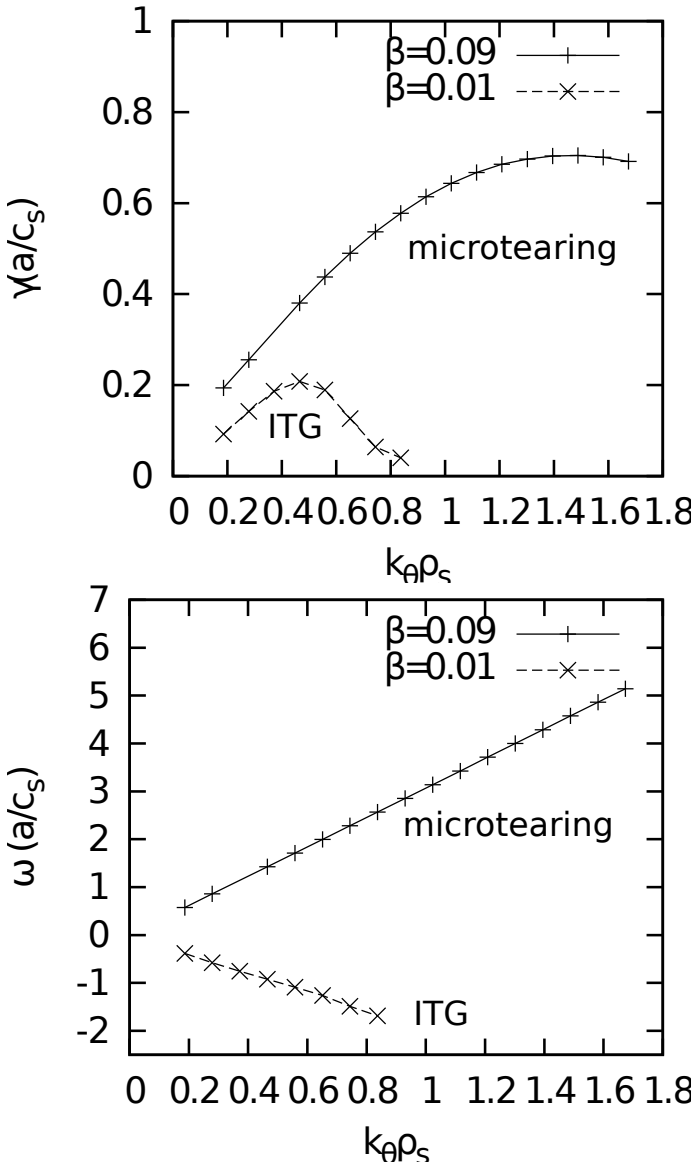

Figure 4.2: Growth rate and frequency as a function of wavenumber $k_\theta \rho_s$ for two different values of β. ITG is seen to be dominant at $\beta = 1\%$, microtearing at $\beta = 9\%$. In this convention, a negative (positive) real frequency indicates a mode in the ion (electron) diamagnetic direction. Collisions are turned off for these simulations.

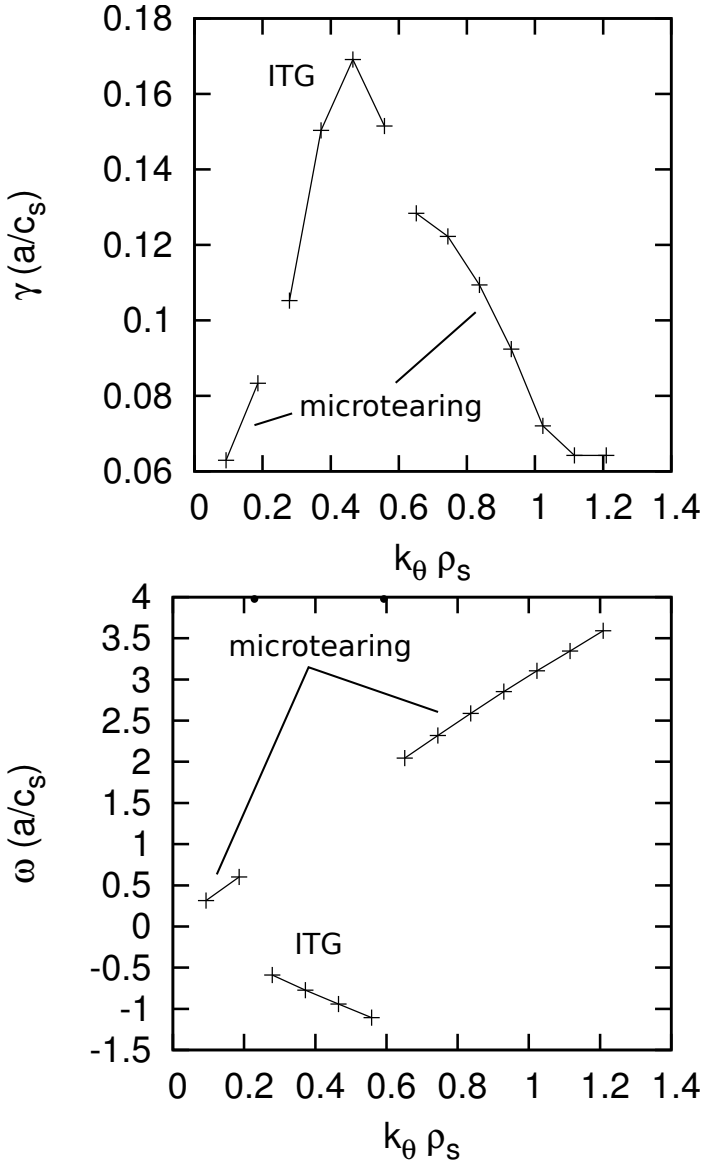

Figure 4.3: Growth rate and mode frequency plotted as a function of $k_\theta \rho_s$ for $\beta = 0.04$. At this value of β ITG and MTM exist at similar scales.

dominant instability at $k_\theta \rho_s = 0.3 - 0.6$, while the microtearing covers a broader range of k_θ. As β increases, the peak of the microtearing mode shifts to higher k_θ. This can be seen in Fig. 4.2, where it is observed that at a $\beta = 9\%$ the MTM not only reaches higher growth rates, but does so over a much larger range of scales, peaking at a value of $k_\theta \rho_s \approx 1.5$.

The range of β simulated covers different modes of operation of MST. A standard discharge will have values of $\beta \sim 4 - 5\%$, a range that means ITG and microtearing

may both be equally strong. Improved confinement pulsed poloidal current drive (PPCD) discharges, on the other hand, may achieve β values of 9% or higher [34], in which case microtearing may be the dominant mode, although for reasons that will be discussed in Ch. 5 certain characteristics of PPCD equilibria make MTM unlikely.

4.3 ITG β Suppression

Finite-β suppression of ITG (a linear effect which may be amplified nonlinearly [65]) has been a topic of study in the context of tokamaks [66], and that analysis will be applied here to ITG in the RFP. In the RFP, ITG growth rates can still be quite strong at values of β where tokamak ITG is typically stable [18], as can be seen in Fig. 4.1. In fact, ITG remains unstable past $\beta = 5\%$ (although subdominant to MTM) and may not stabilize until $\beta \sim 10\%$.

This analysis of the finite-β suppression of the ITG mode follows that of Hirose [66], making the appropriate modifications for the RFP geometry. Ref. [66] is itself an electromagnetic extension to the electrostatic theory presented in Ref. [67]. As discussed before, the RFP modifications are due to the different strengths and scale lengths of the magnetic field. In the tokamak, the scale length of magnetic field variation is proportional to the major radius, $1/L_B = \nabla B/B \sim 1/R_0$, while in the RFP, the appropriate scale is the minor radius, $\nabla B/B \sim 1/a$. As was mentioned above, the parallel derivative term also needs to be modified to account for the equivalent strengths of the poloidal and toroidal fields. Therefore, the modified terms will take the following forms: $k_\parallel = 1/(q_0 R_0(1+(\epsilon_t/q_0)^2)^{1/2})$ for the parallel wavelength, and $\omega_{Dj} = \mathbf{v}_{Dj}\cdot\mathbf{k} = 2cT_j(\nabla\mathbf{B}\times\mathbf{B})\cdot\mathbf{k}/eB^3 \sim 1/L_B$ for the curvature drift, where c is the speed of light and e is the fundamental charge.

The following discussion is based on a fluid analysis of the ITG instability. Starting with the ion continuity equation and the energy equation

$$\frac{3}{2}n_j\left(\frac{\partial}{\partial t}+\mathbf{v}_j\cdot\nabla\right)T_j + p_j\nabla\cdot\mathbf{v}_j = \frac{5}{2}n_j\mathbf{v}_{*j}\cdot\nabla T_j - \frac{5}{2}n_j\mathbf{v}_{Dj}\cdot\nabla T_j \quad , \tag{4.3}$$

and before including the finite-β effects, the ion and electron densities are found to be,

respectively,

$$n_i = \frac{(\omega + 5\omega_{Di}/3)(\omega_{*e} - \omega_{De}) - (\eta_i - 2/3)\omega_{*i}\omega_{De}}{(\omega + 5\omega_{Di}/3)^2 - 10\omega_{Di}^2/9}\frac{e\Phi}{T_e}n_0 \quad , \tag{4.4}$$

and

$$n_e = \frac{e\Phi}{T_e}n_0 \quad , \tag{4.5}$$

where $p_j = n_j T_j$, $\omega_{*j} = \mathbf{v}_{*j} \cdot \mathbf{k} = cT_j(\nabla \ln n_0 \times \mathbf{B}) \cdot \mathbf{k}/eB^2 \sim 1/L_n$, and $\eta_i = d\ln T_i/d\ln n_0$.

The expression for the electron density is modified by the consideration of finite-β effects. This is done by taking into account perpendicular magnetic field perturbations, or, equivalently, perturbations to the parallel magnetic vector potential: $\mathbf{B}_\perp = \nabla \times \mathbf{A}_\parallel$. Including such perturbations in the parallel momentum balance of electrons will result in the electron density taking the form

$$n_e = \left(\Phi - \frac{\omega - \omega_{*e}}{ck_\parallel}A_\parallel\right)\frac{en_0}{T_e} \quad . \tag{4.6}$$

The parallel electron current can be attained from the electron continuity equation and the electron density given in Eq. (4.6):

$$J_{||e} = \frac{n_0 e^2}{k_{||}T_e}((\omega_{*e} - \omega)\Phi + \frac{(\omega - \omega_{De})(\omega - \omega_{*e}) + \eta_e\omega_{*e}\omega_{De}}{ck_{||}}A_{||}) \quad . \tag{4.7}$$

Then, using Ampère's law and the quasineutrality condition, we arrive at the following relation:

$$A_\parallel\left(1 - \frac{\beta}{k_\parallel^2 L_n L_B}\left[2\frac{\varepsilon_n}{\tau^2} + \frac{1}{\tau}(1 + 2\varepsilon_n) + 1 + \eta_e\right]\right) = \frac{\omega_{*e}}{ck_\parallel}\frac{k_{De}^2}{k_\perp^2}\left(1 + 2\frac{\varepsilon_n}{\tau}\right)\Phi \quad , \tag{4.8}$$

where $\tau = T_e/T_i$, $k_{De} = (4\pi n_0 e^2/T_e)^{1/2}$, $\eta_e = d\ln T_e/d\ln n_0$, $k_\perp = \mathbf{k} \cdot \mathbf{B}_\perp \approx k_\theta$, and $\varepsilon_n = L_n/L_B$. Then, as in Ref. [66], we are able to derive the stability condition, with certain terms adjusted to account for the RFP generalizations

$$\beta \geq \frac{\varepsilon_n \epsilon_t^2 \tau^2}{(1 + (\epsilon_t/q_0)^2)q_0^2[(\tau + 2\varepsilon_n)(\tau + 1) + \tau^2\eta_e]} \quad . \tag{4.9}$$

The criterion given above is similar to that of Ref. [66], but for RFP parameters it yields a higher critical β than is seen in tokamaks. This is due primarily to the smaller q_0 and

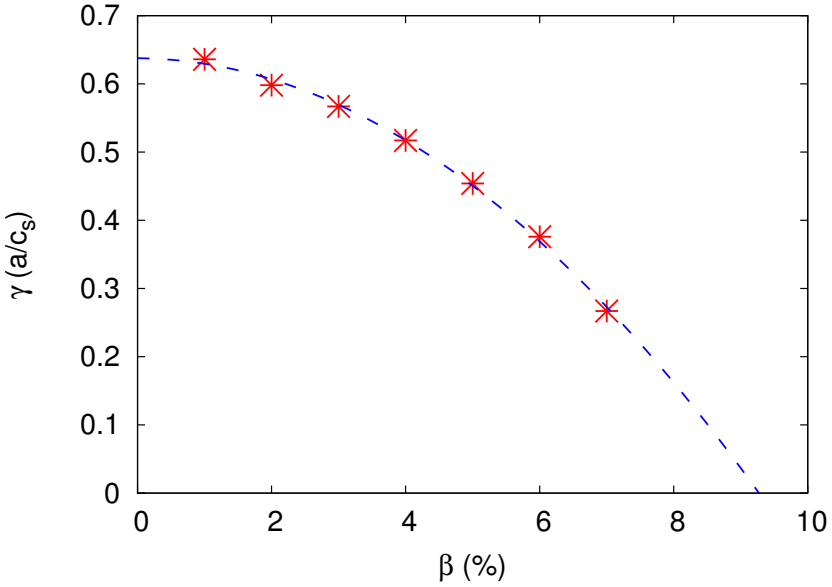

Figure 4.4: Beta stabilization of ITG for the parameters $r/a = 0.4, q = 0.244, a/L_{Te} = 0, a/L_n = 0.08$. A parabolic fit has been used to project out to a critical beta for stabilization of $\sim 9\%$. The critical β estimated by Eq. (4.9) is $\sim 19\%$, roughly a factor of two larger than that seen in the simulations.

shorter connection length that is a result of the equivalent strengths of the poloidal and toroidal fields in the RFP.

For the parameters used in Fig. 4.1 and taking $a/L_B = 1$, the above expression yields a critical β of just above 6% for $a/L_{Te} = 5.0$ and just above 9% for $a/L_{Te} = 3.0$. An alternate case, in which $r_0/a = 0.4, q_0 = 0.244$, and $a/L_{Te} = 0$ is presented in Fig. 4.4, and the resulting critical beta for these parameters is $\sim 19\%$, which differs from the limit seen in the simulations by roughly a factor of two. There is some sensitivity to $1/L_B$ (contained in ε_n) in these calculations and consequently results from the analytic expression should be treated as estimates only, but a general conclusion that may be drawn is that the critical beta calculated for the RFP will be larger than that for a tokamak by approximately a factor of the aspect ratio.

Attention is now turned to the instability observed at higher β, the microtearing mode.

4.4 Microtearing Modes

The dominant instability at higher values of β is identified as a MTM. These modes are characterized by having tearing parity in the parallel direction. This appears as odd parity in the electrostatic potential Φ and even parity in the magnetic potential $A_\parallel$, as seen in the eigenmode structure in Fig. 4.5. This structure, including the small amplitude features occurring every 2π (attributed to poloidal variation) is similar to that seen in other devices, including MAST [68] and RFX-mod [53]. A sample ITG eigenmode structure, by way of comparison, is given in Fig. 4.6. Several parameter scans were performed in order to better characterize the observed MTM. The β value of these scans was taken to be 9%, a value chosen to lie in the potential range for PPCD discharges in MST.

The MTM is known to be driven by the electron temperature gradient rather than the current gradient, as is the case for the large scale tearing mode. Thus, a strong dependence of the growth rate on L_{Te} is expected, and this is seen in Fig. 4.7. Here the mode can be seen to require the threshold gradient of approximately $a/L_{Te} \approx 3.5$, which is higher than that reported in [53] ($(a/L_{Te})_{\text{crit}} \sim 2$). This threshold falls at a similar value as is observed for the ion temperature gradient threshold for the ITG mode. However, it can be seen that the MTM growth rate rises much more steeply with temperature. Such a strong dependence can be expected to lead to profile stiffness, fixing the experimental gradient near the threshold for instability. Additionally, nonlinear simulations in the spherical tokamak have revealed a nonlinear upshift in the effective gradient threshold as compared to linear simulations [69], and the same effect can be expected to occur in the RFP.

In Fig. 4.8 can be seen the effect of varying the temperature ratio T_i/T_e. The MTM shows a strong increase of the growth rate with this ratio. There is an opposite dependence in ITG (see plot b), where the growth rate decreases as T_i/T_e increases. This is consistent with MTM's electron temperature gradient drive.

An interesting aspect in recent gyrokinetic work relating to the MTM is the observation of instability in low-collisionality regimes. This is observed for simulations with both tokamak [68, 62, 69, 63] and RFP geometries [53, 70]. Theoretically, a series of papers

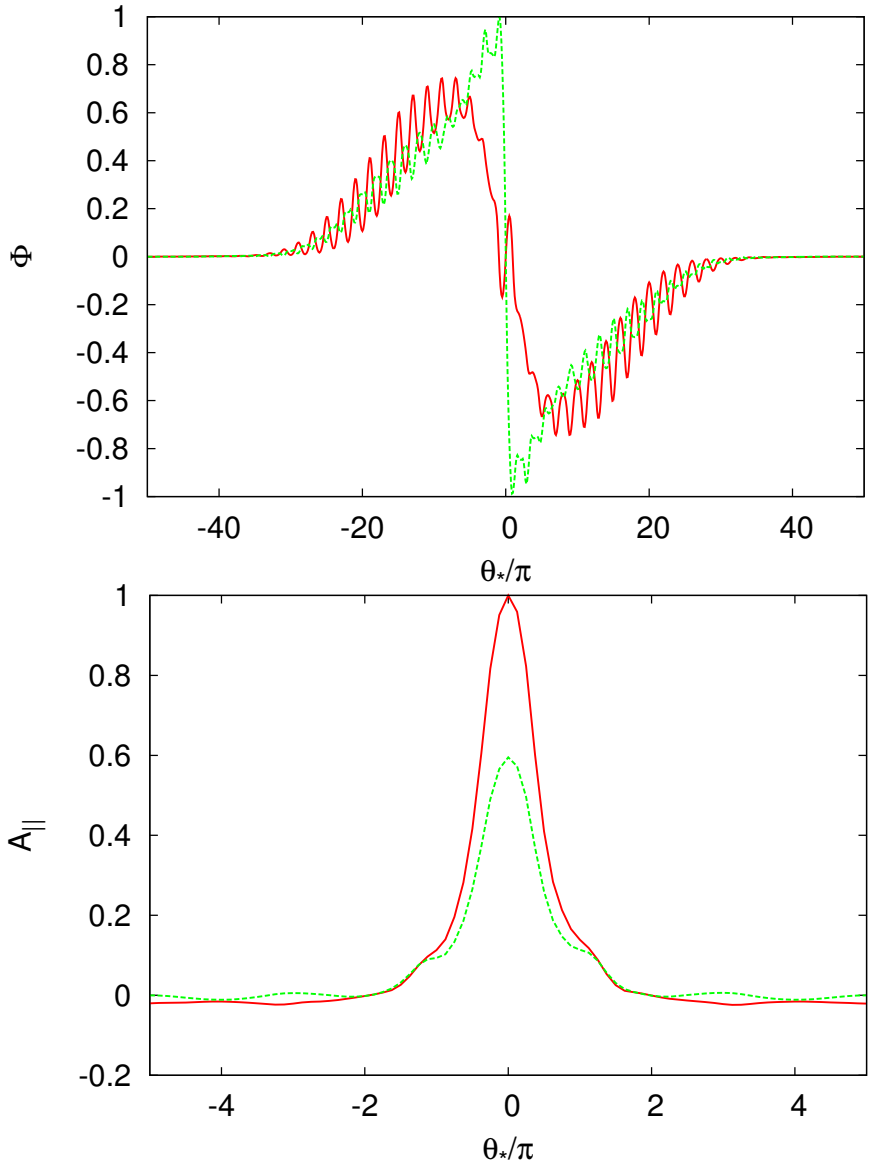

Figure 4.5: Eigenmode structure for the MTM in electrostatic potential Φ and magnetic potential $A_{\|}$ with both real (green dashed curve) and imaginary (red solid curve) components. The fields are plotted against the magnetic-field following ballooning angle θ_*. This mode displays tearing parity, which is recognized as even parity in $A_{\|}$ and odd parity in Φ.

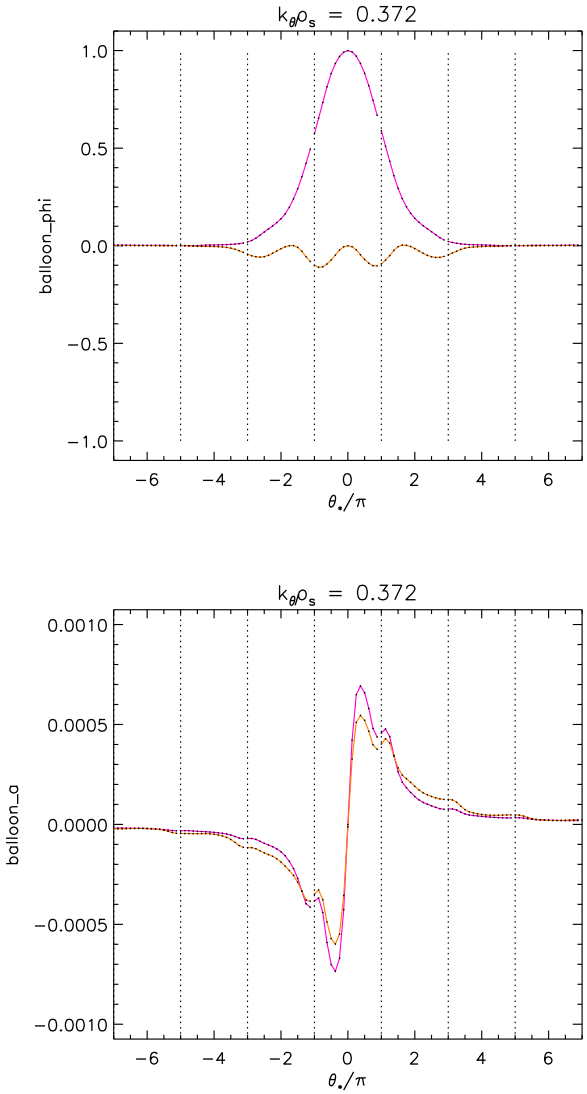

Figure 4.6: Eigenmode structure for the ITG mode in electrostatic potential Φ (upper plot) and magnetic potential $A_\parallel$ (lower plot) with both real (pink curve) and imaginary (orange curve) components. The fields are plotted against the magnetic-field following ballooning angle θ_*. This mode displays ballooning parity, which is recognized as odd parity in $A_\parallel$ and even parity in Φ. As an electrostatic mode plotted for $\beta = 0.001$ the magnetic vector potential fluctuation is quite small.

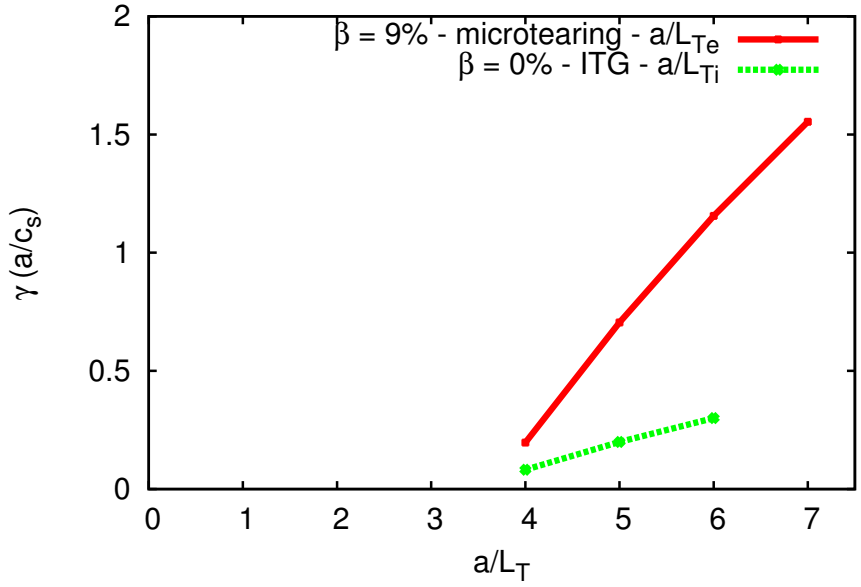

Figure 4.7: Growth rate plotted against temperature gradient for $k_\theta \rho_s = 0.372$ in the case of MTM (red squares) and ITG (green circles). Both instabilities have a threshold around $a/L_T \approx 3.5 - 4.0$, for their respective driving gradients, although these thresholds may differ for an alternate set of parameters.

specific to the tokamak in their approximations have collectively pointed to the conclusion that the microtearing mode is very sensitive to collisionality ν, and should become stable for small collisionality [59, 71, 58, 60]. One design of the current study has been to probe this mismatch between these theoretical predictions and the results of the aforementioned gyrokinetic simulations. A collisionality scan (Fig. 4.9) shows instability at low ν, but behavior with other parameters suggests that there may be two branches of the instability, one at low collisionality, and one at higher values of ν (in the 'semi-collisional' range) that is more compatible with theoretical predictions. We specifically study the possibility, first suggested for RFP tearing modes in Ref. [72], of an RFP MTM branch that is enabled by the large electron curvature drift of the RFP. Artificial variation of the strength of the electron curvature and ∇B drifts shows that the growth rate diminishes toward zero when the magnetic drift falls outside a certain range of values. This is in agreement with recent work done in the spherical tokamak [63] and the RFP [70].

Since collisions are expected to play an important role in the mechanism for instability

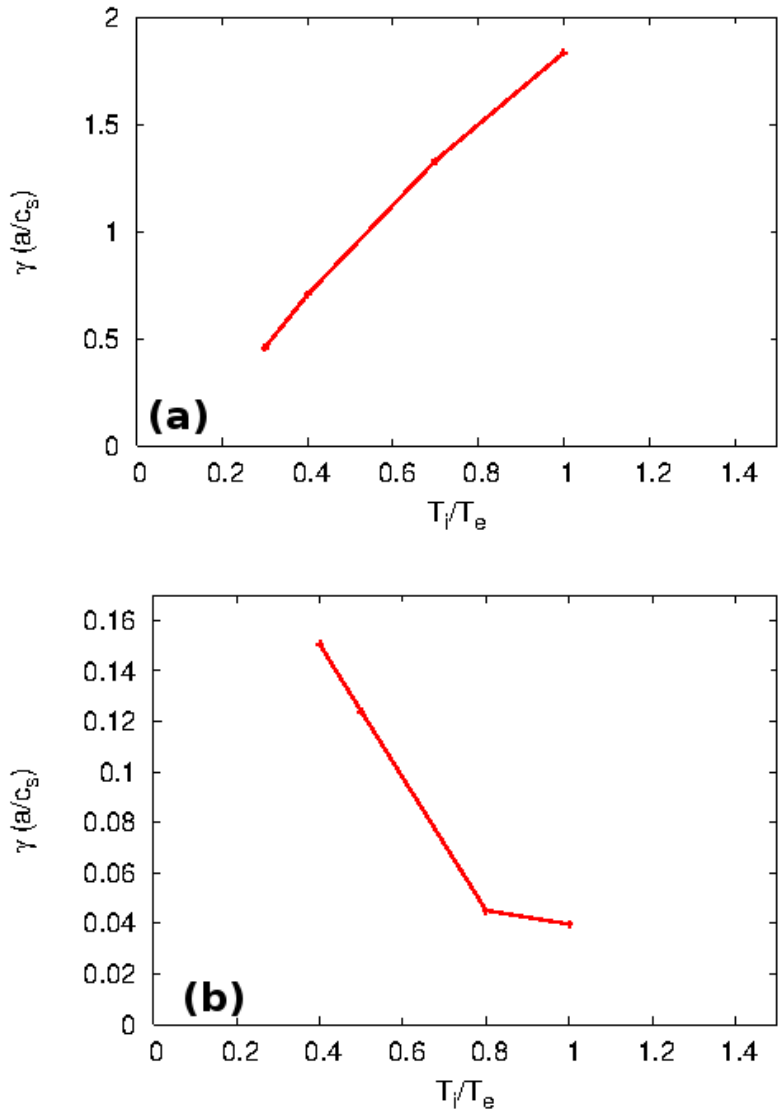

Figure 4.8: Growth rate plotted against the temperature ratio T_i/T_e for $k_\theta \rho_s = 1.488$. Shown are MT (a) and ITG (b). The qualitative dependence is consistent with expectations of modes with either ion or electron gradient drives.

of MTM [57, 59], a scan was performed over the collision frequency, the results of which are given in Fig. 4.9. The collision operator used in GYRO is a pitch-angle scattering operator

$$C(f) = \frac{\nu_e(\epsilon)}{2}\frac{\partial}{\partial\xi}(1-\xi^2)\frac{\partial f}{\partial\xi}, \tag{4.10}$$

where ξ is the pitch angle and $\nu_e(\epsilon) = \nu[Z_{\text{eff}} + H(\epsilon^{1/2})]/\epsilon^{3/2}$, with Z_{eff} the effective nuclear charge, $H(x) = \exp[-x^2]/x\pi^{1/2} + (1 - 1/2x^2)\text{erf}(x)$ and $\epsilon = E_e/T_e = m_e v^2/2T_e$. In these expressions, ν is the control parameter in the simulations.

A notable feature of Fig. 4.9 is the appearance of what seem to be two separate regimes of MTM, with a transition between the two occuring roughly around $\nu \sim 0.1 - 1$. At $\nu \sim 1$ the growth rate achieves a peak and then falls off for higher collisionality. At lower values of ν the growth rate flattens, remaining finite in the limit of zero collisionality. GYRO uses an upwind differencing scheme, which may introduce collisional effects, but additional convergence checks were performed and increased resolution does not result in substantial changes to the growth rate. It should also be noted that the real frequency scales linearly with ν above $\nu \approx 1$.

The collisional dependence of this mode was investigated at several different radii (varying only q_0 and $\hat{s}$ in correspondence with the TBFM and keeping all other parameters fixed). The results of this can be seen in Fig. 4.10. Importantly, the wavenumber spectrum at $\nu = 1$ (a) shows a general stabilization of the mode at larger radius, which might be attributed to the larger shear at these locations. The collisionality scan (b) also shows interesting behavior: in particular, the growth rate at low ν is much more affected by increased radius than at $\nu \sim 1$, and at $r/a = 0.6$ the mode is completely stabilized in the collisionless limit. This behaviour may suggest that there are two distinct varieties of MTMs in these simulations – one at low collisionality and one at moderate collisionality – that have somewhat different physics behind their drive mechanisms. The effects of increasing the pinch parameter Θ are similar to the effects of increasing the radius, as can be seen in Fig. 4.11. This is to be expected from the TBFM, due to the same parametric dependence on r and Θ in that model. As Θ increases the growth rate of the MTM falls and the peak shifts to lower k_θ.

Although the accuracy of the TBFM at $\Theta = 1.7$ is questionable, there is a clear trend. Higher Θ equilibria, corresponding with higher values of local magnetic shear, result in lower growth rates for the MTM. This is especially relevant for PPCD discharges, which may have values of Θ as high as 3. This suggests that the MTM is likely to be stable in PPCD.

The physics of the drive mechanism was investigated further by looking at the role of magnetic drift in the instability. In this study, a scalar factor α (not associated with the α_{MHD} of the s-α model) was placed in front of the magnetic drift term (including both curvature and ∇B drifts) in GYRO and varied to change its relative strength; a value of $\alpha = 1$ corresponds to the physical magnetic drift. The results of this are seen in Fig. 4.12 for $\nu = 0.001$ (a) and $\nu = 1.0$ (b). In both cases, the instability is strongest for $\alpha \approx 1$ and falls off for values much lower or higher than this. An analysis yielding similar results has been conducted using GS2 in RFX-Mod [70]. This behavior is consistent with the magnetic curvature drift instability derived by Finn and Drake (Ref. [72]), in which they describe a semi-collisional drift-tearing mode unstable in the presence of curvature drift and an electron temperature gradient. Ref. [72] is formulated in a cylindrical RFP equilibrium, and they note that this instability is strong only when $\omega_D \sim \omega_*$, a characteristic that makes it more relevant to the RFP, with its associated stronger curvature drifts, than in a standard tokamak. We also note that although Ref. [72] uses fluid theory in the semi-collisional regime, collisions do not play an explicit role in the instability, and it is plausible that this mode may arise in the collisionless limit with proper inclusion of magnetic drifts. Such an analytic approach is taken in Ch. 6. Another possible mechanism may be due to trapped particles, as suggested by recent work in spherical tokamaks [63]. The relationship between these instability drives is not yet clear and more work remains to be done to establish the relevant physics for different devices. It may be the case that there are multiple mechanisms for instability in this regime and a unique collisionless MTM does not exist.

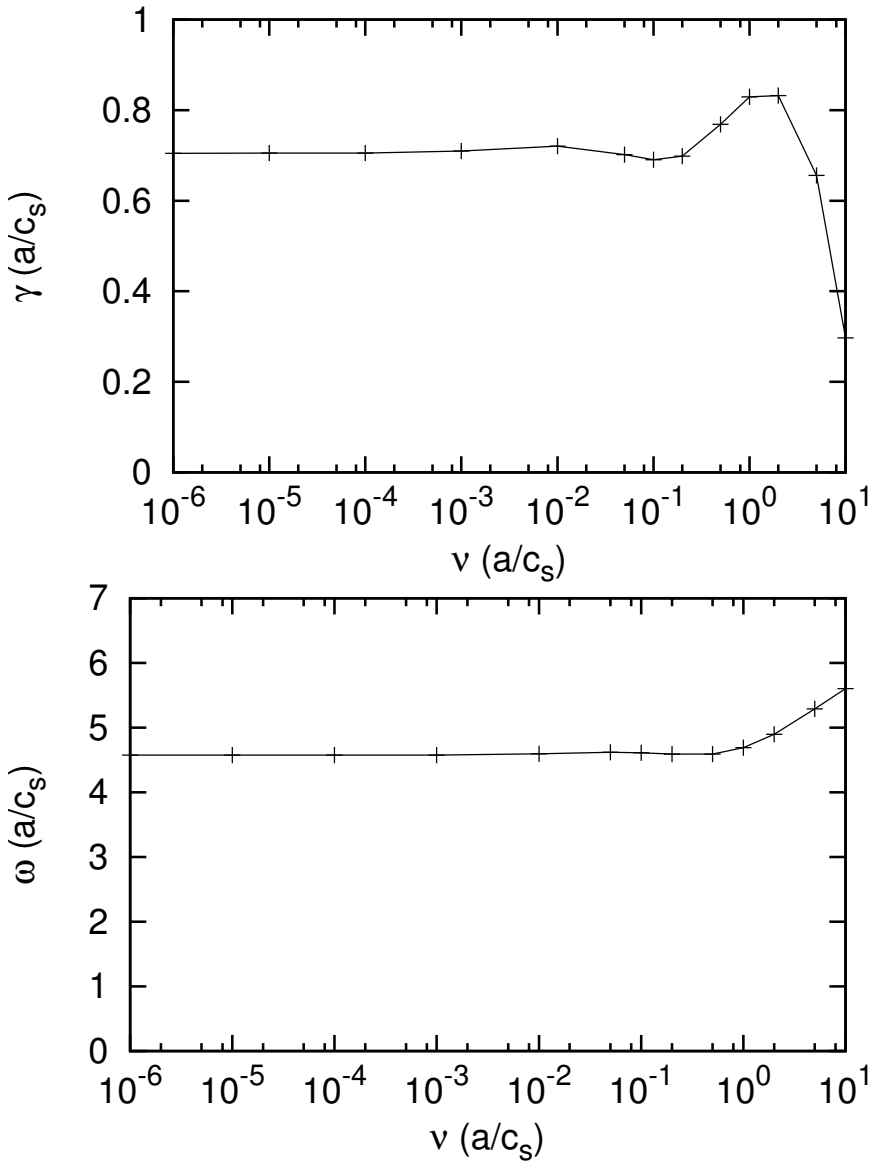

Figure 4.9: MTM growth rate and frequency plotted against ν for $k_\theta \rho_s = 1.488$. There appear to be two distinct regmes: a region of constant growth rate and constant real frequency at low ν and a separate region at ν with a peak in growth rate and a real frequency that scales linearly with ν.

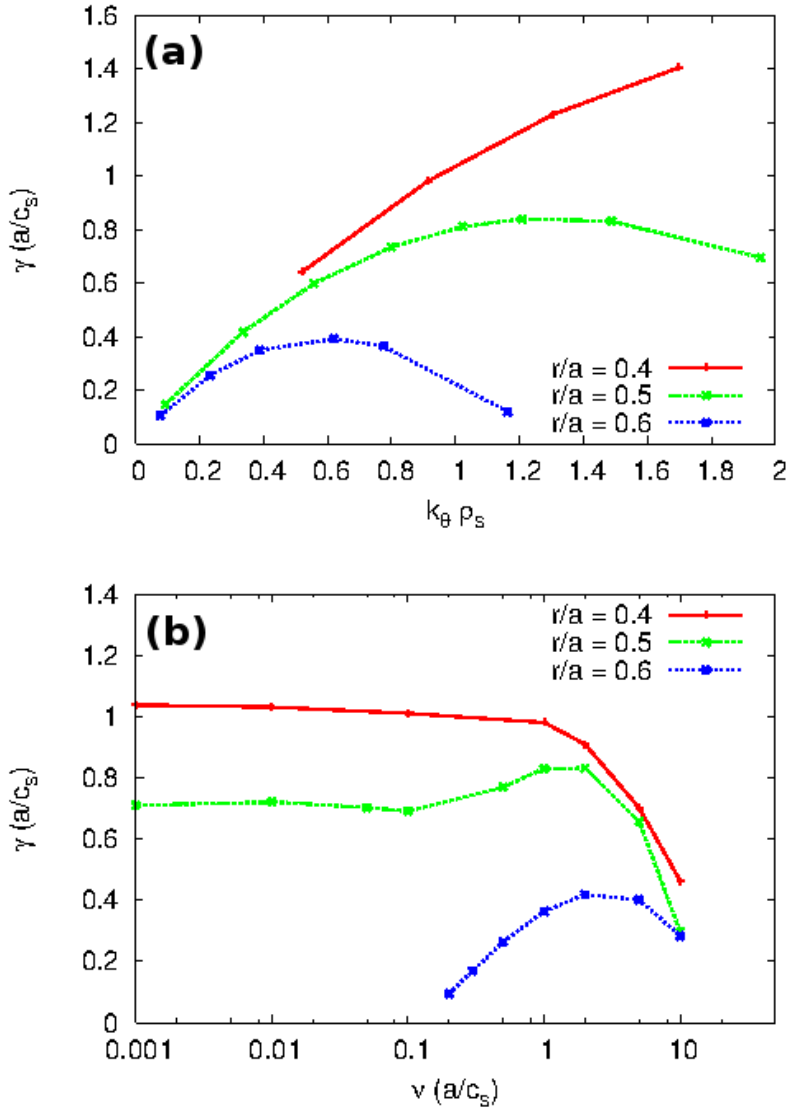

Figure 4.10: MTM wavenumber spectrum at $\nu = 1$ (a) and collisionality scan (b) for different values of r/a. The corresponding values of q_0 and shear are — $r/a = 0.4$: $q_0 = 0.209$, $\hat{s} = -0.382$ (red solid curve); $r/a = 0.5$: $q_0 = 0.186$, $\hat{s} = -0.716$ (green dashed curve); $r/a = 0.6$: $q_0 = 0.155$, $\hat{s} = -1.344$ (blue dotted curve). There is stabilization of MTM with increasing radius r/a, especially prevalent at low ν. Increased radius coincides with increased shear, which may play a role in stabilization.

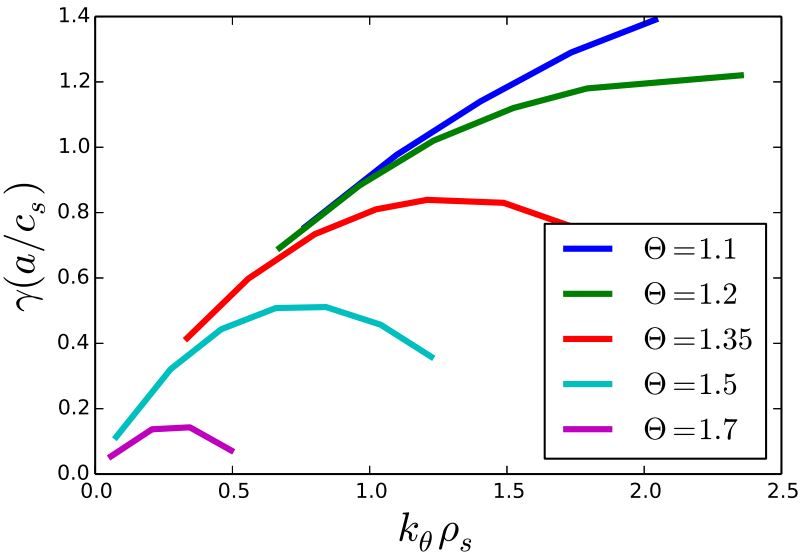

Figure 4.11: MT wavenumber spectrum at $\nu = 1$ for different values of Θ, the RFP pinch parameter. The corresponding values of q_0 and shear are — $\Theta = 1.1$: $q_0 = 0.255$, $\hat{s} = -0.4$ (blue curve); $\Theta = 1.2$: $q_0 = 0.224$, $\hat{s} = -0.507$ (green curve); $\Theta = 1.35$: $q_0 = 0.186$, $\hat{s} = -0.716$ (red curve); $\Theta = 1.5$: $q_0 = 0.153$, $\hat{s} = -1.011$ (cyan curve); $\Theta = 1.7$: $q_0 = 0.115$, $\hat{s} = -1.637$ (purple curve). There is stabilization of MTM with increasing Θ. Increased Θ corresponds to increased shear, which may play a role in stabilization. This also suggests that higher-Θ PPCD discharges may be stable to MTM.

4.5 Chapter Summary

The linear characteristics of microinstabilities in a generic RFP geometry were investigated using the gyrokinetic code Gyro. The equilibrium modeled in this chapter is one of low q and high magnetic shear relative to the tokamak, something that is true generally of RFP equilibria. It is important to note, however, that other RFP equilibria may involve yet lower q and higher shear, and so care should be taken when extrapolating these results to other regimes. Just such a case is the focus of Ch. 5, which investigates microinstabilities in specific improved confinement discharges in MST.

It has been shown that under certain conditions, including high temperature gradients and weak density gradients, MTM supplants the ITG instability as the dominant mode above a critical β value around 5% - 6%. In this transition the dominance of ITG at low β is assured by having an ion temperature gradient above the threshold $a/L_{Ti} \approx 3$.

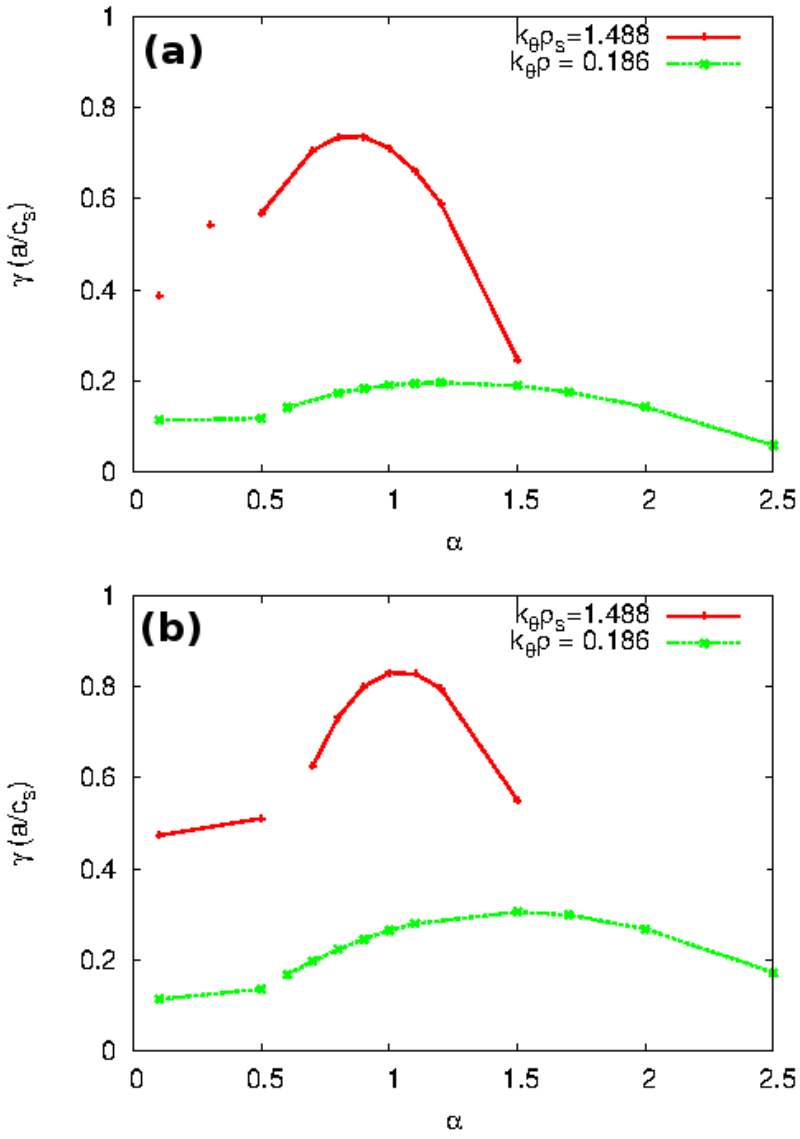

Figure 4.12: The role of magnetic drift in the MTM instability. The parameter α is a factor regulating the strength of the magnetic drift (including both curvature and ∇B drifts) in the code. Shown are $\nu = 0.001$ (a) and $\nu = 1.0$ (b), as well as $k_\theta\rho_s = 1.488$ (red solid curve) and $k_\theta\rho_s = 0.186$ (green dotted curve). This behavior is similar to that seen in Finn and Drake (1986). The points at low α represent a separate mode that has not been studied in detail.

The dominance of microtearing at higher β is assured by having the electron temperature above a similar threshold ($a/L_{Te} \approx 3$). We show that the coupling to Alfvén waves that stabilizes the ITG mode as β increases does so at a higher β in the RFP than in the tokamak because of the shorter parallel connection length associated with the large poloidal field. The MTM is identified on the basis of a mode structure that shows canonical tearing parity in the electromagnetic fields and a frequency in the electron direction. We examine scaling properties of the MT growth rate, including its threshold behavior, its scalings with the temperature ratio, and equilibrium quantities like the pinch parameter Θ. Growth rate scalings with respect to both r and Θ relate to magnetic shear scaling, which in the TBFM is not an independent equilibrium parameter. This work follows a number of recent studies that suggest the microtearing mode may be important in both the tokamak and the RFP [68, 62, 73, 69, 53, 63, 70]. Here our analysis is specific to equilibria consistent with certain regimes of operation of the Madison Symmetric Torus [28]. Moreover, in adapting gyrokinetic codes originally developed for the tokamak, we are careful to capture all of the effects arising from an equilibrium magnetic field with comparable poloidal and toroidal field components. This can be done using the toroidal Bessel function model in the GYRO code [18], with RFP-appropriate representations of the curvature drift and parallel derivative [50].

The MT mode was further investigated by performing a variety of parameter scans. The characteristics of the mode were in agreement with previous simulation work in other devices. Evidence for a collisionless MTM was seen, although further work remains to be done as to be determine the nature of the physics behind this mode. Previous analytic work in tokamaks (see Refs. [57, 59]) has concluded that MTM should be stable in the collisionless limit. Beside the results presented here, evidence contradicting this conclusion has been seen in gyrokinetic simulations in tokamak [62], spherical tokamak [68, 63], and RFP [70] geometries. There is some evidence that magnetic drift plays an important role in the instability, and it may be described by the magnetic curvature drift instability of Finn and Drake [72]. This topic is further explored in Ch. 6.

The results of this work regarding implications for the Madison Symmetric Torus suggest that although MTM may be capable of playing a role in the gyroscale dynamics, various geometric scaling properties suggest that it will be stabilized for the parameter regime of high confinement PPCD discharges. Let us note, however, that for alternate sets of parameters other modes, such as the trapped electron mode or kinetic ballooning mode, may emerge and play a role in the turbulence characteristics. This is the topic of the next chapter, in which a more flexible equilibrium model is used to investigate the microinstability spectrum of PPCD discharges.

Chapter 5

Microturbulence studies of improved confinement discharges

Opening the way to a more in-depth study, the previous chapter addressed many of the fundamental aspects of microinstabilities and their characteristics in a reversed field pinch. In particular it was shown that the stronger poloidal field as compared to a tokamak leads to different stability thresholds, differing from similar tokamak quantities by roughly a factor of the aspect ratio.

Although this fundamental analysis was useful for investigating the general nature of RFP instabilities, the question remains of the type and characteristics of instabilities that may arise in some of the improved confinement discharges in MST, which are described by an RFP pinch parameter Θ at which the TBFM is no longer valid. These improved confinement discharges are a regime with longer energy confinement time than the standard discharges and likely to be more susceptible to microinstability physics.

The technique for achieving these advances is pulsed poloidal current drive (PPCD), a current profile control technique that results in reduced global tearing mode activity and improved energy confinement time [32]. It is important to understand the role that microinstabilities play in this regime of operation. This adds to the previous body of microinstability work in the RFP, which has been done either in a generic, low-Θ equilibrium

current	r/a	q	$\hat{s}$	β	ν_c	R_0/L_T	R_0/L_n
200 kA	0.61	0.04	−5.9	0.065	0.005	15.1	4.4
	0.79	−0.06	10.3	0.017	0.03	21.8	13.9
	0.84	−0.09	6.9	0.010	0.05	29.5	19.4
	0.89	−0.13	4.8	0.004	0.11	45.1	32.1
500 kA	0.76	−0.05	10.0	0.023	0.0012	11.3	19.7
	0.81	−0.09	6.7	0.015	0.0013	14.5	25.1
	0.86	−0.12	5.0	0.007	0.0014	25.4	34.8
	0.91	−0.16	3.8	0.002	0.0022	76.8	71.9

Table 5.1: Physical parameters for the two MST discharges studied in this work, as obtained from the MSTFit equilibrium reconstruction code. It has been assumed that $T_i = 0.4T_e$, and therefore $R_0/L_T = R_0/L_{T_e} = R_0/L_{T_i}$. For more on MSTFit, see Anderson et al. (2004).

[50, 55] (the results of which were described in Ch. 4) or within the context of an internal transport barrier in a single-helical-axis (SHAx) regime [54, 53, 70].

In the present chapter we address the picture of microinstabilities and their associated turbulence in a set of PPCD discharges on the Madison Symmetric Torus (MST) [41]. We find in this case that ITG and TEM are the dominant instabilities. Although ITG has been studied in some detail in the context of the RFP, less is known about the characteristics of TEM. TEM turbulence has been considered to be a source of electron heat transport in tokamaks, but its role in the RFP is not yet certain. The results of this chapter represent the content of a paper submitted to Physics of Plasmas [74].

5.1 Modeling

The modeling in this chapter was performed with the adjusted circular model (ACM) which was introduced in Ch. 3. In this model, the magnetic field is given as

$$\mathbf{B} = \frac{R_0 B_0}{R} |q| f(r/R_0)(\mathbf{e}_\phi + \mathbf{e}_\theta \frac{r}{R_0 \bar{q}}) \quad . \tag{5.1}$$

An earlier version of the ACM which has been employed to produce all numerical results reported in this paper differs from that described above in the use of q rather than $\bar{q}$ in Eq. (5.1). This results in a slight inaccuracy as $r/a \to 1$, but any difference in linear growth rates or nonlinear fluxes is less than 10% for the cases studied here.

The parameters for these simulations are drawn from experimental discharges on the Madison Symmetric Torus, an RFP with a major radius of 1.54 m and a minor radius of 52 cm. Two separate PPCD discharges are modeled here: a 200 kA discharge and a 500 kA discharge. These discharges have been chosen because they represent different regimes of PPCD, the former with the highest achieved value of β and the latter with the highest achieved electron temperature [34]. The goal of performing a microinstability analysis of these discharges is to assess the role of microturbulence in the transport characteristics of PPCD plasmas, as well as provide further information regarding observed differences between the two cases. The set of parameters for each of these cases is presented in Tab. 5.1. Listed are the plasma current for each of the two discharges, the normalized minor radius at which simulations were conducted, the safety factor q, magnetic shear $\hat{s}$, electron $\beta = 8\pi n_0 T_{e0}/B^2_{\text{ref}}$, normalized temperature gradient $R_0/L_T = -(R_0/T)dT/dr$ of both electrons and ions, and normalized density gradient $R_0/L_n = -(R_0/n_0)dn_0/dr$ at each of the radial locations. B_{ref} is the background magnetic field of the flux tube. The collisional frequency is given by $\nu_c = \pi \ln \Lambda e^4 n_0 R/\sqrt{8}T^2_{e0}$, where n_0 is the background density, e is the elementary electric charge, and $\ln \Lambda \approx 10$.

The 200 kA and 500 kA discharges have several key differences. At any given radial location, the 200 kA discharge has larger values of β and normalized temperature gradients that are stronger than the respective density gradient. The 500 kA discharge, conversely, has density gradients that are larger than the temperature gradients. The q and T_i profiles for the 200 kA case are given in Fig. 5.1 and Fig. 5.2 for the 500 kA case. This difference is a determining factor in the type of instability that is dominant in each of these cases.

The experimental profiles are generated using the MSTFit equilibrium reconstruction code [42], which solves the Grad-Shafranov equation with input from external and edge diagnostics on MST. The electron temperature profile is attained from Thomson scattering and soft-X-ray tomography. Density measurements are produced with far-infrared (FIR) interferometry/polarimetry. There are no ion temperature measurements for these discharges, but measurements from some improved confinement discharges have found core

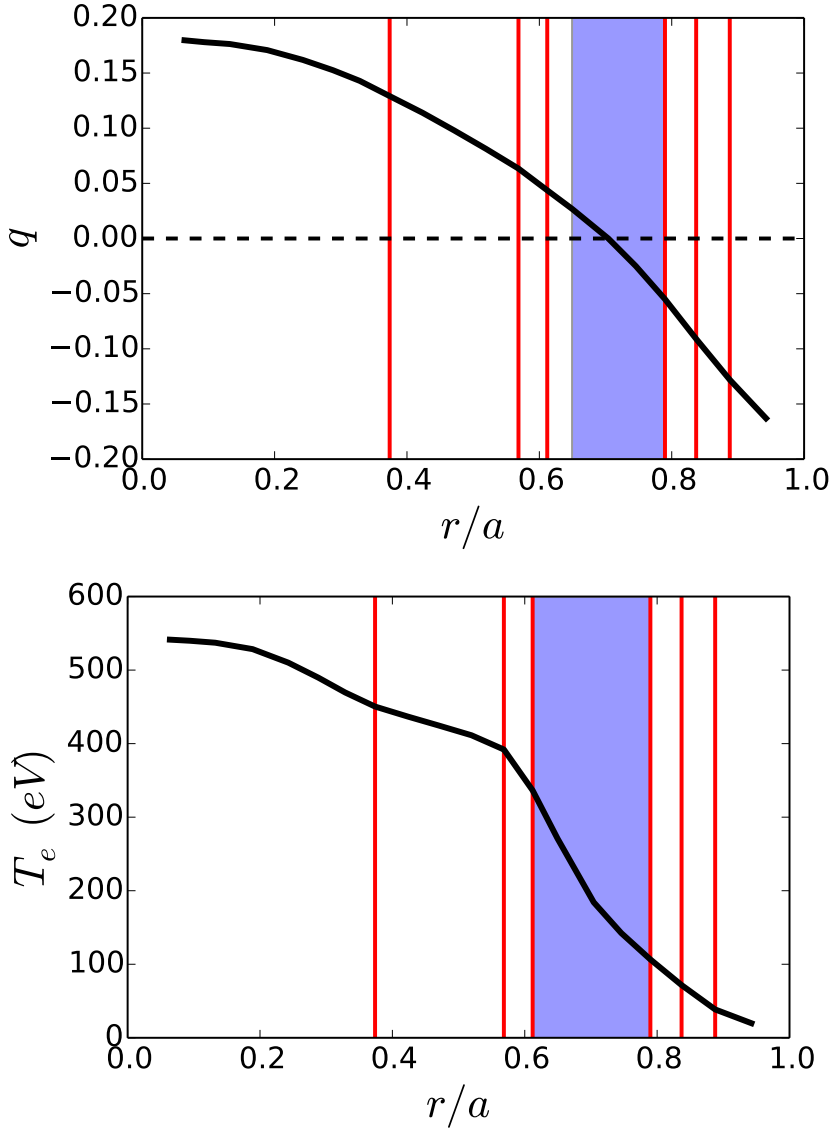

Figure 5.1: Radial profiles for the safety factor and the temperature for the 200 kA case. The red vertical lines indicate the radial locations at which simulations were performed. The blue shaded region indicates high shear ($|\hat{s}| \gtrsim 10$) and has been excluded from modeling.

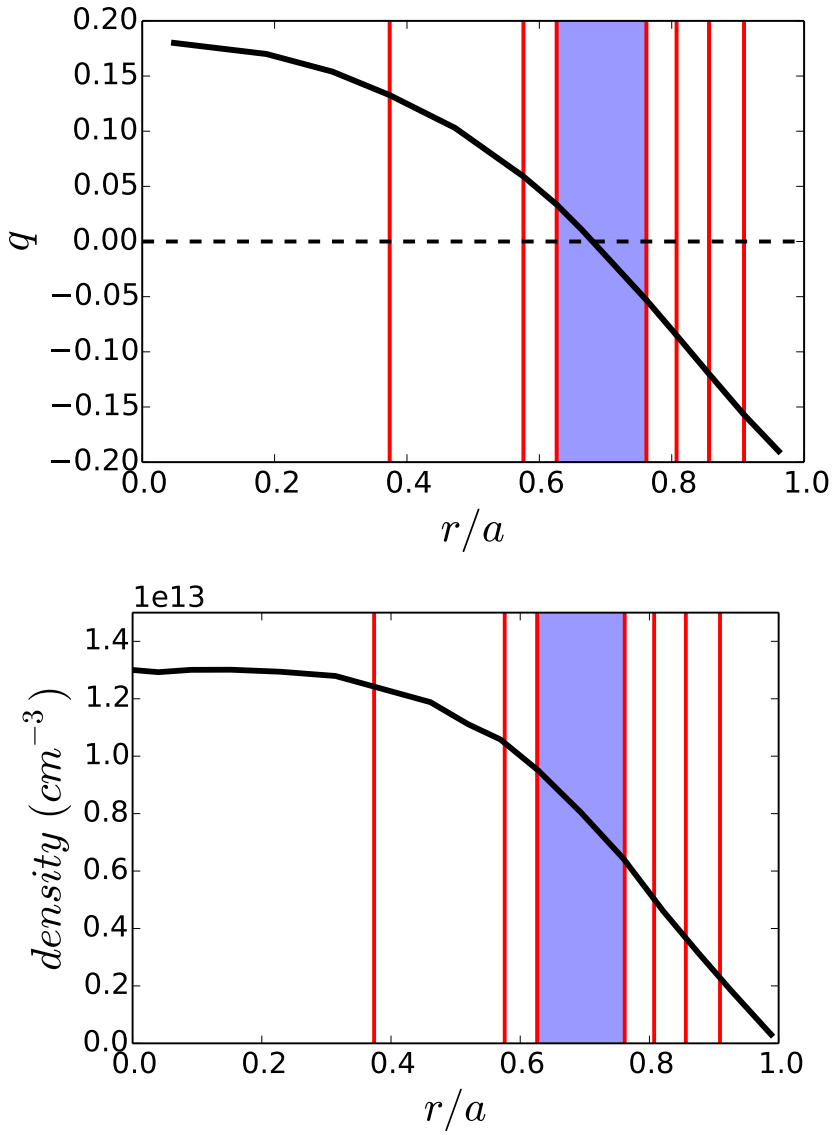

Figure 5.2: Radial profiles for the safety factor and the density for the 500 kA case. The red vertical lines indicate the radial locations at which simulations were performed. The blue shaded region indicates high shear ($|\hat{s}| \gtrsim 10$) and has been excluded from modeling.

ion temperature to be on the order of $30\% - 50\%$ of the core electron temperature [32], so the ion temperature in the present work is assumed to be a constant factor of 0.4 times the electron temperature.

These experimental profiles are used in the GENE code as input for the collisionality, β, and gradient values, and as a magnetic field profile that is replicated using the analytic geometry model detailed above, with $f(r/R_0)$ as a sixth-order polynomial fitted to the reconstructed magnetic field. In all the work that follows, GENE is used in its radially local mode of operation, in which background quantities are assumed to vary linearly over the simulation domain. The nonlinear simulations to follow have radial box sizes of $\approx 17 - 20\rho_s \approx 17 - 20$ cm. Global simulations will therefore become necessary once experimental measurements of heat and particle diffusivities are sufficiently precise to demand corresponding highly accurate theoretical predictions, but local simulations can still be expected to yield good results here, within a few ten percent of the global, physical fluxes. An important distinction must be made here between the tokamak definition of magnetic shear $\hat{s}$ used above and the actual physical shear, referred to here as $\hat{s}_{\mathrm{RFP}}$. Magnetic shear, essentially a measure of the rate of variation of $k_{\|} \sim \mathbf{B} \cdot \nabla$ away from a rational surface, is a well-defined quantity throughout the plasma volume. The quantity $\hat{s}$, however, relies on the tokamak expansion $B_\phi \gg B_\theta$ and has a singularity at the $q = 0$ surface. Near this surface, a new expansion of $k_{\|}$ can be made, with the approximation $B_\theta \gg B_\phi$, and an RFP-specific formula derived. The result of this is the expression $\hat{s}_{\mathrm{RFP}} = Rdq/dr$, which holds as long as $|B| \sim B_\theta$ remains true. The relative ratio $\hat{s}/\hat{s}_{\mathrm{RFP}} = r/Rq$ provides a measure of the inadequacy of the tokamak shear definition near the reversal surface. Note that this inadequacy does not affect the accuracy of the GENE simulations: although $\hat{s}$ is provided as an input parameter to GENE's equilibrium model, it serves only as a means by which to define dq/dr ($dq/dr \equiv (q/r)\hat{s}$) as a diagnostic and for setting flux tube boundary conditions and does therefore not require inherent tokamak assumptions. However, challenges may nevertheless arise in numerical computation. At the reversal surface, for instance, where $q \to 0$ and $\hat{s} \to \infty$, even though dq/dr is well-defined, the quantity $(q/r)\hat{s}$ is not. High values of $|\hat{s}|$,

through the parallel boundary condition that couples k_x modes, require high x resolution, placing a practical constraint on the ability of GENE to model cases with very large $|\hat{s}|$. A region of very high $|\hat{s}|$ (where $|\hat{s}| > 10$) around the reversal surface has therefore been excluded from these modeling studies as a matter of practicality. This region is an area of some interest in the RFP, and modeling it remains an important avenue for future work.

5.2 Linear Results

The dominant instabilities for the 200 kA and 500 kA cases are, respectively, ITG and TEM. A plot of growth rates versus minor radius is given in Fig. 5.3 for both the 200 kA and 500 kA discharges. All modes show typical ballooning parity in the eigenmode structure, marked by even parity in electrostatic potential Φ and odd parity in magnetic potential $A_{\|}$. Both discharges show that growth rates are higher at larger radii, which correspond to larger values of the normalized gradients.

For the 200 kA discharge it is found that the dominant modes for $r/a \leq 0.84$ have frequencies in the ion direction and can be categorized as ITG. The mode at $r/a = 0.89$ for the 200 kA case displays characteristics of an ITG/TEM hybrid, including complicated gradient dependencies and smooth transitions in the frequency from ion to electron direction with the variation of parameters. This shall be further elaborated on below.

The growth rates and frequencies as functions of the wavenumber $k_y\rho_s$ (where k_y is the binormal wavenumber and has the same meaning as k_θ in GYRO, $\rho_s = (T_e/m_i)^{1/2}m_i/eB_{\text{ref}}$ is the ion sound gyroradius, and m_i is the ion mass) are presented for the 200 kA case in Fig. 5.4 for different radial locations. In our convention throughout this chapter, a positive frequency indicates the ion diamagnetic direction. There is an increase in growth rates and a general widening of the spectra to high k_y as we move outward in radius, as well as a shift in the peak of the spectrum. For $r/a \leq 0.84$, the instability is identified as the ion temperature gradient mode on the basis of its frequency in the ion direction and an instability threshold in ion temperature gradient scale length (see Fig. 5.5). By way of contrast, it can be seen in Fig. 5.6 that there is no similar threshold in the electron temperature gradient. The results

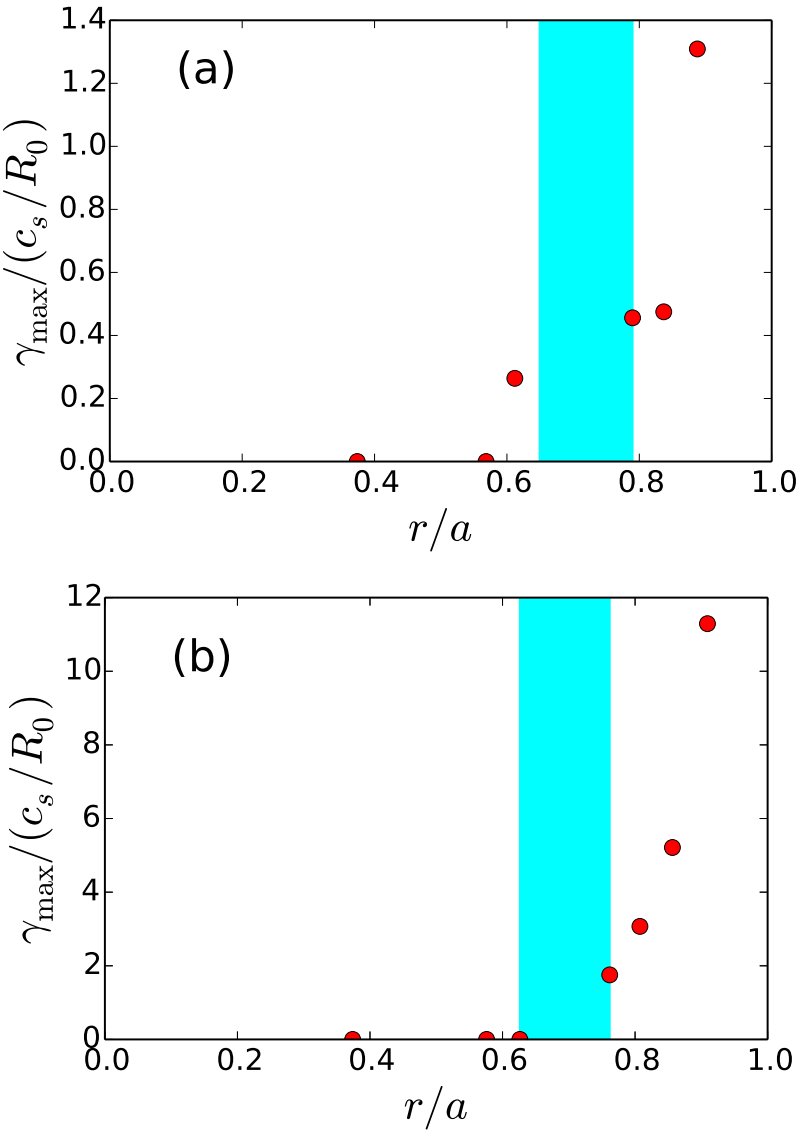

Figure 5.3: Peak growth rates versus minor radius for the 200 kA (a) and 500 kA (b) cases. The blue shaded region indicates high shear ($|\hat{s}| > 10$) and has been excluded from modeling. $\gamma_{\max}$ is the maximum growth rate attained from a k_y scan.

of density gradient scans are presented in Fig. 5.7. The gradient scans are performed at the k_y of the peak growth rate, which occurs in the range of $k_y\rho_s = 0.4 - 0.6$ for the ITG modes and $k_y\rho_s = 0.6$ for the hybrid ITG/TEM. As can be seen in Fig. 5.5, the critical gradient values for the ITG fall within the range $R_0/L_{Ti} \approx 10 - 25$, while the outermost radius shows no critical value. The instability that is present at $r/a = 0.89$ is identified as a hybrid ITG/TEM.

It has been seen in kinetic microinstability calculations that $\eta_i \equiv (d\ln T_{i0}/dr)/(d\ln n_0/dr)$ is an important parameter in determining the dominant instability. The dominant instability tends to be ITG for η_i above a critical value of $\eta_{ic} \sim 1.2 - 1.4$ and TEM for $\eta_i < \eta_{ic}$ [75]. The η ($\eta \equiv \eta_e = \eta_i$ in these runs) values as a function of radial location for the two discharges considered in this work are given in Fig. 5.8, where it can be seen that the 200 kA case lies above the region $\eta_{ic} \sim 1.2 - 1.4$ and the 500 kA case lies predominantly below. Importantly, there are some parameter regimes in which these two modes can merge and form a hybrid. The hybrid tends to be characterized by smooth transitions in the frequency from negative to positive with the variation of the gradient parameters, while marking an exceptional point in parameter space [76]. Additionally, the analogously defined quantity $\eta_e \approx 1$ represents an important transition between density-gradient-driven TEM and temperature-gradient-driven TEM, a differentiation that has important consequences for the physics of nonlinear saturation, as will be discussed in more depth in Sec. 5.3.

Moving on to the characteristics of the other MST discharge, the wavenumber spectrum is given for the 500 kA case in Fig. 5.9. The spectrum can be seen to peak around $k_y\rho_s \approx 0.6$ for each of the radial locations. Although the real frequencies for these modes are predominantly in the electron direction, at the outermost radial locations, $r/a = 0.86$ and $r/a = 0.91$, the frequency becomes positive at high k_y. This mode is often referred to as the "ubiquitous mode" and is a feature of collisionless TEM in the high k_y limit. This behavior has been described previously in numerical calculations and gyrokinetic simulations [75, 77, 78] and analyzed in depth in Coppi et al. (1990) [79].

A density gradient scan is performed at the wavenumber of the peak growth rate for each

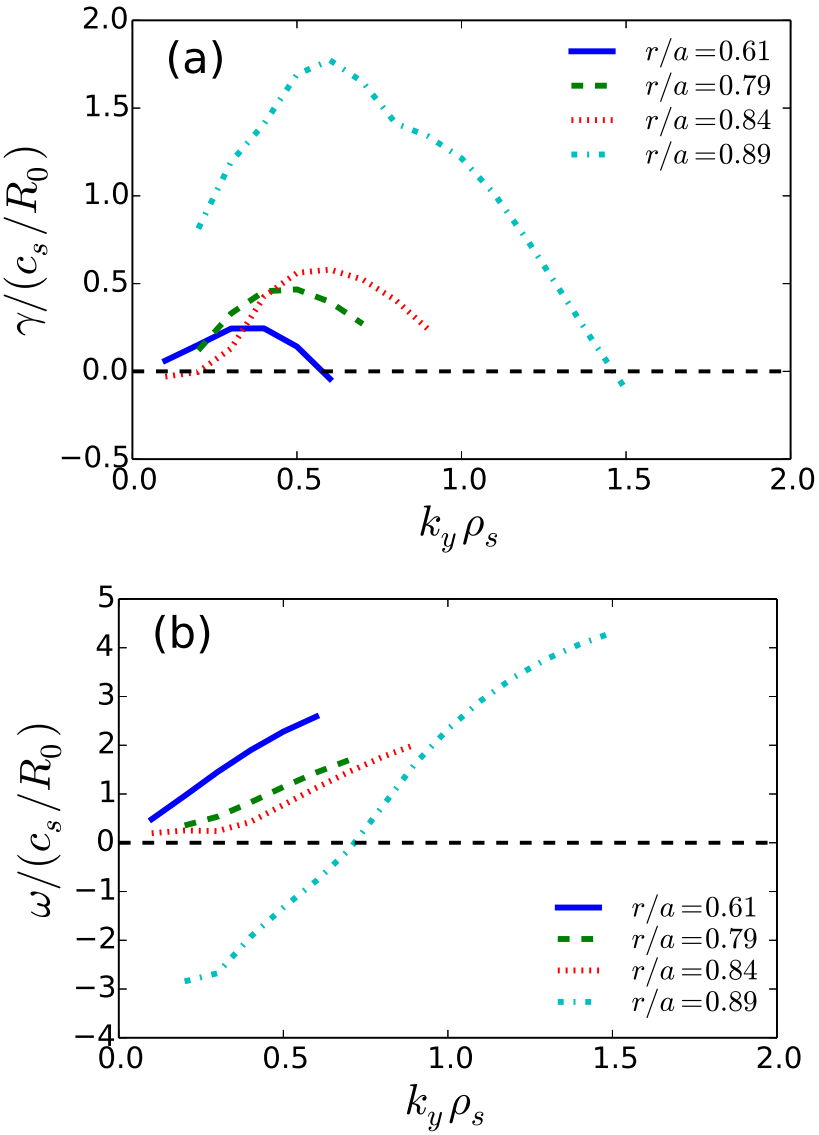

Figure 5.4: Growth rates (a) and frequencies (b) as functions of wavenumber at different radial locations for the 200 kA case. For $r/a \leq 0.84$ the modes are in the ion direction and interpreted to be ITG. The outermost radius displays a smooth transition from electron to ion direction with wavenumber and is identified as an ITG/TEM hybrid.

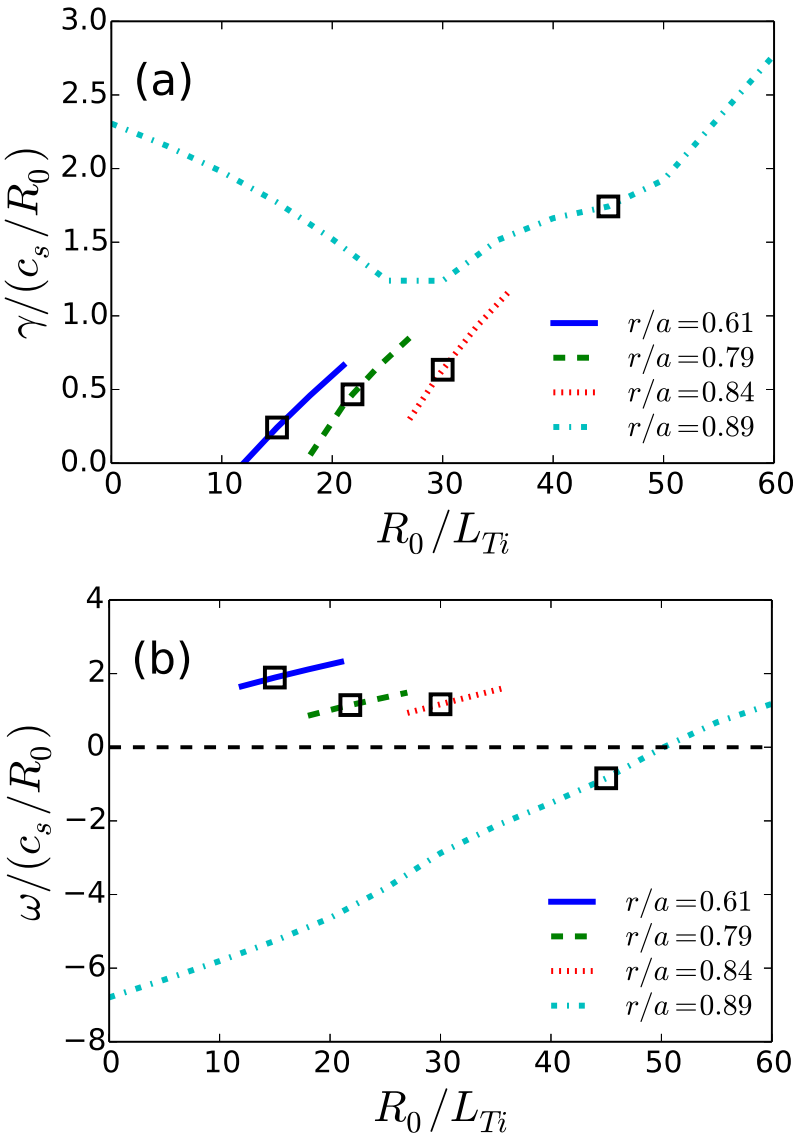

Figure 5.5: Growth rates (a) and frequencies (b) plotted against ion temperature gradient for the 200 kA case for multiple radial locations. The modes at $r/a \leq 0.84$ display a strong dependence on this gradient and are identified as ITG. The black squares denote growth rates and frequencies at the experimental gradients.

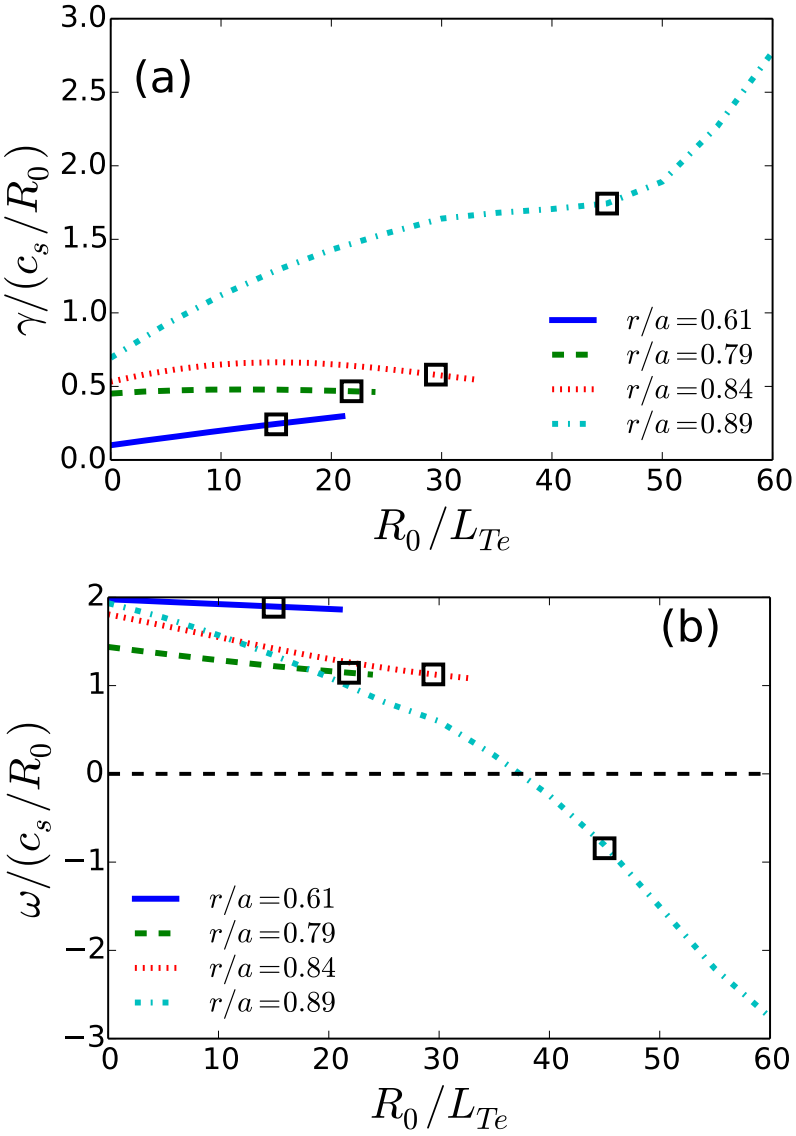

Figure 5.6: Growth rates plotted against electron temperature gradient for the 200 kA case for multiple radial locations. Except for the outermost mode, which has hybrid characteristics, there is not a strong dependence on this gradient.

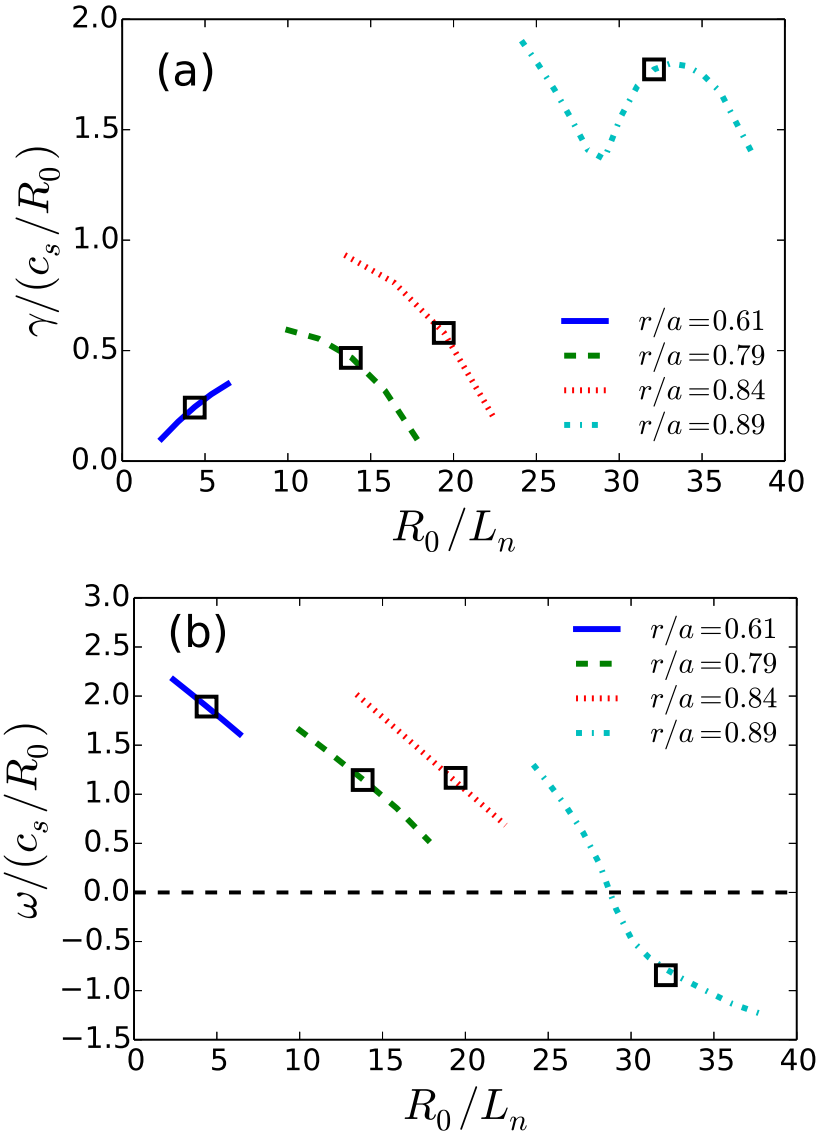

Figure 5.7: Growth rates (a) and frequencies (b) plotted against density gradient for the 200 kA case. The complicated dependence of the instability at $r/a = 0.89$ and a real frequency that transitions smoothly from ion direction to electron direction are characteristics for a hybrid mode. The black squares denote growth rates and frequencies at the experimental gradients.

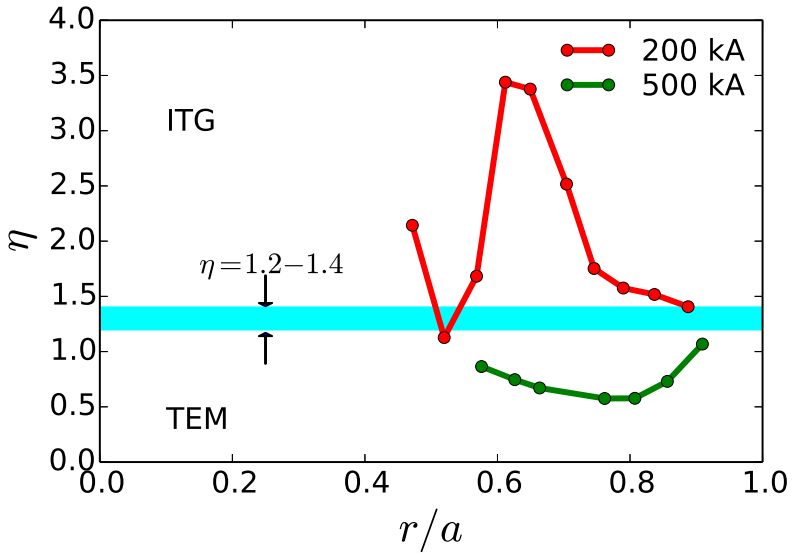

Figure 5.8: The value of $\eta \equiv (d\ln T/dr)/(d\ln n_0/dr)$ versus minor radius. $T_i \propto T_e$ in these runs, so $\eta = \eta_e = \eta_i$. The shaded region indicates the critical range $\eta_i = 1.2 - 1.4$, above which instabilities tend to be ITG and below TEM, in relatively good agreement with the observations from the present simulation data. Near the threshold, the dominant instabilities may become hybrid modes with characteristics of both ITG and TEM.

of the radial locations from Fig. 5.9. The results are presented in Fig. 5.10, where it can be seen that there is a strong dependence of the growth rate on density gradient with a critical gradient occuring around $R_0/L_n \sim 15$ for each radial location. For this reason, and a real frequency in the electron direction, these modes are identified as density-gradient-driven TEM. These modes show some dependence on ion and electron temperature gradients, but no critical values, as can be seen for the electron temperature gradient in Fig. 5.12 and for the ion temperature gradient in Fig. 5.13. It should be noted that for this discharge, the values of collisionality obey the relationships $\nu^* \equiv \nu_c/\omega_b \ll 1$ and $\nu_c/\omega \ll 1$, with ω the real frequency of the instability and the bounce frequency $\omega_b \equiv \epsilon^{1/2} v_{te}/qR_0$ defined in terms of the aspect ratio $\epsilon = r/R_0$ and the electron thermal velocity $v_{te} = (T_{e0}/m_e)^{1/2}$. This is well in the collisionless regime. For the radial location $r/a = 0.86$ there is an ion mode that is dominant at low values of the density gradient and is likely ITG.

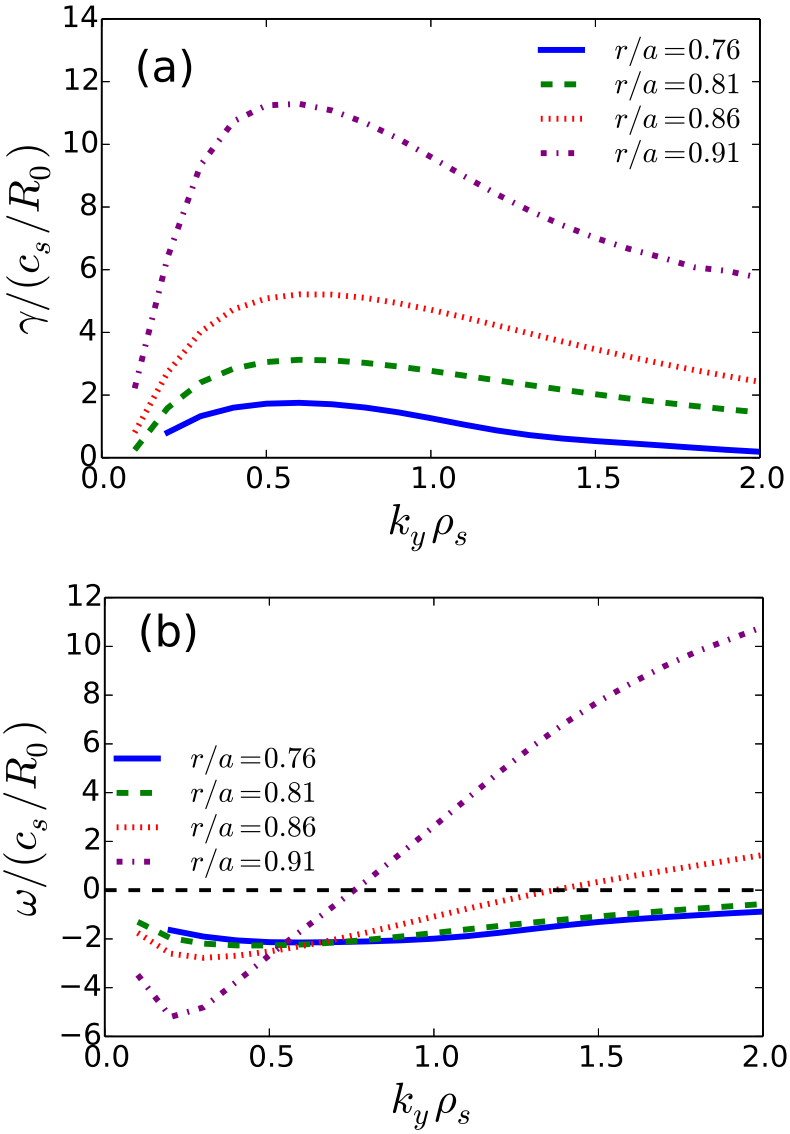

Figure 5.9: Growth rates (a) and frequencies (b) as functions of wavenumber at different radial locations for the 500 kA case. These modes are driven by the density gradient and are identified as TEM; only at the outer radii and higher k_y can signatures of ubiquitous modes be seen.

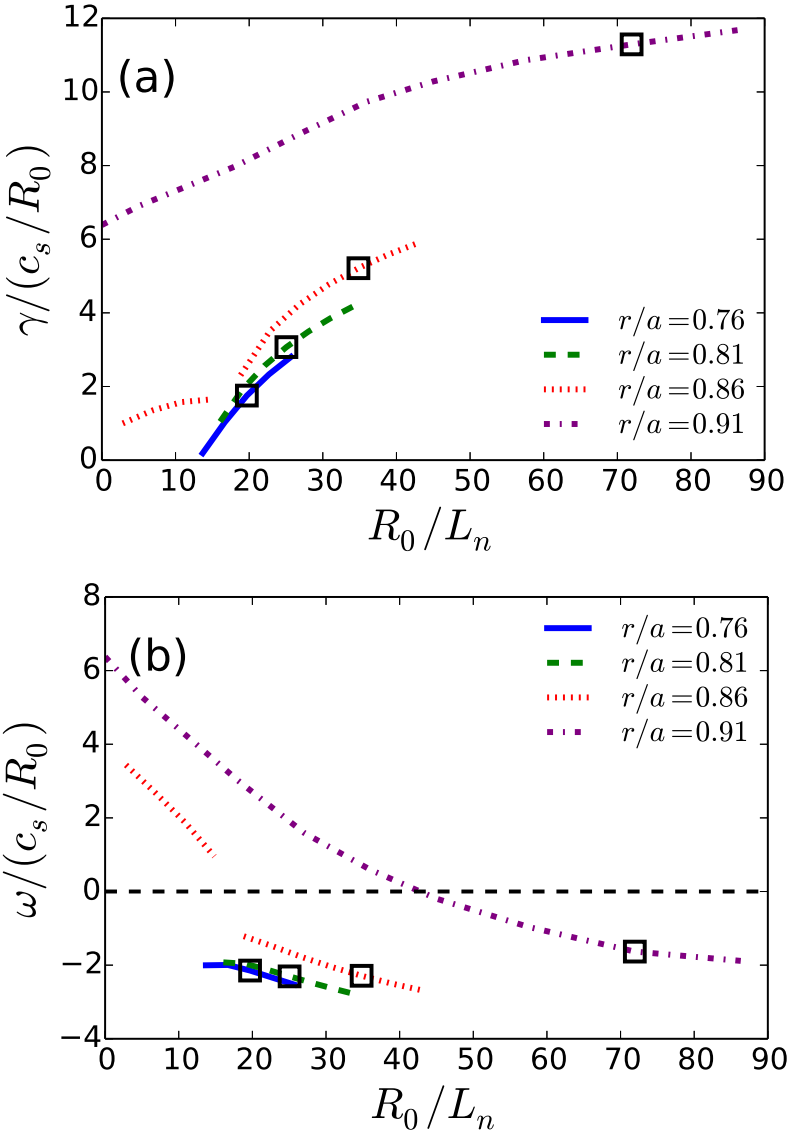

Figure 5.10: Growth rates (a) and frequencies (b) plotted against density gradient for the 500 kA case. The dominant modes for the nominal parameters show a strong dependence on density gradient and are identified as density-gradient-driven TEM. The black squares denote growth rates and frequencies at the experimental gradients.

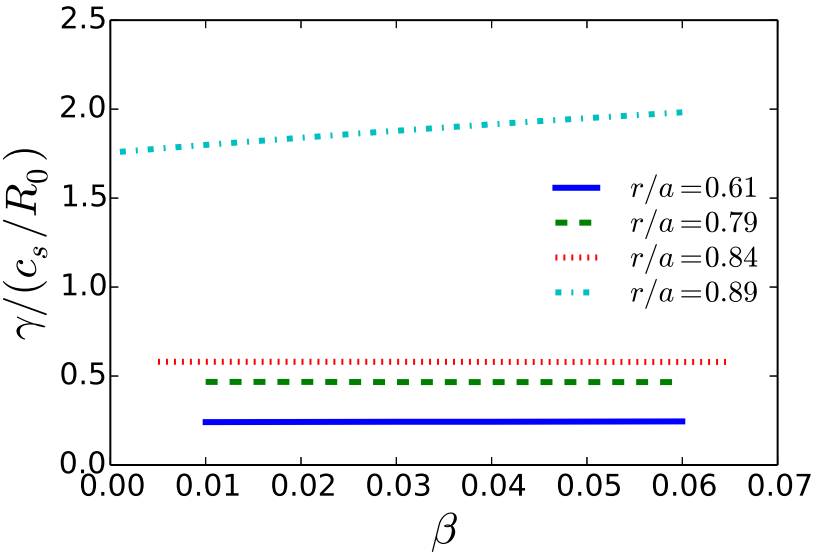

Figure 5.11: Growth rates plotted against β for the 200 kA case. All modes show little variation with β, a characteristic that is related to a high β threshold for electromagnetic instabilities. The frequencies are similarly unaffected by variations of β.

β dependence

These modes all demonstrate an independence with respect to plasma β, a behavior that can be seen for the 200 kA case in Fig. 5.11. Although weak β dependence is a characteristic expected of TEM, ITG is known to be stabilized by increasing β, both linearly [55, 66, 80] (a feature also explored in the previous chapter) and nonlinearly [65, 81]. An important conclusion to draw from these results is that, despite operating at a β that is considered high in the context of tokamaks, the instabilities present in PPCD plasmas are predominantly electrostatic. Notably absent are KBMs and MTMs. All RFP modeling work has thus far shown no evidence of KBMs, a mode known to arise in finite-β simulations in the tokamak at a typical β of $0.6\% - 2\%$ [8, 82, 80]. The absence of KBMs in the RFP may be explained as a consequence of two geometric properties: high magnetic shear and low safety factor. In the tokamak, KBMs are seen to emerge at some considerable fraction (generally about $70\% - 100\%$) of the ideal ballooning mode critical β [83, 80, 65]. In the RFP, however, the critical β for the ideal ballooning mode increases in regions of high shear [84]. If KBMs are tied to this threshold in a similar way, then it can be expected

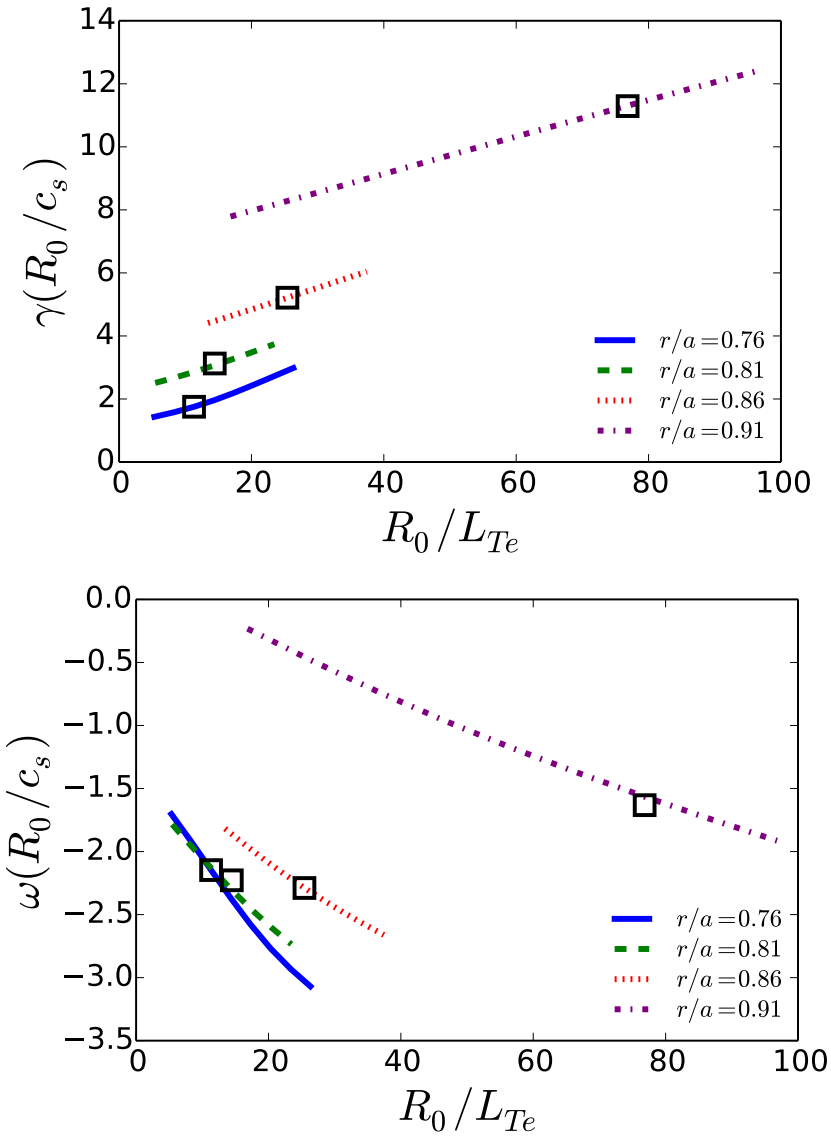

Figure 5.12: Growth rates plotted against electron temperature gradient for the 500 kA case. There is no critical gradient.

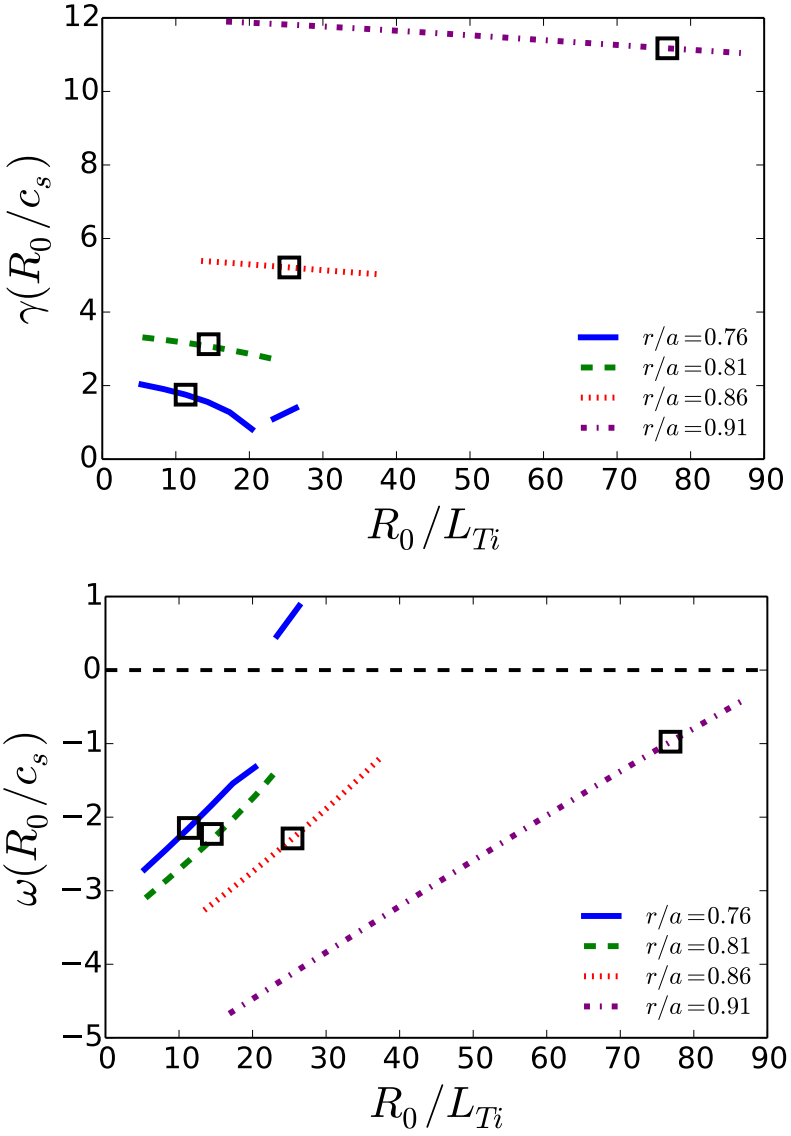

Figure 5.13: Growth rates plotted against ion temperature gradient for the 500 kA case. There is some stabilization of the TEM growth rate with increasing ion temperature gradient, with a likely ITG mode eventually arising for $r/a = 0.76$.

that the KBM threshold will increase as well. Using the plasma ballooning parameter $\alpha_{\rm MHD} = \beta q^2 \left(R_0/L_n + R_0/L_{Te} + (R_0/L_n + R_0/L_{Ti})T_i/T_e\right)$ and a naive use of the tokamak threshold for the critical MHD ballooning limit $\alpha_{\rm MHD}^{\rm crit} = 0.6\hat{s}$ [85], we may make an estimate of the critical MHD ballooning β. This yields a value of $\beta_{\rm crit}^{\rm MHD} \approx 750\%$ for the 200 kA $r/a = 0.84$ case and generally above 50% for all cases studied here. The use of $\hat{s}_{\rm RFP}$ in place of $\hat{s}$ in the α-threshold expression reduces these limits, generally by a factor of $2-3$. Even so, these estimates suggest that the experiment operates well below the range of β where effects tied to the KBM threshold are likely to play a significant role. In a related matter, the same geometric effects that cause the KBM threshold to be pushed up may also be responsible for a higher threshold for shear Alfvén waves, and therefore a lack of ITG stabilization with β. This explains why, in the parameter regime of these discharges, the instabilities remain electrostatic for experimentally relevant β.

Previous work in the RFP (as outlined in the previous chapter) has also shown signs of MTMs [70, 55], which are not present in these PPCD simulations. This may also be explained as a result of high magnetic shear. It has been demonstrated that, in the RFP, the MTM is stabilized by high values of magnetic shear [70] and by high values of the RFP pinch parameter Θ, which also corresponds to high values of shear [55]. In the present PPCD discharges the areas most likely to be unstable to MTM (regions of high β and high electron temperature gradient) are also regions of high magnetic shear. Under these circumstances, the stabilizing effects of the shear are strong enough to overcome the MTM instability drive.

5.3 Nonlinear Results

We report results from the first nonlinear gyrokinetic simulations in PPCD plasmas. These results come from the 500 kA case at $r/a = 0.86$ and $r/a = 0.91$. The relevant physical parameters for these runs can be found in Tab. 5.1.

First, we will make some comments on the resolution requirements. Nonlinear gyrokinetics in the RFP is very resource-intensive, requiring radial resolutions in excess of similar

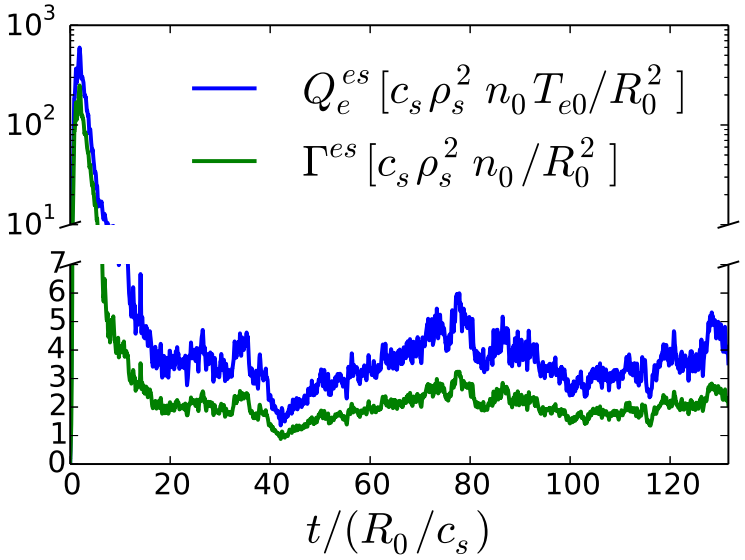

Figure 5.14: A time trace of the nonlinear fluxes for a density gradient of $R_0/L_n = 58.8$. The dominant channels are electron heat flux Q_e^{es} (blue) and particle flux Γ^{es} (green). There is a large overshoot in the beginning due to strong linear growth rates, but this is countered by strong nonlinear saturation mechanisms.

tokamak cases. This is largely due to the high magnetic shear of the RFP, which, because of the parallel boundary condition (requiring for some quantity F, $F(k_x, k_y, z + L_z) = F(k_x', k_y, z)\exp[2\pi i k_y \hat{s} r_0]$, with $k_x' = k_x + 2\pi\hat{s}k_y$ and L_z the parallel box size [14]), sets restrictions on the radial box size and grid spacing. High radial resolution, in turn, results in increased computational expense and more processor-hours required for saturation. For the $r/a = 0.86$ case, the following set of resolutions was used: 24 k_y modes, 24 parallel grid points, 32 parallel velocity grid points, 12 magnetic moment grid points, and 284 radial grid points. A time trace of the saturated transport levels for a sample run is given in Fig. 5.14. Completing a nonlinear run such as this takes roughly 100,000 processor hours on a Cray XT5 computer. The $r/a = 0.91$ case, where $|\hat{s}|$ is smaller, requires less radial resolution and can be performed with fewer hours.

As discussed in the previous section, the dominant linear instability for these sets of parameters is a density-gradient-driven TEM. The nonlinear evolution shows a phase of strong linear growth, at which point nonlinear processes arise and act to saturate the

turbulence and suppress transport fluxes — note that the so-called overshoot is larger than in typical tokamak simulations. This nonlinear saturation is due to the emergence of zonal flows, $k_y = k_\parallel = 0$ fluctuations that provide an energy damping mechanism and place limits on radial transport [86, 87]. Zonal flows are known to be an important element of nonlinear saturation and the formation of transport barriers [88].

The transport spectra are given in Fig. 5.15 for both cases. In comparison, electrostatic particle transport and electrostatic electron heat transport (other transport channels being negligible) peak at around $k_y\rho_s = 0.2$, with minimal transport at the highest k_y. This is significantly below the peak of the linear growth rate spectrum at $k_y\rho_s = 0.6$.

A nonlinear gradient scan was performed for the $r/a = 0.86$ case, the results of which can be seen in Fig. 5.16. This figure shows a scan of the density gradient, along with the respective linear growth rates for comparison. Electron heat transport outweighs ion heat transport, and despite operating at β values (given in Tab. 5.1) that would be considered large in the context of the tokamak (as was discussed in Sec. 5.2), the transport is almost entirely electrostatic. Furthermore, there can be seen a strong shift in the critical gradient as compared with the linear case, with the nonlinear threshold occuring around $R_0/L_n = 35$ as compared to the linear threshold of $R_0/L_n \approx 10 - 15$. This nonlinear upshift in the critical gradient has been discussed before in the context of TEM turbulence in the tokamak [77], but has yet to be addressed in the RFP where a different magnetic geometry may lead to different characteristics. In particular, the magnitude of the shift seen in Fig. 5.16, where the nonlinear threshold is roughly 3 times the linear one, is larger than that seen in the tokamak, where there tends to be an increase of the critical gradient by $10\% - 30\%$ [89, 65]. This suggests that zonal flows may have a much larger impact in the RFP as compared to the tokamak.

As with the tokamak case, the shift here is attributed to the presence of strong zonal flows, which are known to moderate linear instabilities and reduce transport levels. Numerical studies of a variety of both gyrokinetic and fluid models have found zonal flows to play a key role in the transfer of energy to damped modes, an important process for nonlinear

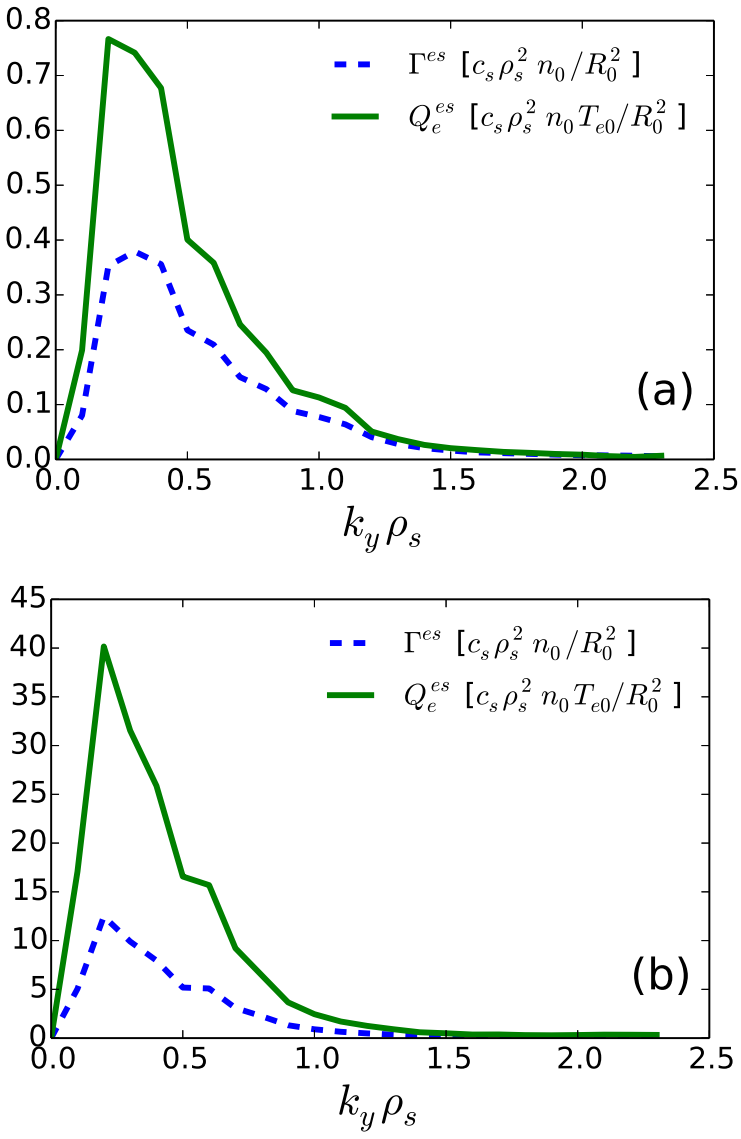

Figure 5.15: The flux spectra for (a) $r/a = 0.86$ and $R_0/L_n = 52.3$ and (b) $r/a = 0.91$ and $R_0/L_n = 71.9$. Shown are the electrostatic particle flux Γ^{es} (blue dashed line) and the electrostatic electron heat flux Q_e^{es} (green solid line). At $r/a = 0.86$, the spectra peak at $k_y\rho_s = 0.3$, while at $r/a = 0.91$ the peak shifts to $k_y\rho_s = 0.2$. In comparison, the linear growth rates peak at $k_y\rho_s = 0.6$ for both cases.

saturation [90, 91, 92]. Clear evidence for zonal flows can be seen in the contours of the electrostatic potential Φ, which is given in Fig. 5.17 along with the contours for the perturbed electron density n_e: A strong contribution from the $k_y = 0$ mode is apparent in the Φ contours. Similarly, $k_y = 0$ features in the density contours indicate a zonal density structure. The normalized density amplitudes are weaker than the Φ amplitudes by roughly a factor of four, indicating the dominance of zonal flows over zonal density, although in some regimes (though not any of those observed in the context of the present study), particularly those where temperature gradients are much stronger than density gradients, the role played by zonal flows in saturation is known to be much diminished, and zonal density emerges as the expected dominant saturation mechanism [93].

An important measure of the zonal flow activity is the $\mathbf{E} \times \mathbf{B}$ shearing rate $\omega_E = d^2\Phi_{\rm zon}/dx^2$, where $\Phi_{\rm zon}$ is the zonal component of the electrostatic potential. The shearing rate is a well known causative effect for transport reduction. However, it is also a proxy for the efficiency of zonal-flow-catalyzed energy transfer to damped modes. Zonal flows are generally considered to be important for nonlinear saturation when the shearing rate is at least as large as the the maximum linear growth rate when taking into account finite frequency corrections [94, 86, 95]. Although these corrections are not included in this analysis, ω_E is consistently an order of magnitude larger than the peak linear growth rate, a commonly used criterion to determine zonal flow impact without utilizing the aforementioned finite-frequency corrections [80, 78]. Fig. 5.18 (a) shows nonlinear density gradient scans at several different values of $\hat{s}$, with the fluxes increasing as $\hat{s}$ is reduced. In Fig. 5.18 (b) we plot the ratio $\omega_E/\gamma_{\rm lin}$ of the zonal flow shearing rate and the peak linear growth rate for these same cases. As shear is reduced, this factor decreases, a result of both an increase in linear growth rate and a decrease in ω_E. At $\hat{s} = 2.5$, the shearing rate falls below $10\gamma_{\rm lin}$, a transition that is associated with higher fluxes (as can be seen in Fig. 5.18).

A nonlinear upshift in the critical density gradient for TEM turbulence has been seen before in gyrokinetic simulations in the context of the tokamak [77] and is seen as a similar process to the Dimits shift observed in the case of ITG turbulence [89]. As in the Dimits

shift, zonal flows play an important role in the suppression of transport fluxes, and it has been found that both magnetic shear and the electron temperature gradient can affect the characteristics of zonal flows in TEM turbulence [96]. In particular, the role of zonal flows in saturating TEM turbulence has been found to depend on η_e, with zonal flows important for $\eta_e < 1$ and relatively unimportant above this critical value, where the TEM is driven by the electron temperature gradient rather than the density gradient [78]. It has been suggested that zonal density generation is responsible for nonlinear saturation in the absence of zonal flows [93]. The η_e radial profile for the 500 kA is given in Fig. 5.8. The value of η_e only becomes greater than 1 above $r/a \simeq 0.9$, suggesting that zonal density may play a greater role towards the edge in MST. Indeed, as can be seen in Fig. 5.17, the relative strength of the zonal density structure as compared to zonal flow is larger at $r/a = 0.91$ (factor of $\approx 1/3$) than at $r/a = 0.86$ (factor of $\approx 1/4$).

Another important result of these simulations is that the nonlinear threshold occurs at roughly the nominal experimental value, indicated by the vertical dashed line in Fig. 5.16. This suggests that the experiment may be operating near a critical threshold and microinstability driven turbulence may be playing an important role driving transport. Although the experiment appears to be operating near marginal stability, the transport seen in the simulations falls significantly below that observed in experiments on MST. At a gradient of $R_0/L_n = 52.3$, which is 50% larger than the nominal experimental density gradient, the value of the electron electrostatic heat diffusivity is found to be $\chi_e^{es} = 1.5\,\mathrm{m^2 s^{-1}}$, lower than the experimental value of $\sim 30\,\mathrm{m^2 s^{-1}}$ [33], though there are large uncertainties in the experimental estimate. Further out, at $r/a = 0.91$ the electron heat diffusivity at experimental gradients is $\chi_e^{es} = 2.9\,\mathrm{m^2 s^{-1}}$, still well below experimental estimates. As shall be demonstrated below, this gap can be bridged, however, by taking into account residual magnetic fluctuations from tearing mode activity and their deleterious impact on zonal flows.

Magnetic perturbations and transport

Thus far we have not accounted for the role played by magnetic stochasticity, an important contributor to transport processes in the RFP, even in the relatively well-behaved PPCD discharges. The effect of stochastic fields in gyrokinetic simulations has been a topic of recent interest [97, 98, 73, 99], revealing that self-consistent magnetic stochasticity may be ubiquitous in tokamak gyrokinetic simulations, arising at low values of β due to the nonlinear excitation of linearly damped microtearing modes. In the present work, at $\beta = 0.7\%$, there is virtually no stochasticity inherent in the nonlinear simulations (see Fig. 5.20 (a)), an outcome related to the increased MHD β limit discussed above. Clearly, the flux surfaces are almost completely intact, and the radial motion of particles streaming along perturbed field lines is essentially negligible. As a consequence, a variety of models concerning the physics of magnetic perturbations are no longer applicable here (at least as long as only self-consistent perturbations are considered, see below), as they require a fully stochastic nonlinear state of the perturbed flux surfaces—compare the (quasi-)linear and nonlinear electron flutter transport reported in Ref. [80]. The degree to which these simulations are in a magnetically nonlinear state can be assessed through the evaluation of the contribution to the overall electromagnetic heat conductivity from the Rechester-Rosenbluth term [48] $\chi_e^{em} = \chi_{e\|}\langle(\tilde{B}_x/B_{\rm ref})\rangle$, where $\chi_{e\|} \approx k_\|^{-1}(T_e/m_e)^{1/2}$. The transport predicted by this formula is far larger than that observed in the simulations, therefore it is reasonable to conclude that this term is not contributing to transport and quasilinear approximations may be used. Similarly, the predictions in Refs. [100, 101] for B_x and related quantities do not hold here. However, this neglects the effect of residual tearing mode fluctuations. In standard discharges of the RFP, large-scale tearing modes, driven by the gradient in the current profile, produce stochastic magnetic fields [102, 103]. Though this is largely controlled with PPCD, some stochasticity still remains [33, 104], and even at the radii considered here (where no fully stochastic field is measured), significant radial excursion of perturbed field lines occurs.

To address the issue of how this may affect microturbulent transport, we have imposed

an artificial Gaussian perturbation on $A_\parallel$ in the z direction with $k_x = 0$ and $k_y = 0.2$, corresponding to a resonant B_x perturbation. The strength of this perturbation can be tuned to introduce a small radial displacement of the magnetic field, in this case leading to a magnetic diffusivity [48, 97] of $D_m = \langle(\Delta r)^2\rangle/2\Delta l \sim 10^{-8}\,\mathrm{m}$, defined in terms of the radial excursion Δr and the field line length l. Without the imposed perturbation this value is $D_m \sim 10^{-10}\,\mathrm{m}$. Fig. 5.20 (b) shows the Poincaré plot associated with such a perturbation. The level of diffusivity introduced here is not enough to lead to true stochastization, but instead serves only to slightly degrade the flux surfaces. Although the experimental value of D_m is not known precisely, the value used here was chosen based on best estimates (see Ref. [104] and Fig. 5.19.)

There are several outcomes of introducing this resonant perturbation. One is the generation of a small amount of electromagnetic heat flux ($\chi_e^{em} = 3.2\,\mathrm{m^2 s^{-1}}$, as compared to $\chi_e^{em} \approx 0$ without the imposed perturbation.) Another, more important effect is an increase in the electrostatic heat flux, which increases by more than a factor of ten to $\chi_e^{es} = 25.2\,\mathrm{m^2 s^{-1}}$. This result can be seen in Fig. 5.21, which shows a time trace comparing the particle and heat fluxes before and after the addition of the perturbation. This increase in transport is due to the weakening of the zonal flows responsible for saturation, an effect known from studies of the nonzonal transition in tokamaks [105, 106, 107, 101]. Fig. 5.22 shows contours of Φ and n for the case with imposed diffusivity, and it can be seen that the $k_y = 0$ structures are very much diminished, both in their absolute amplitudes – despite the increased χ_e – and in relation to the structure with $k_y \neq 0$. The degradation of the zonal flow is caused by the magnetic flutter induced loss of electrons from their radial surface, which creates a radial current that diminishes the zonal potential [105]. The large effect of radial magnetic field perturbations in the present work is likely due to both the strength of the zonal flows as well as the effectiveness of stochasticity in their damping. In particular, the zonal flow decay time as reported in Refs. [105, 106] is linear in q, suggesting that for a large radial region in MST (where q is much lower than in a tokamak), this process is very effective. This analysis suggests that the experimental fluxes may be accounted for by drift

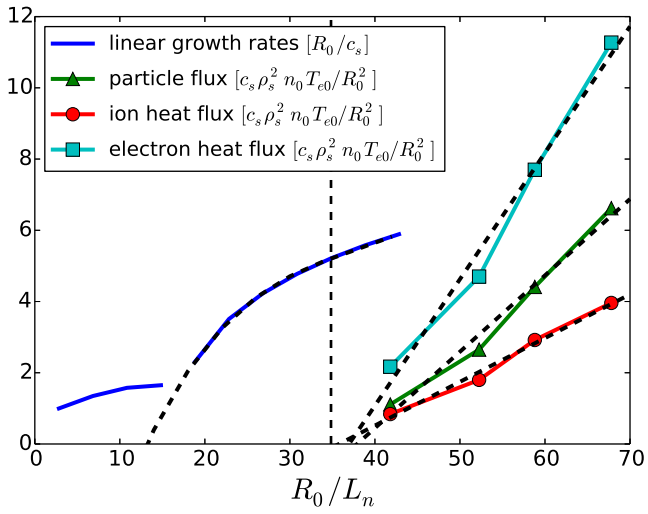

Figure 5.16: Electron heat and particle fluxes are plotted as a function of density gradient for the 500 kA case at $r/a = 0.86$. The linear growth rates for these parameters are also shown for comparison. Straight line fits have been applied to the fluxes, and a cubic fit has been applied to the TEM portion of the linear growth rate curve. The onset for the nonlinear fluxes occurs at $R_0/L_n \approx 37$, roughly a factor of 3 greater than the linear threshold of $R_0/L_n \approx 13$. The vertical dashed line indicates the nominal experimental value of R_0/L_n.

wave turbulence in the presence of a small amount of magnetic diffusivity. However, the value of D_m chosen above serves only as a rough estimate, as the experimental quantity is largely unknown for these discharges [104]. Since there is such sensitivity of these results to the level of magnetic diffusivity, it is highly important to determine this value experimentally as precisely as possible. This presents an area of interest for future work in both experiment and numerical simulation.

5.4 Chapter Summary

We have performed a series of linear and nonlinear gyrokinetic simulations in PPCD discharges of MST plasmas and characterized the gyroscale processes. A 200 kA discharge has been found to be linearly unstable to ITG and a hybrid ITG/TEM, while the higher-current 500 kA discharge has been found to be unstable to a density-gradient-driven TEM. The pa-

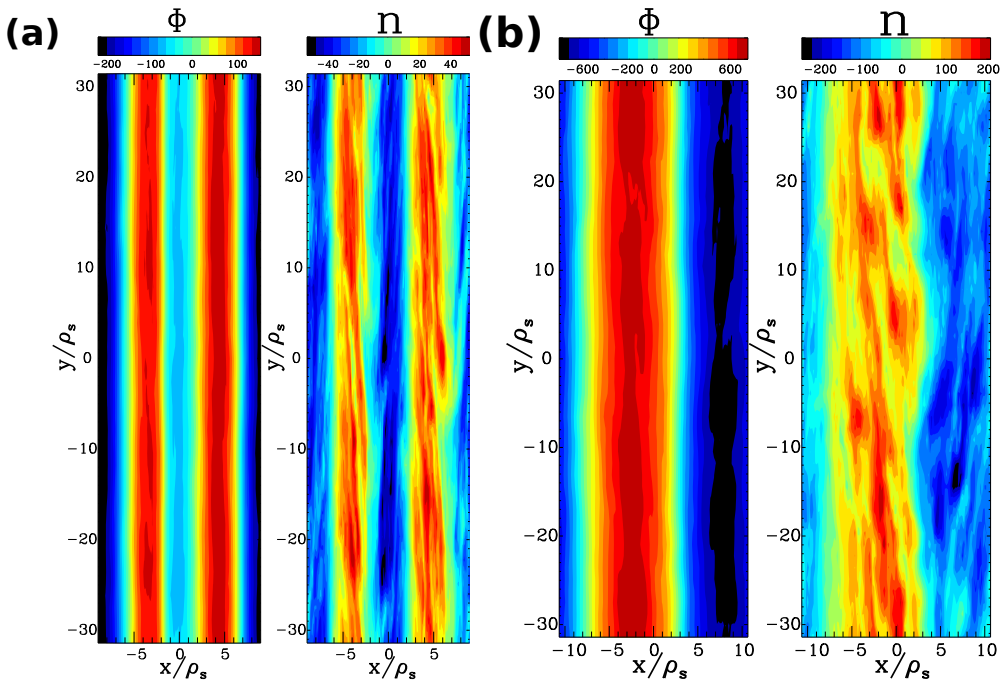

Figure 5.17: Contours of electrostatic potential Φ and electron density n for the 500 kA case at (a) $r/a = 0.86$ and $R_0/L_n = 52.3$ and (b) $r/a = 0.91$ and $R_0/L_n = 71.9$. Strong vertical features ($k_y = 0$) in Φ are indicative of zonal flow activity, while the density contours show some (but relatively weaker) zonal structures as well.

rameter η_i is found to be an important determining factor in the dominant instability type, with TEM prevalent for $\eta_i \lesssim 1.3$ and ITG prevalent for $\eta_i \gtrsim 1.3$. Furthermore, magnetic shear is also an important parameter, and high values of shear – in conjunction with low values of q – contribute to the absence of electromagnetic effects and modes.

Nonlinear simulations performed for the 500 kA discharge showed strong zonal flows and a significant Dimits-like shift, with the nonlinear threshold density gradient approximately three times the value of the linear critical gradient. Although the experiment seems to be operating near marginal stability, the simulations yield transport levels well below that of experimental measurements on MST. To investigate the effect of residual tearing mode fluctuations, a small radial magnetic field perturbation was imposed, which served to greatly reduce the zonal flow strength and bring transport fluxes up to levels more in line with experiment. In general, this work reveals that microinstability-driven transport may be sufficient to explain experimental transport levels, but work remains to be done to

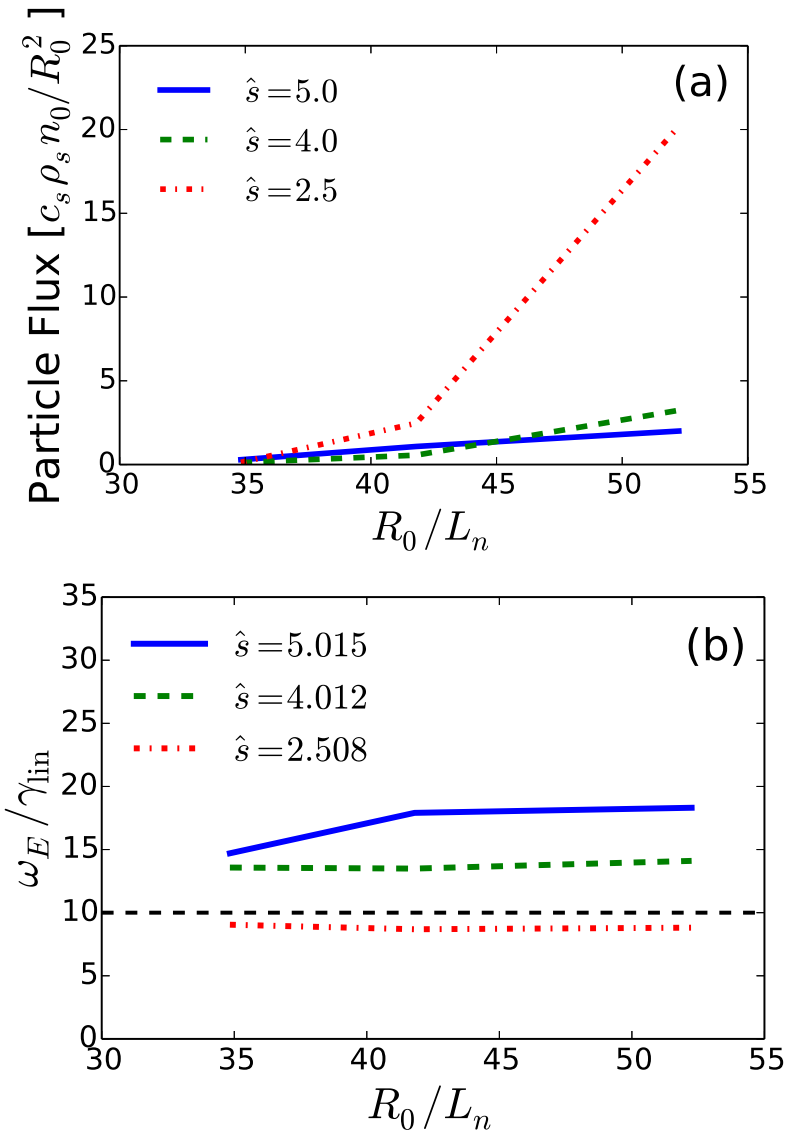

Figure 5.18: (a) Particle flux versus density gradient for three different values of magnetic shear, $\hat{s} = (r/q)(dq/dr)$. (b) Zonal flow shearing rate divided by linear growth rate versus density gradients for different values of magnetic shear. For $\hat{s} = 2.5$ the zonal flow shearing rate drops below $10\gamma_{\rm lin}$ (indicated by the black dashed line in the lower plot) and the flux substantially increases. Other parameters are as given for the 500 kA case at $r/a = 0.86$.

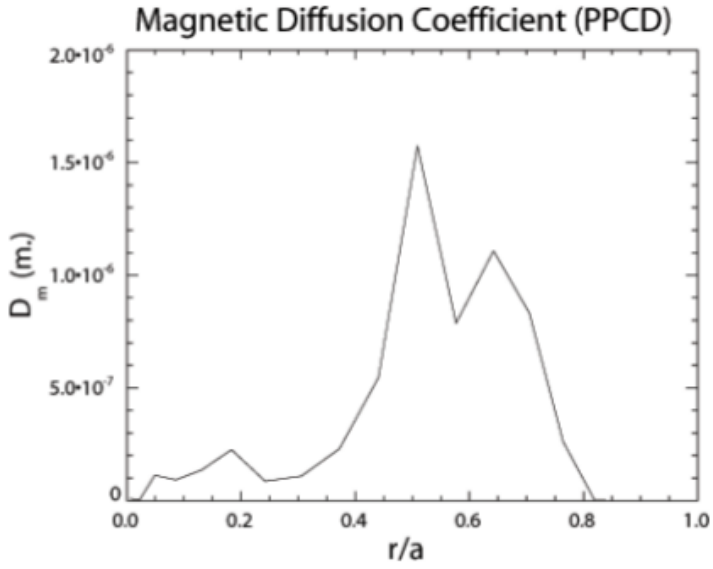

Figure 5.19: A profile of the magnetic diffusivity as calculated by the MAL code. The calculation is only intended to be valid from $r/a = 0.5 - 0.7$, but it serves as an upper limit and a useful order of magnitude of this quantity at the radius simulated in this work. Since the nonlinear fluxes are sensitive to the strength of the imposed field, it is important to determine the experimental magnetic diffusivity as accurately as possible. For the original figure and more on the MAL code and the calculation of D_m, see B. Hudson, Ph.D. Thesis (2006).

better determine important experimental quantities such as gradients and magnetic diffusivity/residual tearing mode stochasticity. This presents important topics for future work and an area for fruitful collaboration between theory and experiment.

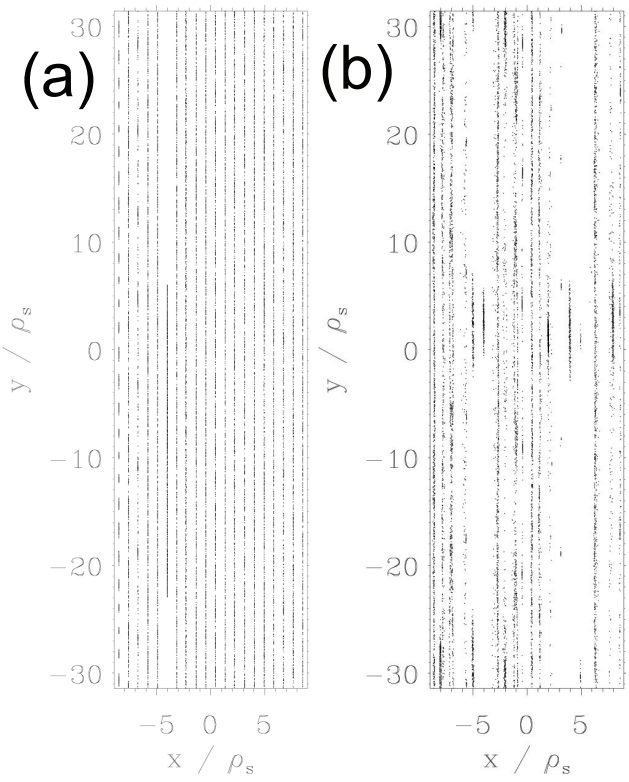

Figure 5.20: Poincaré puncture plots without (a) and with (b) a small added resonant perturbation to $A_\parallel$. Though the flux surfaces are still largely intact, the imposition of a small resonant radial magnetic field leads to the reduction of zonal flows and a large increase in transport. More details on the field line integration routine may be found in Pueschel et al. (2013).

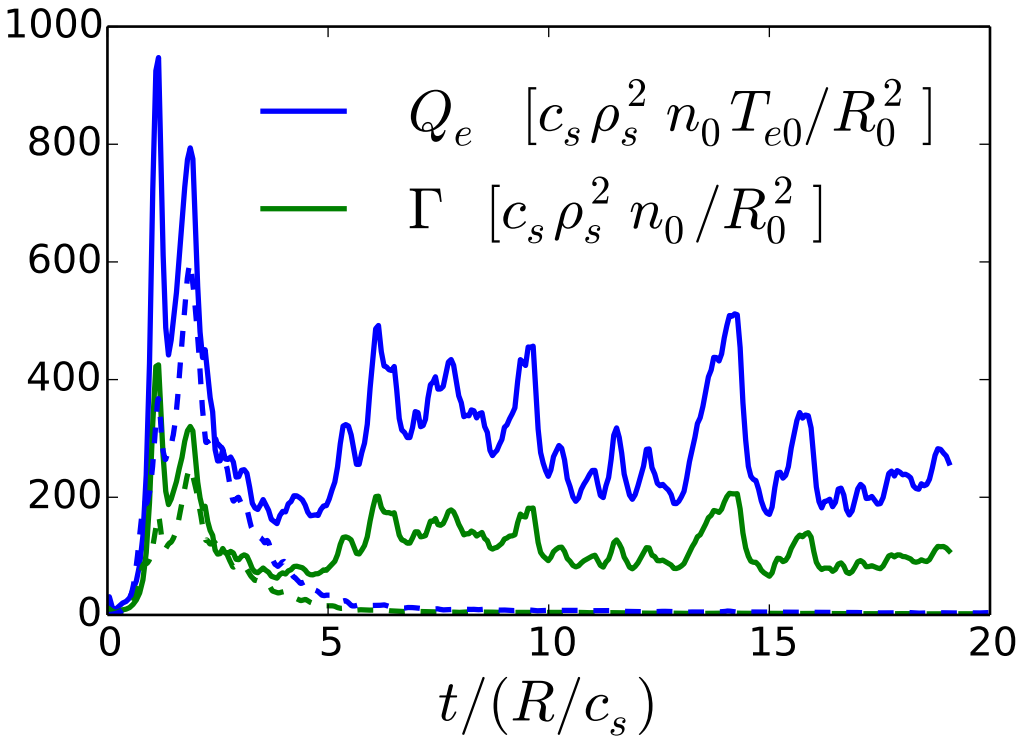

Figure 5.21: Electron heat (blue) and particle flux (green) before and after the inclusion of an imposed perturbation on $A_{\|}$. The imposed magnetic diffusivity weakens zonal structures and results in a large increase in the transport levels. Shown are the fluxes after instituting the artificial perturbation (solid lines) as compared with those same quantities before (dashed lines).

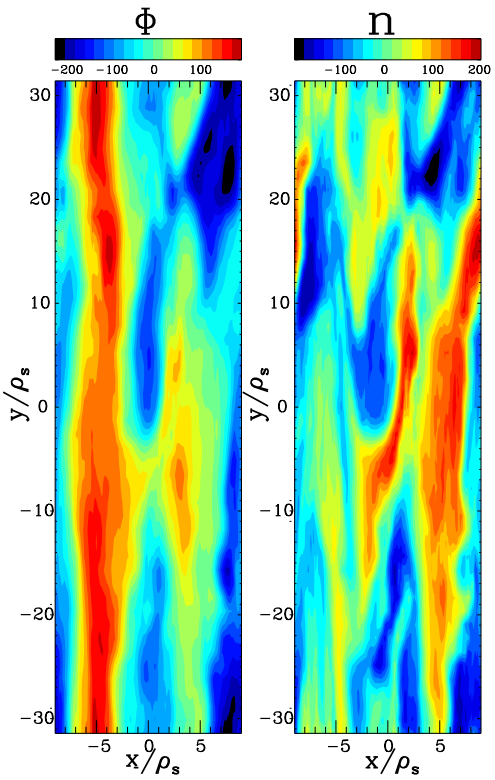

Figure 5.22: Contours of Φ and n for the $r/a = 0.86$ case where a resonant $A_{\|}$ perturbation has been implemented to introduce a small radial perturbation to the magnetic field. The effect is to greatly diminish the zonal structures evident in Fig. 14 (a).

Chapter 6

The collisionless microtearing mode

During the course of the last few years the microtearing mode (MTM) has gained prominence as an important topic of study in magnetic confinement devices [68, 62, 61, 69, 108, 53, 55, 70]. The MTM is a small-scale drift wave driven by the electron temperature gradient [109] and requiring finite β. The temperature gradient drive, separate from the current gradient drive of the global tearing mode, enables the MTM to exist at higher mode numbers than the global mode, with $k \sim \rho_s^{-1}$. As a gyroscale instability, it is expected to make contributions to electron heat and particle transport.

Gyrokinetic simulations across a number of different magnetic geometries have shown signs of the MTM, from tokamaks [62, 61, 110] to spherical tokamaks [68, 69, 108] and reversed field pinches (RFP) [53, 55, 70]. The features of the MTM seen in these simulations largely match those predicted by early analytic theories, i.e., a critical value in the plasma pressure β and in the electron temperature gradient R_0/L_{Te}.

However, one important way in which recent numerical results have differed from early predictions is in the role of collisions in the instability mechanism. Early analytic work was performed across a number of collisionality regimes [58, 57, 56, 71] and found collisions to play an important role in the instability drive. It was therefore concluded that an energy

dependent collision operator is necessary for instability [59]. Contrary to these findings, a number of gyrokinetic studies have shown the MTM to remain unstable even in the collisionless or low collisional frequency regime [68, 70, 61, 55, 63], suggesting the existence of a drive mechanism that is not accounted for in the early literature. The current chapter addresses extensions to previous theories and the role played by magnetic drifts in the collisionless MTM instability drive.

6.1 Microtearing Mechanisms

The microtearing mode arises, much as the global tearing mode [111, 64], from a discontinuity in the magnetic vector potential. This is associated with the existence of a tearing layer in the current profile. The relationship between the plasma current and the magnetic vector potential is expressed in Ampère's law:

$$\Delta' = \frac{1}{A_\parallel}\left(\frac{\partial A_\parallel}{\partial x}\right)\Bigg|_{-\infty}^{\infty} = \frac{1}{A_\parallel}\frac{-4\pi}{c}\int_{-\infty}^{\infty} dx J_\parallel \quad , \tag{6.1}$$

where Δ' is the standard tearing parameter [111]. It has also been assumed that $k_y \ll k_x$ and $J_i \ll J_e$.

For high m number (high k_y) modes, $\Delta' \approx -2k_y$. The growth rate of the collisionless drift-tearing mode is $\gamma = k_y v_{Te}(\Delta' a)/2k_0^2 a l_s \pi^{1/2}$ [58], so a negative Δ' parameter at high k_y results in a stable mode. In this regime an additional mechanism is needed for instability.

The microtearing mode has been addressed analytically in a number of papers [109, 58, 56, 57, 112, 113, 59]. A good review of the microtearing literature is given in the Ph. D. thesis of D. Applegate [114]. A brief summary will be given here.

The kinetic nature of the tearing instability was first addressed in Hazeltine et al. (1975) [109]. Therein a rigorous Fokker-Planck collision operator was employed in the context of the slab tearing mode, and a new drift-tearing instability was discovered that explicitly requires an energy dependent collision operator. This theory was revised somewhat by Drake and Lee (1977) [58], who investigated further the collsional properties of the mode and established several different regimes – collisional, semi-collisional, and collision-

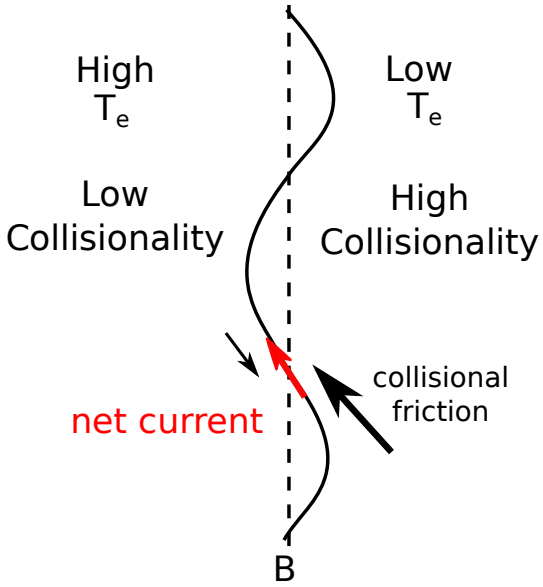

Figure 6.1: Schematic of the thermal force, responsible for the collisional MTM instability mechanism. Electrons streaming along the magnetic field line encounter frictional forces associated with collisions. A radially perturbed magnetic field in the presence of a background temperature gradient leads to an imbalance between the collisional friction and the creation of a parallel current. This parallel current can then reinforce the original magnetic perturbation, leading to instability.

less – finding that the collisionless mode is stable at the wavenumbers at which microtearing would be expected.

The collisional and semi-collisional MTM instability arises due to the thermal force,

$$F_{\text{th}} \sim -n_0 \nabla_{\parallel} T_e \quad . \tag{6.2}$$

In particular it is the time-dependent part of this force that is necessary for the instability to occur [60]. The thermal force is due to a parallel gradient in the electron temperature, which may be established by a radially perturbed magnetic field in the presence of a radial background gradient. Such a gradient leads to different regions of collisionality along the field line and an imbalance of forces that can create a parallel current. When this parallel current reinforces the magnetic field perturbation an instability can occur. A schematic of the thermal force is given in Fig. 6.1.

Additional work was done to expand on the physics of the collisional MTM. Gladd et al. (1980) used numerical calculations to relax some of the simplifying assumptions of

the Drake and Lee work, including retaining fluctuations in electrostatic potential Φ and allowing for the variation of $A_\parallel$ across the tearing layer. Later work by Cowley et al. [113] dealt with FLR effects, finding them to be strongly stablizing. Importantly, they found the approximation of unmagnetized ions to be good within the tearing layer d, although the extended nature of the Φ eigenmode structure can extend far outside this limit and yield a residual current contribution that is stabilizing. Catto and Rosenbluth [71] considered the effect of trapped particles and found an additional instability mechanism that arose from the scattering of electrons across the trapped/passing boundary. This mechanism also requires collisions. In Connor et al. [59] several of these instability mechanisms are considered and extended to lower collisionality in the intermediate range $\nu_e < \omega_e^* < \nu_e/\epsilon$. Again the important conclusion was drawn that the microtearing mode should be stable in the collisionless limit.

One important effect not included in the aforementioned papers is the effect of magnetic drifts on passing electrons. These magnetic drifts may constitute an energy dependent drift that generates a parallel current and allows for an instability mechanism even in the absence of collisions.

The width of the tearing layer d is an important parameter for the analysis of the MTM, partially determing the physical effects that must be considered. In Hazeltine et al. it was assumed that $d \gg \rho_i$, but Drake and Lee find that in the collisionless limit d becomes much smaler than ρ_i. One effect of this result is that ions may be considered unmagnetized, and therefore the approximation $\tilde{n}_i = -en_0\tilde{\Phi}/T_i$ can be made.

The tearing layer width can be determined by considering some important effects that inhibit the growth of a large parallel current. In the absence of collisions, electrons stream along magnetic field lines at the thermal velocity v_{Te}. They will be slowed by an oscillating electric field if the thermal velocity is greater than the phase velocity of the oscillation ($v_{Te} > \omega/k_\parallel$). This implies that the MTM can only exist if the condition $k_\parallel < \omega/v_{Te}$ holds. In the slab approximation, where $k_\parallel = k_y x/L_s$, this corresponds to a tearing layer width of

$$d = \frac{\omega L_s}{k_y v_{Te}} \quad , \tag{6.3}$$

where L_s is the length scale of magnetic shear.

6.2 Microtearing and Magnetic Drifts

The microtearing mode presented in Ch. 4 has some characteristics which have revealed several aspects of its underlying drive mechanism. The most important of these are the collisional independence at low ν and the electron temperature gradient drive.

An important element missing from the early analytical MT theory was the role of magnetic drifts. This simplification was perhaps well justified in many tokamak cases, where magnetic field lengths scales are on the order of the major radius ($L_B \sim R_0$) and magnetic drifts are therefore less of a concern than other effects, but in the RFP, with its associated stronger poloidal magnetic field, the magnetic field length scale can be proportional to the minor radius ($L_B \sim a$), and the magnetic drifts can play a correspondingly larger role. Recent gyrokinetic studies have shown that magnetic drifts are an important part of the instability drive in the collisionless regime [68, 70, 55, 63]. This behavior can be seen in Fig. 6.2. These results are produced using the GENE code, where a scaling parameter f_c has been used to artificially adjust the strength of the magnetic drift, and $f_c = 1$ represents the physical drift.

Different forms of the magnetic drifts may be implemented in GENE by setting the nature of the drift term. For the work conducted here, this term is set to be of the form

$$v_{\mathrm{curv}+\nabla B} \sim \boldsymbol{b} \times \left[\left(v_{\parallel}^2 + \frac{v_{\perp}^2}{2} \right) \frac{\nabla B}{B} + \left(v_{\parallel}^2 + \frac{v_{\perp}^2}{2} \right) \frac{4\pi}{B^2} \nabla p \right] / \Omega \quad . \tag{6.4}$$

Let us note that a further simplified term is used in the analytic derivation corresponding to the $\beta = 0$ limit (ignoring the pressure gradient term)

$$v_{\mathrm{curv}+\nabla B} \sim \boldsymbol{b} \times \left[\left(v_{\parallel}^2 + \frac{v_{\perp}^2}{2} \right) \frac{\nabla B}{B} p \right] / \Omega \quad . \tag{6.5}$$

There was found to be no difference in the gyrokinetic results between the use of these expressions. Even though microtearing is a finite-β mode it would appear that the pressure gradient contribution to the magnetic drift is not important for the instability drive discussed here. For more on the drift terms in GENE, see also the GENE manual [11].

The simulations are further simplified by the use of adiabatic ions and the absence of collisions. Importantly, it is found that instability occurs only for a range of f_c, falling off as f_c becomes much different from 1. Figure 6.2 also shows the dependence of the mode on the parameter $\eta_e = (d \ln T_e/dr)/(d \ln n_e/dr)$, with stronger growth rates for larger values of η_e. In these simulations R_0/L_n is held fixed while R_0/L_{Te} is varied.

A curvature driven mode matching the characteristics of the kind just presented has been described before by Finn and Drake [115, 72]. This work was performed specifically in an RFP geometry using the Braginskii fluid equations. Importantly, it was found that the mode requires an electron temperature gradient and is only unstable when the curvature drift $\omega_c = -2kTB_\theta/eB^2r_s$ and the diamagnetic drift $\omega_{*p} = kp'/neB_\theta$ are similar in magnitude, with the linear growth rate falling off for $\omega_c \lesssim \omega_{*p}$ or $\omega_c \gtrsim \omega_{*p}$. This behavior can be seen in Fig. 6.3, reproduced from Ref. [72], where it can be seen that this relationship to curvature is similar, at least qualitatively, to the relationship that has been found in gyrokinetic simulations, given in Fig. 6.2. This theory was formulated in the context of an RFP, in which the curvature drift is larger than that in a tokamak by roughly a factor of the aspect ratio. When the curvature drift is close to that of the diamagnetic frequency a coupling occurs between the drift-tearing mode and a curvature drift mode, enabling instability even when $\Delta' \leq 0$.

The mechanism for the Finn and Drake curvature driven mode is fundamentally different from the collisional MTM discussed above, since the collisional mode does not appear in the Braginskii fluid formulation unless the time dependent thermal force is explicitly included [60]. Furthermore, the fluid nature of the mode described in Ref. [115] implies that kinetic resonances are unimportant to the physics of the curvature driven mode described there. If the physics of this mode is indeed the same as that of the collisionless MTM, this suggests that insight into the latter mode may be gained by the use of a fluid expansion in the kinetic framework. Such an expansion constitutes the aim of the present work. An analytic inclusion of the magnetic drifts into the drift-kinetic model is developed, essentially constituting an inclusion of the magnetic drift term into the theory of Drake and Lee [58].

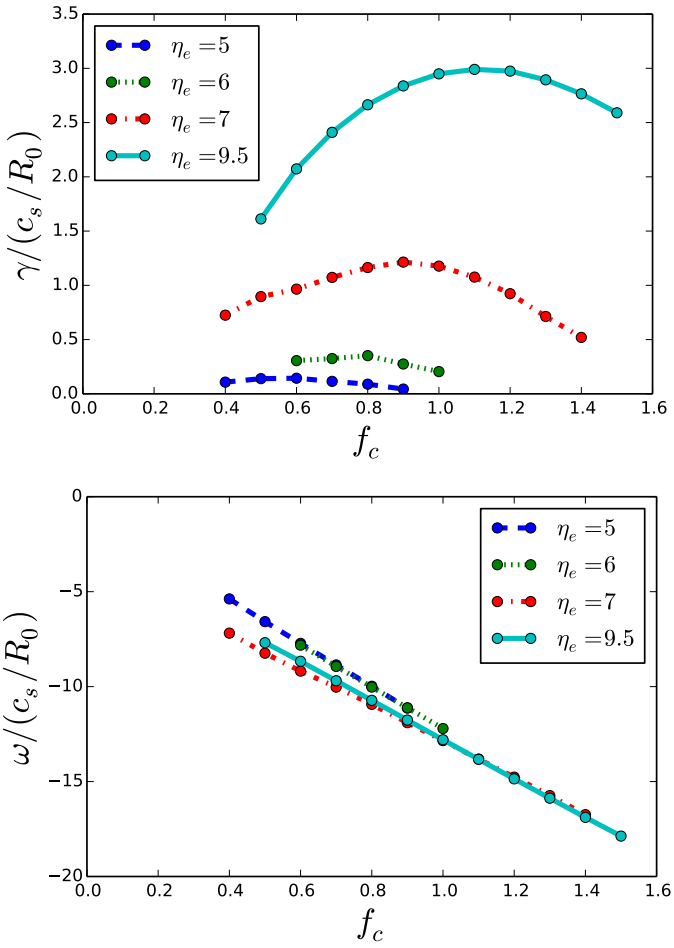

Figure 6.2: Results from the GENE code showing MT growth rate versus f_c, a parameter that scales the strength of the magnetic drift in the Vlasov equation. A parity selection procedure has been implemented acting on Φ and $A_\parallel$ so that only tearing parity modes are allowed. The strength of the instability scales with η_e. Adiabatic ions are used and other parameters are $R_0/L_n = 1.74$, $k_y\rho_s = 1.4$, and $\beta = 0.09$.

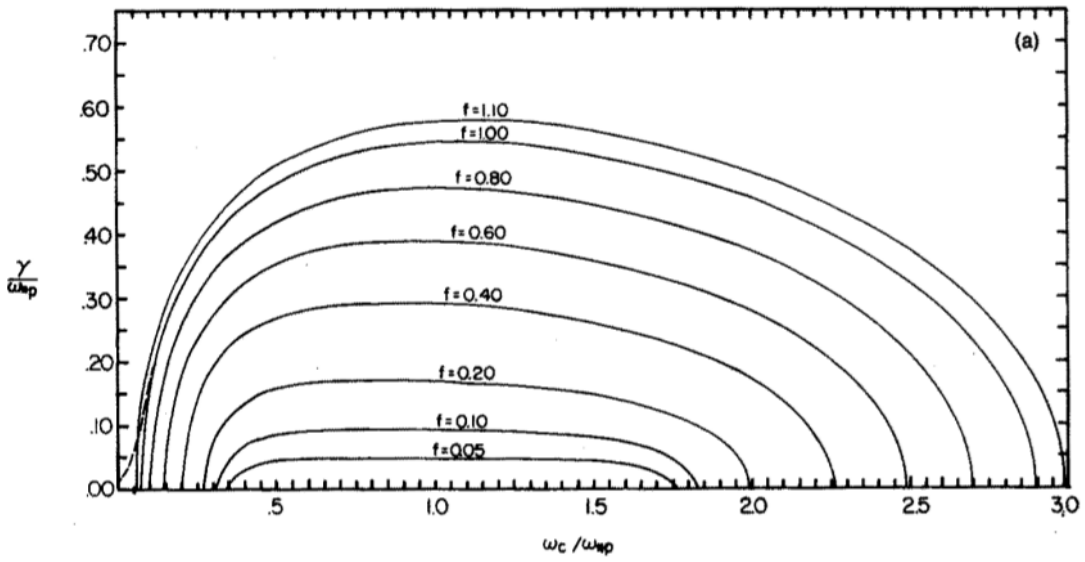

Figure 6.3: Growth rate plotted against curvature drift frequency, with both quantities normalized to the diamagnetic frequency, for the magnetic-curvature drift mode of Finn and Drake. A peak occurs around $\omega_c/\omega_{*p} \simeq 1$. Multiple values of $f \equiv \omega_{*t}/\omega_{*p}$ are shown, so that higher values of f, with constant density gradient, can be associated with a stronger temperature gradient. Note that the parameter f_c in Fig. 6.2 corresponds with ω_c/ω_{*p} here, rather than f. Source: Finn and Drake (1986).

The effect of magnetic drifts on the microtearing mode has been discussed in some detail in Predebon and Sattin (2013) [70]. There the effect of magnetic drifts was considered in a slab geometry in a drift-kinetic model and found to play an important role in the instability mechanism of the collisionless MTM. Magnetic drifts were included in a heuristic fashion and the resultant eigenmode equations solved numerically. The present work can be considered to approach this same task in a more rigorous way. Let us also note that Ref. [70] also found evidence for other instability mechanisms beyond the magnetic drifts, and it is possible that there is not a unique collisionless MTM.

6.3 Derivation

The derivation follows closely that of the collisionless drift-tearing mode as outlined in Ref. [58]. The starting point for this approach is the non-adiabatic part of the perturbed

distribution function,

$$g_e = -\frac{eF_M}{T_e}\frac{\omega - \bar{\omega}_T^*}{\omega - k_\parallel v_\parallel - \bar{\omega}_D}\left(\Phi - \frac{v_\parallel A_\parallel}{c}\right) \quad , \tag{6.6}$$

where e is the electric charge, c is the speed of light, $k_\parallel = k_y x/L_s$ is the parallel wavenumber, L_s is the shear length scale in a toroidal geometry, $x = r - r_s$ is the distance from the rational surface, $\bar{\omega}_T = \omega_n^* + \omega_T^*((v_\perp^2 + v_\parallel^2)/v_{Te}^2 - 3/2)$ is the gradient drive term, $\omega_n^* = -(k_y T_e/eB)(n'/n)$ is the electron diamagnetic frequency, $F_M = \pi^{-3/2} n_0 v_{Te}^{-3} \exp^{(} -(v_\parallel^2 + v_\perp^2)/v_{Te}^2)$ is the Maxwellian distribution function, $v_{Te}^2 = 2T_e/m_e$ is the thermal velocity, T_e is the background electron temperature, and n_0 is the background density. The form for the magnetic drift used here is $\bar{\omega}_D = \omega_D(v_\parallel^2/v_{Te}^2 + v_\perp^2/2v_{Te}^2)$, which represents the combination of both ∇B and curvature drifts in the zero β limit. In this limit the magnetic drift is simplified, so that the curvature and grad-B drifts may be combined to form

$$\bar{\omega}_D = \mathbf{v}_D \cdot \mathbf{k} = (\mathbf{v}_c + \mathbf{v}_{\nabla B}) \cdot \mathbf{k} = \frac{\mathbf{B}_0 \times \nabla B_0}{\Omega_e B_0^2} \cdot \boldsymbol{k}\, (v_\parallel^2 + v_\perp^2/2) = \omega_D(v^2 + u^2/2) \quad , \tag{6.7}$$

where $v = v_\parallel/v_{Te}$ and $u = v_\perp/v_{Te}$. The definition of ω_D becomes

$$\omega_D = -\frac{2T_e \boldsymbol{B}_0 \times \nabla \boldsymbol{B}_0 \cdot \boldsymbol{k}}{eB_0^3} \quad . \tag{6.8}$$

The parallel current may be derived from Eq. (6.6) by taking the first parallel velocity moment $J_\parallel = -e\int d^3 v v_\parallel g_e$. The denominator $\omega - k_\parallel v_\parallel - \bar{\omega}_D$ introduces analytic difficulties in the form of resonances in velocity space. As mentioned before, the work of Finn and Drake using fluid theory suggests that the magnetic drift kinetic resonance is unimportant for the existence of a curvature driven tearing mode. Assuming the unimportance of this resonance and assuming small ω_D, the denominator may be simplified by applying the expansion

$$\frac{1}{\omega - k_\parallel v_\parallel - \bar{\omega}_D} \sim \frac{1}{\omega - k_\parallel v_\parallel}\left(1 + \frac{\bar{\omega}_D}{\omega - k_\parallel v_\parallel} + \mathcal{O}(\bar{\omega}_D^2)\right) \quad . \tag{6.9}$$

With this expansion, it is possible to separate the electron distribution function (Eq. (6.6)) such that

$$g_e = g_{e,0} + g_{e,\omega_D} \quad ,$$

where g_{e,ω_D} consists of all terms proportional to ω_D and $g_{e,0}$ contains all other terms,

$$g_{e,0} = -\frac{eF_M}{T_e}\frac{\omega - \bar{\omega}_T^*}{\omega - k_\parallel v_\parallel}\left(\Phi - \frac{v_\parallel A_\parallel}{c}\right) \quad . \tag{6.10}$$

With this prescription the parallel current also becomes separable:

$$J_\parallel = J_{\parallel,0} + J_{\parallel,\omega_D} \quad , \tag{6.11}$$

where $J_{\parallel,\omega_D}$ is the current that arises as a result of the ω_D terms and $J_{\parallel,0}$ is the collisionless parallel current in the absence of magnetic drifts as derived in Drake and Lee [58],

$$J_{\parallel,0} = \frac{\omega_{pe}^2}{4\pi} iE_\parallel \frac{1}{\omega} s^2 \frac{\omega_n^*}{\omega}\left[\left(\frac{\omega}{\omega_n^*} - 1\right) Z'(s) + \frac{s}{2}\eta_e Z''(s)\right] \quad , \tag{6.12}$$

where $s = \omega/(k_\parallel v_{Te})$. This equation is expressed in terms of the first and second derivatives of the plasma dispersion function $Z(s)$. For reference, these functions are given here:

$$Z(s) = \pi^{-1/2}\int_{-\infty}^{\infty} dt \frac{e^{-t^2}}{t-s} \quad , \tag{6.13}$$

$$Z'(s) = \pi^{-1/2}\int_{-\infty}^{\infty} dt \frac{e^{-t^2}}{(t-s)^2} = -\pi^{-1/2}\int_{-\infty}^{\infty} dt \frac{2t}{t-s}e^{-t^2} \quad , \tag{6.14}$$

$$Z''(s) = \pi^{-1/2}\int_{-\infty}^{\infty} dt \frac{2e^{-t^2}}{(t-s)^3} \quad . \tag{6.15}$$

The task now is to evaluate the parallel current generated as a result of the magnetic drifts. The part of the distribution function proportional to ω_D (and ignoring terms of order ω_D^2) is:

$$g_{e,\omega_D} = -\frac{eF_M}{T_e}\frac{(\omega - \bar{\omega}_T^*)\bar{\omega}_D}{(\omega - k_\parallel v_\parallel)^2}\left(\Phi - \frac{v_\parallel A_\parallel}{c}\right) \tag{6.16}$$

A form for the parallel current $J_{\parallel,\omega_D} = -e\int d^3v v_\parallel g_e^{\omega_D} = J_{\parallel,\omega_D}^{\Phi} + J_{\parallel,\omega_D}^{A_\parallel}$ may be determined from this expression via a number of steps. The derivation of the parallel current terms is given in Appendix A. Therein, expressions for the ω_D-driven parallel current proportional to $A_\parallel$ ($J_{\parallel,\omega_D}^{A_\parallel}$) and Φ ($J_{\parallel,\omega_D}^{\Phi}$) are derived. These expressions are:

$$J_{\parallel,\omega_D}^{\Phi} = \frac{\omega_{pe}^2}{4\pi}\frac{2\pi^{-1/2}}{k_\parallel v_{Te}^2}\frac{\omega_D}{k_\parallel v_{Te}}\int_{-\infty}^{\infty} dv \frac{\omega(v^3 + v/2) - v^3\omega_n^* - v^5\omega_T^* - v/2(\omega_n^* + \omega_T^*/2)}{(s-v)^2}e^{-v^2}\Phi \quad , \tag{6.17}$$

$$J^{A_\parallel}_{\parallel,\omega_D} = -\frac{\omega_{pe}^2}{4\pi c}\frac{2\pi^{-1/2}}{k_\parallel v_{Te}}\frac{\omega_D}{k_\parallel v_{Te}}\int_{-\infty}^{\infty} dv \frac{\omega(v^4+v^2/2)) - v^4\omega_n^* - v^6\omega_T^* - v^2/2(\omega_n^*+\omega_T^*/2)}{(s-v)^2} e^{-v^2} A_\parallel \quad . \tag{6.18}$$

To compare more directly with the $\omega_D = 0$ terms from Drake and Lee, these terms can be rewritten in terms of Z' and Z''. Using these definitions, the Φ component of the magnetic-drift-driven parallel current (Eq. (6.17)) becomes

$$J^{\Phi}_{\parallel,\omega_D} = \frac{\omega_{pe}^2}{4\pi c}\frac{c}{v_{Te}}\frac{1}{\omega}s\frac{2\omega_D}{\omega}\left[\left(s^3\omega_T^* - s(\omega-\omega_n^*-\frac{1}{2}\omega_T^*)\right)Z'(s) + \left(\frac{1}{2}s^4\omega_T^* - \frac{1}{2}s^2(\omega-\omega_n^*+\omega_T^*) - \frac{1}{4}(\omega-\omega_n^*-\frac{1}{2}\omega_T^*)\right)Z''(s)\right]\Phi \quad . \tag{6.19}$$

And doing the same with the $A_\parallel$ term (Eq. (6.18)),

$$J^{A_\parallel}_{\parallel,\omega_D} = -\frac{1}{\omega}\frac{\omega_{pe}^2}{4\pi c}\frac{2\omega_D}{\omega}A_\parallel s^2\left[\left(s^4\omega_T^* - s^2(\omega-\omega_n^*) - \frac{1}{2}\left(\omega-\omega_n^*-\omega_T^*\right)\right)Z'(s) + \left(\frac{1}{2}s^5\omega_T^* - \frac{1}{2}s^3\left(\omega-\omega_n^*+\frac{3}{2}\omega_T^*\right) - \frac{1}{4}s\omega_T^*\right)Z''(s)\right] \quad . \tag{6.20}$$

In order to derive a dispersion relation from these expressions, it is necessary to find a relationship between Φ and $A_\parallel$. This is done through the quasineutrality equation.

Quasineutrality

The quasineutrality equation is given by

$$\frac{ne^2\Phi}{T_e}(1+\tau) = e\int d^3v g_e \quad , \tag{6.21}$$

expressed in terms of the non-adiabatic part of the distribution function (Eq. (6.6)), where $\tau = T_e/T_i$. Ions are assumed to be adiabatic, so that $g_i = 0$ and $f_i = -\frac{e\Phi}{T_i}f_M$.

As with the expressions for the parallel current, the relationship between Φ and $A_\parallel$ as given by the quasineutrality relationship is derived in Appendix A. The result of this is the

expression

$$\Phi = \frac{v_{Te}}{c} A_{\parallel} \left[\left[s^4 \hat{\omega}_D \eta - s^2 \hat{\omega}_D (\hat{\omega} - 1 - \eta/2) + \frac{\hat{\omega}}{2} (\hat{\omega} - 1) \right] Z'(s) \right.$$
$$\left. + \left[s^5 \hat{\omega}_D \eta - s^3 \hat{\omega}_D (\hat{\omega} - 1 + \eta) + \frac{s}{2} (\hat{\omega}\eta - \hat{\omega}_D \hat{\omega} + \hat{\omega}_D + \hat{\omega}_D \eta/2)) \right] Z''(s)/2 \right] /$$
$$\left[(1+\tau)\hat{\omega}^2/s + \left[s^3 \hat{\omega}_D \eta + s\hat{\omega}(\hat{\omega} - 1) \right] Z'(s) \right.$$
$$\left. + \left[s^4 \hat{\omega}_D \eta - s^2 \hat{\omega}_D (\hat{\omega} - 1 + \eta/2) + \hat{\omega}(\hat{\omega} + \eta/2 - 1) \right] Z''(s)/2 \right] \quad , \tag{6.22}$$

where all frequencies are normalized to ω_n^*, so that $\hat{\cdot} \equiv \cdot/\omega_n^*$ and $\eta \equiv \omega_T^*/\omega_n^*$.

The parallel current terms are restated here using the same normalization,

$$J_{\parallel,\omega_D}^{A_\parallel} = -\frac{\omega_{pe}^2}{4\pi c} \frac{2\hat{\omega}_D}{\hat{\omega}^2} s^2 \left[\left(s^4 \eta - s^2 (\hat{\omega} - 1) - \frac{1}{2} (\hat{\omega} - 1 - \eta) \right) Z'(s) \right.$$
$$\left. + \left(\frac{1}{2} s^5 \eta - \frac{1}{2} s^3 \left(\hat{\omega} - 1 + \frac{3}{2}\eta \right) - \frac{1}{4} s\eta \right) Z''(s) \right] A_\parallel \quad , \tag{6.23}$$

$$J_{\parallel,\omega_D}^{\Phi} = \frac{\omega_{pe}^2}{4\pi c} \frac{2\hat{\omega}_D}{\hat{\omega}^2} s^2 \left[\left(s^3 \eta - s \left(\hat{\omega} - 1 - \frac{1}{2}\eta \right) \right) Z'(s) \right.$$
$$\left. + \left(\frac{1}{2} s^4 \eta - \frac{1}{2} s^2 (\hat{\omega} - 1 + \eta) - \frac{1}{4} \left(\hat{\omega} - 1 - \frac{1}{2}\eta \right) \right) Z''(s) \right] \left(\frac{c}{v_{Te}} \right) \Phi \quad . \tag{6.24}$$

6.4 Parallel Current Structure

Before attempting to solve the above set of expressions analytically, it is useful to first consider the structure of the parallel current, and how this structure changes with the variation of important parameters. Fig. 6.4 shows the real and imaginary parts of the parallel current for the $\omega_D = 0$ case. The other parameters are $\tau = 1$ and $\eta = 10$. The magnitude of the current for these same parameters is plotted in Fig. 6.5. Without solving for $\hat{\omega}$ explicitly, it is necessary to make some assumption for its form. For the purpose of visualizing the structure of the parallel current expression, it has been assumed that $\hat{\omega} = 1 + \eta$. These structures are plotted against x/d, for d given in Eq. (6.3).

The effect of the ω_D components on this structure can also be explored. Fig. 6.6 shows the curve from Fig. 6.5 ($\hat{\omega}_D = 0$) plotted along with the curve for $\hat{\omega}_D = 1$. In Fig. 6.7 is

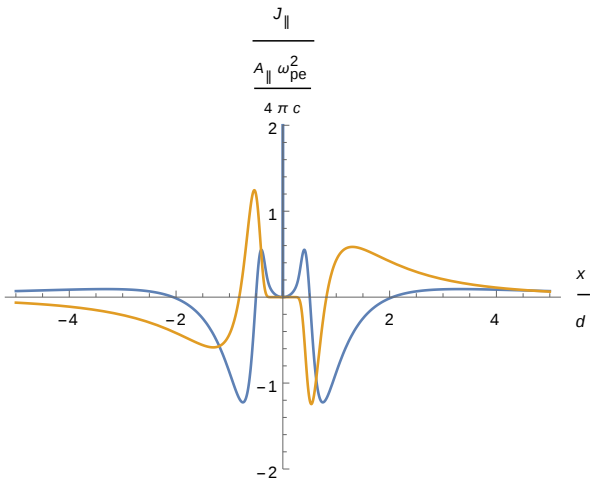

Figure 6.4: Real (blue curve) and imaginary (orange curve) portions of $J_\parallel(x)$ for $\hat{\omega}_D = 0$, $\eta = 10$, $\tau = 1$. The assumption $\hat{\omega} = 1 + \eta$ has been used. The real part is even in x while the imaginary part is odd.

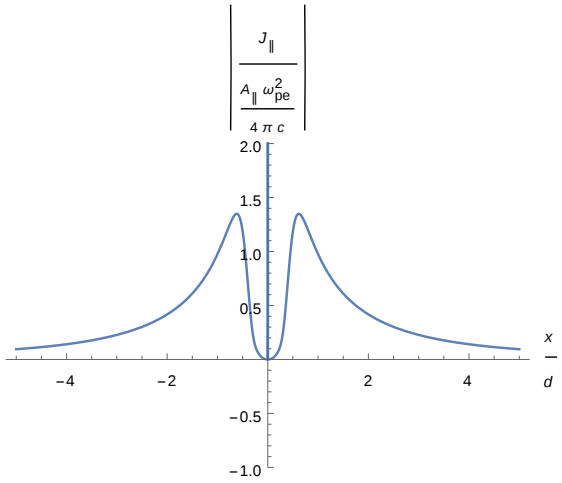

Figure 6.5: $|J_\parallel(x)|$ for $\hat{\omega}_D = 0$, $\eta = 10$, $\hat{\omega} = 1 + \eta$, $\tau = 1$.

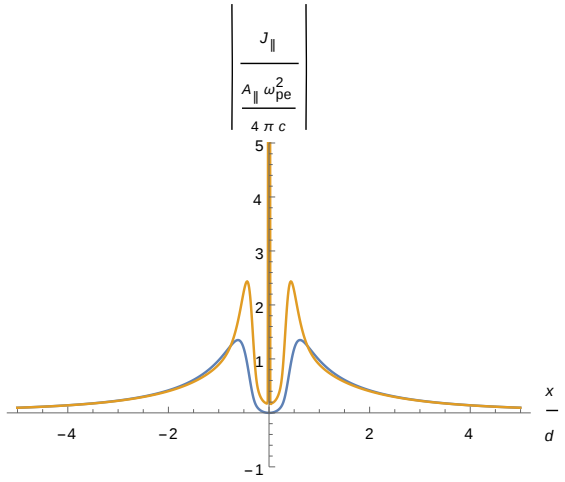

Figure 6.6: $|J_\parallel(x)|$ for $\hat{\omega}_D = 0$ (blue curve) and $\hat{\omega}_D = 1$ (orange curve). Other parameters are $\eta = 10$, $\hat{\omega} = 1 + \eta$, and $\tau = 1$.

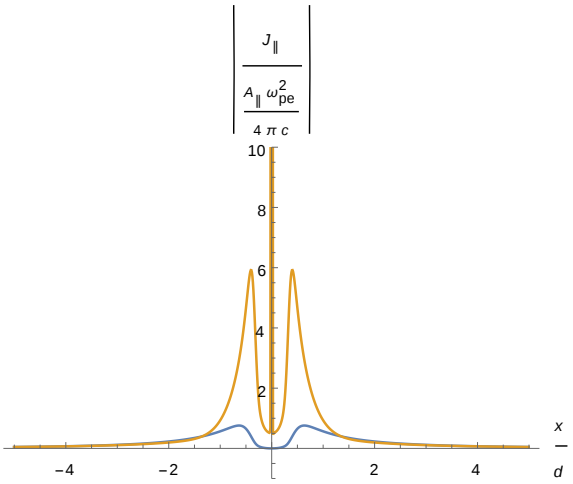

Figure 6.7: $|J_\parallel(x)|$ for $\hat{\omega}_D = 0$ (blue curve) and $\hat{\omega}_D = 1$ (orange curve). Other parameters are $\eta = 1$, $\hat{\omega} = 1 + \eta$, and $\tau = 1$.

shown these same values ($\hat{\omega}_D = 0$ and $\hat{\omega}_D = 1$), but for $\eta = 1$. It can be seen that both η and $\hat{\omega}_D$ have an effect on the sharp peaks seen at $x/d \approx \pm 0.5$-1.

One piece of information that may be gleaned from these plots is the behavior of $J_\parallel$ at large s (small x). In Sec. 6.6, the large-s limit of the parallel current expressions will be taken. In those expressions, the behavior of the current will become like $J_\parallel \propto x^2$. Consequently, the integral in Ampère's law cannot be taken from $x = -\infty$ to $x = \infty$ and will instead be restricted to $x/d = -1$ to $x/d = 1$. This may discard important information,

but it is a necessary component of investigating the limiting behavior.

6.5 $\Phi = 0$ Result

It has been found that in some gyrokinetic simulations the electrostatic potential fluctuation Φ is a necessary component of instability [68]. This scenario can be investigated by choosing $\Phi = 0$ and ignoring the J^{Φ} terms, a step taken in Drake and Lee (1977) [58] (where the collisionless MTM was found to be stable). As discussed above, the MT mode will be damped away if the phase velocity of the mode is less than the electron thermal velocity. This imposes an upper limit on the parallel wavenumber and suggests that only the inductive term needs to be considered in the parallel electric field $E_{\parallel} = -\frac{\omega}{c}A_{\parallel} + k_{\parallel}\Phi$.

Ampère's Law was previously stated as an integral over x, but the parallel current is now written as a function of s, reading $s = \omega/(k_{\parallel}v_{Te}) = ((\omega L_s)/(k_y v_{Te}))(1/x) = d/x$. In order to perform this integral we must perform a variable substitution:

$$\int_{-\infty}^{\infty} dx \rightarrow -\frac{\omega L_s}{k_y v_{Te}} \int_{-\infty}^{\infty} \frac{ds}{s^2} \quad .$$

Knowing the asymptotic behavior of Z' and Z'' will be also important here, so the expansion of these functions in the large s limit is presented here:

$$Z'(s) \simeq i\pi^{1/2}\sigma e^{-s^2}(-2s) + \frac{1}{s^2} + \frac{3}{2}\frac{1}{s^4}, \quad Z''(s) \simeq i\pi^{1/2}\sigma e^{-s^2}(-2+4s^2) - \frac{2}{s^3} - \frac{6}{s^5} \quad . \tag{6.25}$$

Now, the $A_{\parallel}$ contributions in Ampere's law can be considered to arise from two terms: the $\omega_D = 0$ term Δ'_0 (considered in Drake and Lee (1977)) and the ω_D contribution Δ'_{ω_D} that comes from integrating Eq. (6.23):

$$\begin{aligned}\Delta'_{\omega_D} = \frac{4\pi}{c} d \int_{-\infty}^{\infty} \frac{ds}{s^2} \sim \int_{-\infty}^{\infty} ds \Bigg[\left(s^4\eta - s^2\left(\hat{\omega} - 1\right) - \frac{1}{2}\left(\hat{\omega} - 1 - \eta\right) \right) Z'(s) + \\ \left(\frac{1}{2}s^5\eta - \frac{1}{2}s^3\left(\hat{\omega} - 1 + \frac{3}{2}\eta\right) - \frac{1}{4}s\eta \right) Z''(s) \Bigg] \quad .\end{aligned} \tag{6.26}$$

As will be shown, with the assumption that $\Phi = 0$, the parameter Δ'_{ω_D} evaluates to zero due to a number of cancellations that occur among these terms.

We first look at the terms proportional to $\hat{\omega} - 1$, given by

$$-\left(\hat{\omega} - 1\right) \int_{-\infty}^{\infty} ds \left[s^2 Z'(s) + \frac{s^3}{2} Z''(s) + \frac{1}{2} Z'(s) \right] \quad . \tag{6.27}$$

Consider the highest s-order term, proportional to $s^3 Z''$. Using some algebraic manipulations, including integration by parts and the identity $sZ + 2 = -Z'/2$, this can be written in another form:

$$\begin{aligned}\int_{-\infty}^{\infty} ds \frac{s^3}{2} Z''(s) &= \int_{-\infty}^{\infty} ds \left[\frac{s^3}{2} \left(Z''(s) + \frac{2}{s^3} \right) - 1 \right] \\ &= \underbrace{\frac{s^3}{2} \left(Z'(s) - \frac{1}{s^2} \right) \Big|_{-\infty}^{\infty}}_{=0} - \int_{-\infty}^{\infty} ds \left[\frac{3}{2} s^2 \left(Z' - \frac{1}{s^2} \right) + 1 \right] \quad . \end{aligned} \tag{6.28}$$

The boundary term evalutes to zero at both $s = 0$ and $s = \pm\infty$, so although these expressions could be written in a more mathematically rigorous way to encompass $s = 0$, this is not done here.

Now, doing the same with the $s^2 Z'$ term,

$$\int_{-\infty}^{\infty} ds\, s^2 Z'(s) = \int_{-\infty}^{\infty} ds \left[s^2 \left(Z'(s) - \frac{1}{s^2} \right) + 1 \right] \quad . \tag{6.29}$$

We can now combine Eq. (6.28) with Eq. (6.29) to give

$$\begin{aligned}\int_{-\infty}^{\infty} ds \left[s^2 Z'(s) + \frac{s^3}{2} Z''(s) \right] &= -\frac{1}{2} \int_{-\infty}^{\infty} ds s^2 \left(Z'(s) - \frac{1}{s^2} \right) \\ &= \underbrace{-\frac{s^2}{2} \left(Z + \frac{1}{s} \right) \Big|_{-\infty}^{\infty}}_{=0} + \int_{-\infty}^{\infty} ds\, \underbrace{s \left(Z + \frac{1}{s} \right)}_{=-\frac{1}{2} Z'(s)} \quad . \end{aligned} \tag{6.30}$$

This will cancel with the $(\hat{\omega} - 1) Z'(s)$ term, so that Eq. (6.27) evaluates to zero.

Now we turn our attention to the terms in Eq. (6.26) proportional to η:

$$\eta \int_{-\infty}^{\infty} ds \left[\left(\frac{1}{2} s^5 - \frac{3}{4} s^3 - \frac{1}{4} s \right) Z''(s) + (s^4 + \frac{1}{2}) Z'(s) \right] \quad . \tag{6.31}$$

We first rewrite the $s^5 Z''$ term,

$$\begin{aligned}\int_{-\infty}^{\infty} ds \frac{s^5}{2} Z''(s) &= \int_{-\infty}^{\infty} ds \frac{s^5}{2} \left(Z''(s) + \frac{2}{s^3} + \frac{6}{s^5} - \frac{2}{s^3} - \frac{6}{s^5} \right) \\ &= \underbrace{\frac{s^5}{2} \left(Z'(s) - \frac{1}{s^2} - \frac{3}{2s^4} \right) \Big|_{-\infty}^{\infty}}_{=0} - \int_{-\infty}^{\infty} ds \left[\frac{5}{2} s^4 \left(Z' - \frac{1}{s^2} - \frac{3}{2s^4} \right) + s^2 + 3 \right] \quad . \end{aligned} \tag{6.32}$$

We can then do the same with the $s^4 Z'$ term,

$$\begin{aligned}\int_{-\infty}^{\infty} ds\, s^4 Z'(s) &= \int_{-\infty}^{\infty} ds s^4 \left(Z'(s) - \frac{1}{s^2} - \frac{3}{2s^4} + \frac{1}{s^2} + \frac{3}{2s^4} \right) \\ &= \int_{-\infty}^{\infty} ds \left[s^4 (Z' - \frac{1}{s^2} - \frac{3}{2s^4}) + s^2 + \frac{3}{2} \right] \quad .\end{aligned} \tag{6.33}$$

Eq. (6.32) and Eq. (6.33) can be combined to give

$$\begin{aligned}\int_{-\infty}^{\infty} ds \left[s^4 Z'(s) + \frac{s^5}{2} Z''(s) \right] &= \int_{-\infty}^{\infty} ds \left[-\frac{3}{2} s^4 \left(Z'(s) - \frac{1}{s^2} - \frac{3}{2s^4} \right) - \frac{3}{2} \right] \\ &= 0 + \int_{-\infty}^{\infty} ds \left[6s^3 \left(Z(s) + \frac{1}{s} + \frac{1}{2s^3} \right) - \frac{3}{2} \right] \\ &= \int_{-\infty}^{\infty} ds \left[6s^2 \left(sZ(s) + 1 \right) + \frac{3}{2} \right] \\ &= \int_{-\infty}^{\infty} ds \left[-3s^2 Z'(s) + \frac{3}{2} \right] \\ &= \int_{-\infty}^{\infty} ds \left[6s \left(Z(s) + \frac{1}{s} \right) - 3 + \frac{3}{2} \right] \\ &= \int_{-\infty}^{\infty} ds \left[-3Z'(s) - \frac{3}{2} \right] \quad .\end{aligned} \tag{6.34}$$

Then we rewrite the $s^3 Z''$ term

$$\begin{aligned}-\int_{-\infty}^{\infty} ds \frac{3s^3}{4} Z''(s) &= -\int_{-\infty}^{\infty} ds \frac{3s^3}{4} \left(Z''(s) + \frac{2}{s^3} - \frac{2}{s^3} \right) \\ &= \underbrace{-\frac{3s^3}{4} \left(Z'(s) - \frac{1}{s^2} \right) \Big|_{-\infty}^{\infty}}_{=0} + \int_{-\infty}^{\infty} ds \left[\frac{9}{4} s^2 \left(Z' - \frac{1}{s^2} \right) + \frac{3}{2} \right] \\ &= \int_{-\infty}^{\infty} ds \left[\frac{9}{4} Z'(s) + \frac{3}{2} \right] \quad .\end{aligned} \tag{6.35}$$

Adding Eq. (6.34) and Eq. (6.35) gives

$$\int_{-\infty}^{\infty} ds \left[\left(\frac{1}{2} s^5 - \frac{3}{4} s^3 \right) Z''(s) + s^4 Z'(s) \right] = -\int_{-\infty}^{\infty} ds \frac{3}{4} Z''(s) \quad . \tag{6.36}$$

And finally now consider the sZ'' and Z' terms from Eq. (6.31),

$$\begin{aligned}\int_{-\infty}^{\infty} ds \left[-\frac{s}{4} Z''(s) + \frac{1}{2} Z'(s) \right] &= \underbrace{-\frac{s}{4} Z'(s) \Big|_0^{\infty}}_{=0} + \int_{-\infty}^{\infty} ds \left[\frac{1}{4} Z'(s) + \frac{1}{2} Z'(s) \right] \\ &= \int_{-\infty}^{\infty} ds \left[\frac{3}{4} Z'(s) \right] \quad ,\end{aligned} \tag{6.37}$$

which, when added to Eq. (6.36) yields zero. This means that the full η expression (Eq. (6.31)) evaluates to zero.

The final results of performing the integration over s is that $\int (ds/s^2) J^{A_\parallel}_{\parallel,\omega_D}/A_\parallel = 0$, so that there is no additional contribution to Δ' from curvature terms, at least in the case that $\Phi = 0$. Thus, in the absence of Φ there is no ω_D driven instability. As mentioned, this result has been seen in certain regimes [68], although other work has shown evidence for the collisionless MTM even in the $\Phi = 0$ case [70], and it is likely that there are additional effects not captured in these limits.

6.6 $\Phi \neq 0$ Result

In the previous section, it was found that there is no contribution to the tearing parameter Δ' from $J^{A_\parallel}_{\parallel,\omega_D}$. In the more general case, where Φ is non-zero, it is necessary to make use of the quasineutrality equation to derive a relationship between Φ and $A_\parallel$. This relationship (Eq. (6.22) given above) is difficult to incorporate analytically into the expression for Δ', and so some simplifications will be made to enable an analytic approach.

An additional simplification can be made by assuming the frequency ω to be much larger than both $k_\parallel v_\parallel$ and ω_D. As can be seen from Fig. 6.2, near the physical value of the magnetic drift ($f_c = 1$) the real frequency is $\omega \approx 12 c_s/R_0 \approx 15\omega_n^*$ for the parameters studied there. This means that the analysis that follows should be expected to be valid for $\hat{\omega}_D \sim 1$. The expansion $\omega - k_\parallel v_\parallel \gg \omega_D$ has already been used to simplify the equations. Enforcing $\omega \gg k_\parallel v_\parallel$ is equivalent to taking the large s $\left(s = \omega/k_\parallel v_{Te}\right)$ limit of Z' and Z''. This expansion, however, places restrictions on the extent of the x integral (or s integral, equivalently) in Ampère's law. In fact, we must restrict the integral to a thin region around the resonant surface $x = 0$. Taking the limits of the x integral to be from -d to d, this translates to limits in s from $-\infty$ to -1 and 1 to ∞.

The large-s expansion of the parallel current

To proceed, we must take the large-s limits of the above expressions for the parallel current. This is done by using the large argument expansions for Z' and Z'' given in Eq. (6.25). The imaginary component (proportional to e^{-s^2}) is neglected.

For the original, non-magnetic-drift terms (from Eq. (6.12)) this expansion yields

$$J_{\parallel,0}^{A_\parallel} \to \frac{\omega_{pe}^2}{4\pi c} A_\parallel \frac{1}{\hat{\omega}} s^2 \left[(\eta + 1 - \hat{\omega}) \frac{1}{s^2} + \left(3\eta + \frac{3}{2}(1 - \hat{\omega}) \right) \frac{1}{s^4} \right] \tag{6.38}$$

and

$$J_{\parallel,0}^{\Phi} \to -\frac{\omega_{pe}^2}{4\pi c} \left(\frac{c}{v_{Te}} \Phi \right) \frac{1}{\hat{\omega}} s^2 \left[(\eta + 1 - \hat{\omega}) \frac{1}{s^3} + \left(3\eta + \frac{3}{2}(1 - \hat{\omega}) \right) \frac{1}{s^5} \right] \quad . \tag{6.39}$$

The magnetic drift terms (Eqs. 6.23 and 6.24) become in the large-s limit

$$J_{\parallel,\omega_D}^{A_\parallel} \to -\frac{\omega_{pe}^2}{4\pi c} A_\parallel \frac{2\hat{\omega}_D}{\hat{\omega}^2} s^2 \left[\left(\frac{22}{4}\eta + \hat{\omega} - 1 \right) \frac{1}{s^2} + \left(\frac{9}{4}\eta - \frac{3}{4}(\hat{\omega} - 1) \right) \frac{1}{s^4} \right] \tag{6.40}$$

and

$$J_{\parallel,\omega_D}^{\Phi} \to \frac{\omega_{pe}^2}{4\pi c} \Phi \frac{c}{v_{Te}} \frac{2\hat{\omega}_D}{\hat{\omega}^2} s^2 \left[\left(\frac{7}{2}\eta + 2(\hat{\omega} - 1) \right) \frac{1}{s^3} + \left(-\frac{3}{4}\eta + \frac{3}{2}(\hat{\omega} - 1) \right) \frac{1}{s^5} \right] \quad . \tag{6.41}$$

Finally, the quasineutrality expression (which contains contributions from both $\omega_D = 0$ and $\omega_D \neq 0$ terms) becomes:

$$\Phi/s \to A_\parallel \frac{v_{Te}}{c} \frac{N(s)}{D(s)} \quad , \tag{6.42}$$

where the functions that comprise the numerator and denominator are given by

$$\begin{aligned} N(s) = -s \left(-\hat{\omega} \left(2\eta \left(s^2 + 3 \right) + s^2(2 - 8\hat{\omega}_D) - 6\hat{\omega}_D + 3 \right) + \right. \\ \left. \hat{\omega}_D \left(\eta \left(14s^2 - 3 \right) - 8s^2 - 6 \right) + \left(2s^2 + 3 \right) \hat{\omega}^2 \right) \end{aligned} \tag{6.43}$$

and

$$\begin{aligned} D(s) = 2 \left(s^2 \hat{\omega}_D \left(2\eta s^2 - 3\eta + 2s^2 + 6 \right) + \hat{\omega} \left(\eta \left(s^2 + 3 \right) - 2s^4(\hat{\omega}_D - 1) + s^2(1 - 6\hat{\omega}_D) - 6 \right) \right. \\ \left. -\hat{\omega}^2 \left(2s^4(\tau + 2) + s^2 - 6 \right) \right) \quad , \end{aligned} \tag{6.44}$$

respectively.

This expression can be further simplified by taking only the largest s^n terms of the numerator and denominator, resulting in an expression proportional to s^{-1}:

$$\Phi \to -\frac{1}{2} \frac{1}{s} \frac{-\eta\hat{\omega} - \hat{\omega} + 4\hat{\omega}\hat{\omega}_D + 7\eta\hat{\omega}_D - 4\hat{\omega}_D + \hat{\omega}^2}{\eta\hat{\omega}_D + \hat{\omega}_D + \hat{\omega} - \hat{\omega}\hat{\omega}_D - \hat{\omega}^2(\tau + 2)} \left(\frac{v_{Te}}{c} \right) A_\parallel \tag{6.45}$$

The above expressions can be combined and integrated in Ampère's law, yielding a dispersion relation of fourth order in ω.

Starting with Ampère's law, expressed in terms of s:

$$\begin{aligned}\Delta' &= \frac{4\pi}{c} d \left[\int_{-\infty}^{-1} \frac{ds}{s^2} \frac{1}{A_\parallel} J_\parallel + \int_1^\infty \frac{ds}{s^2} \frac{1}{A_\parallel} J_\parallel \right] \\ &= G_0^{A_\parallel} + G_0^\Phi + G_{\omega_D}^{A_\parallel} + G_{\omega_D}^{A_\parallel} \quad ,\end{aligned} \tag{6.46}$$

the large-s limit expressions for the parallel currents derived above can now be substituted into this expression and the integrals performed.

For the $J_{\parallel,0}^{A_\parallel}$ term,

$$G_0^{A_\parallel} = -\frac{\omega_{pe}^2}{c^2} \frac{d}{\hat{\omega}} \left(3 + 4\eta - 3\hat{\omega}\right) \quad . \tag{6.47}$$

For the $J_{\parallel,0}^{\Phi}$ term,

$$G_{\omega_D}^{\Phi} = \frac{\omega_{pe}^2}{c^2} \frac{d}{\hat{\omega}} \frac{1}{30} \left(-28\eta + 19(\hat{\omega} - 1)\right) \frac{-\eta\hat{\omega} - \hat{\omega} + 4\hat{\omega}\hat{\omega}_D + 7\eta\hat{\omega}_D - 4\hat{\omega}_D + \hat{\omega}^2}{\eta\hat{\omega}_D + \hat{\omega}_D + \hat{\omega} - \hat{\omega}\hat{\omega}_D - \hat{\omega}^2(\tau + 2)} \quad . \tag{6.48}$$

For the $J_{\parallel,\omega_D}^{A_\parallel}$ term,

$$G_{\omega_D}^{A_\parallel} = -\frac{\omega_{pe}^2}{c^2} \frac{d}{\hat{\omega}} \frac{\hat{\omega}_D}{\hat{\omega}} \left(3 - 25\eta - 3\hat{\omega}\right) \quad . \tag{6.49}$$

For the $J_{\parallel,\omega_D}^{\Phi}$ term,

$$G_0^{\Phi} = \frac{\omega_{pe}^2}{c^2} \frac{d}{\hat{\omega}} \frac{\hat{\omega}_D}{\hat{\omega}} \frac{1}{30} \left(61\eta + 58(\hat{\omega} - 1)\right) \frac{-\eta\hat{\omega} - \hat{\omega} + 4\hat{\omega}\hat{\omega}_D + 7\eta\hat{\omega}_D - 4\hat{\omega}_D + \hat{\omega}^2}{\eta\hat{\omega}_D + \hat{\omega}_D + \hat{\omega} - \hat{\omega}\hat{\omega}_D - \hat{\omega}^2(\tau + 2)} \quad . \tag{6.50}$$

These expression can all be combined to yield the following dispersion relation:

$$\begin{aligned}\Delta' = \left(\frac{\omega_{pe}^2}{c^2} \frac{d}{\hat{\omega}}\right) \Bigg(&-3 - 4\eta + 3\hat{\omega} - \frac{\hat{\omega}_D}{\hat{\omega}}(3 - 25\eta - 3\hat{\omega}) + \\ &\frac{1}{30} \left((-28\eta + 19(\hat{\omega} - 1)) + \frac{\hat{\omega}_D}{\hat{\omega}} (61\eta + 58(\hat{\omega} - 1)) \right) \frac{-\eta\hat{\omega} - \hat{\omega} + 4\hat{\omega}\hat{\omega}_D + 7\eta\hat{\omega}_D - 4\hat{\omega}_D + \hat{\omega}^2}{\eta\hat{\omega}_D + \hat{\omega}_D + \hat{\omega} - \hat{\omega}\hat{\omega}_D - \hat{\omega}^2(\tau + 2)} \Bigg) \quad ,\end{aligned} \tag{6.51}$$

where

$$\frac{\Delta'}{d} \hat{\omega} \frac{c^2}{\omega_{pe}^2} \to -2k_y \frac{\Omega_i}{c_s} \frac{L_n}{L_s} \frac{v_{Te}}{c_s} \frac{c^2}{\omega_{pe}^2} = -2(k_y \rho_s) \frac{v_{Te}}{c_s} \frac{L_n}{L_s} \left(\frac{\delta_e}{\rho_s}\right)^2 \quad , \tag{6.52}$$

and the definition of d given in Eq. (6.3) has been used. The ratio between the electron skin depth δ_e and the ion sound gyroradius ρ_s can also be written as

$$\left(\frac{\delta_e}{\rho_s}\right)^2 = \frac{1}{2}\frac{m_i}{m_e}\frac{1}{\beta_e} \quad .$$

Eq. (6.51) can be investigated in a simplified scenario by first assuming that $\Delta' = 0$. This simplification is motivated by the fact that the tearing parameter Δ' is not a fundamental component of the MTM, and it was found in Ref. [115] that the magnetic curvature-drift instability was able to occur even for $\Delta' = 0$.

The dispersion relation, as a fourth order equation in $\hat{\omega}$, yields four separate roots. The behavior of these roots with the variation of the key parameters η and $\hat{\omega}_D$ is studied. A benefit of plotting all modes is that, since there are some issues in the numerical solver with root tracking / labeling, it is easier to discern the important behavior. A key difficulty arises in identifying the roots of the dispersion relation, and looking at the behavior of these roots with various parameters can help in this process.

Figure 6.8 shows the roots of the dispersion relation with $\hat{\omega}_D = 0$ and $\tau = 1$. There is a root with features of the drift-tearing mode, with a real frequency $\hat{\omega} \approx 1 + 4\eta/3$, which is stable. Since all frequencies are normalized to ω_n^*, a positive real frequency indicates the electron direction.

Figure 6.9 shows the dependence of the roots on the magnetic drift frequency $\hat{\omega}_D$ for $\eta = 10$. It can be seen that there is an unstable root for positive $\hat{\omega}_D$ with the real frequency of this root in the electron direction, a consequence of mode coupling. The behavior on η for $\hat{\omega}_D = 1$ is given in Fig. 6.10, where it can be seen that this mode is destabilized by increasing η, although there is no critical threshold. Although the characteristics of the instability share many qualities with the MTM, more work remains to confidently identify the modes present in the dispersion relation and their relationship to the MTM.

In Fig. 6.11 is shown the dependence of the instability growth rate on $R = -\Delta'\hat{\omega}c^2/(d\omega_{pe}^2) \propto \beta^{-1}$. The existence of a threshold near $R \approx 500$ implies that there is a critical β value, a feature of the MTM.

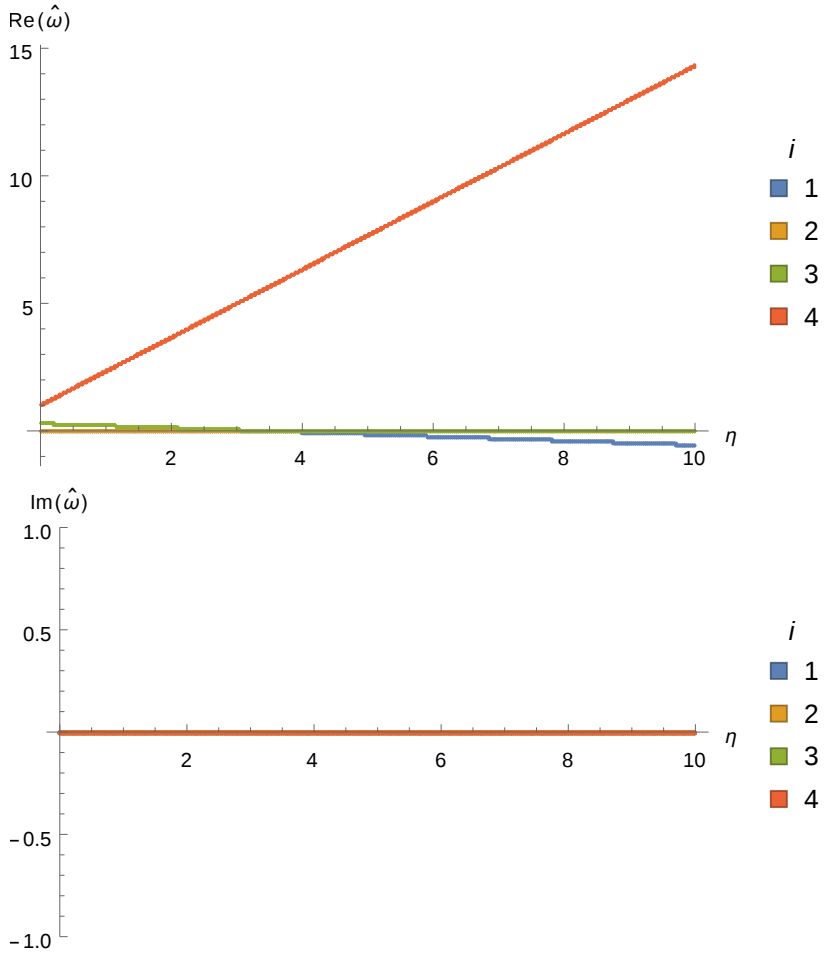

Figure 6.8: Real frequency (top plot) and growth rate (bottom plot) as functions of η for $\hat{\omega}_D = 0$. All roots of the dispersion relation are shown. Quantities are normalized to ω_n^*. Root 4 has features of the drift-tearing mode, with $\omega \approx 1 + 4\eta/3$ and in the direction of ω_n^* (electron direction). All roots are stable.

6.7 Chapter Summary

The role of magnetic curvature drift in the collisionless microtearing mode was investigated using the drft-kinetic framework. Using an expansion in $\omega_D/(\omega - k_\parallel v_\parallel)$, the magnetic-drift-driven contributions to the parallel current were calculated and the effect on instability assessed.

It was demonstrated that including only $A_\parallel$ contributions to the parallel current, ignoring the inclusion of the electrostatic potential terms, results in no contribution from $\hat{\omega}_D$

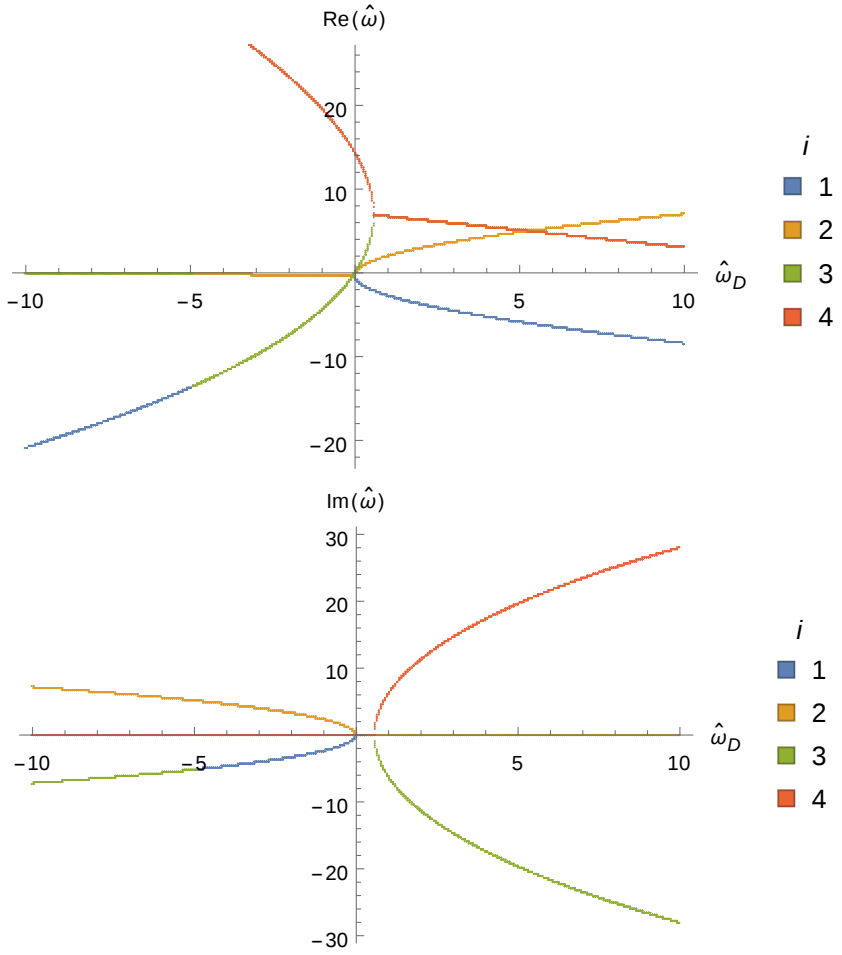

Figure 6.9: Real frequency (top plot) and growth rate (bottom plot) as functions of $\hat{\omega}_D$ for $\eta = 10$. Quantities are normalized to ω_n^*. For positive $\hat{\omega}_D$ a coupling occurs between modes, yielding an instability in the electron direction driven by the magnetic drift.

terms in Ampère's law. This indicates that, at least with the present assumptions, Φ is a necessary element of the instability. This is in agreement with some gyrokinetic simulations [68], although others find instability even in the absence of Φ fluctuations [70], and so there may be mechanisms for instability not considered here.

Including Φ terms and expanding terms in the large-s yielded a fourth order dispersion relation with several unstable roots. The dependence of these roots on $\hat{\omega}_D$ and η was investigated, and it was found that for some value of $\hat{\omega}_D$ an instability occurs as the result of a coupling between an apparent drift-tearing mode and a curvature driven mode. This

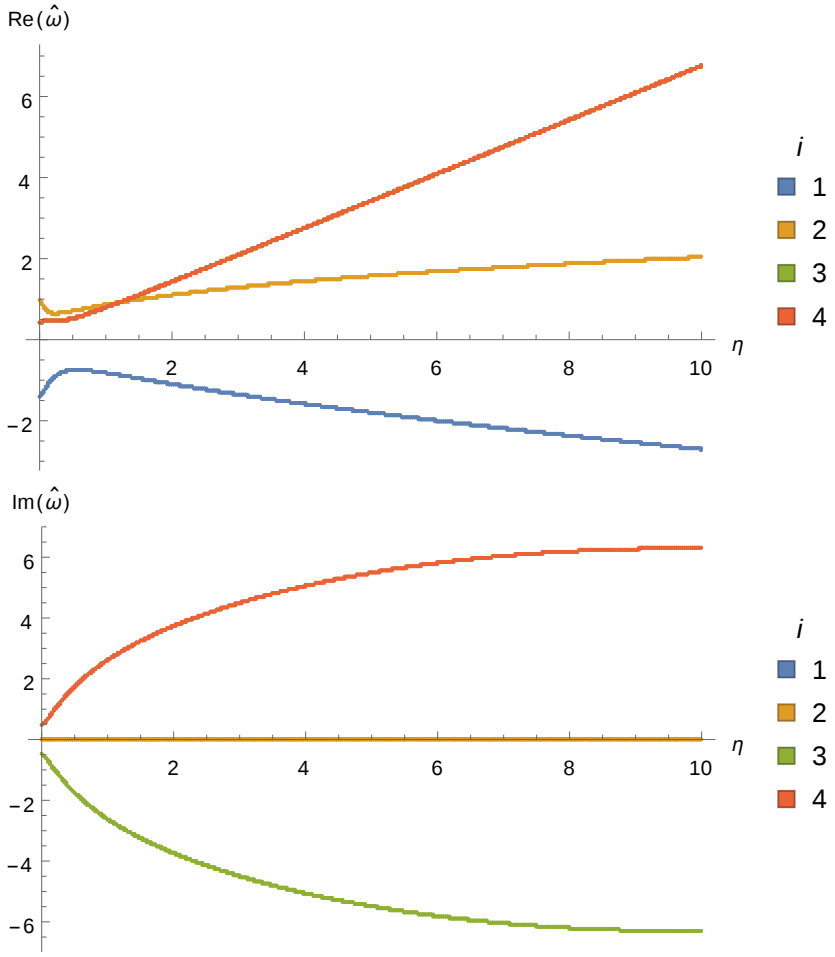

Figure 6.10: Real frequency (top plot) and growth rate (bottom plot) as functions of η for $\hat{\omega}_D = 1$. Quantities are normalized to ω_n^*. The parameter η is destabilizing, although there is no critical threshold.

instability has some features of the collisionless MTM, including a frequency in the electron direction, a dependence on η, and a critical β, but more work remains to make a positive identification. Specifically, this would take the form of detailed comparisons between the roots of the dispersion relation and gyrokinetic simulations. Particular care must be taken in considering the relative normalizations and definitions, especially for the magnetic drifts.

It should also be noted that there is evidence that multiple instability mechanisms exist [70], possibly associated with the magnetic shear and the density gradient. The effect of these parameters in the current derivation was not considered. There are several

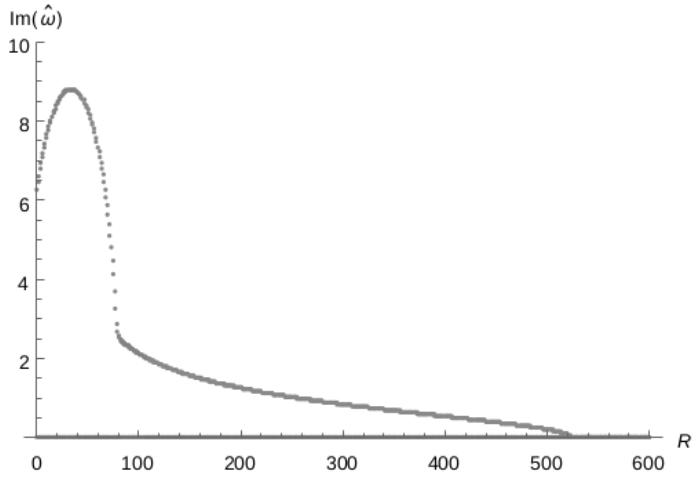

Figure 6.11: Growth rate versus $R = -\Delta'\hat{\omega}c^2/(d\omega_{pe}^2) \propto \beta^{-1}$ for the $\hat{\omega}_D$-driven mode with $\eta = 10$ and $\hat{\omega}_D = 1$. The growth rate goes to zero near $R \approx 500$, implying that there is a critical β threshold for this instability.

additional avenues for potential further exploration, including taking higher order terms in the expansions and considering more carefully the effect of the tearing layer width. A finite, positive Δ' may also have important effects on the instability spectrum.

Chapter 7

Conclusions

Years of progress in experimental RFP research have lead to conditions of enhanced heat and particle confinement, in which microinstability-driven turbulence is expected to be making contributions to heat and particle transport. This thesis presented a theoretical analysis of the microturbulence characteristics of the reversed field pinch using the gyrokinetic framework, with particular attention paid to the experimental conditions of the Madison Symmetric Torus.

The reversed field pinch has made serious advances as a magnetic confinement fusion concept in recent years. Improved confinement regimes in the RFP have been responsible for increases in the energy confinement time by at least a factor of ten. As the RFP continues to find innovative ways to improve confinement and heating, the effects of microinstabilities on transport will play an ever increasing role. As experimental techniques are developed and implemented to assess this role, it is important to develop concurrently the ability to characterize and understand these instabilities from a theoretical perspective. One way this is realized is in the identification of the likely instabilities for particular MST discharges and their identifying characteristics. This also takes the form of various scaling relationships that determine how instability properties, such as linear growth rate or nonlinear fluxes, depend on important parameters such as machine size, β, temperature, density, magnetic field geometry, and magnetic diffusivity. The major results presented in this work are now

summarized below.

7.1 Summary of Results

The first obstacle to modeling gyroscale physics in the RFP is to incorporate an accurate RFP equilibrium model into the gyrokinetic framework. This was done in the present work through the use of two different models: the toroidal Bessel function model (TBFM) and the adjusted circular model (ACM), the latter of which is now incorporated into the GENE code. Both of these models enable the key elements of the RFP geometry – namely, low q and high magnetic shear – to be implemented into numerical gyrokinetic solvers. Although both models are limited by the requirement of circular flux surfaces, this is a condition well satisfied in most MST discharges. While the TBFM is best suited for low-Θ discharges, which are more reflective of 'standard' MST discharges and therefore less likely to have microinstability-driven physics play an important role, the ACM is flexible enough to model more general axisymmetric RFP geometries. In particular, this includes the improved confinement PPCD discharges in which microinstabilities are expected to be present and perhaps dominating the turbulent spectrum.

Linear Results

This present work (along with the work of others) has shown that many of the microinstabilities known from tokamak studies may also arise in the RFP. This list includes ion-temperature gradient modes, trapped electron modes, and microtearing modes.

Ch. 4 described the results of fundamental studies of drift wave instabilities in the RFP using the TBFM implemented in the GYRO code, and this work was originally published in Carmody et al. (2014) [55]. In this geometry, two drift wave instabilities were identified: the ion temperature gradient (ITG) mode, and the microtearing mode (MTM). Although similar in many of their fundamental characteristics, such as drive mechanism and parameter dependencies, the RFP versions of these instabilities differ in several important ways to their tokamak counterparts. Among these differences is the location of critical parameter values

for instability onset, which have been found to be dependent on geometric characteristics. The gradient thresholds, for instance, are found to be larger than in the tokamak by roughly a factor of the aspect ratio, so that $(R/L)^{\text{crit}}_{\text{tok}} \approx (a/L)^{\text{crit}}_{\text{RFP}}$. A similar relationship was found for the ITG suppression β limit. The MTM was found to be stabilized by the RFP pinch parameter Θ (associated with higher magnetic shear), a property that suggests the MTM is unlikely to be unstable in high-Θ PPCD discharges.

One instability missing from all RFP gyrokinetic results so far is the kinetic ballooning mode (KBM), an electromagnetic instability driven by the pressure gradient. This is related to another important β consideration: the KBM β limit, the β value at which KBM becomes unstable, the ratio $\beta/\beta^{\text{crit}}_{\text{KBM}}$ serving as a proxy for other electromagnetic effects as well. The low q and high magnetic shear found in the RFP geometry can push this limit quite high, so that even in high β conditions (as compared to the tokamak) discharges may remain predominantly electrostatic with regard to the microturbulence characteristics. These effects were discussed in Ch. 5.

Linear results from two experimental PPCD discharges on the Madison Symmetric Torus were presented in Ch. 5, and those results have also been submitted in a paper to Physics of Plasmas [74]. These equilibria were modeled using the ACM implemented in the GENE code. From a microinstability standpoint, PPCD discharges can perhaps be best characterized in terms of their dominant gradient – i.e., whether a discharge is dominated by temperature gradients or by density gradients to a large extent determines the type of instability that will be most unstable. This dominance can be determined in a quantitative way through the parameter $\eta \equiv (\nabla T/T)/(\nabla n/n)$. It was found that for $\eta_i < 1.2 - 1.4$ the dominant instability is likely to be density-gradient-driven TEM, and for $\eta_i > 1.2 - 1.4$ ITG is the likely instability, although other parameters, such as temperature ratio, also enter into the picture and there is perhaps not a rigid boundary. Within the range $\eta_i = 1.2 - 1.4$ it is possible to have a hybrid mode with characteristics of both ITG and TEM. For TEM dominant discharges, the parameter η_e may be important for differentiating between density-gradient-driven TEM (expected for $\eta_e < 1$) and temperature-gradient-driven TEM (expected for

$\eta_e > 1$), a transition that holds for tokamaks but which was not explored in detail in the present work.

In Ch. 6 the linear collisionless MTM, seen in gyrokinetic simulations in some parameter regimes in the RFP (although not for typical PPCD discharges), was investigated analytically using the drift-kinetic formalism. The effect of magnetic drifts, ignored in many previous theories, was included using a fluid expansion. The mode was found to be stable in the absence of fluctuations in the electrostatic potential. Including the electrostatic potential led to a dispersion relation that contained roots with some of the properties of the MTM, including a frequency in the electron direction, a dependency on the electron temperature gradient and the magnetic drift frequency, and a threshold in β, although more work remains to positively identify this mode as the collisionless MTM.

Nonlinear Results

Results from the first nonlinear gyrokinetic evaluation of improved confinement PPCD discharges were presented in Ch. 5. These results have also been submitted to Physics of Plasma [74]. A discharge linearly unstable to density-gradient-driven TEM was modeled nonlinearly, and a large Dimits-like shift was found to occur, with the nonlinear density gradient threshold roughly a factor of three above the critical linear value. This shift, and the nonlinear saturation mechanism in general, was found to be due to the presence of strong zonal flows. Zonal flows are an important element of plasma turbulence as they act to suppress transport through shear flow and the transfer of energy to damped modes.

The nonlinear critical threshold was found to occur near the value of the experimental density gradient, but the electron heat diffusivity present in the simulations was well below experimental estimates. This discrepancy could be accounted for through the inclusion of added magnetic diffusivity. An important element of the RFP is the global tearing mode spectrum, and although this spectrum is largely suppressed in PPCD discharges, some residual activity may remain. To consider the effect of these residual tearing mode fluctuations, an imposed magnetic perturbation was added, leading to increased levels of

magnetic diffusivity. This resulted in the degradation of the zonal flows and an order of magnitude increase in the transport fluxes. Although the specific nature and strength of the imposed perturbation remains to be determined, it is apparent that the proper inclusion of residual magnetic fluctuations is an important part of gyrokinetic modeling in the RFP.

7.2 Future Work

The specific role played by the microinstabilities discussed in this thesis in the Madison Symmetric Torus is still an open topic, and understanding this role constitutes one of the main thrusts of future work. One path this could take is the development of synthetic diagnostics, so that the output of nonlienar simulations may be more directly compared with experimental measurements. There are also a variety of effects not considered in the present work, and the inclusion of these effects in modeling may have important consequences. For instance, all nonlinear runs performed in the preceding chapters used the local approximation, in which background quantities were assumed to vary linearly over some finite spatial domain. While often a good approximation, this assumption means that results are not entirely self-consistent. Performing global nonlinear runs could lead to new effects and different results, although global runs near or including the reversal surface present additional challenges associated with the low safety factor and high magnetic shear at that location.

Another issue of geometry that was not addressed is the simulation of the reversal surface. This location was not modeled due to difficulties posed by the high $\hat{s}$ and zero toroidal field. This is an area of some interest as the reversal surface lies at an intersection between the high gradients near the edge and the high β present in the core. As such, this location may enable the existence of electromagnetic instabilities not seen at other radii. This uncertainty is further compounded by the somewhat exotic nature of low q. While there is nothing inherently unmanageable about this parameter space, it does require some careful consideration. A full microinstability characterization of the RFP would likely be incomplete without the inclusion of this region.

Another important consideration is the large amount of uncertainty in several critical

experimental quantities. These include the temperature and density gradients, which may have uncertainties of as much as a factor of two (or more, in the case of the ion temperature), and the magnetic diffusivity, which for the radial locations of interest in the PPCD discharges is perhaps only known to within an order of magnitude. The magnetic diffusivity due to residual tearing mode activity is of particular importance for determining the nonlinear transport fluxes, and it was found that the fluxes were sensitive to the strength of the imposed resonant magnetic perturbation. Since the imposed pertubation has such an important effect on the saturation mechanism it may be expected that the Dimits shift will be smaller, and performing a gradient scan with the imposed magnetic diffusivity could yield important results.

Aside from geometrical or equilibrium effects, there are other physics effects that are of interest. The physics of damped modes is one that has been explored in some detail in tokamak turbulence, but the nature of these mechanisms in the RFP is as yet unknown. Damped modes may play a similar role in regulating turbulence in the RFP, but the exact nature of the energy transfer mechanisms still remains to be investigated.

Finally, more work remains to be done on the linear theory of the collisionless MTM. Although an unstable mode was found with many features of the MTM, comparisons with gyrokinetic simulations are needed to determine how well the modes present in the dispersion relation represent the behavior of the collisionless MTM.

Appendix A

Derivation of expressions for the collisionless microtearing mode

This appendix provides the derivation of the parallel current terms $J^{A_\parallel}_{\parallel,\omega_D}$ (Eq. (A.28)) and $J^{A_\parallel}_{\parallel,\bar{\omega}_D}$ (Eq. (A.29)) used in Ch. 6, as well as the relationship between Φ and $A_\parallel$ from the quasineutrality expression (Eq. (A.27)).

A.1 Parallel current

The non-adiabatic part of the distribution function is

$$g_e = -\frac{eF_M}{T_e}\frac{\omega-\bar{\omega}^*_T}{\omega-k_\parallel v_\parallel-\bar{\omega}_D}\left(\Phi-\frac{v_\parallel A_\parallel}{c}\right) \quad , \tag{A.1}$$

where e is the electric charge, c is the speed of light, $k_\parallel = k_y x/L_s$, L_s is the shear length scale, x is the distance from the rational surface $x = r-r_s$, $\bar{\omega}_T = \omega^*_n+\omega^*_T((v^2_\perp+v^2_\parallel)/v^2_{Te}-3/2)$, $\omega^*_n = -(k_y T_e/eB)(n'/n)$, $F_M = \pi^{-3/2}n_0 v^{-3}_{Te}\exp(-(v^2_\parallel+v^2_\perp)/v^2_{Te})$ is the Maxwellian distribution function, $v^2_{Te} = 2T_e/m_e$, T_e is the electron temperature, and n_0 is the background density. The form for the magnetic drift used here is $\bar{\omega}_D = \omega_D(v^2_\parallel/v^2_{Te}+v^2_\perp/2v^2_{Te})$, which represents the combination of both ∇B and curvature drifts in the zero β limit.

The part of the distribution function proportional to ω_D (ignoring terms of order ω^2_D)

is

$$g_{e,\omega_D} = -\frac{eF_M}{T_e}\frac{(\omega-\bar{\omega}_T^*)\bar{\omega}_D}{(\omega-k_\parallel v_\parallel)^2}\left(\Phi - \frac{v_\parallel A_\parallel}{c}\right) \quad , \tag{A.2}$$

and the $\omega_D = 0$ component is

$$g_{e,0} = -\frac{eF_M}{T_e}\frac{\omega-\bar{\omega}_T^*}{\omega-k_\parallel v_\parallel}\left(\Phi - \frac{v_\parallel A_\parallel}{c}\right) \quad . \tag{A.3}$$

A form for the parallel current ($J_{\parallel,\omega_D} = -e\int d^3v v_\parallel g_{e,\omega_D}$) may be determined from this expression via a number of steps. First, the $v_\perp$ dependence contained in $\bar{\omega}_T^*$, $\bar{\omega}_D$, and F_M can be removed analytically. What remains will then be written in terms of the derivatives of the plasma dispersion function, Z' and Z'':

$$Z(s) = \pi^{-1/2}\int_{-\infty}^{\infty} dt \frac{e^{-t^2}}{t-s} \quad , \tag{A.4}$$

$$Z'(s) = \pi^{-1/2}\int_{-\infty}^{\infty} dt \frac{e^{-t^2}}{(t-s)^2} = -\pi^{-1/2}\int_{-\infty}^{\infty} dt \frac{2t}{t-s}e^{-t^2} \quad , \tag{A.5}$$

$$Z''(s) = \pi^{-1/2}\int_{-\infty}^{\infty} dt \frac{2e^{-t^2}}{(t-s)^3} \quad . \tag{A.6}$$

For the purpose of clarity, the curvature contribution to the parallel current will be broken up into separate terms,

$$J_\parallel^{\omega_D} = J_{\parallel,\omega_D}^{\Phi} + J_{\parallel,\omega_D}^{A_\parallel} \quad , \tag{A.7}$$

with

$$J_{\parallel,\omega_D}^{\Phi} = \frac{n_0 e^2 \pi^{-3/2}}{T_e}\frac{2\pi}{k_\parallel^2 v_{Te}}\int_0^\infty duu\int_{-\infty}^{\infty} dvv \frac{\omega\omega_D(v^2+u^2/2) - (\omega_n^* + \omega_T^*(v^2+u^2-3/2))\bar{\omega}_D}{(s-v)^2}e^{-v^2-u^2}\Phi \tag{A.8}$$

and

$$J_{\parallel,\omega_D}^{A_\parallel} = -\frac{n_0 e^2 \pi^{-3/2}}{T_e}\frac{2\pi}{k_\parallel^2 v_{Te}}\frac{v_{Te}}{c}\int_0^\infty duu\int_{-\infty}^{\infty} dvv^2 \frac{\omega\omega_D(v^2+u^2/2) - (\omega_n^* + \omega_T^*(v^2+u^2-3/2))\bar{\omega}_D}{(s-v)^2}e^{-v^2-u^2}A_\parallel \quad , \tag{A.9}$$

where $s = \omega/(k_\parallel v_{Te})$, $v = v_\parallel/v_{Te}$, and $u = v_\perp/v_{Te}$.

For performing various of the integrals over velocity space, the following formulae will also be useful:

$$\int_0^\infty dx x e^{-x^2} = \frac{1}{2}, \;\; \int_0^\infty dx x^3 e^{-x^2} = \frac{1}{2}, \;\; \int_0^\infty dx x^5 e^{-x^2} = 1 \tag{A.10}$$

and

$$\int_{-\infty}^\infty dx x^2 e^{-x^2} = \frac{\sqrt{\pi}}{2}, \;\; \int_{-\infty}^\infty dx x^3 e^{-x^2} = 0, \;\; \int_{-\infty}^\infty dx x^4 e^{-x^2} = \frac{3\sqrt{\pi}}{4}, \;\; \int_{-\infty}^\infty dx x^6 e^{-x^2} = \frac{15\sqrt{\pi}}{8} \quad . \tag{A.11}$$

First, we turn our attention to the $J^{\Phi}_{\parallel,\omega_D}$ term (Eq. (A.8)). The first term in the numerator will be designated by $J^{\Phi-1}_{\parallel,\omega_D}$ and the second by $J^{\Phi-2}_{\parallel,\omega_D}$. Performing the the u integral (to remove $v_\perp$ dependence) yields

$$\begin{aligned} J^{\Phi-1}_{\parallel,\omega_D} &= \frac{n_0 e^2 \pi^{-3/2}}{T_e} \frac{2\pi}{k_\parallel^2 v_{Te}} \int_0^\infty du u \int_{-\infty}^\infty dv v \frac{\omega \omega_D (v^2 + u^2/2)}{(s-v)^2} e^{-v^2-u^2} \Phi \\ &= \frac{n_0 e^2 \pi^{-3/2}}{T_e} \frac{2\pi}{k_\parallel^2 v_{Te}} \frac{1}{2} \int_{-\infty}^\infty dv v \frac{\omega \omega_D (v^2 + 1/2)}{(s-v)^2} e^{-v^2} \Phi \quad . \end{aligned} \tag{A.12}$$

Doing the same with $J^{\Phi-2}_{\parallel,\omega_D}$ yields

$$\begin{aligned} J^{\Phi-2}_{\parallel,\omega_D} = \frac{n_0 e^2 \pi^{-3/2}}{T_e} \frac{2\pi}{k_\parallel^2 v_{Te}} \int_0^\infty du u \int_{-\infty}^\infty dv v \\ \frac{-(\omega_n^* + \omega_T^*(v^2 + u^2 - 3/2))\omega_D (v^2 + u^2/2)}{(s-v)^2} e^{-v^2-u^2} \Phi \end{aligned} \tag{A.13}$$

$$\begin{aligned} J^{\Phi-2}_{\parallel,\omega_D} &= \frac{n_0 e^2 \pi^{-3/2}}{T_e} \frac{2\pi\omega_D}{k_\parallel^2 v_{Te}} \int_0^\infty du u \int_{-\infty}^\infty dv v \\ &\quad \frac{-v^2(\omega_n^* + \omega_T^*(v^2 + u^2 - 3/2)) - u^2/2(\omega_n^* + \omega_T^*(v^2 + u^2 - 3/2))}{(s-v)^2} e^{-v^2-u^2} \Phi \\ J^{\Phi-2}_{\parallel,\omega_D} &= \frac{n_0 e^2 \pi^{-3/2}}{T_e} \frac{2\pi\omega_D}{k_\parallel^2 v_{Te}} \frac{1}{2} \int_{-\infty}^\infty dv v \frac{-v^2(\omega_n^* + \omega_T^*(v^2 - 1/2)) - 1/2(\omega_n^* + \omega_T^*(v^2 + 1/2))}{(s-v)^2} e^{-v^2} \Phi \\ &= \frac{n_0 e^2 \pi^{-3/2}}{T_e} \frac{2\pi\omega_D}{k_\parallel^2 v_{Te}} \frac{1}{2} \int_{-\infty}^\infty dv v \frac{-v^2\omega_n^* - v^4\omega_T^* - 1/2(\omega_n^* + \omega_T^*/2)}{(s-v)^2} e^{-v^2} \Phi \quad . \end{aligned} \tag{A.14}$$

Now, we turn our attention to evaluating the $J^{A_\parallel}_{\parallel,\omega_D}$ term (Eq. (A.9)). The integral is almost the same as the $J^{\Phi}_{\parallel,\omega_D}$ term, but with an additional factor of $-v(v_{Te}/c)$. Again this

expression is broken up into two parts, $J_{\parallel,\omega_D}^{A_\parallel-1}$, given by

$$J_{\parallel,\omega_D}^{A_\parallel-1} = -\frac{n_0 e^2 \pi^{-3/2}}{T_e}\frac{2\pi}{k_\parallel^2 v_{Te}}\frac{1}{2}\frac{v_{Te}}{c}\int_{-\infty}^{\infty} dv v \frac{\omega\omega_D(v^3+v/2)}{(s-v)^2} e^{-v^2} A_\parallel \quad , \tag{A.15}$$

and $J_{\parallel,\omega_D}^{A_\parallel-2}$, given by

$$J_{\parallel,\omega_D}^{A_\parallel-2} = -\frac{n_0 e^2 \pi^{-3/2}}{T_e}\frac{2\pi\omega_D}{k_\parallel^2 v_{Te}}\frac{1}{2}\frac{v_{Te}}{c}\int_{-\infty}^{\infty} dv v \frac{-v^3\omega_n^* - v^5\omega_T^* - v/2(\omega_n^*+\omega_T^*/2)}{(s-v)^2} e^{-v^2} A_\parallel \tag{A.16}$$

Putting all this together, and recognizing that $n_0 e^2/T_e = 2\omega_{pe}^2/(4\pi v_{Te}^2)$, gives the following expressions:

$$J_{\parallel,\omega_D}^{\Phi} = \frac{\omega_{pe}^2}{4\pi}\frac{2\pi^{-1/2}}{k_\parallel}\frac{1}{v_{Te}^2}\frac{\omega_D}{k_\parallel v_{Te}}\int_{-\infty}^{\infty} dv \frac{\omega(v^3+v/2) - v^3\omega_n^* - v^5\omega_T^* - v/2(\omega_n^*+\omega_T^*/2)}{(s-v)^2} e^{-v^2}\Phi \tag{A.17}$$

and

$$J_{\parallel,\omega_D}^{A_\parallel} = -\frac{\omega_{pe}^2}{4\pi}\frac{2\pi^{-1/2}}{k_\parallel}\frac{1}{v_{Te}^2}\frac{\omega_D}{k_\parallel v_{Te}}\frac{v_{Te}}{c}\int_{-\infty}^{\infty} dv \frac{\omega(v^4+v^2/2)) - v^4\omega_n^* - v^6\omega_T^* - v^2/2(\omega_n^*+\omega_T^*/2)}{(s-v)^2} e^{-v^2} A_\parallel \quad . \tag{A.18}$$

To write in a slightly more compact way, and to compare with the $\omega_D = 0$ terms from Ref. [58], these expressions will be rewritten in terms of $Z'(s)$ and $Z''(s)$. These terms are sufficiently complex so as to prevent a simple and obvious identification as forms of derivatives of the plasma dispersion function. However, it is still possible to rewrite them in this form using a more formal method.

Rewriting the parallel current

To rewrite the parallel current terms given above, recognize that these expressions all can be written as a summation of integrals of the form

$$\int_{-\infty}^{\infty} dv \frac{\alpha v^n}{(s-v)^2} e^{-v^2} \quad ,$$

where n is an integer and α indicates some coefficient independent of v (although through $k_{\|}$ it does have a dependency on s).

Integrals of this form can be rewritten in terms of $Z'(s)$ and $Z''(s)$ using a series of algebraic manipulations and integration by parts operations. This is done for polynomials up to v^6, with the steps written out explicitly for a few of the expressions as examples.

$$\int_{-\infty}^{\infty} dv \frac{1}{(s-v)^2} e^{-v^2} = \pi^{1/2} Z'(s)$$

$$\int_{-\infty}^{\infty} dv \frac{v}{(s-v)^2} e^{-v^2} = -\pi^{1/2} Z''(s)/2$$

$$\begin{aligned}
\int_{-\infty}^{\infty} dv \frac{v^2}{(s-v)^2} e^{-v^2} &= \frac{1}{2} \int_{-\infty}^{\infty} dv \left[\frac{1}{(s-v)^2} + \frac{2v}{(s-v)^3} \right] e^{-v^2} \\
&= \pi^{1/2} Z'(s)/2 + \int_{-\infty}^{\infty} dv \frac{-(s-v)+s}{(s-v)^3} e^{-v^2} \\
&= \pi^{1/2} Z'(s)/2 - \pi^{1/2} Z'(s) - \pi^{1/2} s Z''(s)/2 \\
&= \pi^{1/2} \left(-\frac{1}{2} Z'(s) - \frac{1}{2} s Z''(s) \right)
\end{aligned}$$

$$\begin{aligned}
\int_{-\infty}^{\infty} dv \frac{v^3}{(s-v)^2} e^{-v^2} &= \frac{1}{2} \int_{-\infty}^{\infty} dv \left[\frac{2v}{(s-v)^2} + \frac{2v^2}{(s-v)^3} \right] e^{-v^2} \\
&= -\pi^{1/2} Z''(s)/2 + \int_{-\infty}^{\infty} dv \frac{-v(s-v) - s(s-v) + s^2}{(s-v)^3} e^{-v^2} \\
&= -\pi^{1/2} Z''(s)/2 + \pi^{1/2} Z''(s)/2 - s\pi^{1/2} Z'(s) - s^2 \pi^{1/2} Z''(s)/2 \\
&= \pi^{1/2} \left(-s Z'(s) - \frac{1}{2} s^2 Z''(s) \right)
\end{aligned}$$

$$\int_{-\infty}^{\infty} dv \frac{v^4}{(s-v)^2} e^{-v^2} = \pi^{1/2} \left(\left(-\frac{1}{4} - s^2 \right) Z'(s) + \left(\frac{1}{4} s - \frac{1}{2} s^3 \right) Z''(s) \right)$$

$$\int_{-\infty}^{\infty} dv \frac{v^5}{(s-v)^2} e^{-v^2} = \pi^{1/2} \left(\left(-\frac{1}{2} s - s^3 \right) Z'(s) + \left(\frac{1}{2} s^2 - \frac{1}{2} s^4 \right) Z''(s) \right)$$

$$\int_{-\infty}^{\infty} dv \frac{v^6}{(s-v)^2} e^{-v^2} = \pi^{1/2} \left(\left(-\frac{3}{8} - s^4 \right) Z'(s) + \left(\frac{3}{8}s + \frac{3}{4}s^3 - \frac{1}{2}s^5 \right) Z''(s) \right)$$

With these expressions we can now express $J^{\Phi}_{\parallel,\omega_D}$ and $J^{A_\parallel}_{\parallel,\omega_D}$ in terms of derivatives of $Z(s)$.

The Φ component of the magnetic-drift-driven parallel current (Eq. (A.17)) becomes

$$J^{\Phi}_{\parallel,\omega_D} = \frac{\omega_{pe}^2}{4\pi} \frac{2}{k_\parallel} \frac{1}{v_{Te}^2} s \frac{\omega_D}{\omega} \left[\left(s^3 \omega_T^* - s \left(\omega - \omega_n^* - \frac{1}{2}\omega_T^* \right) \right) Z'(s) \right.$$
$$\left. + \left(\frac{1}{2}s^4 \omega_T^* - \frac{1}{2}s^2 \left(\omega - \omega_n^* + \omega_T^* \right) - \frac{1}{4} \left(\omega - \omega_n^* - \frac{1}{2}\omega_T^* \right) \right) Z''(s) \right] \Phi \quad , \tag{A.19}$$

while the $A_\parallel$ component (Eq. (A.18)) becomes,

$$J^{A_\parallel}_{\parallel,\omega_D} = -\frac{1}{\omega} \frac{\omega_{pe}^2}{4\pi} \frac{2}{v_{Te}^2} \frac{v_{Te}^2}{c} \frac{\omega_D}{\omega} A_\parallel s^2 \left[\left(s^4 \omega_T^* - s^2 \left(\omega - \omega_n^* \right) - \frac{1}{2} \left(\omega - \omega_n^* - \omega_T^* \right) \right) Z'(s) \right.$$
$$\left. + \left(\frac{1}{2}s^5 \omega_T^* - \frac{1}{2}s^3 \left(\omega - \omega_n^* + \frac{3}{2}\omega_T^* \right) - \frac{1}{4}s\omega_T^* \right) Z''(s) \right] \tag{A.20}$$

Quasineutrality

It will also be necessary to have a relationship between Φ and $A_\parallel$. This comes from the quasineutrality equation, which is given as

$$\frac{n_0 e^2 \Phi}{T_e} (1+\tau) = e \int d^3 v g_e \quad , \tag{A.21}$$

where g_e is the non-adiabatic part of the distribution function (Eq. (A.1)) and where n_0 is the background plasma density and $\tau = T_e/T_i$. Ions are assumed to be adiabatic, so that $g_i = 0$ and $f_i = -\frac{e\Phi}{T_i} f_M$.

As before, an expansion is performed, and this is broken up into ω_D and $\omega_D = 0$ terms. After performing the $v_\perp$ integral, the non-magnetic-drift term becomes (coming from integrating Eq. (A.3))

$$e \int d^3 v g_{e,0} = -\left(\frac{n_0 e^2}{T_e} \right) \frac{2\pi^{-1/2}}{k_\parallel v_{Te}} \frac{1}{2} \left[\Phi \int_{-\infty}^{\infty} dv \frac{\omega - \omega_n^* \omega_T^* (v^2 - 1/2)}{s - v} e^{-v^2} \right.$$
$$\left. - \frac{v_{Te}}{c} A_\parallel \int_{-\infty}^{\infty} dv \; v \; \frac{\omega - \omega_n^* \omega_T^* (v^2 - 1/2)}{s - v} e^{-v^2} \right] \quad . \tag{A.22}$$

Separating this into the Φ and $A_\parallel$ components and writing in terms of Z' and Z'' yields

$$e\int d^3v g^{\Phi}_{e,0} = -\left(\frac{n_0e^2}{T_e}\right)\frac{1}{k_\parallel v_{Te}}\left[s(\omega-\omega_n^*)Z'(s)+\frac{1}{2}\left(\omega-\omega_n^*+\frac{1}{2}\omega_T^*\right)Z''(s)\right]\Phi \quad \text{(A.23)}$$

and

$$e\int d^3v g^{A_\parallel}_{e,0} = \left(\frac{n_0e^2}{T_e}\right)\frac{1}{k_\parallel v_{Te}}\left[\frac{1}{2}(\omega-\omega_n^*)Z'(s)+\left(\frac{s}{4}\omega_T^*\right)Z''(s)\right]\frac{v_{Te}}{c}A_\parallel \quad . \quad \text{(A.24)}$$

As before, the curvature contributions can be broken up into Φ and $A_\parallel$ components. The derivation of these terms proceeds in a similar manner to that of the parallel current, with the integrands differing by a factor of $(-v_\parallel)$. The result of this for g^{Φ}_{e,ω_D} is

$$\begin{aligned} e\int d^3v g^{\Phi}_{e,\omega_D} &= -\left(\frac{n_0e^2\pi^{-1/2}\omega_D}{T_e(k_\parallel v_{Te})^2}\right)\int_{-\infty}^{\infty}dv\frac{\omega(v^2+1/2)-v^2\omega_n^*-v^4\omega_T^*-(\omega_n^*+\omega_T^*/2)/2}{(s-v)^2}e^{-v^2}\Phi \\ &= -\left(\frac{n_0e^2\omega_D}{T_e(k_\parallel v_{Te})^2}\right)\left[s^2\omega_T^*Z'(s)+\frac{1}{2}\left(s^3\omega_T^*-\frac{s}{2}\left(\omega-\omega_n^*+\frac{1}{2}\omega_T^*\right)\right)Z''(s)\right]\Phi \quad , \end{aligned} \quad \text{(A.25)}$$

and for $g^{A_\parallel}_{e,\omega_D}$ this is

$$\begin{aligned} e\int d^3v g^{A_\parallel}_{e,\omega_D} &= \left(\frac{n_0e^2}{T_e}\right)\frac{1}{k_\parallel v_{Te}}\frac{\omega_D}{k_\parallel v_{Te}}\frac{v_{Te}}{c}\int_{-\infty}^{\infty}dv \\ &\quad \frac{\omega(v^3+v/2))-v^3\omega_n^*-v^5\omega_T^*-v/2(\omega_n^*+\omega_T^*/2)}{(s-v)^2}e^{-v^2}A_\parallel \\ &= \left(\frac{n_0e^2}{T_e}\right)\frac{1}{k_\parallel v_{Te}}\frac{\omega_D}{k_\parallel v_{Te}}\left[\left(s^3\omega_T^*-s\left(\omega-\omega_n^*-\frac{1}{2}\omega_T^*\right)\right)Z'(s)\right. \\ &\quad \left.+\left(\frac{1}{2}s^4\omega_T^*-\frac{1}{2}s^2\left(\omega-\omega_n^*+\omega_T^*\right)-\frac{1}{4}\left(\omega-\omega_n^*-\frac{1}{2}\omega_T^*\right)\right)Z''(s)\right]\frac{v_{Te}}{c}A_\parallel \quad . \end{aligned} \quad \text{(A.26)}$$

Schematically, the form that Φ takes is

$$\Phi \sim \frac{\int g^{A_\parallel}_{e,\omega_D}+\int g^{A_\parallel}_{e,0}}{\frac{n_0e^2}{T_e}(1+\tau)+\int g^{\Phi}_{e,\omega_D}+\int g^{\Phi}_{e,0}}A_\parallel \quad .$$

Combining all terms and solving for Φ, we arrive at the following expression,

$$\begin{aligned}\Phi = \frac{v_{Te}}{c}A_{\parallel}\Bigg[\Bigg[s^4\hat{\omega}_D\eta - s^2\hat{\omega}_D\left(\hat{\omega}-1-\eta/2\right)+\frac{\hat{\omega}}{2}(\hat{\omega}-1)\Bigg]Z'(s) \\ +\left[s^5\hat{\omega}_D\eta - s^3\hat{\omega}_D(\hat{\omega}-1+\eta)+\frac{s}{2}(\hat{\omega}\eta-\hat{\omega}_D\hat{\omega}+\hat{\omega}_D+\hat{\omega}_D\eta/2))\right]Z''(s)/2\Bigg]\Big/ \\ \left[(1+\tau)\hat{\omega}^2/s+\left[s^3\hat{\omega}_D\eta+s\hat{\omega}(\hat{\omega}-1)\right]Z'(s)\right. \\ \left.+\left[s^4\hat{\omega}_D\eta-s^2\hat{\omega}_D(\hat{\omega}-1+\eta/2)+\hat{\omega}(\hat{\omega}+\eta/2-1)\right]Z''(s)/2\right] \quad ,\end{aligned} \tag{A.27}$$

where all frequencies are normalized to ω_n^*, so that $\hat{\cdot} \equiv \cdot/\omega_n^*$ and $\eta \equiv \omega_T^*/\omega_n^*$.

The parallel current terms derived before are restated here with the same normalization:

$$\begin{aligned}J_{\parallel,A_\parallel}^{\omega_D} = -\frac{\omega_{pe}^2}{4\pi c}\frac{2\hat{\omega}_D}{\hat{\omega}^2}s^2\Bigg[\left(s^4\eta-s^2(\hat{\omega}-1)-\frac{1}{2}(\hat{\omega}-1-\eta)\right)Z'(s) \\ +\left(\frac{1}{2}s^5\eta-\frac{1}{2}s^3\left(\hat{\omega}-1+\frac{3}{2}\eta\right)-\frac{1}{4}s\eta\right)Z''(s)\Bigg]A_\parallel\end{aligned} \tag{A.28}$$

and

$$\begin{aligned}J_{\parallel,\Phi}^{\omega_D} = \frac{\omega_{pe}^2}{4\pi c}\frac{2\hat{\omega}_D}{\hat{\omega}^2}s^2\Bigg[\left(s^3\eta-s\left(\hat{\omega}-1-\frac{1}{2}\eta\right)\right)Z'(s) \\ +\left(\frac{1}{2}s^4\eta-\frac{1}{2}s^2\left(\hat{\omega}-1+\eta\right)-\frac{1}{4}\left(\hat{\omega}-1-\frac{1}{2}\eta\right)\right)Z''(s)\Bigg]\left(\frac{c}{v_{Te}}\right)\Phi \quad .\end{aligned} \tag{A.29}$$

Eqs. (A.27), (A.28), and (A.29) provide the basis for important results derived in Ch. 6.

Bibliography

[1] R. Kerr, "How Much Coal Is Left," *Science*, vol. 323, p. 1420, 2009.

[2] J. Freidberg, *Plasma Physics and Fusion Energy*. Cambridge: Cambridge University Press, 2007.

[3] H. Bethe, "Energy Production in Stars," *Physical Review*, vol. 55, no. 5, p. 434, 1939.

[4] J. D. Lawson, "Some Criteria for a Power Producing Thermonuclear Reactor," *Proceedings of the Physical Society. Section B*, vol. 70, pp. 6–10, Jan. 1957.

[5] K. Ikeda, "ITER on the road to fusion energy," *Nuclear Fusion*, vol. 50, p. 014002, Jan. 2010.

[6] W. Horton, "Drift waves and transport," *Society*, vol. 71, no. 3, pp. 735–778, 1999.

[7] National Research Council (U.S.). Plasma 2010 Committee, *Plasma science: advancing knowledge in the national interest*. Washington, D.C.: National Academies Press, 2007.

[8] J. Candy and R. E. Waltz, "Anomalous Transport Scaling in the DIII-D Tokamak Matched by Supercomputer Simulation," *Physical Review Letters*, vol. 91, pp. 4–7, July 2003.

[9] M. Fahey and J. Candy, "GYRO: A 5-D Gyrokinetic-Maxwell Solver," *Proceedings of the ACM/IEEE SC2004 Conference*, pp. 26–26, 2008.

[10] F. Jenko, W. Dorland, M. Kotschenreuther, and B. N. Rogers, "Electron temperature gradient driven turbulence," *Physics of Plasmas*, vol. 7, no. 5, 2000.

[11] G. code, "http://gene.rzg.mpg.de."

[12] A. J. Brizard and T. S. Hahm, "Foundations of nonlinear gyrokinetic theory," *Reviews of Modern Physics*, vol. 79, p. 421, 2007.

[13] J. R. Cary and R. G. Littlejohn, "Noncanonical Hamiltonian mechanics and its application to magnetic field line flow," *Annals of Physics*, vol. 151, pp. 1–34, Nov. 1983.

[14] T. Goerler, *Multiscale Effects in Plasma Microturbulence*. PhD thesis, University of Ulm, 2009.

[15] M. J. Pueschel, *Electromagnetic Effects in Gyrokinetic Simulations of Plasma Turbulence 2009*. PhD thesis, University of Munster, 2009.

[16] F. Merz, *Gyrokinetic Simulation of Multimode Plasma Turbulence*. PhD thesis, University of Munster, 2008.

[17] X. Lapillonne, *Local and global Eulerian gyrokinetic simulations of microturbulence in realistic geometry with applications to the TCV Tokamak*. PhD thesis, École polytechnique fédérale de Lausanne, 2009.

[18] J. Candy and R. E. Waltz, "An Eulerian gyrokinetic-Maxwell solver," *Journal of Computational Physics*, vol. 186, pp. 545–581, Apr. 2003.

[19] E. A. Frieman, "Nonlinear gyrokinetic equations for low-frequency electromagnetic waves in general plasma equilibria," *Physics of Fluids*, vol. 25, no. 3, p. 502, 1982.

[20] R. G. Littlejohn, "A guiding center Hamiltonian: A new approach," *Journal of Mathematical Physics*, vol. 20, no. 12, p. 2445, 1979.

[21] R. G. Littlejohn, "Linear relativistic gyrokinetic equation," *Physics of Fluids*, vol. 27, no. 4, p. 976, 1984.

[22] General Atomic Theory Group, "https://fusion.gat.com/."

[23] J. Candy and E. A. Belli, "GYRO Technical Guide," 2010.

[24] G. D. Team, "The Gyrokinetic Plasma Turbulence Code Gene : User Manual," 2013.

[25] X. Lapillonne, S. Brunner, T. Dannert, S. Jolliet, A. Marinoni, L. Villard, T. Goerler, F. Jenko, and F. Merz, "Clarifications to the limitations of the s-α equilibrium model for gyrokinetic computations of turbulence," *Physics of Plasmas*, vol. 16, no. 3, p. 032308, 2009.

[26] R. L. Miller, M. S. Chu, J. M. Greene, Y. R. Lin-Liu, and R. E. Waltz, "Noncircular, finite aspect ratio, local equilibrium model," *Physics of Plasmas*, vol. 5, no. 4, p. 973, 1998.

[27] J. B. Taylor, "Relaxation of Toroidal Plasma and Generation of Reverse Magnetic Fields," *Physical Review Letters*, vol. 33, pp. 1139–1141, Nov. 1974.

[28] S. C. Prager, A. F. Almagri, S. Assadi, J. A. Beckstead, R. N. Dexter, D. J. Den Hartog, G. Chartas, S. a. Hokin, T. W. Lovell, T. D. Rempel, J. S. Sarff, W. Shen, C. W. Spragins, and J. C. Sprott, "First results from the Madison Symmetric Torus reversed field pinch," *Physics of Fluids B: Plasma Physics*, vol. 2, no. 6, p. 1367, 1990.

[29] T. D. Rempel, A. F. Almagri, S. Assadi, D. J. Den Hartog, S. A. Hokin, S. C. Prager, J. S. Sarff, W. Shen, K. L. Sidikman, C. W. Spragins, J. C. Sprott, M. R. Stoneking, and E. J. Zita, "Turbulent transport in the Madison Symmetric Torus reversed-field pinch," *Physics of Fluids B: Plasma Physics*, vol. 4, no. 7, p. 2136, 1992.

[30] J. S. Sarff, A. F. Almagri, M. Cekic, C.-S. Chaing, D. Craig, D. J. Den Hartog, G. Fiksel, S. A. Hokin, R. W. Harvey, H. Ji, C. Litwin, S. C. Prager, D. Sinitsyn, C. R. Sovinec, J. C. Sprott, and E. Uchimoto, "Transport reduction by current profile control in the reversed-field pinch," *Physics of Plasmas*, vol. 2, no. 6, p. 2440, 1995.

[31] J. Sarff, N. Lanier, S. Prager, and M. Stoneking, "Increased Confinement and β by Inductive Poloidal Current Drive in the Reversed Field Pinch," *Physical Review Letters*, vol. 78, pp. 62–65, Jan. 1997.

[32] B. E. Chapman, A. F. Almagri, J. K. Anderson, T. M. Biewer, P. K. Chattopadhyay, C.-S. Chiang, D. Craig, D. J. Den Hartog, G. Fiksel, C. B. Forest, A. K. Hansen, D. Holly, N. E. Lanier, R. OConnell, S. C. Prager, J. C. Reardon, J. S. Sarff, M. D. Wyman, D. L. Brower, W. X. Ding, Y. Jiang, S. D. Terry, P. Franz, L. Marrelli, and P. Martin, "High confinement plasmas in the Madison Symmetric Torus reversed-field pinch," *Physics of Plasmas*, vol. 9, no. 5, p. 2061, 2002.

[33] J. S. Sarff, A. F. Almagri, J. K. Anderson, T. M. Biewer, A. P. Blair, M. Cengher, B. E. Chapman, P. K. Chattopadhyay, D. Craig, D. J. D. Hartog, F. Ebrahimi, G. Fiksel, C. B. Forest, J. A. Goetz, D. Holly, B. Hudson, T. W. Lovell, K. J. McCollam, P. D. Nonn, R. O'Connell, S. P. Oliva, S. C. Prager, J. C. Reardon, M. A. Thomas, M. D. Wyman, D. L. Brower, W. X. Ding, S. D. Terry, M. D. Carter, V. I. Davydenko, A. A. Ivanov, R. W. Harvey, R. I. Pinsker, and C. Xiao, "Tokamak-like confinement at a high beta and low toroidal field in the MST reversed field pinch," *Nuclear Fusion*, vol. 43, pp. 1684–1692, Dec. 2003.

[34] B. E. Chapman, J. W. Ahn, A. F. Almagri, J. K. Anderson, F. Bonomo, D. L. Brower, D. R. Burke, K. Caspary, D. J. Clayton, S. K. Combs, W. A. Cox, D. Craig, B. H. Deng, D. J. Den Hartog, W. X. Ding, F. Ebrahimi, D. A. Ennis, G. Fiksel, C. B. Forest, C. R. Foust, P. Franz, S. Gangadhara, J. A. Goetz, M. C. Kaufman, J. G. Kulpin, A. Kuritsyn, R. M. Magee, M. C. Miller, V. V. Mirnov, P. D. Nonn, R. O'Connell, S. P. Oliva, S. C. Prager, J. A. Reusch, J. S. Sarff, H. D. Stephens, M. D. Wyman, and T. Yates, "Improved-confinement plasmas at high temperature and high beta in the MST RFP," *Nuclear Fusion*, vol. 49, p. 104020, Oct. 2009.

[35] D. J. Thuecks, C. A. Kletzing, F. Skiff, S. R. Bounds, and S. Vincena, "Tests of collision operators using laboratory measurements of shear Alfven wave dispersion and damping," *Physics of Plasmas*, vol. 16, no. 5, p. 052110, 2009.

[36] Y. Ren, A. Almagri, G. Fiksel, S. Prager, J. S. Sarff, and P. W. Terry, "Experimental Observation of Anisotropic Magnetic Turbulence in a Reversed Field Pinch Plasma," *Physical Review Letters*, vol. 107, pp. 1–5, Oct. 2011.

[37] M. Zuin, S. Spagnolo, I. Predebon, F. Sattin, F. Auriemma, R. Cavazzana, a. Fassina, E. Martines, R. Paccagnella, M. Spolaore, and N. Vianello, "Experimental Observation of Microtearing Modes in a Toroidal Fusion Plasma," *Physical Review Letters*, vol. 110, p. 055002, Jan. 2013.

[38] J. R. Duff, B. E. Chapman, J. S. Sarff, D. R. Carmody, P. W. Terry, D. J. Den Hartog, L. A. Morton, L. Lin, W. X. Ding, and D. L. Brower, "Measurement of high-frequency, small scale density fluctuations in improved confinement RFP plasmas," in *Bull. Am. Phys. Soc.*, 2014.

[39] D. J. Thuecks, A. F. Almagri, Y. Ren, J. S. Sarff, and P. W. Terry, "Characterization of electrostatic turbulence in the MST reversed field pinch," in *Bull. Am. Phys. Soc.*, 2010.

[40] B. V. Chirikov, "A universal instability of many-dimensional oscillator systems," *Physics Reports*, vol. 52, pp. 263–379, May 1979.

[41] R. N. Dexter, D. W. Kerst, T. W. Lovell, S. C. Prager, and J. C. Sprott, "The Madison Symmetric Torus," *Fusion Technology*, vol. 19, p. 131, 1991.

[42] J. K. Anderson, C. B. Forest, T. M. Biewer, J. S. Sarff, and J. C. Wright, "Equilibrium reconstruction in the Madison Symmetric Torus reversed field pinch," *Nuclear Fusion*, vol. 44, pp. 162–171, Jan. 2004.

[43] D. Craig, D. J. Den Hartog, G. Fiksel, V. I. Davydenko, and A. A. Ivanov, "First charge exchange recombination spectroscopy and motional Stark effect results from

the Madison Symmetric Torus reversed field pinch," *Review of Scientific Instruments*, vol. 72, no. 1, p. 1008, 2001.

[44] D. L. Brower, Y. Jiang, W. X. Ding, S. D. Terry, N. E. Lanier, J. K. Anderson, C. B. Forest, and D. Holly, "Multichannel far-infrared polarimeter-interferometer system on the MST reversed field pinch," *Review of Scientific Instruments*, vol. 72, no. 1, p. 1077, 2001.

[45] J. S. Sarff, S. A. Hokin, H. Ji, S. C. Prager, and C. R. Sovinec, "Fluctuation and Transport Reduction in a Reversed Field Pinch by Inductive Poloidal Current Drive," *Physical Review Letters*, vol. 72, no. 23, p. 3670, 1994.

[46] D. Escande, P. Martin, S. Ortolani, A. Buffa, P. Franz, L. Marrelli, E. Martines, G. Spizzo, S. Cappello, A. Murari, R. Pasqualotto, and P. Zanca, "Quasi-single-helicity reversed-field-pinch plasmas," *Physical review letters*, vol. 85, pp. 1662–5, Aug. 2000.

[47] J.-H. Kim and P. W. Terry, "Magnetic turbulence suppression by a helical mode in a cylindrical geometry," *Physics of Plasmas*, vol. 19, no. 12, p. 122304, 2012.

[48] A. B. Rechester and M. Rosenbluth, "Electron Heat Transport in a Tokamak with Destroyed Magnetic Surfaces," *Physical Review Letters*, vol. 40, no. 1, p. 38, 1978.

[49] J. W. Connor, R. J. Hastie, and J. B. Taylor, "Shear, Periodicity, and Plasma Ballooning Modes," 1978.

[50] V. Tangri, P. W. Terry, and R. E. Waltz, "A circular equilibrium model for local gyrokinetic simulations of ion temperature gradient fluctuations in reversed field pinches," *Physics of Plasmas*, vol. 18, no. 5, p. 052310, 2011.

[51] H. Grad and H. Rubin, "Hydrodynamic equilibria and force-free fields.," *Journal of Nuclear Energy*, vol. 7, no. 3, p. 284, 1954.

[52] V. D. Shafranov, "On Magnetohydrodynamical Equilibrium Configurations," *Soviet Journal of Experimental and Theoretical Physics*, vol. 6, no. 545, 1958.

[53] I. Predebon, F. Sattin, M. Veranda, D. Bonfiglio, and S. Cappello, "Microtearing Modes in Reversed Field Pinch Plasmas," *Physical Review Letters*, vol. 105, pp. 1–4, Nov. 2010.

[54] I. Predebon, C. Angioni, and S. C. Guo, "Gyrokinetic simulations of ion temperature gradient modes in the reversed field pinch," *Physics of Plasmas*, vol. 17, no. 1, p. 012304, 2010.

[55] D. Carmody, M. J. Pueschel, and P. W. Terry, "Gyrokinetic studies of microinstabilities in the reversed field pinch," *Physics of Plasmas*, vol. 20, no. 5, p. 052110, 2013.

[56] N. T. Gladd, J. F. Drake, C. L. Chang, and C. S. Liu, "Electron temperature gradient driven microtearing mode," *Phys. Fluids*, vol. 23, no. 2011, p. 1182, 1980.

[57] J. F. Drake, N. T. Gladd, C. S. Liu, and C. L. Chang, "Microtearing Modes and Anomalous Transport in Tokamaks," *Physical Review Letters*, vol. 44, no. 15, pp. 994–997, 1980.

[58] J. F. Drake and Y. C. Lee, "Kinetic theory of tearing instabilities," *Physics of Fluids*, vol. 20, no. 8, 1977.

[59] J. W. Connor, S. C. Cowley, and R. J. Hastie, "Micro-tearing stability in Tokamaks," *Plasma Physics*, vol. 799, 1990.

[60] A. B. Hassam, "Fluid theory of tearing instabilities," *Physics of Fluids*, vol. 23, no. 12, p. 2493, 1980.

[61] H. Doerk, F. Jenko, T. Goerler, D. Told, M. J. Pueschel, and D. R. Hatch, "Gyrokinetic prediction of microtearing turbulence in standard tokamaks," *Physics of Plasmas*, vol. 19, no. 5, p. 055907, 2012.

[62] H. Doerk, F. Jenko, M. J. Pueschel, and D. R. Hatch, "Gyrokinetic Microtearing Turbulence," *Physical Review Letters*, vol. 106, pp. 1–4, Apr. 2011.

[63] D. Dickinson, C. M. Roach, S. Saarelma, R. Scannell, A. Kirk, and H. R. Wilson, "Microtearing modes at the top of the pedestal," *Plasma Physics and Controlled Fusion*, vol. 55, p. 074006, July 2013.

[64] F. Porcelli, "Collisionless m=1 Tearing Mode," *Physical Review Letters*, vol. 66, no. 4, pp. 425–428, 1991.

[65] M. J. Pueschel and F. Jenko, "Transport properties of finite-β microturbulence," *Physics of Plasmas*, vol. 17, no. 6, p. 062307, 2010.

[66] A. Hirose, "On finite beta stabilization of the toroidal ion temperature gradient mode," *Physics of Plasmas*, vol. 7, no. 2, pp. 433–436, 2000.

[67] A. Jarmén, P. Andersson, and J. Weiland, "Fully toroidal ion temperature gradient driven drift modes," *Nuclear Fusion*, vol. 27, pp. 941–949, June 1987.

[68] D. J. Applegate, C. M. Roach, J. W. Connor, S. C. Cowley, W. D. Dorland, R. J. Hastie, and N. Joiner, "Micro-tearing modes in the mega ampere spherical tokamak," *Plasma Physics and Controlled Fusion*, vol. 49, pp. 1113–1128, Aug. 2007.

[69] W. Guttenfelder, J. Candy, S. Kaye, W. M. Nevins, E. Wang, R. Bell, G. Hammett, B. LeBlanc, D. Mikkelsen, and H. Yuh, "Electromagnetic Transport from Microtearing Mode Turbulence," *Physical Review Letters*, vol. 106, pp. 1–4, Apr. 2011.

[70] I. Predebon and F. Sattin, "On the linear stability of collisionless microtearing modes," *Physics of Plasmas*, vol. 20, no. 4, p. 040701, 2013.

[71] P. J. Catto and M. Rosenbluth, "Trapped electron modifications to tearing modes in the low collision frequency limit," *Phys. Fluids*, vol. 24, p. 243, 1981.

[72] J. M. Finn and J. F. Drake, "Magnetic curvature drift instability," *Physics of Fluids*, vol. 29, no. 11, p. 3672, 1986.

[73] D. Hatch, M. J. Pueschel, F. Jenko, W. Nevins, P. W. Terry, and H. Doerk, "Origin of Magnetic Stochasticity and Transport in Plasma Microturbulence," *Physical Review Letters*, vol. 108, pp. 1–5, June 2012.

[74] D. Carmody, M. J. Pueschel, and P. W. Terry, "Microturbulence studies of pulsed poloidal current drive discharges in the reversed field pinch," *submitted to Physics of Plasma*, 2014.

[75] G. Rewoldt and W. M. Tang, "Toroidal microinstability studies of high-temperature tokamaks," *Physics of Fluids B: Plasma Physics*, vol. 2, no. 2, p. 318, 1990.

[76] M. Kammerer, F. Merz, and F. Jenko, "Exceptional points in linear gyrokinetics," *Physics of Plasmas*, vol. 15, no. 5, p. 052102, 2008.

[77] D. R. Ernst, P. T. Bonoli, P. J. Catto, W. Dorland, C. L. Fiore, R. S. Granetz, M. Greenwald, A. E. Hubbard, M. Porkolab, M. H. Redi, J. E. Rice, and K. Zhurovich, "Role of trapped electron mode turbulence in internal transport barrier control in the Alcator C-Mod Tokamak," *Physics of Plasmas*, vol. 11, no. 5, p. 2637, 2004.

[78] D. R. Ernst, J. Lang, W. M. Nevins, M. Hoffman, Y. Chen, W. Dorland, and S. Parker, "Role of zonal flows in trapped electron mode turbulence through nonlinear gyrokinetic particle and continuum simulation," *Physics of Plasmas*, vol. 16, no. 5, p. 055906, 2009.

[79] B. Coppi, S. Migliuolo, and Y.-K. Pu, "Candidate mode for electron thermal energy transport in multi-keV plasmas," *Physics of Fluids B: Plasma Physics*, vol. 2, no. 10, p. 2322, 1990.

[80] M. J. Pueschel, M. Kammerer, and F. Jenko, "Gyrokinetic turbulence simulations at high plasma beta," *Physics of Plasmas*, vol. 15, no. 10, p. 102310, 2008.

[81] J. Citrin, F. Jenko, P. Mantica, D. Told, C. Bourdelle, R. Dumont, J. Garcia, J. W. Haverkort, G. M. D. Hogeweij, T. Johnson, and M. J. Pueschel, "Ion temperature profile stiffness: non-linear gyrokinetic simulations and comparison with experiment," *Nuclear Fusion*, vol. 54, p. 023008, Feb. 2014.

[82] A. Ishizawa, T.-H. Watanabe, H. Sugama, S. Maeyama, and N. Nakajima, "Electromagnetic gyrokinetic turbulence in finite-beta helical plasmas," *Physics of Plasmas*, vol. 21, p. 055905, May 2014.

[83] C. Z. Cheng, "Kinetic theory of collisionless ballooning modes," *Physics of Fluids*, vol. 25, no. 6, p. 1020, 1982.

[84] R. Y. Dagazian and R. B. Paris, "The effects of high shear on ideal ballooning," *Plasma Physics*, vol. 24, pp. 661–670, June 1982.

[85] J. Wesson, *Tokamaks*. London: Oxford University Press, 1997.

[86] P. H. Diamond, S.-I. Itoh, K. Itoh, and T. S. Hahm, "Zonal flows in plasma - a review," *Plasma Physics and Controlled Fusion*, vol. 47, pp. R35–R161, May 2005.

[87] D. R. Hatch, P. W. Terry, W. M. Nevins, and W. Dorland, "Role of stable eigenmodes in gyrokinetic models of ion temperature gradient turbulence," *Physics of Plasmas*, vol. 16, no. 2, p. 022311, 2009.

[88] P. W. Terry, "Suppression of turbulence and transport by sheared flow," *Reviews of Modern Physics*, vol. 72, pp. 109–165, Jan. 2000.

[89] A. M. Dimits, B. I. Cohen, N. Mattor, W. M. Nevins, D. E. Shumaker, S. E. Parker, and C. Kim, "Simulation of ion temperature gradient turbulence in tokamaks," *Nuclear Fusion*, vol. 40, pp. 661–666, Mar. 2000.

[90] K. D. Makwana, P. W. Terry, J.-H. Kim, and D. R. Hatch, "Damped eigenmode saturation in plasma fluid turbulence," *Physics of Plasmas*, vol. 18, no. 1, p. 012302, 2011.

[91] K. D. Makwana, P. W. Terry, and J.-H. Kim, "Role of stable modes in zonal flow regulated turbulence," *Physics of Plasmas*, vol. 19, no. 6, p. 062310, 2012.

[92] K. D. Makwana, P. W. Terry, M. J. Pueschel, and D. R. Hatch, "Subdominant Modes in Zonal-Flow-Regulated Turbulence," *Physical Review Letters*, vol. 112, p. 095002, Mar. 2014.

[93] J. Lang, S. E. Parker, and Y. Chen, "Nonlinear saturation of collisionless trapped electron mode turbulence: Zonal flows and zonal density," *Physics of Plasmas*, vol. 15, no. 5, p. 055907, 2008.

[94] T. S. Hahm, M. A. Beer, Z. Lin, G. W. Hammett, W. W. Lee, and W. M. Tang, "Shearing rate of time-dependent ExB flow," *Physics of Plasmas*, vol. 6, no. 3, 1999.

[95] P. Xanthopoulos, F. Merz, T. Görler, and F. Jenko, "Nonlinear Gyrokinetic Simulations of Ion-Temperature-Gradient Turbulence for the Optimized Wendelstein 7-X Stellarator," *Physical Review Letters*, vol. 99, p. 035002, July 2007.

[96] J. Lang, Y. Chen, and S. E. Parker, "Gyrokinetic δf particle simulation of trapped electron mode driven turbulence," *Physics of Plasmas*, vol. 14, no. 8, p. 082315, 2007.

[97] W. M. Nevins, E. Wang, and J. Candy, "Magnetic Stochasticity in Gyrokinetic Simulations of Plasma Microturbulence," *Physical Review Letters*, vol. 106, p. 065003, Feb. 2011.

[98] E. Wang, W. M. Nevins, J. Candy, D. R. Hatch, P. W. Terry, and W. Guttenfelder, "Electron heat transport from stochastic fields in gyrokinetic simulations," *Physics of Plasmas*, vol. 18, no. 5, p. 056111, 2011.

[99] D. R. Hatch, M. J. Pueschel, F. Jenko, W. M. Nevins, P. W. Terry, and H. Doerk, "Magnetic stochasticity and transport due to nonlinearly excited subdominant microtearing modes," *Physics of Plasmas*, vol. 20, no. 1, p. 012307, 2013.

[100] M. J. Pueschel, F. Jenko, M. Schneller, T. Hauff, S. Günter, and G. Tardini, "Anomalous diffusion of energetic particles: connecting experiment and simulations," *Nuclear Fusion*, vol. 52, p. 103018, Oct. 2012.

[101] M. J. Pueschel, P. W. Terry, and D. R. Hatch, "Aspects of the non-zonal transition," *Physics of Plasmas*, vol. 21, p. 055901, May 2014.

[102] T. Biewer, C. Forest, J. Anderson, G. Fiksel, B. Hudson, S. Prager, J. Sarff, J. Wright, D. Brower, W. Ding, and S. Terry, "Electron Heat Transport Measured in a Stochastic Magnetic Field," *Physical Review Letters*, vol. 91, pp. 1–4, July 2003.

[103] J. B. Taylor, "Relaxation and magnetic reconnection in plasmas," *Reviews of Modern Physics*, vol. 58, pp. 741–763, July 1986.

[104] B. Hudson, *Fast Ion Confinement in The Reversed-Field Pinch*. PhD thesis, University of Wisconsin - Madison, 2006.

[105] P. W. Terry, M. J. Pueschel, D. Carmody, and W. M. Nevins, "The effect of magnetic flutter on residual flow," *Physics of Plasmas*, vol. 20, no. 11, p. 112502, 2013.

[106] M. J. Pueschel, P. W. Terry, F. Jenko, D. R. Hatch, W. M. Nevins, T. Görler, and D. Told, "Extreme Heat Fluxes in Gyrokinetic Simulations: A New Critical Beta," *Physical Review Letters*, vol. 110, p. 155005, Apr. 2013.

[107] M. J. Pueschel, D. R. Hatch, T. Goerler, W. M. Nevins, F. Jenko, P. W. Terry, and D. Told, "Properties of high-β microturbulence and the non-zonal transition," *Physics of Plasmas*, vol. 20, no. 10, p. 102301, 2013.

[108] W. Guttenfelder, J. Candy, S. M. Kaye, W. M. Nevins, E. Wang, J. Zhang, R. E. Bell, N. A. Crocker, G. W. Hammett, B. P. LeBlanc, D. R. Mikkelsen, Y. Ren, and H. Yuh, "Simulation of microtearing turbulence in national spherical torus experiment," *Physics of Plasmas*, vol. 19, no. 5, p. 056119, 2012.

[109] R. D. Hazeltine, D. Dobrott, and T. S. Wang, "Kinetic theory of tearing instability," *Physics of Fluids*, vol. 18, no. 12, p. 1778, 1975.

[110] L. Vermare, C. Angioni, A. Bottino, and A. G. Peeters, "eta Dependence of Micro-Instabilities Using Linear Gyrokinetic Simulations," *Journal of Physics: Conference Series*, vol. 123, p. 012040, July 2008.

[111] H. P. Furth, J. Killeen, and M. N. Rosenbluth, "Finite-Resistivity Instabilities of a Sheet Pinch," *Physics of Fluids*, vol. 6, no. 4, p. 459, 1963.

[112] D. A. D'Ippolito, Y. C. Lee, and J. F. Drake, "Linear stability of high-m drift-tearing modes," *Physics of Fluids*, vol. 23, no. 4, p. 771, 1980.

[113] S. C. Cowley, R. M. Kulsrud, and T. S. Hahm, "Linear stability of tearing modes," *Plasma Physics and Fusion Technology*, vol. 17, no. 24, 1986.

[114] D. J. Applegate, *Gyrokinetic Studies of a Spherical Tokamak H-mode Plasma*. PhD thesis, University of London, 2007.

[115] J. M. Finn and J. F. Drake, "Magnetic Curvature-Drift Instability," *Physical Review Letters*, vol. 53, no. 24, pp. 2308–2311, 1984.